Volume II:
Near-Field and Altered-Zone Environment Report

Dale G. Wilder
Scientific Editor

August 1996

9960224 0019 - Part 3

DISCLAIMER

This document was prepared as an account of work sponsored by an agency of the United States Government. Neither the United States Government nor the University of California nor any of their employees, makes any warranty, express or implied, or assumes any legal liability or responsibility for the accuracy, completeness, or usefulness of any information, apparatus, product, or process disclosed, or represents that its use would not infringe privately owned rights. Reference herein to any specific commercial products, process, or service by trade name, trademark, manufacturer, or otherwise, does not necessarily constitute or imply its endorsement, recommendation, or favoring by the United States Government or the University of California. The views and opinions of authors expressed herein do not necessarily state or reflect those of the United States Government or the University of California and shall not be used for advertising or product endorsement purposes.

This report has been reproduced
directly from the best available copy.

Available to DOE and DOE contractors from the
Office of Scientific and Technical Information
P.O. Box 62, Oak Ridge, TN 37831
Prices available from (615) 576-8401, FTS 626-8401

Available to the public from the
National Technical Information Service
U.S. Department of Commerce
5285 Port Royal Rd.,
Springfield, VA 22161

Prepared by Yucca Mountain Site Characterization Project (YMP) participants as part of the Civilian Radioactive Waste Management Program. The YMP is managed by the Yucca Mountain Site Characterization Project Office of the U.S. Department of Energy, Las Vegas, Nevada.

Recycled
Recyclable

Contents

Chapter 1.0 Hydrothermal Modeling 1.1-2
1.1 Introduction 1.1-2
1.1.1 Organization of This Chapter 1.1-2
1.1.2 Key Thermal-Hydrological Issues for Site Viability and Waste Isolation 1.1-5
1.1.3 Modeling and Analysis Methodologies 1.1-11
1.2 Background and Available Data on Yucca Mountain 1.2-2
1.2.1 Matrix and Fracture Saturation 1.2-2
1.2.2 Infiltration and Percolation 1.2-10
1.3 Episodic Non-Equilibrium Fracture-Matrix Flow 1.3-2
1.3.1 Matrix-Dominated and Fracture-Dominated Flow Regimes 1.3-3
1.3.2 Implications of Flow Regimes on Engineered Barrier System/Near Field Performance 1.3-3
1.3.3 Summary of Fracture-Matrix Interaction at Yucca Mountain 1.3-4
1.4 Preferential Flow Pathways 1.4-2
1.5 Spatial and Temporal Variability of Percolation Flux 1.5-2
1.5.1 Observations of Percolation Flux 1.5-3
1.5.2 Controlling Inflow in Openings below the Water Table and its Implications for Fracture Characteristics 1.5-5
1.5.3 Conceptual Models 1.5-6
1.5.4 Comparison of Log-Normal Seepage Distribution to the Weeps Model 1-5-8
1.6 (REV 1) Impact of Repository Construction/Operational Activities 1.6-2
References 1.6-5
1.7 Thermal-Hydrological Processes 1.7-2
1.7.1 Fundamental Thermal-Hydrological-Geomechanical-Geochemical Processes 1.7-2
1.7.2 Fracture-Matrix Vapor Transport and Condensate Flow 1.7-4
1.7.3 Coupling with Geochemical Phenomena 1.7-8
1.7.4 Coupling with Geomechanical Phenomena 1.7-8
1.8 Understanding and Managing the Thermal-Hydrological Effects of Decay Heat 1.8-2
1.8.1 The Importance of Decay Heat on Moisture Movement and the Moisture Balance at Yucca Mountain 1.8-2
1.8.2 Thermal Loading Strategies 1.8-5
1.8.3 Importance of Thermal-Hydrology on Radionuclide Containment in Waste Packages 1.8-6
1.8.4 Importance of Thermal-Hydrology for Radionuclide Release and Transport 1.8-8
1.8.5 Major Thermal-Hydrological Flow Regimes 1.8-8
1.9 Thermal-Hydrological Testing 1.9-2
1.9.1 Overview 1.9-2
1.9.2 Use of Hypothesis Testing 1.9-3
1.9.3 Purpose of Thermal-Hydrological Testing 1.9-5
1.9.4 Factors Affecting Thermal Test Size and Duration 1.9-6
1.9.5 Physical Criteria Affecting Thermal Test Size and Duration 1.9-6
1.9.6 Numerical Models and Assumptions 1.9-8
1.9.7 Post-Test Analysis of G-Tunnel Single-Element Heater Test 1.9-11
1.9.8 Pre-Test Analysis of ESF Thermal Tests 1.9-13
1.10 Analysis of Drift-Scale Thermal-Hydrological Behavior in the Repository 1.10-2
1.10.1 Overview 1.10-2
1.10.2 Analysis of Localized and Extended Dryout Regimes 1.10-14
1.10.3 Performance Attributes of Engineered Backfill 1.10-19
1.10.4 Analysis of Engineered Backfill Scenarios for the FY95 Total Systems Performance Assessment (TSPA95) 1.10-23
1.10.5 Influence of Repository Design on Thermal-Hydrological Behavior 1.10-32
1.10.6 Influence of Ambient Percolation Flux and Edge-Cooling/Rewetting/Shedding Effects on Thermal-Hydrological Behavior 1.10-167
1.10.7 Comparison of Discrete-Fracture Model with Equivalent Continuum Model 1.10-225

References 1.10-229
Chapter 2.0 Laboratory-Determined Hydrologic Properties and Processes 2-2
2.1 Laboratory-Determined Hydrologic Properties 2-3
2.1.1 Moisture Retention at Elevated Temperatures 2-4
2.1.2 Water Permeability at Elevated Pressures and Temperatures 2-6
2.1.3 Electrical Resistivity as a Function of Water Saturation at Elevated Temperatures 2-7
2.1.4 Relative Humidity as a Function of Water Saturation at Elevated Temperatures 2-9
2.2 Laboratory Study of Thermal-Hydrological-Chemical Processes 2-11
2.2.1 Condensation Along a Fracture 2-11
2.2.2 Fracture Flow vs. Matrix Imbibition at Elevated Temperatures 2-14
2.2.3 Fracture Healing 2-19
2.3 References 2-22
Chapter 3.0 Geochemistry 3-2
3.1 Summary of Recent Studies Concerning Geochemical and Mineralogical Evolution of the Near-Field Environment 3-2
3.1.1 Near-Field Environment 3-2
3.2 Ambient Conditions 3-5
3.3 Processes That Will Modify Ambient Conditions Within the Near-Field Environment 3-6
3.3.1 References for Sections 3.1, 3.2 and 3.3 3-10
3.4 Results of Recent Geochemical Research Relating To Near-Field Geochemistry And Mineralogy 3-13
3.4.1 Equilibrium Bounds on Water Chemistry and Mineralogical Changes Produced by Near-Field Relative Humidity Changes, by William E. Glassley, Lawrence Livermore National Laboratory 3-13
3.4.2 Testing EQ3/6 and GEMBOCHS Using Fluid-Mineral Equilibria in the WairakeiGeothermal System, by Carol Bruton, Lawrence Livermore National Laboratory 3-21
3.4.3 Mineralogy-Petrology Observations Regarding the Near-Field Environment, by David L. Bish, J. William Carey, Schon S. Levy and Steve J. Chipera, Los Alamos National Laboratory 3-36
Chapter 4.0 Geomechanics 4-2
4.1 Introduction 4-2
4.2 Ambient Conditions 4-3
4.2.1 Physical, Thermal, and Mechanical Properties of Rock Mass and Intact Rock 4-3
4.2.2 Temperature and Stress 4-9
4.3 Processes That Perturb the Waste Package Environment 4-12
4.3.1 Excavation of the Repository 4-13
4.3.2 Thermal Effects of Waste Emplacement 4-13
4.3.3 Time-Dependent Effects 4-15
4.3.4 Radiation Effects of Waste Emplacement 4-17
4.3.5 Seismic Loading 4-18
4.4 Geomechanics Modeling 4-20
4.4.1 Discussion of Model Approaches 4-20
4.4.2 Applications to the Near Field Environment at Yucca Mountain 4-24
4.5 References 4-26
Chapter 5.0 Radiation Effects 5-2
5.1 Reference 5-2
Chapter 6.0 Introduced (Man-Made) Materials 6-2
6.1 Materials Identification and Evaluation 6-2
6.1.1 Original Post-Construction Conditions 6-2
6.1.2 Evaluation of Materials by Function 6-18
6.1.3 Tracers, Fluids and Materials Database: Retrieval of Information 6-22
6.1.4 Assessment of Materials Considered for Repository Construction 6-24
6.2 Post-Closure Chemical Processes That May Modify Predicted Geochemistry 6-25
6.2.1 Abiotic Chemistry 6-27

6.2.2 Biotic Chemistry (microbially mediated chemistry) 6-58
6.2.3 Discussion 6-74
6.3 Understanding the Processes 6-75
6.3.1 Experimental Studies 6-75
6.3.2 Historical Analogs as Long Term Experiments 6-83
6.3.3 Modeling Activities 6-84
6.4 Summary and Conclusions 6-95
6.5 Acknowledgments 6-95
Appendix A: Polymer Chemistry 6-112
Appendix B: Curing of Cementitious Material 6-116
Chapter 7.0 Integrated Testing 7-2
7.1 Introduction 7-2
7.1.1 Scope of Integrated Testing Activities 7-2
7.1.2 Relationship of Integrated Testing Activities to Other YMP Activities 7-2
7.2 Data Inputs Required for Bounding Transport and Source Terms 7-3
7.3 Chemical, Mineralogical, and Physical Characteristics of EBS/NFE Components Expected to Significantly Affect Radionuclide Transport Through the EBS/NFE 7-4
7.3.1 Waste Form 7-4
7.3.2 Container Corrosion Products 7-5
7.3.3 Backfill 7-6
7.3.4 Characterization of Natural Colloids at Yucca Mountain 7-6
7.3.5 Cementitious Materials 7-9
7.3.6 Altered Host Rock Adjacent to the Engineered Barrier 7-10
7.4 Transport Studies in Host Rock and Minerals 7-10
7.4.1 Characterization of Repository Rock Pore Size Distribution and Diffusion of Actinides 7-10
7.4.2 Diffusion of Radionuclides in Clinoptilolite 7-12
7.4.3 Flow and Transport Through Topopah Spring Tuff 7-14
7.5 Field Testing Sorption Models Under Conditions of Fracture Dominated Flow 7-19
7.5.1 Cation Exchange 7-20
7.5.2 Surface Complexation 7-24
7.6 Summary 7-29
7.7 Summary of Gaps in Information Required to Bound Radionuclide Transport in the EBS/NFE 7-30
7.8 References 7-31
Chapter 8.0 Electrical Potentials 8-2
8.1 Introduction 8-2
8.2 Self-Potentials 8-2
8.2.1 Streaming Potential 8-3
8.2.2 Thermoelectric Potential 8-4
8.2.3 Electrochemical Potential 8-4
8.3 Summary 8-4
8.4 References 8-5
Chapter 9.0 Field Thermal Tests 9-2
9.1 Introduction 9-2
9.2 G-Tunnel Tests (*A. Ramirez*) 9-4
9.2.1 Parameters Measured 9-5
9.2.2 Test Description 9-7
9.2.3 Changes in Rock Mass Moisture Content 9-8
9.2.4 Temperature Measurements 9-11
9.2.5 Changes in Air Permeability 9-13
9.2.6 Steam Invading the Heater Emplacement Borehole 9-14
9.2.7 Summary 9-15
9.3 Large Block Test 9-17
9.4 ESF Thermal Tests 9-22
9.4.1 Single Heater Test 9-22

9.4.2 Drift Scale Test 9-23
9.5 Large-Scale Long Duration Test 9-25
9.6 Confirmation Monitoring 9-26
9.7 References 9-26
Chapter 10.0 Altered Zone Environment 10.1-2
Introduction 10.1-2
10.1 Mountain-Scale Unsaturated Zone (UZ) Thermal-Hydrology 10.1-3
10.1.1 Models and Assumptions 10.1-7
10.1.2 Influence of Fracture Permeability Distribution 10.1-12
10.1.3 Influence of Matrix Hydrological Property Distribution 10.1-25
10.1.4 Influence of Overburden Thickness 10.1-42
10.2 Mountain-Scale Saturated Zone (SZ) Thermal-Hydrology 10.2-2
10.2.1 Influence of SZ Heatflow on UZ Heatflow 10.2-2
10.2.2 Buoyancy-Driven SZ Flow and Transport 10.2-3
10.3 Geochemistry and Mineralogy of the Altered Zone (William E. Glassley) 10.3-2
10.4 Summary of Recent Studies Concerning Geochemical and Mineralogical Evolution of the Alterned Zone (William E. Glassley) 10.4-1
10.4.1 Hydrothermal Alteration of Vitric Tuff from Yucca Mountain, by Kevin G. Knauss and Sally A. Copenhaver, Lawrence Livermore National Laboratory 10.4-4
10.4.2 Kinetics of Rock-Water Interaction: Amorphous Silica Precipitation (60 to 120°C); Comparison of Laboratory and Field Rates, by Susan Carroll, Edward Mroczek, Maureen Alai, and Margeret Ebert; Earth Sciences Division, Lawrence Livermore National Laboratory, Livermore CA, USA, Institute of Geological & Nuclear Sciences, Wairakei Research Center, Wairakei, New Zealand 10.4-9
10.4.3 Thermal Effects in the Altered Zone: Preliminary Bounds on the Water Composition and Secondary Mineral Development in the Altered Zone That May Influence the Near-Field Environment, by Michael Whitbeck and William Glassley, Lawrence Livermore National Laboratory 10.4-27
10.4.4 Formation of Flow and Transport Barriers Within the Altered Zone, by James W. Johnson and William Glassley, Lawrence Livermore National Laboratory 10.4-39
Chapter 11.0 Introduction to the Thermodynamic Data Determination 11-2
11.1 The Database 11-2
11.2 U.S. Contribution to the NEA Organization for Economic Co-operation and Development (OECD) Critical Reviews of the Chemical Thermodynamics of the Actinides and Fission Products 11-3
11.2.1 Lawrence Livermore National Laboratory's Role 11-4
11.2.2 Procedure 11-4
11.2.3 Auxiliary Data 11-5
11.3 Qualification of Data for Using in Quality Affecting Calculations 11-5
11.4 Review of Thermodynamic Data 11-6
11.4.1 Chemical Thermodynamics of Uranium 11-6
11.4.2 Chemical Thermodynamics of Americium 11-7
11.4.3 Chemical Thermodynamics of Technetium 11-7
11.4.4 Chemical Thermodynamics of Plutonium and Neptunium 11-9
11.5 References 11-9

Appendix A Old References (copied from the PNFER)
Appendix B Identification of Q and non-Q data
Appendix C Technical Data Tracking

Acronyms and Abbreviations

ACD	advanced conceptual design
APD	areal power density
ASTM	American Society for Testing and Materials
bfs	blast furnace slag
BHW	borehole wall
CEC	cation exchange capacity
CHnv	Calico Hills, nonwelded, vitric
CHnz	Calico Hills, nonwelded, zeolitized
DFM	discrete fracture model
DHLW	defense high-level waste
DOE	U.S. Department of Energy
DST	drift scale test
EBS	engineered barrier system
EBSFT	engineered barrier system field tests
ECM	equivalent continuum model
ERT	electrical resistivity tomography
ESF	Exploratory Studies Facility
ESFTT	ESF thermal tests
FMM	fracture-matrix model
GTUF	G-Tunnel Underground Facility
GWTT	groundwater travel time
HLW	high-level waste
LA	license application
LAD	license application design
LBT	large block tests
LLNL	Lawrence Livermore National Laboratory
LSLDT	large-scale long-duration tests
MPBX	multiple borehole extensometer
NF	near field
NFE	near-field environment
NFER	*Near-Field Environment Report*
NTS	Nevada Test Site
NWTRB	Nuclear Waste Technical Review Board
PEBSFT	prototype engineered barrier system field test
PPw	Prow Pass, welded
PTn	Paintbrush, nonwelded
QA	quality assurance
REKA	rapid estimation of K (thermal conductivity) and alpha (diffusivity)
RIB	*Reference Information Base* (DOE, 1990)
RMR	rock-mass rating
RTD	resistance temperature device
SCP	*Site Characterization Plan* (DOE, 1988)
SCPCDR	Site Characterization Plan Conceptual Design Report
SCSSS	Standard Canadian Shield Saline Solution
SEAMIST	Science Engineering Associate Mambrane Insitu Sampling Technology
SEM	scanning electron microscopy
SF	spent fuel
SHT	single-heater tests
SIMS	secondary ion mass spectrometry
SP	spontaneous electrical potentials
TCw	Tiva Canyon, welded
TMHC	thermal-mechanical-hydrological-chemical

Acronyms and Abbreviations (continued)

Tpt	Topopah Spring Member of the Paintbrush tuff
TSw1	Topopah Spring, welded, lithophysae-rich
TSw2	Topopah Spring, welded, lithophysae-poor
TSw3	Topopah Spring, welded, vitric
UNE	underground nuclear explosion
WP	waste package
WPP	*Waste Package Plan* (Harrison-Giesler et al., 1991)
XRD	x-ray diffraction
YM	Yucca Mountain
YMP	Yucca Mountain Site Characterization Project
YMPO	Yucca Mountain Site Characterization Project Office

Contents

Chapter 2.0 Laboratory-Determined Hydrologic Properties and Processes....2-2
2.1 Laboratory-Determined Hydrologic Properties....2-3
2.1.1 Moisture Retention at Elevated Temperatures....2-4
2.1.2 Water Permeability at Elevated Pressures and Temperatures....2-6
2.1.3 Electrical Resistivity as a Function of Water Saturation at Elevated Temperatures....2-7
2.1.4 Relative Humidity as a Function of Water Saturation at Elevated Temperatures....2-9
2.2 Laboratory Study of Thermal-Hydrological-Chemical Processes....2-11
2.2.1 Condensation Along a Fracture....2-11
2.2.2 Fracture Flow vs. Matrix Imbibition at Elevated Temperatures....2-14
2.2.3 Fracture Healing....2-19
2.3 References....2-22

Chapter 2.0 Laboratory-Determined Hydrologic Properties and Processes

W. Lin and J. Roberts

Understanding the movement of moisture—including liquid water, steam, and vapor—in the near-field environment (NFE) of the potential nuclear-waste repository at Yucca Mountain, Nevada, is one of the goals of the waste-package environment hydrologic investigations. This chapter discusses how thermal loading resulting from waste package emplacement will affect the preconstruction hydrologic properties and processes of the NFE.

One of the main concerns about the NFE of a nuclear-waste repository is the quantity and quality of water that may be present and that may contact the waste and waste packages (near field) and be in the rock mass surrounding the repository. Water can cause property changes in the altered zone. Processes that may affect the quantity and quality of water are coupled thermal-mechanical-hydrological-chemical (TMHC) processes. The TMHC processes may involve the *in-situ* pore water in the Topopah Spring tuff, water present in fractures, and/or condensate that results from water mobilized by heat, as well as any water introduced (either naturally or artificially) after the emplacement of the wastes. Field and laboratory tests are conducted to enhance our understanding of the coupled TMHC processes and to measure physical properties. The field tests are reported in Chapter 9.0. The laboratory tests of hydrologic properties and processes will be used as input data to model calculations of the coupled TMHC processes, to improve the understanding of the model calculations, to gain insight into physical processes and thus learn under what conditions specific coupled processes become dominant or important, and to help in analyzing the results of the field tests. The laboratory-determined hydrologic properties reported in this document include moisture-retention curves at elevated temperatures, water permeability at elevated temperatures and pressures, electrical resistivity as a function of water saturation at elevated temperatures, and relative humidity as a function of water saturation at elevated

temperatures. The laboratory studies of the thermal-hydrological-chemical processes include fracture flow vs. matrix imbibition at elevated temperatures, fracture healing, and condensation along a fracture. All of the laboratory test results are not qualified, as defined in the quality assurance procedures.

2.1 Laboratory-Determined Hydrologic Properties

The work described here can generally be classified into two different areas with regard to the NFE: (1) preconstruction conditions and processes and (2) the perturbed environment. Preconstruction conditions and processes are those processes that occur prior to any disturbance; that is, they occur naturally.

The perturbed environment is the region that has changed because of some human activity. During the post-emplacement period, the near field may experience at least one dehydration-rehydration cycle. After waste emplacement, the rock in the near field is expected to dehydrate as a result of heating. The rate of dehydration and the movement of moisture in the rock will depend on, among other factors, the initial moisture content in the rock, the geometry and configuration of fractures, and the force of gravity. Later, as the rock temperature decreases below the boiling point of water, rehydration of the near field is expected to occur. The dehydration and rehydration processes and the effect of temperature on the hydrologic properties of tuff are discussed below.

The laboratory work described in the NFER Rev. 0 was divided into these two sections. Because of the increased number of experiments, many of them performed over a range of conditions including ambient condition, it was decided in this report to describe each experiment and the results separately. In addition, in reporting laboratory test results, it is easier to appreciate the effect of temperature on the properties if the results at room temperature and elevated temperatures are presented together. Generally, work performed at near-ambient temperatures (20–25°C) applies to preconstruction conditions, while work at higher temperatures is relevant to the perturbed environment. Obvious exceptions to this are the

measured physical properties at ambient conditions after a cycle of heating, pressure, or fluid flow.

2.1.1 Moisture Retention at Elevated Temperatures

The suction potential of rock determines the imbibition of water in the matrix. That, in turn, affects the relative importance of matrix flow and fracture flow because greater suction potential enhances matrix flow. Moisture content as a function of matric potential (moisture retention curves) of Topopah Spring tuff samples at elevated temperatures was determined using a constant-relative-humidity chamber. The method of measurement was described in Daily and Lin (1991), Roberts and Lin (1995a), and Roberts and Lin (1996a). Some of the test results have been published in Daily and Lin (1991), Roberts and Lin (1995a), and Roberts and Lin (1996a). Daily and Lin (1991) reported results of measurements at 20 and 70°C on Topopah Spring tuff samples from the USW H-1 borehole at a depth range from 333 to 350 m and from outcrops at Fran Ridge, Nevada Test Site. The Topopah Spring tuff samples used in the tests by Roberts and Lin included cores from borehole USW G-4 at a depth of about 360 m (1147 ft) and cores from the Large Block Test. Figures 2-1 to 2-4 show the results of Daily and Lin (1991). As noted on the figures, suction potential is a strong function of saturation below 20–30% saturation but is less dependent on saturation above 30% (varying between 200–400 atm). At near-ambient temperatures the suction potential decreases much more rapidly with increasing saturation during wetting than it does during drying (samples from USW H-1). This difference in behavior between wetting and drying is also seen at elevated temperatures, although the difference is not as pronounced as for ambient temperatures. Figure 2-5 summarizes the results of Roberts and Lin (1995a and 1996a) and shows the moisture retention curves of USW G-4 samples at temperatures of 24.8, 78.4, and 93.6°C for both drying and wetting phases. In this study there was not a consistent difference between wetting and drying curve shape, although there is a difference in the curves for 93.6°C.

Peters et al. (1984) and Klavetter and Peters (1987) used psychrometers to measure the suction potential of both welded and non-welded tuff from Yucca Mountain at

20°C during the dehydration phase. Our data at 20°C are within the spread of corresponding results of Klavetter and Peters, as noted on Fig. 2-3 of NFER Rev. 0.

Results from another experiment using five samples of Grouse Canyon tuff from the G-Tunnel showed that in a 100% relative humidity environment, the suction of water into rock samples is quite different from that in an environment of liquid water, although both have zero water potential (NFER Rev. 0). The samples were placed in a constant-humidity chamber at 100% humidity for more than 917 hours, after which they were removed and submersed in liquid water. Under 100% humidity the suction of moisture was limited to no more than 20% of the sample porosity. Yet, when the samples were removed from the 100% humidity environment and submersed in liquid water, the degree of saturation increased overnight to ~70% of their porosity, and then continued to increase. This implies that in the NFE the moisture-content change in the matrix during the flow of steam or vapor through fractures will be quite different from that of the change during the flow of liquid water, also indicating that after the liquid water has been driven off as a result of thermal loading from waste emplacement, the rock's saturation level will not be elevated to above ~20% until liquid water is able to return to the NFE. During the G-Tunnel field experiments, rehydration took place much more slowly than did dehydration, supporting the observation that saturation levels do not increase without liquid water (Ramirez et al., 1991).

Generally speaking, water saturation at a constant matric potential decreases with increasing temperature. Hysteresis between the drying and wetting phases exists at most of the temperatures. The hysteresis at 78.4°C is much smaller than at other temperatures. For most of the samples the hysteresis is that more moisture is retained in the samples during drying than during wetting. However at 93.6°C the hysteresis was reversed. The explanation for this discrepancy requires further investigation. No process has been identified that can explain smaller hysteresis at 78.4°C than at other temperatures, or explain the hysteresis reversal at 93.6°C. However, in this test the samples were heated from 24.8°C to 93.6°C then cooled to 78.4°C. This heating history may have some effect on the moisture-retention curves.

2.1.2 Water Permeability at Elevated Pressures and Temperatures

Water permeability in Topopah Spring tuff samples as functions of pressure and temperature has been measured to provide input data for model calculations. The techniques used to measure the permeability were described by Lin and Daily (1984). As expected, water permeability in intact Topopah Spring tuff samples was different than in fractured samples; however, it was determined that permeabilities of fractured samples responded to elevated temperature in a fundamentally different way than for unfractured samples (see Section 2.2.3) (Lin and Daily, 1984; Daily et al., 1987; Lin and Daily, 1988; Lin, 1991; Roberts and Lin, 1995b; Lin et al., 1995). The water permeability of intact Topopah Spring tuff samples is reported in this section. The water permeability of fractured tuff samples is reported in Section 2.2.3, "Fracture Healing."

An intact Topopah Spring tuff sample machined from an outcrop at Fran Ridge, Nevada Test Site, was used by Lin and Daily (1984) to measure water permeability at various times during a series of three dehydration and rehydration cycles. The sample was under a constant confining pressure of about 5 MPa, and temperatures up to 140°C. The water permeability of the intact tuff sample was independent of temperature, time, and dehydration and rehydration cycles. At 21°C, before starting the dehydration-rehydration processes, the permeability was 0.34×10^{-18} m^2 (0.34 μD); after the first drying phase, at 98°C, the permeability was 0.32×10^{-18} m^2 (0.32 μD); then at 140°C, also after the first drying phase, the permeability was 0.31×10^{-18} m^2 (0.31 μD); after three drying phases at 98°C the permeability was 0.35×10^{-18} m^2 (0.35 μD). The steam permeability after two drying phases, at 140°C, was 1.99×10^{-18} m^2 (1.99 μD). The greater steam permeability may be a result of the effect of gas flow on permeability, as normally seen in gas permeability measurements due to the Klinkenberg effect. Recently, water permeability of an intact core from the Large Block Test was measured by Lin and Roberts. The results are shown in Table 2-1. The water permeability of the intact tuff sample is again independent of temperature and ranges from 0.09 to 0.67×10^{-18} m^2 (0.09 to 0.67 μD). For

comparison, Ramirez et al. (1991) reported water permeability, at 20°C, of intact Grouse Canyon tuff from G-Tunnel, Nevada Test Site, to be about 10^{-18} m^2 (1 μD). Moore et al. (1986) reported that the water permeability of Topopah Spring tuff samples at 20°C ranged from 0.85 to 64×10^{-18} m^2 (0.85 to 64 μD). It is not clear if the samples used by Moore et al. were intact or fractured.

2.1.3 Electrical Resistivity as a Function of Water Saturation at Elevated Temperatures

Spatial distribution and temporal variation of moisture content in the rock mass in the repository horizon are among the most important parameters needed to understand the coupled TMHC processes. There are no direct methods for measuring moisture content other than drying and weighing, therefore geophysical methods are required to determine the moisture content in a rock mass. Electrical resistivity tomography (ERT) is one of the few geophysical methods that can effectively determine the distribution of moisture content in a two-dimensional plane and/or a three-dimensional region. ERT determines the distribution of electrical resistivity in an imaging region. Laboratory-determined relationships between electrical resistivity and moisture content over a range of temperatures are required to interpret the ERT results in terms of moisture content. Measuring the electrical resistivity as a function of moisture content at various frequencies can also provide information about the microscopic wetting and drying processes in rocks (Roberts and Lin, 1996b).

Laboratory-determined electrical resistivities of Topopah Spring tuff as a function of water saturation at elevated temperatures have been reported by Roberts and Lin (1994a, 1994b, and 1996b). Topopah Spring tuff samples used in this study were from holes U3hg-1 at 399-m depth, USW GU-3 at 330-m depth, and USW G-4 at 374-m depth. The connected porosity of the samples were 25–28% for U3hg-1, 9–14% for USW G-4, and 9–10% for USW GU-3. The electrical properties measurement techniques were described in Roberts and Lin (1994a and 1994b). Briefly, the two-electrode method was used on thin disc-shaped samples that had sputtered gold electrodes backed by gold foil. Samples were placed in holders to

inhibit the uptake or loss of moisture to the surrounding atmosphere. Water was added to the samples in small increments, and saturations were determined gravimetrically. Electrical resistivity measurements were conducted after each addition of water until a constant value was reached, at which point it was assumed the water was evenly distributed throughout the sample. This redistribution of fluid generally took between 4 and 6 hours but was dependent on saturation and the amount of sample area to which fluid was added. The time-dependent monitoring of samples was discontinued after the length of time for re-equilibration to occur was established, and measurements were made approximately daily (or 4 to 6 times as long as needed for re-equilibration to occur). We used four samples of each rock, each having a different thickness. This was done for several reasons: to check the effect of electrode contact impedance on the measurement (minimal at 1 kHz), to measure heterogeneity (most of the scatter in Figs. 2-6 through 2-9 results from the multiplicity of samples for each rock), and to provide more data points.

Figures 2-6 to 2-8 show the electrical resistivity of these rock samples at room temperature as a function of water saturation. The resistivity measured during the drying process is slightly greater than that measured during the wetting process. For all of these rocks the resistivity is most sensitive to the water saturation when the water saturation is below 20%. The slope of the resistivity vs. saturation trend is related to the connected porosity: the U3hg-1 samples had the steepest slope; the USW G-4 samples had the most gentle slope. Roberts and Lin (1994b) also reported that the electrical resistivity in USW G-4 has only slight anisotropy: that is the rock is slightly less resistive for electrical current that flows along the bedding planes, but the difference in the resistivity is small and most likely will not affect the use of electrical resistivity measurements for determining water saturation in laboratory and field tests.

Figure 2-9 shows the electrical resistivity of samples from USW G-4 as a function of water saturation at various temperatures from 23 to 95°C during wetting. As expected, the resistivity decreases with increasing temperature. The temperature effect is very small when the water saturation is less than 10%. The maximum decrease in resistivity as a result of temperature occurs in the 20–40% saturation

range, when the decrease in resistivity due to increased saturation is also very high. Above 40% saturation the difference due to temperature is greater than the difference due to saturation.

Figure 2-10 shows the resistivity of USW G-4 samples as a function of temperature for 40 and 75% saturation. The individual data points were selected from the total data set for points that ended up having similar saturations. This means that the curve for 40% saturation, for instance, might have data points for different G-4 samples; thus there is some inherent scatter in the data. Despite this, there is a clear trend in the data. Note that the resistivity axis is linear in this case. Resistivity decreases by about a factor of 3 to 4 from 20 to 100°C. The data are described by simple power-law fits of the form $\rho = a(T^{-b})$ where ρ is the resistivity in ohm-m, T is temperature in °C, and a and b are fitting parameters. The fits shown have values of 23920 and 19896 for a and values of 0.9184 and 0.9811 for b for 40 and 75% saturation respectively. These values are relevant only to the specific data set for which they were derived, and we caution that more data points are needed to confirm any systematic relationship.

Based on these results, we conclude that using electrical resistivity to determine the distribution and variation of moisture content in Topopah Spring tuff is most effective when the saturation is less than 40%. For greater levels of saturation, the method is still useful but potentially with less accuracy, depending on how well temperature changes can be determined. It will be necessary to have a separate determination of temperature to get the most accurate saturation estimates. For water saturation greater than 50%, relative permittivity (dielectric constant) may be more sensitive to water saturation than resistivity (Roberts and Lin, 1994b).

2.1.4 Relative Humidity as a Function of Water Saturation at Elevated Temperatures

Relative humidity in the waste package environment is a key factor affecting the integrity of the waste canister. The purposes of determining the relative humidity as a function of water saturation in Topopah Spring tuff are to provide experimental data for comparison with the calculated relative humidity in the near-field

environment, to assess the ambient (pre-heat) relative humidity in the repository, and to understand the diffusion process of vapor through the matrix of the tuff.

The technique of measuring the relative humidity as a function of water saturation was described in Lin et al. (1996). One cylindrical Topopah Spring tuff sample was machined from a small block of the tuff collected at the Large Block Test site. A Humicap humidity sensor was sealed in a hole about 1.0 cm in diameter, in the central portion of the sample. Distilled water was added to the outer surface of the sample, and the relative humidity was monitored continuously until a steady state was reached. The experiment is still under way, and at this reporting time the experiment has only been completed at room temperature. Although it is planned to conduct the experiment at elevated temperatures, we do not believe that increasing temperature in the sample will change the conclusions reported here.

Figure 2-11 shows the current status of the test results. Prior to adding water to the sample, as is indicated by the first spike in the figure, the relative humidity in the entire system was monitored for about one week. Because the experiment started with a dry sample, the relative humidity inside the sample was approximately zero during the pre-test monitoring period, while the room humidity was about 30 to 40%. Water was added to the sample in increments. Each spike in the figure was due to exposing the Humicap to the room air during the water-adding processes. The three spikes in the last segment of the relative-humidity curve were due to some electronic noise of unknown source occasionally received by the data acquisition system. The noise does not seem to affect the quality of the data. The water saturation at each increment of relative humidity shown in the figure was determined based on the amount of water in the sample (by weighing the sample) when the relative humidity had reached a steady state. Currently the relative humidity in the sample is approaching 95% with a saturation level of about 15.9%.

These experimental results indicate that in a closed system very high relative humidity can be reached with very small moisture content. The ambient moisture content in the Exploratory Studies Facility (ESF) is estimated to be about 85%. With this ambient moisture content we expect that the relative humidity in the waste

package environment, without drying out the rock and without considering thermal gradients, to be near 100%. Corrosion rates in AISI carbon steel were observed to increase notably at relative humidities above 75–80% (Estill and Gdowski, 1996). The moisture content in the rock will have to be below about 10% saturation to maintain an environment that dry. At greater temperatures we expect the relative humidity at a given saturation level to be less than shown here, but we don't expect the temperature effect to be great enough to alter the conclusion for the rock itself. However, thermal gradients can modify the relative humidity in drifts or near waste packages by a significant amount. Another observation in this test is the slowness of the vapor diffusion in an intact rock. If this process also occurs in the Topopah Spring tuff rock mass, the increase of moisture content in the matrix due to vapor flow in the fractures will be very slow. Earlier tests indicate that moisture content increases via vapor diffusion are limited to about 20% saturation. This is consistent with data presented in Section 2.1.1 that show a large decrease in suction potential at saturations near 20%. For greater saturations, the suction potential decreases very little with increasing saturation, an indication that matrix saturation above 20% by way of vapor transport alone is unlikely.

2.2 Laboratory Study of Thermal-Hydrological-Chemical Processes

2.2.1 Condensation Along a Fracture

Thermal-hydrological model calculations predict that radioactive decay heat from the waste packages will dry out the surrounding rock mass by evaporating the pore water and will move the vapor away from the waste packages. Based on hydrological tests, both in the laboratory and in the field, and on model calculations, it is believed that fractures are fast paths for the movement of vapor and steam. How the vapor flows within fractures and how the water, which is condensed from the vapor/steam, moves within the fractures affects the moisture distribution in the near field environment. To help understand the thermal-hydrological model predictions and future field thermal tests, we are conducting a laboratory test on a core to study the condensation of vapor in a single fracture.

The core is about 5 cm in diameter and 35.56 cm in length. It was machined from a Topopah Spring tuff block that was collected from the Large Block Test site. The core was split in two by a longitudinal saw cut. Eleven pairs of gold shims, 25 μm in thickness, were placed evenly along both edges of the saw cut to serve as electrodes and to control the aperture. The 11 electrode pairs were used to measure electrical resistance in the saw cut, and the measured electrical resistance was used to detect moisture movement within the saw cut. A high-input impedance bridge was used to measure the resistance (1 kHz measurement frequency) of each electrode pair at regular time intervals. The largest resistance measurable was 100 MΩ. Ten thermocouples were mounted in holes in the sample 90° from the plane of the saw cut. One thermocouple was placed in each of the top and bottom brass end-caps; one thermocouple was placed in the rock about 2 mm from the top and bottom ends; six thermocouples were placed within the core, evenly spaced along its axis. The measuring tips of the thermocouples were located very close to the saw cut (within ~3 mm). Water was added to the core to obtain a water saturation level of about 95%. The cylindrical surface of the core was coated with high-temperature RTV silicon cement to prevent moisture loss. The sample assembly was placed vertically on a hot plate. A vapor release tube was installed in the top end-cap and connected to a water collecting bottle. Fiberglass insulation was used to cover the entire cylindrical surface of the core. The core was heated to a constant temperature of about 160°C at the bottom; the temperature at the top of the core reached and stayed at about 33°C. Copper coils for a heat exchanger to control the top temperature were installed on the top of the core, but it was not necessary to use the heat exchanger in this test. Ambient temperature and electrical resistance data were collected for a few hours before the heating started. The sample was heated for about 245 hours, then the heater was turned off. The experiment is now at about 700-hour elapsed time. Data acquisition continued throughout the heating and cool-down phases. Some observations of the test are summarized in the following paragraph. The test is still in progress, therefore the observations and conclusions presented below are preliminary and are subject to reinterpretation upon conclusion of the test.

Figure 2-12 shows the temperature distribution in the sample assembly for the first 300 hours of the test. For the rest of the test beyond 300-hour elapsed time, the temperatures in the sample are all at room temperature. Thermocouple #1 (Tc1) and thermocouple #10 (Tc10) were in the bottom brass end-cap and top brass end-cap respectively. Tc2 and Tc9 were located about 2 mm from the bottom and top of the core respectively. Tc3 to Tc8 were evenly distributed along the core axis from bottom to top respectively. During most of the test the temperatures in the sample were constant. The step-down in temperature at the 200-hour mark was probably caused by an unplanned decrease in the power output from the hot plate. Just before the heater was turned off, at about 245 hours, we opened the insulation material to inspect the integrity of the RTV moisture coating. No obvious breakage in the RTV was observed. Based on the temperature distribution in the core, cooling of the core seems to be slightly faster than the heating. This may be related to the different thermal capacities of the saturated versus partially saturated rock. The reason for the step-up in temperature at the 100-hour mark (Tc2 to Tc10) is unknown. It was probably a real temperature increase, because there was a simultaneous resistance decrease at electrode pairs 6 to 8. Figure 2-13 shows the electrical resistance measured from electrode pairs 1 to 8 for the entire 700-hour duration of the test. The resistance of electrode pairs 9 to 11 were off-scale during the entire period of this test, and therefore are not shown in Fig. 2-2 through 2-13. The high resistance in the upper portion of the core was probably due to water loss in the upper portion of the core. The water loss was likely due to gravity drainage to the lower portion of the core or through a leak near the vapor collection system at the top of the sample. The resistance of all electrode pairs went off-scale at about the 220-hour mark, indicating substantial dry-out before the heater was turned off. This figure shows sequential drying of the saw cut from the bottom upward. Figures 2-14 and 2-15 show more detailed variance of the resistance at electrode pairs 1-4 and 5-8 respectively. The resistance decreased at the beginning of the experiment because of the heating of the pore water. As heating continued, resistance increased when the saw cut was drying out because of evaporation. The changing slope of the resistance-time trend in electrode pairs 3 to 8 may be caused by the slowing down of the dry-out process in

these portions of the saw cut. The slowing down of the dry-out process may be caused by many factors, such as slower dry-front propagation rate into the matrix, and moisture supply from above, in the form of condensate refluxing. In addition, the resistivity as a function of saturation and temperature for tuff is not a simple relationship, as demonstrated in Section 2.1.3. More detailed observation will be conducted in the future to determine the real cause of this phenomenon.

No vapor was observed to exit the top of the core, and no water was collected in the bottle. The temperature in the core has been decreased to room temperature for at least 350 hours, but no change in the electrical resistance, which would indicate re-wetting, has been observed. Future tests to verify the current observations will be conducted. Those include model calculation of the experimental setup, measurement of electrical resistance perpendicular to the saw cut, thickening the RTV layer to minimize vapor loss, and an improved vapor collection system at the top.

2.2.2 Fracture Flow vs. Matrix Imbibition at Elevated Temperatures

As mentioned in Section 2.1.4, the diffusion of vapor into the matrix because of the vapor flow in fractures may not be very effective in transporting moisture. The understanding of how water imbibes into the matrix during fracture flow will become more important for enhancing our knowledge about the coupled TMHC processes. The purpose of this test is to visualize the fracture flow and matrix imbibition process when the sample is at elevated temperatures. By this visualization we hope to determine the parameters, such as fracture aperture, infiltration rate (i.e., the fracture flow rate), initial moisture content of the matrix, and thermal gradient, that may affect the coupling between water flow in fractures and the imbibition into the matrix. The experimental techniques and procedures, and some of experimental results were reported by Roberts and Lin (1996c). Basically, a linear x-ray source of 160 kVp was used to conduct vertical scans of blocks of Topopah Spring tuff containing vertical fractures. Water, doped with KI to enhance the x-ray attenuation contrast, was introduced into the top of the fracture. X-ray radiographs were taken periodically to image the movement of water in the fracture

and the matrix. Images were normalized using aluminum standards. After the normalization, difference images were created by subtracting a beginning image from the subsequent images. In this manner only the relative changes in the x-ray images are studied. All the x-ray images presented in this report use the following convention: darker shades indicate higher x-ray attenuation (or changes in attenuation) and imply higher water content, and lighter shades indicate relatively low x-ray attenuation (or changes in attenuation) and imply lower water content. Quantitative saturation fields can be calculated but are not presented here (see Tidwell and Glass, 1994, or Roberts and Lin, 1996c).

So far four experiments have been conducted: (1) fracture flow and matrix imbibition in an artificially induced tensile fracture without shims; (2) fracture flow and matrix imbibition in the same fracture as in experiment (1) with four shims of 25-μm thickness; (3) after completion of test (2), dehydration of the sample under a thermal gradient of about 95°C at the bottom and 33°C at the top; and (4) fracture flow and matrix imbibition against a thermal gradient, tested in another Topopah Spring tuff block that contained nine 25-μm gold shims. The results of the first three experiments were reported in Roberts and Lin (1996c) and are summarized later in this report. The sample dimensions for experiments (1), (2), and (3) were 14 × 10 × 2.5 cm (length, height, width). Experiment (4) is described in the following paragraph, and its results are summarized later, along with the results of the first three experiments.

In the fourth experiment, a dry block of Topopah Spring tuff machined from a small block of the rock collected at the Large Block Test site was used. The dimensions of the block were 29.21 cm tall by 15.1 cm wide by 2.65 cm thick. The sample preparation and test procedures were similar to the preceding experiments, with the exceptions noted here. Nine 25-μm gold shims were placed inside the tensile fracture at regular intervals. Five thermocouples were placed inside the rock at 0.2, 7.5, 14.8, 22.1, and 29.1 cm, from the bottom of the sample to the top, respectively. The temperatures in the dry rock prior to flow were 115, 48.4, 33.8, 29.4, and 28.1°C, from bottom to top. The temperature between the heater and the bottom

of the sample was 126°C. Even though insulation was used wherever possible, a relatively large temperature gradient existed at the bottom of the sample. Initial images were taken, and then water was permitted to pond on the sample. Only the fractured region on top (~1 cm wide) was exposed directly to the ponded water, the other areas having been coated with RTV.

The results of the four fracture flow and matrix imbibition experiments are summarized here. Figure 2-16 shows the x-ray difference image of fracture flow and matrix imbibition in a tensile fracture without shims, at room temperature. The fracture is located near the left edge of the image. Water was ponded at the top of the image. The darker region represents the region where water has wetted the sample, 47.3 hours after the ponding started. The roughly V-shaped wetted region, with the tip of the "V" at the front of the fracture flow, is very similar to that of fracture flow in a block of plaster of Paris with 25-μm shims that had been used as a test of analytical approaches of fracture/matrix interactions (Fig. 2-17). The matrix permeability of the tuff is about 3 orders of magnitude less than that of the plaster of Paris. The result of this experiment indicates that fracture flow and matrix imbibition in an unshimmed tensile fracture in tuff is qualitatively similar to that in a material with a higher permeability matrix that contains a fracture with greater aperture. Figure 2-18 shows a sequence of x-ray difference images of fracture flow and matrix imbibition in the same fracture shown in Fig. 2-16, except that four gold shims of 25-μm thickness were placed in the fracture. The test was also conducted at room temperature. There is no V-shaped wetted region, as seen in Figs. 2-16 and 2-17. Water flowed through the fracture within a couple of minutes (Fig. 2-18a), then matrix imbibition began. The imbibition into the matrix was faster on the right side of the sample as compared to the left side. This is more evident at longer times (Fig. 2-18c). Examination of the fractured sample after the experiment revealed pumice fragments near the areas where lateral imbibition was the fastest. Small microfractures around the edges of these fragments are believed responsible for the enhanced lateral imbibition.

The larger fracture aperture changed significantly both the volume of flow through the fracture and the rate and amount of imbibition into the matrix. These effects are being studied further because they have bearing on models of repository performance.

Figure 2-19 shows the movement of the wetting front versus the square root of time for three locations: within the fracture (~1/3 the distance from the top of the sample on both sides of the fracture) and the top of the sample (~3.5 cm from the left edge of the sample). The wetting front was arbitrarily defined as 75–80% saturated. The large variability in matrix imbibition is evident in this figure. The imbibition from ponded water on top of the sample was slowed considerably by a relatively impermeable crystal-lined cavity (low attenuation region—may be porous area) ~1 cm beneath the surface. After an initial time lag, all three locations are linear with respect to time$^{1/2}$. The slope of this line is related to permeability.

Figure 2-20 shows the x-ray image of the drying process of the sample as in experiment (2) after the infiltration had totally wetted the sample. Again, as in the previous experiment, the fracture had four shims of 25-μm thickness within it. The drying was created by using a heater at the bottom of the sample to maintain the temperature there at about 95°C, while the temperature at the top of the block was about 30°C. The image shows that the fracture was dried out within hours after the heater was turned on. A darker horizontal region near the lower part of the image seems to indicate greater x-ray attenuation. The greater attenuation may be because of increase in water saturation or deposition of KI. Because the higher attenuation band changed shape and moved up and down slightly during the sequence, it is believed that it represents increased saturation in this instance.

As mentioned previously, the fourth experiment was designed to visualize the fracture flow and matrix imbibition in a heated block of fractured Topopah Spring tuff. Based on examination of difference images, several important features were noted. Figure 2-21(a, b, c) shows images taken at 1.7, 73.5, and 360 hours respectively and illustrates most of the following points. Initially, water flowed relatively quickly into the rock with minimal lateral imbibition into the matrix from the fracture,

similar to that in Experiment (2). By 1.6 hours, water had flowed ~16 cm down the fracture with the width of the highly saturated zone ~0.8 to 1.5 cm (Fig. 2-21a). At this point, downward flow slowed considerably and lateral imbibition continued. The most likely reason for the stop in downward flow is the existence of a low density (i.e., more porous) pumice fragment at ~16 cm from the top. After ~23 hours the water began to move past this region as a V-shaped wetting front. The highly saturated zone was ~2.2 to 3.5 cm wide. Water continued to travel down the fracture until ~27 hours, when a narrow region of high x-ray attenuation began to develop in the fracture between ~22.6 and 26.3 cm (from top). At longer periods of time, a circular region of high x-ray attenuation developed near the bottom of the sample, centered on the fracture (Fig. 2-21b). Because this is the hottest region of the rock, where temperature was above the boiling point of water, a likely reason is the concentration of KI (used as a dopant to increase x-ray attenuation) in these regions. Water never penetrated the entire sample; that is, water never was observed to exit the bottom of the sample past the "boiling zone." Although dependent upon many factors (i.e., hydraulic head, porosity, permeability, pore size distribution), this could be a very important observation because it indicates that condensate will not penetrate the boiling zone for fractures less than some critical aperture. Additional studies are needed to verify and determine the aperture dependence. Continued lateral imbibition was observed up until the experiment was stopped at ~360 hours elapsed time; however, it appeared that the rate of advancement of the wetting front slowed as time progressed (Fig. 2-21c).

The results of this experiment suggest that rock heterogeneity plays a significant role in the speed at which water flows down gradient in a fracture. Although not conclusive, the existence of a boiling region stopped downward flow, while lateral imbibition continued. Post-experimental examination of the fracture surface near the boiling zone revealed small crystals. It is thought that these are KI crystals indicative of boiling and would explain the higher x-ray attenuation discussed above. Thus the resultant increased x-ray attenuation in the boiling region was probably a result of crystal formation rather than of increased saturation.

2.2.3 Fracture Healing

As mentioned in Section 2.1.2, the laboratory-determined water permeability of fractured Topopah Spring tuff samples at elevated temperatures behaves differently than that of intact samples. The water permeability in the fractured tuff samples decreases with increasing temperature. A series of laboratory experiments were conducted to understand the mechanism(s) that may cause the fracture healing. Those experiments have been reported by Lin and Daily (1984), Daily et al. (1987), Lin and Daily (1988), Lin (1991), Roberts and Lin (1995b), and Lin et al. (1995). The experimental techniques were described in Lin and Daily (1984). All of these experiments were designed to measure water permeability in fractured Topopah Spring tuff samples as functions of temperature, under various sample and experimental conditions that included reopened natural fractures, introduced tensile fracture, saw cut without shims, naturally fractured sample in a thermal gradient, and naturally fractured sample with variable pressure differences (confining pressure minus pore pressure). To understand the fracture healing process, we also conducted tests to investigate the effects of temperature and pressure on dry gas permeability, the effect of heating a saturated sample with water not flowing on the water permeability at room temperature, and the effect of flowing steam on gas permeability. In some of these experiments, the water that flowed through the samples was analyzed for concentration of certain elements, such as Si, Ca, K, etc. Also for some experiments the scanning electron microscope (SEM) was used to image the fracture surfaces before and after the experiments. The results of earlier experiments and a discussion of the mechanisms of fracture healing were reported in NFER Rev. 0. The results of these experiments are summarized in the following paragraphs.

The results of all of these experiments showed that flowing high-temperature (greater than 90°C) water through fractured tuff samples under compression caused water permeability to decrease significantly. This was true for both uniformly heated samples and samples under a thermal gradient. Flowing steam through a naturally fractured sample for about one week also decreased the dry N_2 permeability

measured at room temperature before and after the steam-flowing by about one order of magnitude. Flowing dry N_2 gas in fractured tuff samples under the same temperature and pressure conditions did not affect the gas permeability. Heating a saturated fractured tuff sample when water was not allowed to flow during heating did not affect the water permeability at room temperature. Based on these observations and the results of chemical analyses of the water, and SEM studies of the fracture surfaces, we concluded that dissolution and deposition of minerals, such as silica by the water in the fracture surfaces, may smooth out asperities and cause the fracture aperture to decrease under confining pressure. These processes are relatively insensitive to the type of fracture surface, such as natural fracture, rough tensile fracture, and smooth saw cut (NFER Rev. 0).

Recent study of fracture healing at various differential pressures reveals more detailed information about the healing mechanism. Figure 2-22 shows the water permeability of a naturally fractured tuff sample with respect to time. The figure also shows water permeability and confining pressure with respect to time during the experiment. The pore pressure in the sample was kept constant at 0.5 MPa, therefore the variation of confining pressure equals the variation of differential pressure. The experiment consisted of several parts. First the confining pressure was cycled from 1 to 5 to 1 MPa at ambient temperature. Next were several cycles in temperature, from approximately 25 to 150 to 25°C at constant confining pressures (1, 2, 3, and 5 MPa).

The first decrease in permeability, as shown in Fig. 2-22 at about 400 hours elapsed time, was caused by increasing confining pressure at room temperature. When the confining pressure was released, the permeability recovered to its original value. This shows that a confining pressure of 5 MPa at room temperature is not enough to cause any nonelastic deformation on the fracture surfaces. Upon heating, the permeability began to decrease as soon as temperature started to increase, even at the lowest differential pressure, 0.5 MPa. For the entire experiment the permeability decreased from about 18×10^{-15} m^2 (18 mD) to about 2×10^{-15} m^2 (2 mD). Most of that decrease in permeability was accomplished during the first heating cycle.

Figure 2-23 shows the Si concentration in the water that flowed through the sample during the test, and temperature as a function of the elapsed time. The two x's at the zero elapsed time are the Si concentration in the virgin J-13 water, before it flowed through the sample. With regard to Si concentration and permeability decreases, the experiment can be divided into two parts as indicated by the line at ~2000 hr on both Figure 2-22 and 2-23. The largest decrease in permeability occurred during the first thermal cycle prior to 2000 hr (from 18×10^{-15} m^2 to about 6×10^{-15} m^2 [18 to 6 mD]). Also note that during the first thermal cycle the Si concentration in the water was below that in the virgin J-13 water until the temperature reached 150°C, and the fluid exiting the sample was undersaturated with respect to Si during this period. This indicates that during the first heating phase Si may have been deposited on the fracture surfaces. After 2000 hr, during subsequent heating cycles, the permeability change is much less than the first thermal cycle (about 6×10^{-15} m^2 to 2×10^{-15} m^2 [6 to 2 mD]) and the water is saturated with respect to Si (α-cristobalite; W. Glassley, personal communication, 1995). As observed in Figure 2-23, the Si concentration is strongly correlated with temperature during this period. During this period permeability does show a relationship with confining pressure, because permeability decreases with increasing confining pressure. As shown in Fig. 2-22, slight increases in permeability were observed at the end of thermal cycles because of cooling (e.g., 2900 hr). Under the condition of Si saturation, both dissolution and deposition of Si can occur. However, the dissolution and deposition were probably not very active because the corresponding decreases in permeability were not significant. In addition, during the later part of the test the fracture surfaces may be smoother than before; therefore the effect of dissolution and deposition on permeability may be reduced.

The coupled processes that are evident in this experiment demonstrate a complex relationship, and the subsequent effect they have on the permeability is often difficult to fully understand. This experiment provides us with some indication of which specific process is active during the different portions of the test. During the first temperature cycle, thermal-chemical processes seem to dominate

hydrologic changes. Later, when the Si concentration reached saturation, thermal-mechanical processes appear to most affect the permeability. This test confirms the previous conclusion that rock-water interaction is probably the cause of the fracture healing. In addition, it shows that permeability in fractured tuff samples can decrease even at very low pressure. It also indicates that the rock-water interaction was most active during the initial heating of the sample. In terms of modeling and understanding repository design and performance, this is an extremely important result and is worthy of more study. If the laboratory-observed phenomena also occur *in situ*, these coupled processes can have a potentially large effect on the movement of condensate, the importance of preferential pathways, and the effective local permeability, as well as on other issues related to repository design.

2.3 References

Daily, W., W. Lin, and T. Buscheck, 1987, "Hydrology of Topopah Spring Tuff—Laboratory Measurements," *J. Geophys. Res.* 92, No. B8, pp. 7854–7864. NNA.19900123.0064

Daily, W., and W. Lin, 1991, "Laboratory Determined Suction Potential of Topopah Spring Tuff at High Temperatures," *Proceedings of the Second Annual International Conference on High Level Radioactive Waste Management*, Las Vegas, NV, April 28–May 3, 1991, American Nuclear Society, Inc., La Grange Park, IL, pp. 583–588. NNA.19910304.0097

Estill, J.C., and G.E. Gdowski, 1996, "Water vapor effects of the corrosion of carbon steel," *Proceedings of the Seventh Annual International Conference on High Level Radioactive Waste Management*, Las Vegas, NV, April 29–May 3, 1996, American Nuclear Society, Inc., La Grange Park, IL, pp. 457–458.

Klavetter, E.A., and R.R. Peters, 1987, *An Evaluation of the Use of Mercury Porosimetry in Calculating Hydrologic Properties of Tuff from Yucca Mountain, Nevada*, SAND86-0286, Sandia National Laboratory, Albuquerque, NM. NNA19890327.0056

Lin, W., 1991, "Variation of Permeability with Temperature in Fractured Topopah Spring Tuff Samples," *Proceedings of the Second Annual International Conference on High Level Radioactive Waste Management*, Las Vegas, NV, April 28–May 3, 1991, American Nuclear Society, Inc., La Grange Park, IL, pp. 988–993. NNA.19910523.0105

Lin, W., and W. Daily, 1984, *Transport Properties of Topopah Spring Tuff*, Lawrence Livermore National Laboratory UCRL-53602, Livermore, CA. NNA.19891026.0025

Lin, W., and W. Daily, 1988, "Hydrological Properties of Topopah Spring Tuff under a Thermal Gradient, Laboratory Results," *International Journal of Rock Mechanics*, 27, #5, pp. 373–385. NNA.19880503.0014

Lin, W., J.J. Roberts, W. Glassley, and D. Ruddle, 1995, *The Effect of Rock-water Interaction on Permeability*, Lawrence Livermore National Laboratory UCRL-JC-119574, Livermore, CA. MOL.19960416.0275

Lin, W., J.J. Roberts, and D. Ruddle, 1996, "Relative humidity in the near-field environment," *Proceedings of the Seventh Annual International Conference on High Level Radioactive Waste Management*, Las Vegas, NV, April 29–May 3, 1996, American Nuclear Society, Inc., La Grange Park, IL, pp. 128–129. MOL.19960422.0127

Moore, D.E., C.A. Morrow, and J.D. Byerlee, 1986, "High-temperature permeability and groundwater chemistry of some Nevada Test Site Tuffs," *J. Geophys. Res.*, 91, No. B2, pp. 2163–2171.

Peters, R.R., E.A. Klavetter, I.J. Hall, S.C. Blair, P.R. Heller, and W.G. Gee, 1984, *Fracture and Matrix Hydrologic Characteristics of Tuffaceous Materials from Yucca Mountain, Nye County, Nevada*, SAND84-1471, Sandia National Laboratory, Albuquerque, NM. NNA.19900810.0674

Ramirez, A., T. Buscheck, R. Carlson, W. Daily, K. Lee, W. Lin, N. Mao, T. Ueng, H. Wang, and D. Watwood, 1991, *Prototype Engineered Barrier System Field Test (PEBSFT) Final Report*, A. Ramirez, Scientific Editor, Lawrence Livermore National Laboratory UCRL-ID-106159, Livermore, CA. NNA.19910711.0047

Roberts, J.J., and W. Lin, 1994a, *Hydrological Property Measurements of Topopah Spring Tuff*, Lawrence Livermore National Laboratory UCRL-ID-119033, Livermore, CA. MOL.19950501.0032

Roberts, J.J., and W. Lin, 1994b, "Electrical properties of Topopah Spring tuff as a function of saturation," *Proceedings of the Fifth Annual International Conference on High Level Radioactive Waste Management*, Las Vegas, NV, May 22–26, 1994, American Nuclear Society, Inc., La Grange Park, IL, pp. 2112–2120. NNA.19940524.0018

Roberts, J.J., and W. Lin, 1995a, *Hydrological Property Measurements of Topopah Spring Tuff*, Lawrence Livermore National Laboratory UCRL-ID-119033, Livermore, CA. MOL.19950501.0032

Roberts, J.J., and W. Lin, 1995b, "Permeability of Fractured Tuff as Functions of Temperature and Confining Pressure," *Proceedings of the Sixth Annual International Conference on High Level Radioactive Waste Management*, Las Vegas, NV, April 30–May 5, 1995, American Nuclear Society, Inc., La Grange Park, IL, pp.44–45. MOL.19960109.0097

Roberts, J.J., and W. Lin, 1996a, *Report on Laboratory Tests of Drying and Re-Wetting of Intact Rocks*, Lawrence Livermore National Laboratory UCRL-ID-121513, Livermore, CA. MOL.19960409.0179

Roberts, J.J., and W. Lin, 1996b, *Electrical Properties of Partially Saturated Topopah Spring Tuff: Water Distribution as a Function of Saturation*, Lawrence Livermore National Laboratory UCRL-JC-123763, Livermore, CA. (submitted to Water Resources Research)

Roberts, J.J., and W. Lin, 1996c, "X-ray radiography of fracture flow and matrix imbibition," *Proceedings of the Seventh Annual International Conference on High Level Radioactive Waste Management*, Las Vegas, NV, April 29–May 3, 1996, American Nuclear Society, Inc., La Grange Park, IL, pp. 128–129. MOL.19960409.0159

Tidwell, V.C., and R.J. Glass, 1994, "X-ray and visible light transmission for laboratory measurement of two-dimensional saturation fields in thin-slab systems," *Water Resources Research*, 30, 2873–2882.

Data Tracking Information in this Chapter:

2.1.1 Moisture Retention at Elevated Temperatures
(Data Tracking Numbers: LL950404604242.012 and LL950812704242.017)

2.1.3 Electrical Resistivity as a Function of Water Saturation at Elevated Temperatures
(Data Tracking Numbers: LL950404604242.012 and LL960201404244.011)

2.1.4 Relative Humidity as a Function of Water Saturation at Elevated Temperatures
(Data Tracking Numbers: LL960100604244.007 and LL960201304244.010)

2.2.2 Fracture Flow vs. Matrix Imbibition at Elevated Temperatures
(Data Tracking Number: LL960100704244.008)

2.2.3 Fracture Healing
(Data Tracking Numbers: LL950404604242.012, LL950916504242.018, LL950406104242.016, and LL940800704242.002)

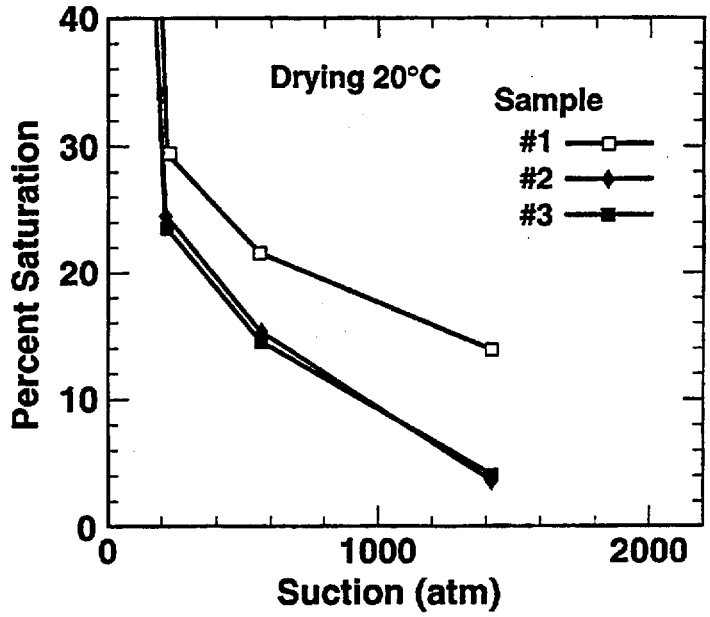

Figure 2-1. Percent saturation as a function of suction potential measured at 20°C for three samples of Topopah Spring tuff. Samples were initially saturated so that these data are the capillary suction for drying. All samples were taken from USW H-1 core.

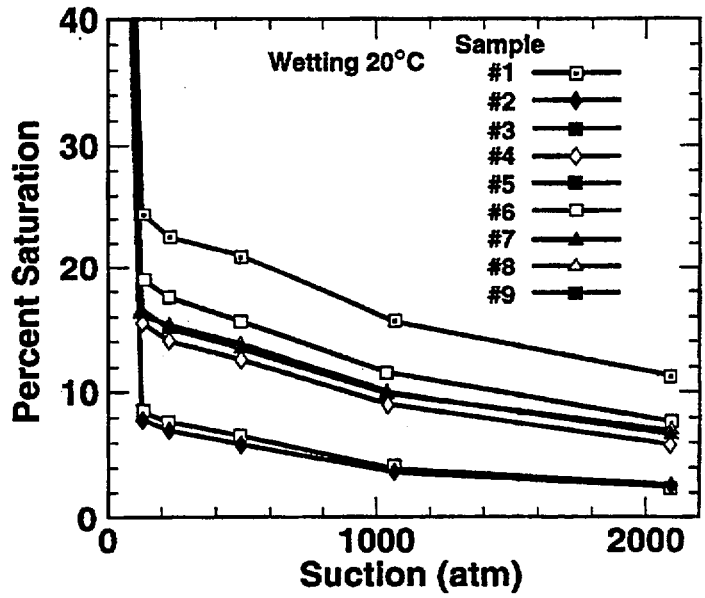

Figure 2-2. Percent saturation as a function of suction potential measured at 20°C for nine samples of Topopah Spring tuff. Samples were initially dry so that these data are the capillary suction for wetting. Samples 1–3 were taken from USW H-1 core; samples 4–9 were taken from Fran Ridge outcrop.

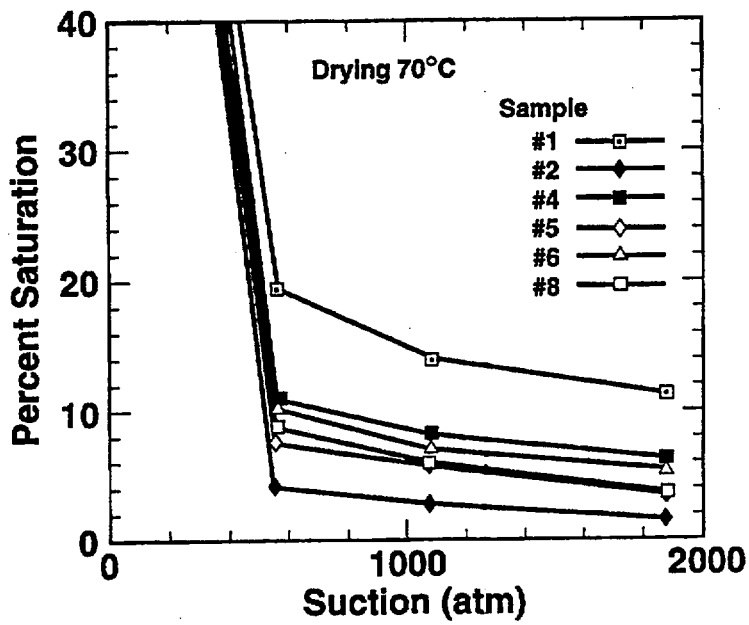

Figure 2-3. Percent saturation as a function of suction potential measured at 70°C for six samples of Topopah Spring tuff. Samples were initially saturated so that these data are the capillary suction for drying. Samples 1 and 2 were taken from USW H-1 core, and the others were taken from Fran Ridge outcrop.

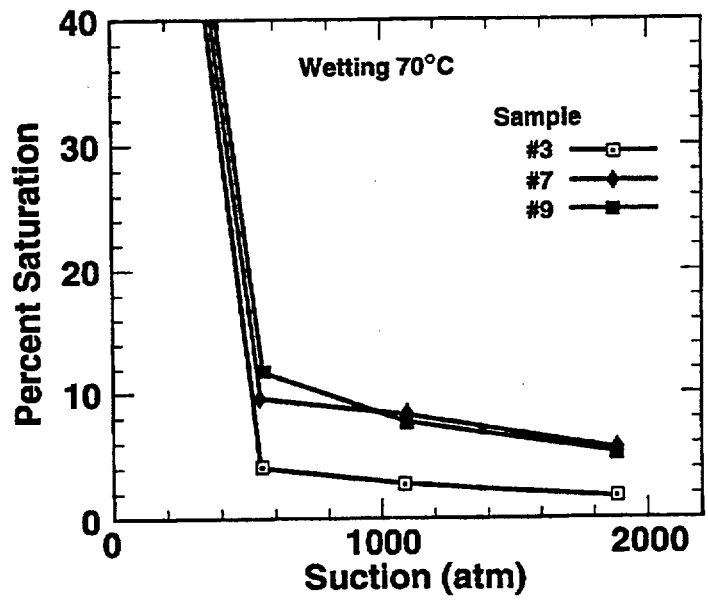

Figure 2-4. Percentage saturation as a function of suction potential measured at 70°C for three samples of Topopah Spring tuff. Samples were initially dry so that these data are the capillary suction for wetting. Sample 3 was taken from USW H-1 core; samples 7 and 9 were taken from Fran Ridge outcrop.

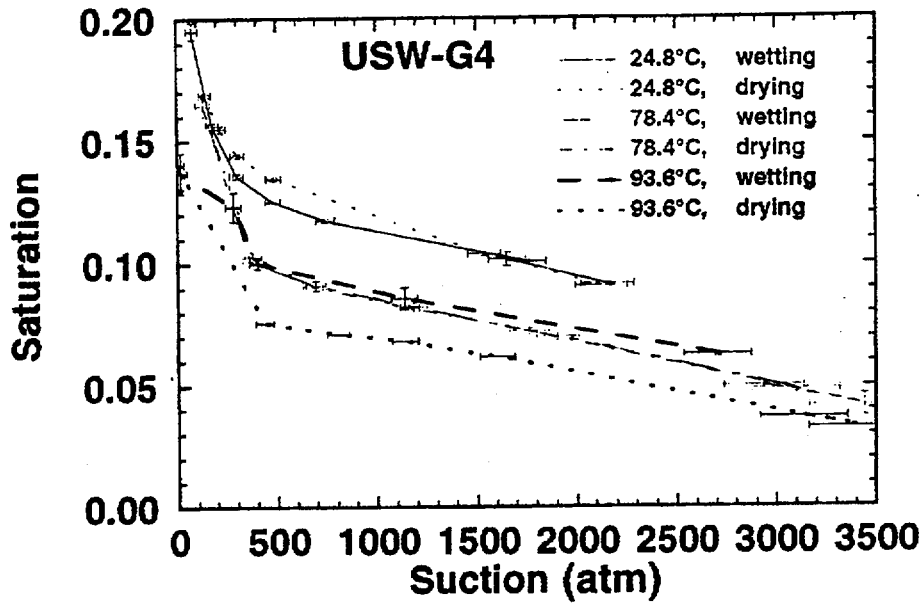

Figure 2-5. Saturation as a function of suction (atmospheres) for USW G-4. Wetting and drying curves are shown for three temperatures. The lines are not fitted curves but indicate the connection between points that are averaged for several samples. Error bars for suction assume 2% error in the relative humidity measurement. Note the reversal in hysteresis from low to high temperature.

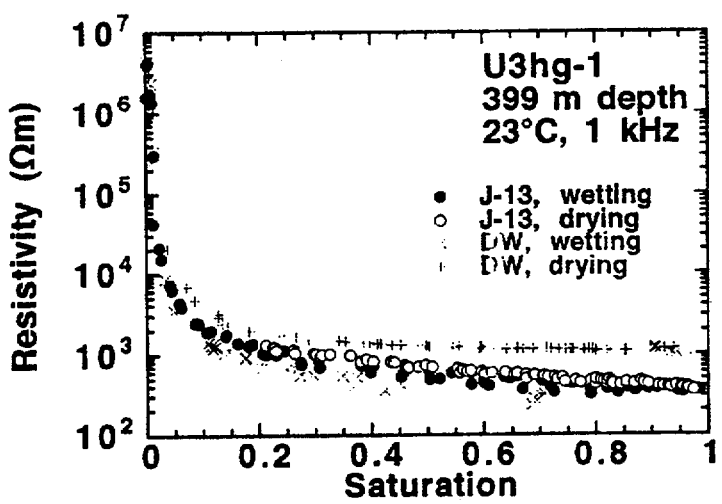

Figure 2-6. Electrical resistivity of U3hg-1 samples as a function of water saturation at room temperature, using J-13 water and distilled water (DW) as saturating fluid.

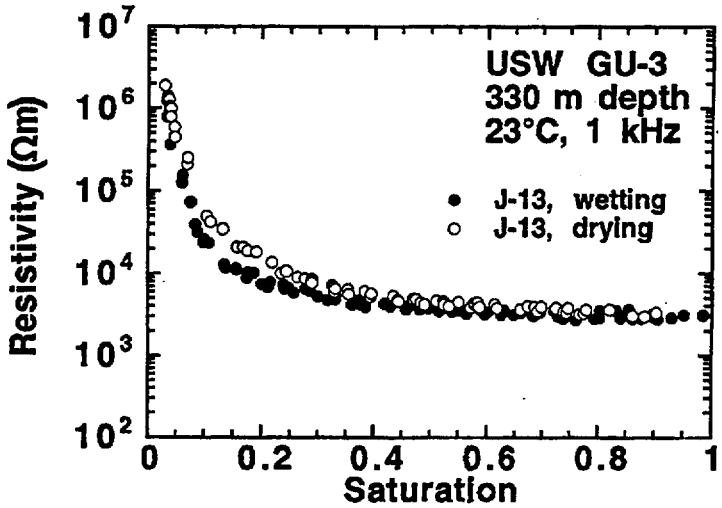

Figure 2-7. Electrical resistivity of USW GU-3 samples as a function of water saturation at room temperature, using J-13 water as saturating fluid.

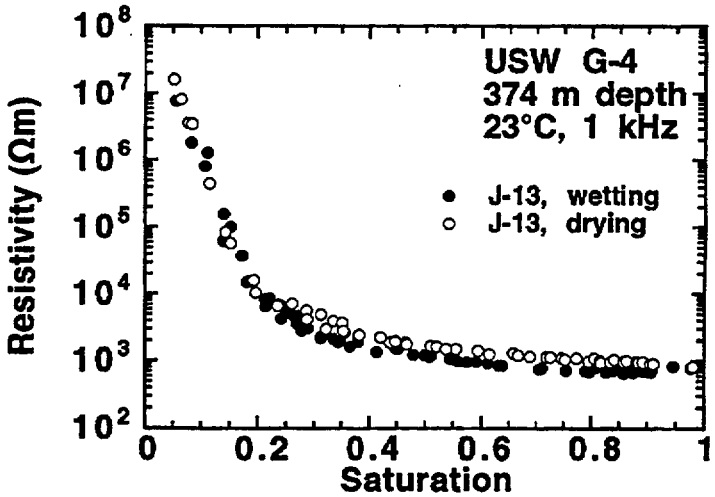

Figure 2-8. Electrical resistivity of USW G-4 samples as a function of water saturation at room temperature, using J-13 water as saturating fluid.

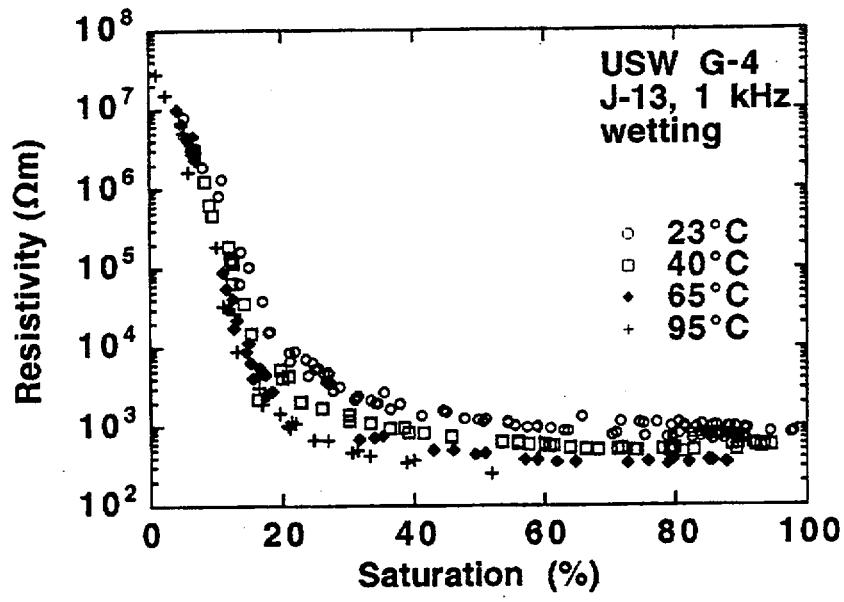

Figure 2-9. Electrical resistivity of USW G-4 samples as a function of water saturation at elevated temperatures, using J-13 water as saturating fluid.

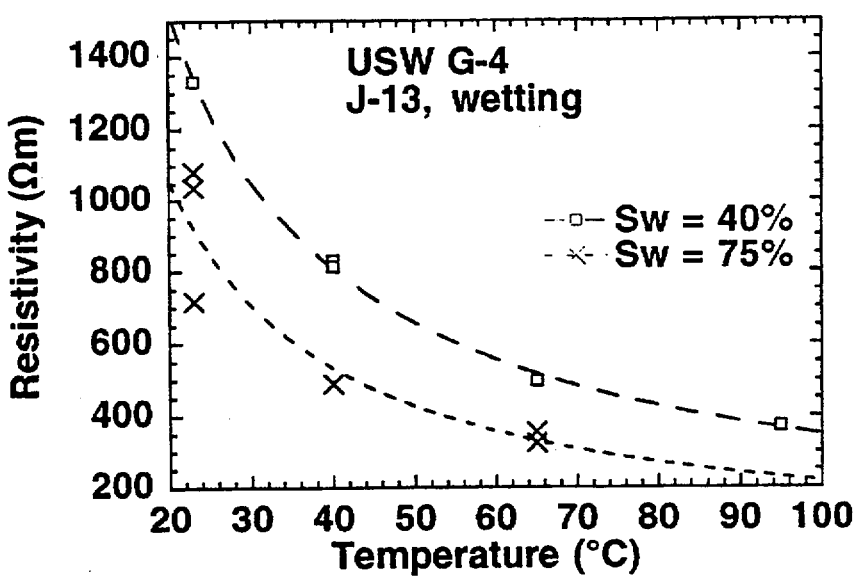

Figure 2-10. Resistivity (Ωm) of Topopah Spring tuff as a function of temperature for two saturations, 40 and 75%. Data are for the saturation cycle of samples from USW G-4 using J-13 water. Curves are power law fits. Between 20 and 100°C there is approximately a factor of 3 to 4 reduction in resistivity. Over the same temperature span the resistivity of J-13 water decreases by about a factor of 2.

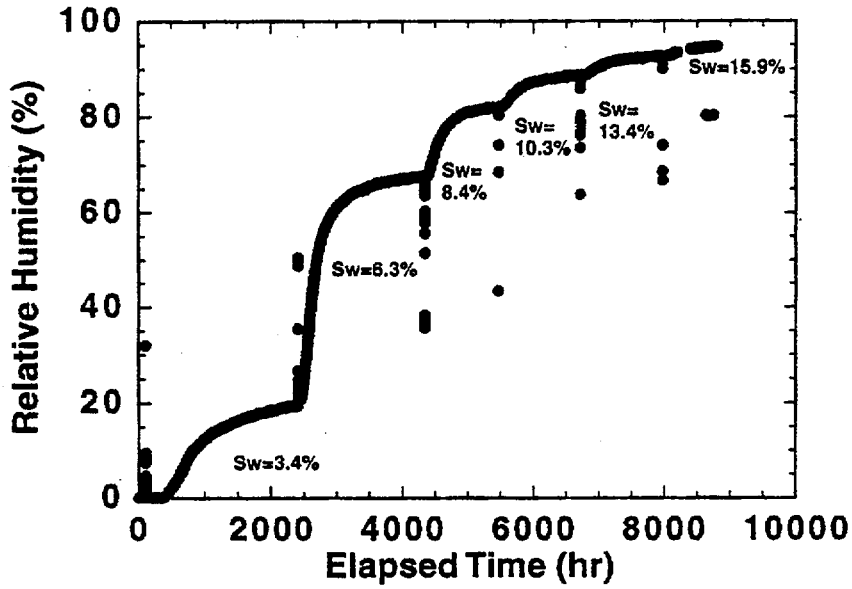

Figure 2-11. Relative humidity in an intact Topopah Spring tuff sample and water saturation as a function of elapsed time.

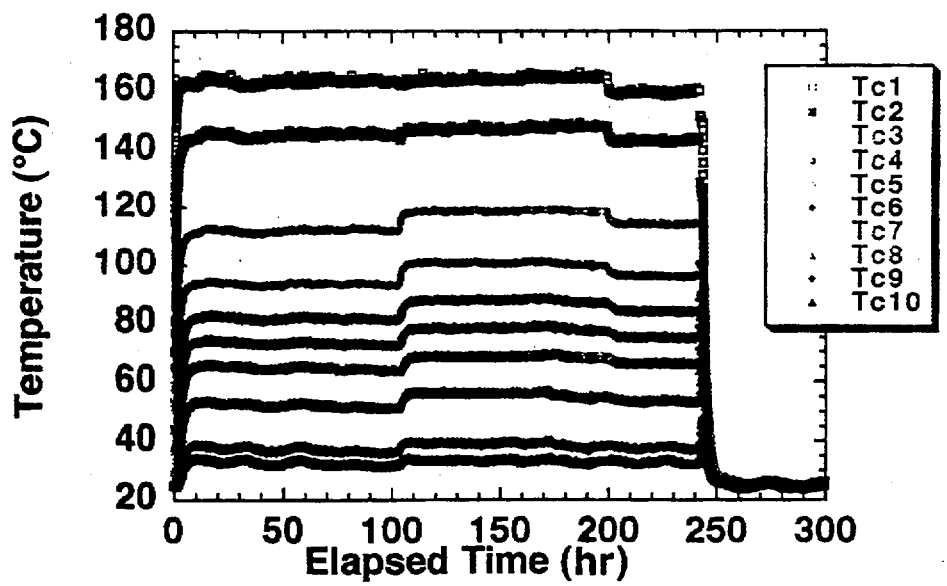

Figure 2-12. Temperatures in the 35.56-cm core during the vapor condensation along a fracture experiment as a function of time. Thermocouples Tc1 to Tc10 are from the bottom to the top of the sample, respectively.

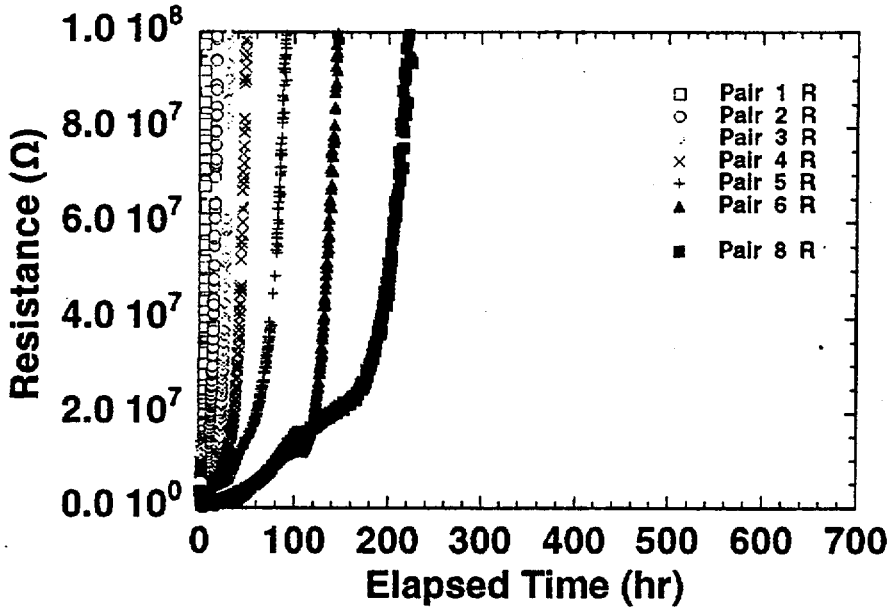

Figure 2-13. Electrical resistance in the 35.56-cm core during the vapor condensation along a fracture experiment as a function of time. Electrode pairs 1 to 8 are from the bottom to the top of the sample, respectively.

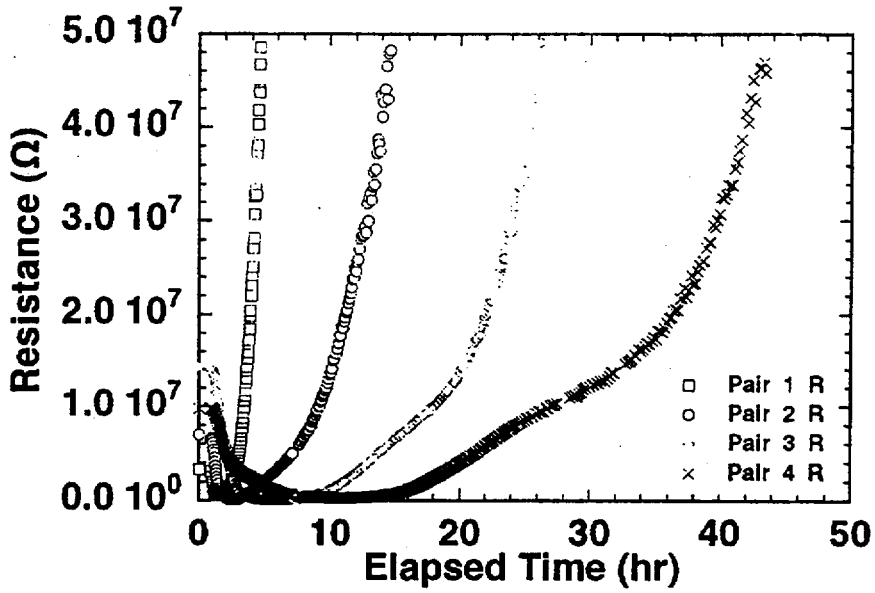

Figure 2-14. Electrical resistance at electrode pairs 1 to 4 in the 35.56-cm core during the vapor condensation along a fracture experiment as a function of time.

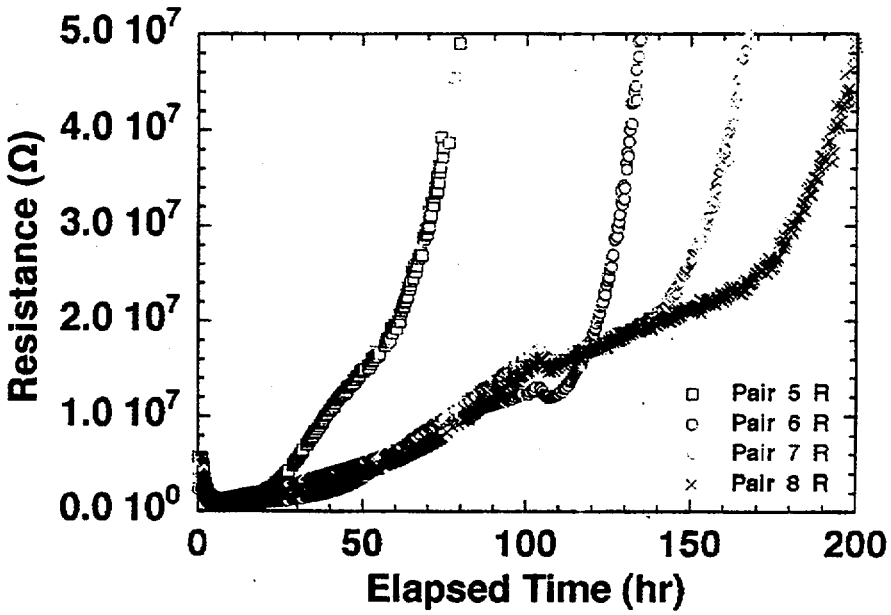

Figure 2-15. Electrical resistance at electrode pairs 5 to 8 in the 35.56-cm core during the vapor condensation along a fracture experiment as a function of time.

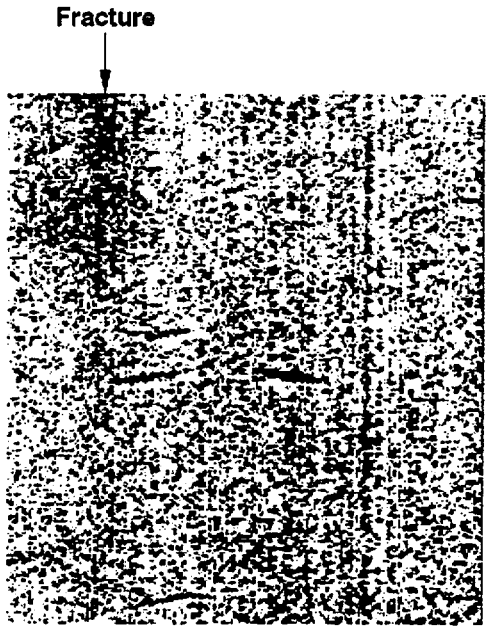

Figure 2-16. X-ray difference image sequence of radiographs of tuff containing a tensile fracture. No shim was put in the fracture. The experiment was performed at room temperature. Water containing KI to enhance attenuation of x rays was ponded on top of the sample. A roughly V-shape wetting front was observed at 47.5 hours.

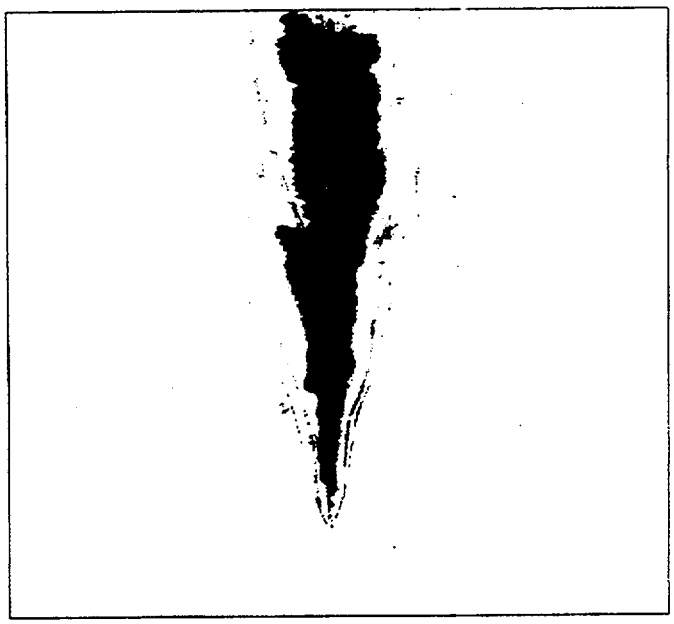

Figure 2-17. Fracture flow and matrix imbibition in plaster of Paris. Liquid containing dye was ponded on top of the sample and flowed into the fracture. The fracture was held open by 25-μm gold shims. The lines indicate the progress of the wetting front as a function of time (hours).

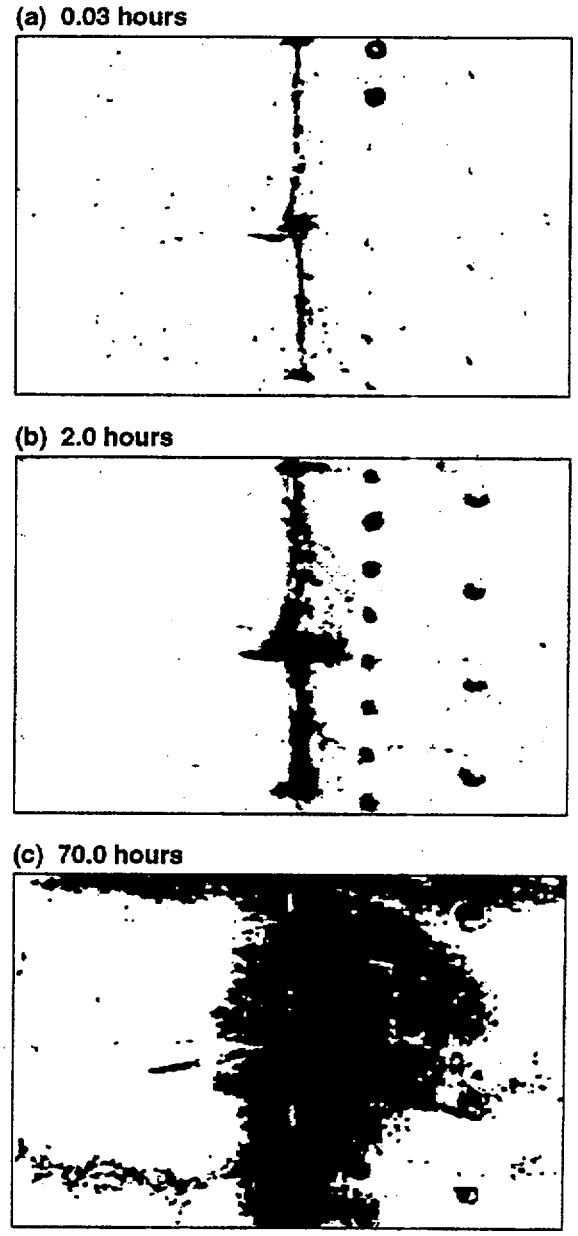

Figure 2-18. X-ray difference image sequence of radiographs of tuff containing a tensile fracture. Four 2-μm gold shims held the fracture open. The experiment was performed at room temperature. Water containing KI to enhance attenuation of x rays was ponded on top of the sample. The elapsed time of each image is (a) 0.03, (b) 2.0, and (c) 70.0 hours. Darker shades represent a large change in attenuation (the addition of water from the first radiograph). The spots on the right side of the images are holes that were plugged with RTV after the start of the experiment. (a) After 0.03 hours, water had already flowed the length of the fracture. (b) At later times, 2.0 hours, water began to imbibe laterally into the matrix. (c) After 70 hours the non-uniformity of matrix imbibition is evident (see text).

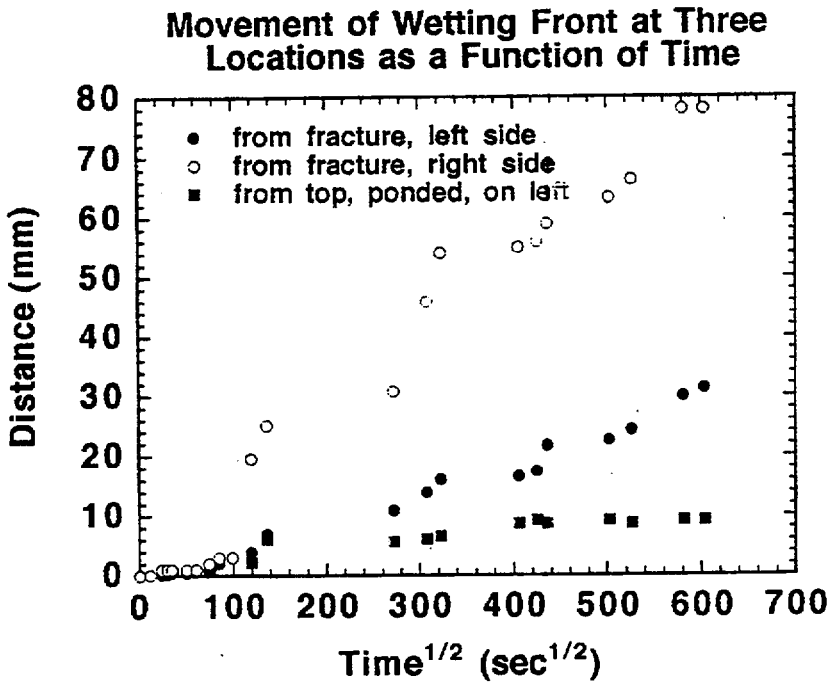

Figure 2-19. Tracking of the wetting front in the experiment shown in Fig. 2-18 plotted as distance (mm) vs the square root of time for three separate locations. The different slope of each line indicates difference imbibition rates for each location, demonstrating the heterogeneity of the rock.

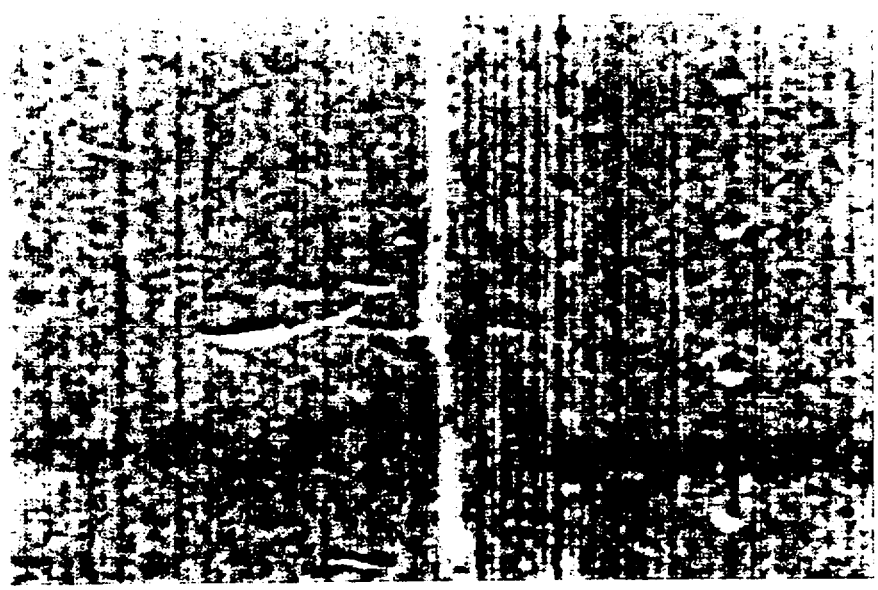

Figure 2-20. X-ray radiography image of the dry-out of the same fracture as in Fig. 2-18 after it was wetted.

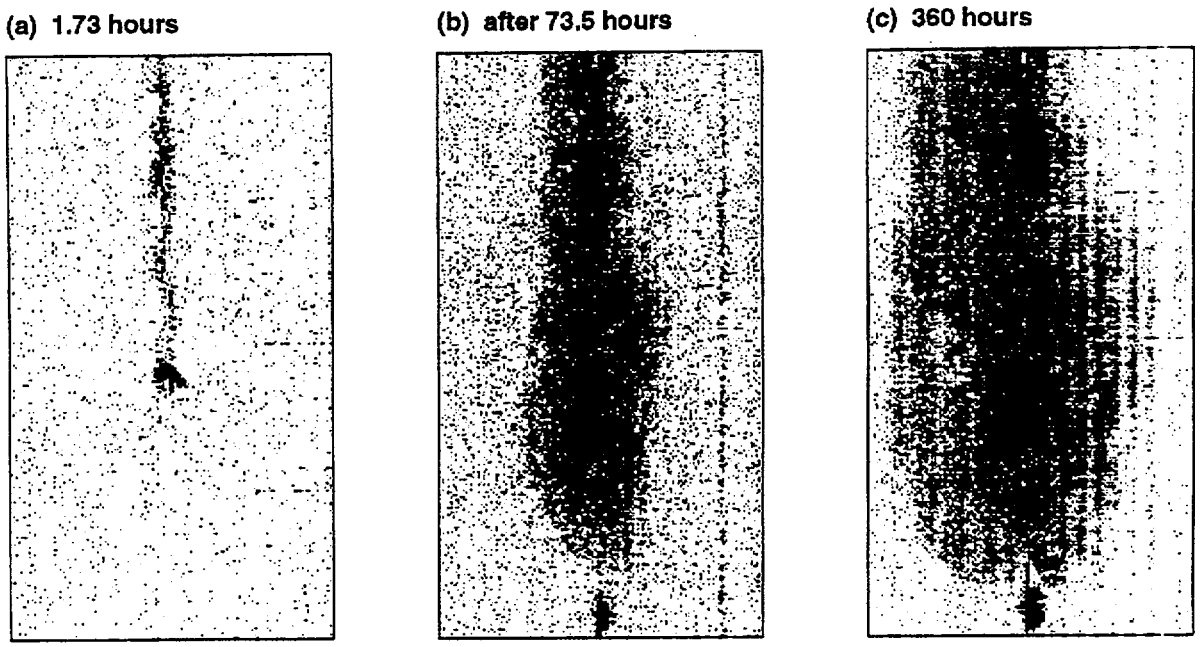

Figure 2-21. X-ray difference image sequence of radiographs of tuff containing a natural fracture. Nine 25-μm gold shims held the fracture open. The sample was initially heated (faint traces of the thermocouples can be seen) to above boiling at the bottom of the sample. The top of the sample was approximately 28°C. Water was ponded on top of the sample near the fracture only (as opposed to the entire sample top). Water quickly flowed into the fracture (similar to the unheated experiment in Fig. 2-18) after which the progress of the fracture flow slowed, shown in (a) 1.73 hours. The point at which flow slowed was found to be a relatively porous low x-ray attenuation region intersected by the fracture. At greater times, flow eventually proceeded past this region (after ~23 hours). There was also considerable lateral imbibition by this time. (b) Shows progress of fluid after 73.5 hours. The darkest region indicates the porous region now highly saturated. At the bottom of the sample centered on the fracture is a second dark region. This is interpreted as a region of high attenuation because of KI precipitation during boiling. (c) At 360 hours, water continued to imbibe laterally but never penetrated past the bottom of the sample.

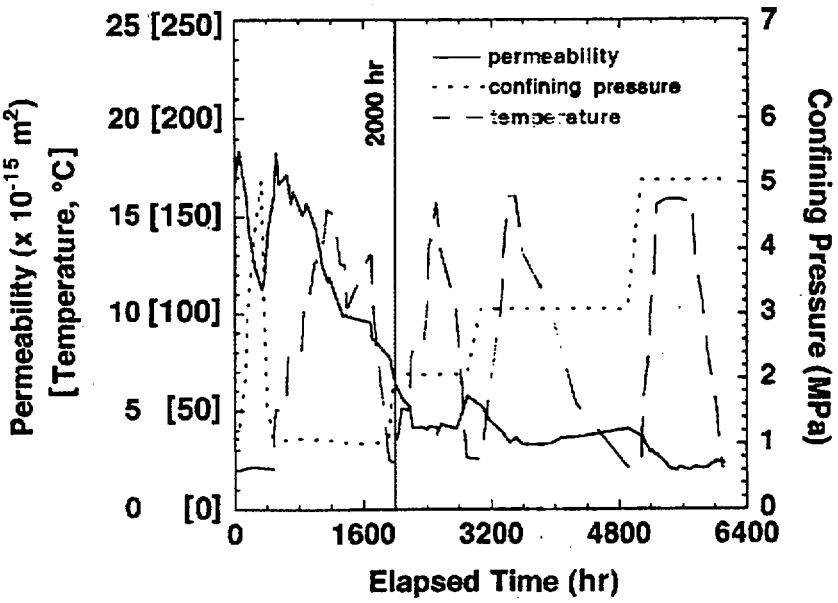

Figure 2-22. Permeability, confining pressure, and temperature of tuff containing a single fracture as a function of elapsed time. The vertical line at 2000 hr is explained in the text.

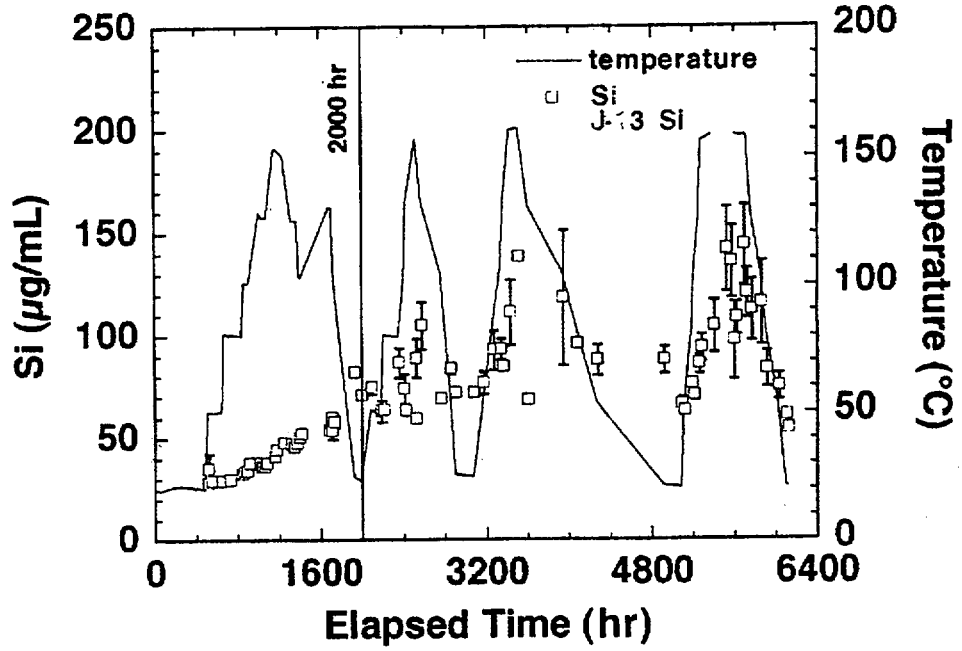

Figure 2-23. Si concentration at selected times during the experiment. Temperature of the experiment is also shown. During the initial pressure and heating cycles before 2000 hr, the Si concentration is relatively low. This is the period of the largest decrease in permeability. After 2000 hr, Si concentration is correlated with temperature (and is saturated with respect to α-cristobalite). Only a small decrease in permeability occurred during the period after 2000 hr.

Table 2-1. Permeability Measurements on Intact Core Sample SPC00504573.4

Temperature, °C	Confining Pressure, MPa	Differential Pressure, MPa	Permeability, μD
23	5.06	1.92	0.12
25	5.07	2.47	0.14
26	5.06	2.59	0.67
26	5.06	2.61	0.20
53	5.06	2.42	0.11
53	5.06	1.91	0.15
83	5.06	2.02	0.17
91	5.06	2.17	0.14
92	5.06	1.60	0.14
130	5.05	1.46	0.13
130	5.05	2.04	0.11
154	5.06	1.61	0.09

Contents

Chapter 3.0 Geochemistry....3-2
3.1 Summary of Recent Studies Concerning Geochemical and Mineralogical Evolution of the Near-Field Environment....3-2
3.1.1 Near-Field Environment....3-2
3.2 Ambient Conditions....3-5
3.3 Processes That Will Modify Ambient Conditions Within the Near-Field Environment....3-6
3.3.1 References for Sections 3.1, 3.2 and 3.3....3-10
3.4 Results of Recent Geochemical Research Relating To Near-Field Geochemistry And Mineralogy....3-13
3.4.1 Equilibrium Bounds on Water Chemistry and Mineralogical Changes Produced by Near-Field Relative Humidity Changes, by William E. Glassley, Lawrence Livermore National Laboratory....3-13
3.4.2 Testing EQ3/6 and GEMBOCHS Using Fluid-Mineral Equilibria in the Wairakei Geothermal System, by Carol Bruton, Lawrence Livermore National Laboratory....3-21
3.4.3 Mineralogy-Petrology Observations Regarding the Near-Field Environment, by David L. Bish, J. William Carey, Schon S. Levy and Steve J. Chipera, Los Alamos National Laboratory....3-36

Chapter 3.0 Geochemistry

3.1 Summary of Recent Studies Concerning Geochemical and Mineralogical Evolution of the Near-Field Environment

This section provides a brief summary of the more detailed results presented in Sections 3.4 and Chapters 10.3 and 10.4 of this report. As appropriate, reference is made to the relevant subsections where the detailed information can be located. The results described here use, as a basis, the research summarized in the Preliminary Near-field Environment Report, Volumes I and II. The primary change between the PNFER and this report reflects a change in modeling approach, rather than a change in models or data. The results described in Sections 3.4.2, 3.4.3, and Chapters 10.3 and 10.4, document that limitations in thermodynamic and kinetic data, which are used to describe future mineralogical and chemical changes, constrain our ability to simulate future mineralogical and chemical conditions. Therefore an approach is proposed in which general mineral assemblages ('facies') will be used to describe future mineralogical and chemical conditions, rather than detailed descriptions of mineral assemblages that include specific mineral types and compositions. See Section 3.4.2 for a thorough discussion of this issue.

3.1.1 Near-Field Environment

The results of three studies are reported here that consider the geochemical and mineralogical evolution of the NFE. Since the temperature in this region will be significantly above ambient for many years, evaporation of pore water will occur. One study (Section 3.4.1, Equilibrium Bounds on Water Chemistry and Mineralogical Changes Produced by Near-Field Relative Humidity Changes) examines these effects through numerical simulation of water chemistry changes resulting from evaporation. This study found that the main controls on water composition, and the secondary minerals precipitated as water evaporates, are the composition of the gas phase in equilibrium with the water, and the degree of

evaporation. The numerical simulations show that the coexisting gas phase composition primarily influences pH and redox state of the pore water. If the water remains in equilibrium with air, for example, pH increases significantly, reaching values in excess of 9.5, while the Eh decreases to values on the order of +500 mv. On the other hand, if the water is isolated from the atmosphere and the coexisting gas phase evolves in equilibrium with the water, pH decreases to values less than 6.75 and the Eh becomes more oxidizing, reaching values in excess of +650 mv.

The numerical simulations show that carbonates, phosphate, Al-silicates, and Si polymorphs are saturated in the water at very low degrees of evaporation (<10%). However, the only phases that may develop in significant abundance ($>10^{-3}$ moles per kilogram of water) are carbonate and Si-polymorphs, even at relatively high degrees of evaporation (70% to 90%). At higher degrees of evaporation, chloride salts may precipitate, in volumes that are ca. 10^{-6} of the original fluid volume. However, it is also to be expected that, as evaporation approaches 100%, very small volume films of high salinity brines will form in restrictions (pore throats, restricted channels, etc.), and persist to high temperatures due to the effect of salinity on water vapor pressure. These results suggest that the initial volumes of water entering the dry-out region, after the initial thermal pulse, should be expected to have ionic strengths and salinities that are elevated above ambient, due to dissolution of the previously precipitated mineral phases.

A second study (Section 3.4.2, Testing EQ3/6 and GEMBOCHS Using Fluid-Mineral Equilibria in the Wairakei Geothermal System) was undertaken to determine the extent to which numerical simulations could provide detailed descriptions of which minerals may develop as the repository heats up and cools down. This study used detailed chemical and mineralogical data obtained from the Wairakei Geothermal system in New Zealand, where rocks that are virtually identical to those that make up Yucca Mountain are undergoing alteration as they interact with water at elevated temperatures.

These observational data were compared to the results of numerical simulations, which used thermodynamic data from different sources. Employing a technique which considers the computed temperature-dependent affinity of several different

mineral species, it is possible to identify suites of minerals that are predicted to stably coexist.

Comparison of these predicted mineral suites to the observed mineral assemblages in the Wairakei rocks, allows one to determine the adequacy of different thermodynamic data sets. In all cases, it was possible to select a thermodynamic data set that best reproduced the observed mineral assemblages. Nevertheless, regardless of the data set employed, some minerals are predicted to occur which are not observed in the natural assemblages. This result leads to the conclusion that a facies concept should be used when describing the mineralogical evolution of the repository block. In such a concept, it is recognized that a specific suite of mineral types are expected to occur, but precise prediction of the mineral structures and compositions is not attempted, since small, local variations in intensive and extensive parameters, and uncertainties in thermodynamic and kinetic data, will lead to variations among the mineral assemblages that may actually form.

A third study (Section 3.4.3 Mineralogy-Petrology Observations Regarding the Near-Field Environment; also see "Summary and Synthesis Report on Mineralogy and Petrology Studies for the Yucca Mountain Site Characterization Project," 3-volume report, in preparation) summarizes host rock mineralogy, and some data on mineral stability relevant for near-field processes. The bulk-rock mineralogy within the near-field environment varies with depth and laterally across Yucca Mountain. Comparatively soluble silica phases, including cristobalite, tridymite, opal-CT, and volcanic glass are ubiquitous within the NFE. Limited data illustrate that major amounts of clinoptilolite and mordenite are common directly underlying the host rock in the eastern portion of Yucca Mountain, in and below the lower vitrophyre of the Topopah Spring Tuff. Natural alteration in the lower vitrophyre exemplifies hydrothermal modification of rock porosity by the dissolution of volcanic glass and precipitation of smectite, zeolite, and silica. This is consistent with several previous detailed studies which documented that significant changes in bulk rock solid volume will occur during rock-water interaction and temperature change, and that these changes may significantly modify rock and

fracture porosity and permeability (Meike and Glassley, 1990; Glassley, 1993; Glassley et al., 1994; Lin et al., 1995). Simplified mass balance calculations are presented in Section 3.4.3 that substantiate those previous conclusions. The rates at which mineral reactions will occur in the presence of water are dependent upon dissolution and precipitation kinetics of mineral phases. This was pointed out in the PNFER, where studies completed to 1990 were sumarized in Section 3.3.2, "Kinetics". Since then, several additional studies have been completed (kaolinite, Carroll and Walther, 1990, Nagy, et al., 1991, Nagy and Lasaga, 1993; gibbsite, Nagy and Lasaga, 1992; heulandite, Ragnarsdottir, 1993; cristobalite, Carroll et al., 1995, Renders et al., 1995) that established the kinetics of dissolution for a variety of phases important for modeling repository-relevant rock-water interaction as a function of time. As an addition to this database, recent results of dissolution kinetics experiments on clinoptilolite and analcime are discussed in Section 3.4.3, as well as recent data on the thermodynamic properties of analcime and clinoptilolite. Based on existing data, the dissolution of clinoptilolite appears to be slower than analcime, by a factor near 100. The energetics of solid-solutions and cation exchange models were discussed in the PNFER, Section 3.3.3. In this report, additional models for exchange are discussed in Section 3.4.3.

3.2 Ambient Conditions

The rock unit that is being characterized for waste emplacement is within the Topopah Spring member of the Paintbrush Tuff and has been designated as unit TSw2 on the thermal and mechanical stratigraphic map of the region (Ortiz et al., 1985). TSw2 is a devitrified, welded, rhyolitic tuff and consists of intact blocks separated by fractures. Price et al. (1987) report that the majority of the rock contains fine-grained matrix regions and gray-colored, vapor-phase-altered regions. In addition to these main components, the rock contains small lithophysae (open and closed) and fractures, some of which are filled with quartz, calcite, or other minerals. The porosities of the matrix and vapor-phase-altered regions are between 8 and 49% (Price et al., 1985; 1987). The matrix in the potential repository horizon has an

estimated mean water saturation of 65% (Montazer and Wilson, 1984). Existing data also indicate that the fracture density may be approximately 40 per m^3, and predominantly oriented in the vertical direction (Scott and Castellanos, 1984).

Field, petrographic, electron microprobe, scanning electron microscopy, and X-ray diffraction analyses (Carlos, 1985, 1987, 1989; Schuraytz et al., 1986; Broxton et al., 1987, 1989; Bish and Chipera, 1989; Chipera and Bish, 1989; Carlos et al., 1990, 1993; 1995; Levy et al., 1996) have shown that the tuff consists of both primary and secondary minerals. The primary minerals (sanidine, plagioclase, quartz, biotite, Fe-Ti oxides, allanite, and zircon) were formed at temperatures in excess of 600°C in a magma chamber prior to eruption of the tuff. Secondary minerals such as cristobalite, opal, tridymite, quartz, alkali feldspar, carboantes, and smectite collectively make up a substantial portion of the rock and were formed at temperatures less than 500°C, either during cooling, or later as alteration products. See Section 3.4.3 for a more detailed discussion.

3.3 Processes That Will Modify Ambient Conditions Within the Near-Field Environment

Emplacement of waste packages in this environment will modify the thermal and radiation fields experienced by the host rock, and may lead to complex chemical reactions between the near-field fluids and minerals. The nature of these reactions will depend on a variety of parameters, including the temperature of the environment, the composition of the fluid phase, the rate at which the thermal field changes, the kinetics of reactions, fluid movement rates and pathways, and the amount and nature of radiolysis products. The values of these parameters will change through time as the thermal and radiation fields decay.

Numerous simulations of the hydrological evolution of the WP environment (Nitao and Buscheck, 1989; Buscheck et al., 1991, 1993, 1994; Buscheck and Nitao, 1992, 1993; Nitao et al., 1992) have suggested that four different hydrothermal regimes will form in the vicinity of WPs:

A. A regime in which temperatures are elevated, but are below the boiling point;

B. A regime in which boiling occurs;

C. A regime in which temperatures are above boiling and relative humidities may be low (<95%)

D. A regime in which rock properties are permanently modified, such that rock characteristics during cool down do not recover to pre-emplacement state or values.

These regimes form because pore water will be heated as energy is transferred from the WPs to the surrounding rock. This heating will lead to (1) evaporation of pore water as temperature rises, (2) condensation of water vapor in cooler regions, and (3) boiling and dessication in those regions that reach or exceed the nominal boiling temperature. The local heat budget will thus reflect the local balance between convective and conductive processes. The kinds of processes and effects that may develop are described below.

Regime A: Temperature < $T_{boiling}$. This regime encompasses those areas in which the temperature is between ambient and boiling. It is therefore significant for all regions that undergo heating. As heating occurs, *in situ* pore water is heated and evaporates. Water vapor moving in fractures to lower temperature regions will condense on fracture surfaces. The condensed water either will be imbibed into the matrix by capillary suction or will flow along fracture surfaces, depending on the degree of matrix saturation and the permeability of the fracture surfaces.

Within a few tens of meters of the walls of drifts within which waste has been emplaced, Regime A will persist for a very brief period of time (less than 10 years) because of the rapid rate of heat deposition. In contrast, rock that is hundreds of meters from emplacement drifts will heat up slowly, resulting in the persistence of Regime A for hundreds to thousands of years.

Regime B: $T = T_{boiling}$. Between Regime A and the WPs, temperatures will eventually reach the boiling point for virtually all scenarios with APDs greater than 20 kW/acre. When this condition is met, pore water will vaporize and the resulting steam will migrate to cooler regions where it will condense. Imbibition of the

condensed steam into the matrix of fracture-bound blocks will eventually result in fully saturated rock adjacent to fractures transporting steam. Thus, this rock volume is one in which temperature is essentially constant at the nominal boiling point (~96°C), and much of the rock may be at 100% saturation. Above the repository, this may lead to a region of water refluxing in which water will cycle from the boiling zone to the condensation front (as vapor), and back again (as liquid). Below the repository, refluxing will not occur, but the saturation zone will be widened as condensed hot water flows downward along fractures.

The water that condenses is distilled, and thus must be treated as a liquid that is far from equilibrium with either the host rock or fracture lining minerals. Extensive dissolution of rock matrix and fracture lining minerals must be anticipated for this region.

This regime grows in volume as long as the thermal envelope around the repository is expanding. The regime thickness varies, being virtually zero at the edge of emplacement drift walls when the boiling point is first reached shortly after waste emplacement, to thicknesses that may be in excess of 100 meters several hundred to thousands of years after the repository is closed. This regime will be one of the most chemically active since a high temperature is achieved at full saturation for long time periods (10's to 100's of years).

Regime C: $T > T_{boiling}$. Regime C is bounded by the boiling point isotherm outward, and the repository inward, and represents the region within which temperatures are above the boiling point and relative humidity is variable (<90%). Local persistence of liquid water to very high temperatures, perhaps as high as 150 to 210°C, may result from (1) vapor pressure lowering due to increased salinity of trapped water in restricted pores, (2) boiling point elevation associated with high vapor pressures in block interiors, where vapor migration to fractures may be restricted, or (3) water adsorbed onto mineral surfaces. In general, however, it is expected that this regime will be one dominated by relative drying of the rock, with a persistent but very small volume of water remaining.

Regime D: $T < T_{local\ max}$. This regime develops after the local thermal maximum has been achieved. It encompasses rock that has been physically modified during the

heat-up period, either as a result of mineral dissolution or precipitation or both, or because of mechanical effects. These effects will be evident as changes in bulk and fracture porosity and permeability, and mineralogy. In those regions where saturation had increased above pre-emplacement ambient values, slow removal of water will lead to decreasing saturation. Those regions that had experienced decreased saturation relative to pre-emplacement ambient saturations will begin to rehydrate slowly as the local thermal maximum passes. Current modeling suggests that the rates of resaturation are so slow that it will be 100's of 1000's of years before pre-emplacement ambient saturations are approached. This regime could be realized in all of the other regimes, as cooldown proceeds.

Preliminary modeling has suggested that regimes A and B may quickly pass through the NFE, if thermal loadings are > 100 kw/acre (Nitao, 1988). Nevertheless, complex coupling of fluid velocities and mineralogical reactions in fractures and matrix blocks suggests that mineralogical equilibrium may be approached for some portions of the NFE, even under these conditions (Glassley, 1993). This work has shown that, as evaluated using classic Damkohler numbers or characteristic times of silicate reactions, reaction rates are fast enough to establish chemical steady state relative to transport rates in all regions except the immediate vicinity of emplacement drifts, or in regions of rapid refluxing and rapid fracture flow. At lower thermal loadings, or for certain scenarios in which there is wide spacing between emplacement drifts, regimes A and B may persist within portions of the NFE for hundreds of years. For this reason, the effects of all regimes must be considered as potentially significant for the NFE.

The composition of water that may contact waste containers will depend on the mineralogy of the near-field which, in turn, will be influenced by recrystallization processes that will occur during the period of time prior to incursion of liquid water (see Bish et al., this volume), and on the presence of materials placed within emplacement drifts during construction (see the Introduced and Man-Made Materials Chapter in this report). Within this section (Section 3) only those effects that result from interaction with the *in situ* rock will be discussed.

The primary chemical and mineralogical effects will be the result of interaction of the distilled, condensed water with rock matrix and fracture lining minerals. The main mechanisms responsible for the chemical evolution of the water will be dissolution and precipitation of along flow pathways. Water composition will also be influenced by evaporation, boiling, mixing of waters from different sources or regions, and infiltration. The effects of some of these processes on near-field water composition are discussed in Sections 3.4 and Chapter 10.3.

Such effects of rock-water interaction will change the local hydrological properties of the rock by dissolving pre-existing materials, and thus increasing local porosity and permeability, or precipitating minerals, thus decreasing porosity and permeability. Efforts to characterize these effects along flow pathways are in progress.

3.3.1 References for Sections 3.1, 3.2 and 3.3

Bish, D.L. and S.J. Chipera (1989), *Revised Mineralogical Summary of Yucca Mountain, Nevada,* Los Alamos National Laboratory, NM, LA-11497-MS, 57p.

Broxton, D.E., Bish, D.L., and Warren, R.G., 1987, Distribution and chemistry of diagenetic minerals at Yucca Mountain, Nye County, Nevada. Clays and Clay Minerals, v. 35, p. 89–110.

Broxton, D.E., Warren, R.G., and F.M. Byers, 1989, Chemical and mineralogic trends within the Timber Mountain-Oasis Valley caldera complex, Nevada: evidence for multiple cycles of chemical evolution in a long-lived silicic magma system. J. Geophys. Res., v. 94, p.5961–5985.

Bruton, C.J., Glassley, W.E., and Meike, A., 1995, *Geothermal Areas As Analogues To Chemical Processes In The Near-Field And Altered Zone of Potential Yucca Mountain, Nevada Repository,* Lawrence Livermore National Laboratory, Livermore, Calif., UCRL-ID-119842.

Buscheck, T. A., and J. J. Nitao (1992), *The Impact of Thermal Loading on Repository Performance at Yucca Mountain,* Lawrence Livermore National Laboratory, Livermore, Calif., UCRL-JC-109232.

Buscheck, T. A., and J. J. Nitao (1993), *The Impact of Repository Heat on Thermo-hydrological Performance at Yucca Mountain,* Lawrence Livermore National Laboratory, Livermore, Calif., UCRL-JC-114791.

Buscheck, T. A., D.G. Wilder, and J. J. Nitao, 1993, *Large-scale in situ heater tests for hydrothermal characterization at Yucca mountain,* Lawrence Livermore National Laboratory, Livermore, Calif., UCRL-JC-112445.

Buscheck, T. A., J. J. Nitao and S.F. Saterlie (1994), *Evaluation of Thermo-Hydrological Performance in Support of the Thermal Loading Systems Study,* In Proceedings of the 5th International High Level Nuclear Waste Management Conference, Las Vegas, NV, American Nuclear Society, La Grange, IL, p. 592-610.

Buscheck, T. A., J. J. Nitao, and D.A Chesnut, 1991, *The impact of episodic nonequilibrium fracture-matrix flow on repository performance at the potential Yucca mountain site,* Lawrence Livermore National Laboratory, Livermore, Calif., UCRL-JC-107920.

Carlos, B.A., 1985, Minerals in fractures of the unsaturated zone from drill core USW G-4, Yucca Mountain, Nye County, Nevada. Los Alamos National Laboraotry, LA-10415-MS.

Carlos, B.A., 1987, Minerals in fractures of the saturated zone from drill core USW G-4, Yucca Mountain, Nye County, Nevada. Los Alamos National Laboraotry, LA-10927-MS.

Carlos, B.A., 1989, Fracture-coating minerals in the Topopah Spring Member and Upper Tuff of Calico Hills from drill hole J-13. Los Alamos National Laboraotry, LA-11504-MS.

Carlos, B.A., Bish, D.L., and Chipera, S.J, 1990, Manganese oxide minerals in fractures of the Crater Flat Tuff in drill core USW G-4, Yucca Mountain, Nevada, Los Alamos National Laboratory, LA-11787-MS.

Carlos, B.A., Chipera, S.J., Bish, D.L., and Craven, S.J., 1993, Fracture-lining manganese oxide minerals in silicic tuff, Yucca Mountain, Nevada, U.S.A. Chemical Geology, v. 107, p. 47–69.

Carlos, B.A., Chipera, S.J., Bish, D.L., and Raymond, R., 1995, Distribution and chemistry of fracture-lining zeolites at Yucca Mountain, Nevada, in Natural Zeolites '93 (D.W. Ming and F.A. Mumpton, eds), Int. Comm. Natural Zeolites, Brockport, N.Y., p. 547–563.

Carroll S. A., Mroczek, E., Bourcier, B., Alai, M. and Ebert, M. (1995) Comparison of field and laboratory precipitation of amorphous from geothermal waters at 100°C. Lawrence Livermore National Laboratory Yucca Mountain Site Characterization Project Milestone MOL207.

Carroll, S.A. and Walther, J. V., 1990. Kaolinite dissolution at 25oC, 60oC, and 80oC. Amer. j. Sci., v. 290, p. 797-810.

Chipera, S. J., and D. L. Bish (1989), *Quantitative X-ray Diffraction Analyses of Samples Used for Sorption Studies by the Isotope and Nuclear Chemistry Division, Los Alamos National Laboratory,* Los Alamos National Laboratory, Los Alamos, NM, LA-11669-MS, 19 pp.

Glassley, W.E. (1993), Coupled Hydro-Geochemical Processes and Their Significance for Yucca Mountain Site Characterization, in *Proceedings of FOCUS '93,* Las Vegas, NV, American Nuclear Society, La Grange, IL, p. 221–224

Glassley, W.E., Bruton, C.J., Bourcier, W.L., 1994, Testing long-term predictions from hydrogeochemical models. Materials Res. Soc. Symposium Proc. Vol 333, p.805-810.

Levy, S.S., Norman, D.I., and Chipera, S., 1996, Alteration history studies in the exploratory studies facility, Yucca Mountain, Nevada, USA *Mat. Res. Soc. Symp.,* v. 412, p. 783–790.

Lin, W., Roberts, J.J., Glassley, W.E., and Ruddle, D., 1995. The effect of rock-water interaction on permeability. Proceedings of the Eigth International Congress on Rock Mechanics, Tokyo, Japan, and Lawrence Livermore National Laboratory UCRL-JC-119574.

Meike, A. and Glassley, W.E., 1990, In situ observation of the alpha/beta cristobalite transition using high voltage electron microscopy. Materials Res. Soc. Symposium Proc. Vol 178, p. 631-639.

Montazer, P., and W. E. Wilson, 1984, *Conceptual Hydrologic Model of Flow in the Unsaturated Zone, Yucca Mountain, Nevada,* U.S. Geol. Survey, Denver, CO, Water Resources Inv. Rep. 84-4345.Scott and Castellanos, 1984

Nagy, K.L., and Lasaga, A.C., 1992, Dissolution and precipitation kinetics of gibbsite at 80oC and pH 3: The dependence on solution saturation state. Geochim. Cosmochim. Acta, v. 56, p.3093-3111.

Nagy, K.L., and Lasaga, A.C., 1993, Simultaneous precipitation kinetics of kaolinite and gibbsite at 80oC and pH 3. Geochim. Cosmochim. Acta, v. 57, p.4329-4336.

Nagy, K.L., Blum, A.E., and Lasaga, A.C., 1991, Dissolution and precipitation kinetics of kaolinite at 80oC and pH 3: The dependence on solution saturation state. Amer. J. Sci., v. 291, 649-686.

Nitao, J.J. (1988), *Numerical Modeling of the Thermal and Hydrological Environment Around a Nuclear Waste Package Using the Equivalent Continuum Approximation: Horizontal Emplacement,* Lawrence Livermore National Laboratory, Livermore, CA, UCID-21444.

Nitao, J.J. and T.A. Buscheck, 1989, *On the movement of a liquid front in an unsaturated, fractured porous medium, Part I.* , Lawrence Livermore National Laboratory, Livermore, Calif., UCID-21714.

Nitao, J.J., T.A. Buscheck and D.A. Chesnut, 1992, *The implications of episodic nonequilibrium fracture-matrix flow on site stability and total system performance* , Lawrence Livermore National Laboratory, Livermore, Calif., UCRL-JC-109216.

Ortiz, T. S., R. L. Williams, F. B. Nimick, B. C. Whittet, and D. L. South (1985), *A Three-Dimensional Model of Reference Thermal/Mechanical and Hydrologic Stratigraphy at Yucca Mountain, Southern Nevada,* Sandia National Laboratories, Albuquerque, NM, SAND84-1076.

Price, R. H., F. B. Nimick, J. R. Connolly, K. Keil, B. M. Schwartz, and S. J. Spence (1985), *Preliminary Characterization of the Petrologic Bulk and Mechanical Properties of a Lithophysal Zone within the Topopah Spring Member of the Paintbrush Tuff,* Sandia National Laboratories, Albuquerque, NM, SAND84-0860.

Price, R. H., J. R. Connolly, and K. Keil (1987), *Petrologic and Mechanical Properties of Outcrop Samples of the Welded, Devitrified Topopah Spring Member of the Paintbrush Tuff,* Sandia National Laboratories, Albuquerque, NM, SAND86-1131.

Ragnarsdottir, K.V., 1993, Dissolution kinetics of heulandite at pH 2-12 and 25 degrees C. Geochim. Cosmochim. Acta, v. 57, p. 2439-2449.

Renders, P. J. N., Gammons, C. H., and Barnes, H. L. (1995) Precipitation and dissolution rate constants for cristobalite from 150 to 300°C. *Geochimica et Cosmochimica Acta,* 59, 77-85.

Schuraytz, B. C., T. A. Vogel, and L. W. Younker (1986), *Geochemical Gradients on the Topopah Spring Member of the Paintbrush Tuff: Evidence for Eruption Across a Magmatic Interface,* Lawrence Livermore National Laboratory, Livermore, CA, UCRL-53698.

3.4 Results of Recent Geochemical Research Relating To Near-Field Geochemistry And Mineralogy

3.4.1 Equilibrium Bounds on Water Chemistry and Mineralogical Changes Produced by Near-Field Relative Humidity Changes, by William E. Glassley, Lawrence Livermore National Laboratory

3.4.1.1 Introduction. Radioactive decay heat will lead to interaction of rock and water at high temperatures in the vicinity of emplacement drifts (Buscheck and Nitao, 1992; Nitao et al., 1992; Buscheck, et al., 1993). In order to determine how possible thermal histories will affect water chemistry and near-field mineralogy, the evolution of water compositions over a range of scenarios must be determined. This section describes how water chemistry may change due to evaporation. It does not consider the role of rock-water interaction, or the role of boiling, in the development of water compositions. Those aspects will be treated in a later report.

Evaporation of water is an important consideration for establishing the nature of secondary precipitates that may be deposited along fracture surfaces, in rock pores during various phases of the thermal evolution of the repository, or on waste containers from dripping water. The specific precipitates that may develop will reflect the initial water composition. In using J-13 well water (see below) this study considers those scenarios in which water evaporation begins with a dilute water that is close to equilibrium with high silica rhyolite similar to that which makes up the repository horizon at Yucca Mountain.

The chemical consequences of evaporation are distinct from those of boiling, due to the contrast in behavior of dissolved gases during evaporation and boiling. During open-system boiling, dissolved, volatile weak electrolytes (e.g., CO_2, H_2S) will exsolve from the liquid phase to varying degrees, depending upon the water composition. Their behavior can be described by means of Henry's law relationships which can take into account the relative "volatilities" of the dissolved species (Drummond and Ohmoto, 1985). Rayleigh distillation models can then be used to describe the overall evolution of the water chemistry during boiling (e.g., Arthur and Murphy, 1989; Criscenti and Arthur, 1991). Evaporation, on the other hand, can

be approximated as a simple removal of water from a system, with the dissolved gas behavior expressed by temperature-dependent changes in the equilibrium partial pressure of the gas coexisting with the water.

3.4.1.2 Previous Work. Numerous studies have summarized the chemical characteristics of natural ground waters and pore waters in the vicinity of the repository block (Ogard and Kerrisk, 1984; Benson and McKinley, 1985; Yang et al., 1988; Bruton, et al., 1993). Those waters provide an indication of the degree of local compositional variability that may be expected. As a step in determining how these water compositions may be influenced by evaporation, a water composition typical of well J-13 was used in the simulations described here. This water was selected because it is a typical example of the type of water that occurs in the region, that is, it is a relatively dilute chloride- and sulfide- and sulfate-poor, bicarbonate groundwater (Glassley, 1986; Harrar, et al, 1990; Bruton, Glassley and Viani, 1993). Other water compositions will be considered as funding permits.

3.4.1.3 Approach. Evaporation of J-13 water was simulated using the EQ3/6 code package (Wolery, 1992 a,b; Wolery and Daveler, 1992) by removing water at a specified rate during reaction progress in an EQ6 simulation (Wolery and Daveler, 1992). Water was evaporated at constant temperatures of 31°C and 90°C. It was also evaporated at increasing temperatures using arbitrary relationships between amount of water evaporated, and temperature change, from 31°C to 95°C (see Fig. 3.4-1 for the different temperature-evaporation trends used). Differences in the relationship between temperature and the moles of water evaporated had no discernible effect on the results. The variable temperature calculations allowed consideration of the effects of disequilibrium between heating and evaporation rate.

These simulations were conducted with and without controls on the composition of the coexisting gas phase. The simulations done without gas-phase controls simulate scenarios in which there is no influence of atmospheric gases on the composition of the evolving gases or water. Simulations conducted in which O_2 and CO_2 gas fugacities were assumed to remain constant at their atmospheric values (.2 and .0004 bars, respectively) address scenarios in which equilibration of atmospheric gases with pore waters is rapid, relative to the rate at which

evaporation occurs. Although disequilibrium may occur between water and gas, these simulations bound the extreme case where equiulibrium is achieved, and water pH may be most severely affected by carbonate.

Simulations were conducted with and without precipitation of quartz, tridymite and talc. Suppression of these phases simulates scenarios in which metastable precipitation of other phases is allowed to occur. This is consistent with experimental studies in which the aqueous SiO_2 concentration is controlled by the least stable silica polymorph present in the coexisting rock, and the fact that, at low temperatures similar to those considered here, the minerals that form most readily are those which most significantly lower the system's free energy and not necessarily the phases that are thermodynamically stable (see summary in Bruton et al., 1993). Although a number of other phases could also be justifiabley suppressed, these particular ones were selected because they are among those phases which commonly occur as precipitates in simulations, but which are not observed in experimental studies. Simulations in which these minerals were not suppressed consider scenarios in which the most thermodynamically stable phases precipitate. These contrasting approaches allow consideration of the relative importance of metastable precipitation of phases on the aqueous chemistry.

As a note of caution, it must be pointed out that the phases which occur as the "most thermodynamically stable" are identified as such on the basis of the thermodynamic properties compiled in the EQ3/6 database. Uncertainties in the values of thermodynamic properties, which are inherent in a compilation of this sort (see Johnson, et al., 1992 for discussion of this issue), make problematic the identification of the actual phases that would precipitate during evaporation. The phases that appear in the simulations, therefore, must be viewed as an approximation to the mineral assemblages that would develop in the course of evaporation. In addition, metastable crystallization of phases, due to nucleation or other kinetic effects in real systems, may also influence the actual sequence of minerals that would form during evaporation. Hence, the general sequence of precipitation that is obtained during the simulations may not be the same as that observed in the laboratory or in nature. However, efforts to evaluate the accuracy of

simulations have been undertaken, using data from the New Zealand geothermal system (see Section 3.4.2).

Interaction with rock was not considered. These simulations, therefore, apply to the extreme case where evaporation occurs at very high rates, relative to the rates of dissolution or precipitation of rock components. Although later studies were planned that would consider the consequences of reacting rock with evaporating waters, such studies have been indefinitely postponed due to budgetary and schedule constraints. Laboratory studies and simulations of rock interacting with J-13 well water have been carried out over a range of conditions, and are reported elsewhere (Knauss and Peiffer, 1986; Knauss et al., 1986; Knauss, 1987; Delaney 1985; Bruton et al, 1993).

The simulations reported here were conducted using the extended Debye-Hückle activity coefficient model (Helgeson, 1969; Helgeson et al., 1970). This model is applicable only to systems in which the ionic strength is less than ca. 0.5 molal, which is approximately equivalent to evaporation of 55 moles of water from 1 kg of J-13 well water (1 kg of water equals ca. 55.51 moles of water). Although the simulations were carried to higher degrees of evaporation, only the results that were obtained well within the region over which the extended Debye-Hückle approach is valid (i.e., for <53 moles of evaporated water, which is approximately 95% evaporation) are reported here. Simulations at higher ionic strengths, using more appropriate models of ion interactions, will be conducted when applicable data are available.

3.4.1.4 Results and Discussion. The results of the simulations are shown in Figs. 3.4-2 through 3.4-14.

The effect of controlling gas composition can be dramatic, for some aqueous species and solids. In those cases where the effect is evident, *circles* are used in the figures to indicate values computed with no gas phase controls. *Squares* are used to indicate cases where gas phase controls were implemented. Solid symbols indicate simulations in which quartz, tridymite and talc precipitation was not suppressed, and *open* symbols are used for cases where they were suppressed.

Although calculations were conducted for both constant temperature and varying temperature conditions, the results were similar. Hence, the following discussion and data presentations only deal with the case in which temperature changed during evaporation.

Evaporation that occurs in the absence of any controls on the composition of the coexisting gases results in water compositions in which the pH remains near neutral, and the Eh slightly oxidizing (Figs. 3.4-2 and 3.4-3). In addition, Na (Fig. 3.4-4), S (Fig. 3.4-5), Cl (Fig. 3.4-6), and F (Fig. 3.4-7) concentrations increase linearly as the activity of H_2O decreases. For Na, S, and Cl, no solids precipitate that incorporate these elements, hence their concentrations increase by the same factor (i.e., 23 times). F, on the other hand, is incorporated into fluor-apatite and fluorite during evaporation. However, fluor-apatite precipitates during the very early stages of evaporation and remains constant in abundance, and fluorite only occurs in small concentrations toward the end of the evaporation, hence the relative behavior of F in solution mimics that of Na, S, and Cl, but at a lower degree of enrichment (ca. 15 times).

The concentrations of Ca (Fig. 3.4-8), P (Fig. 3.4-9), and Si (Fig. 3.4-10), on the other hand, are effected by precipitation of carbonates, phosphates, and silicates as evaporation proceeds. Changes in Ca concentration mainly correlate with precipitation of calcite, which is the most abundant precipitate formed, after the silica polymorphs (Fig. 3.4-11). Dolomite precipitation also influences Ca concentration, but to a small degree (Fig. 3.4-12). P variation reflects the effects of precipitation of fluor-apatite. Si variation is controlled by the solubility limits of quartz and chalcedony, with which the waters are saturated; the particular polymorph that occurs in the simulations reflects whether quartz precipitation was inhibited.

For conditions in which the coexisting gas phase is fixed at atmospheric O_2 and CO_2 fugacities, the fluid composition evolution is significantly different in pH, Eh, Ca, and Si. Because of the effect CO_2 fugacity has on the stability of carbonate and bicarbonate ions, the pH is more alkaline, reaching values >9.0. In addition, the Eh is more oxidizing at low temperature, but becomes more reducing at high

temperatures, than for the simulations in which the gas composition is uncontrolled. This behavior reflects both the effect of CO_2 abundance on the carbonate-bicarbonate system, and the retrograde solubility of calcite at elevated temperatures. Together, these processes influence the relative solubilities of components that make up the main redox couples in the system (ferric-ferrous and sulfide-sulfate). These effects lead to much greater Ca and Si concentrations in solution. Cl, F, S, and P concentrations are virtually the same as in the case where gas composition is not controlled.

It is clear in these simulations that the specific silica polymorph that is allowed to precipitate has only a second order effect on the solution composition. This is mainly expressed in the Si and Ca concentrations. The latter is sensitive to the impact of Si concentration on the occurrence of Ca-bearing aluminosilicates (e.g, saponite clays and the zeolite stilbite; Figs. 3.4-13 and 3.4-14).

In all of these simulations, regardless of the specific conditions imposed on the system, fluor-apatite, nontronite, and pyrolusite occur as small abundance precipitates at constant concentration regardless of the degree of evaporation. Their occurrence reflects the low solubilities of these solids.

3.4.1.5 Conclusions. Simulated evaporation of J-13 well water suggests that the most significant variable that controls the evolution of the water chemistry and the solids that precipitate, is the composition of the coexisting gas phase, and whether that gas phase is in equilibrium with the water. The most significant effects can be seen in the divergence of pH and Eh (Figs. 3.4-2 and 3.4-3) as evaporation proceeds with and without equilibrium with a gas phase. These effects influence total concentration of elements that occur in silicates and carbonates that have solubilities sensitive to moderate changes in solution pH. Conservative elements (Cl, F, S) change concentration linearly as evaporation proceeds, since they do not play a role in any of the precipitates that form.

Further work should focus on how these changes will be modified by rock-water interaction during evaporation, and on bounding the range of water variability using the spectrum of water chemistries exhibited by the analyzed groundwaters.

3.4.1.6 References

Arthur, R.C., and W.M. Murphy, 1989, An Analysis of Gas-Water-Rock Interactions During Boiling in Partially Saturated Tuff, Sci. Geol. Bulletin, vol. 42, #4, p. 313–327.

Benson, L.V., and P.W. McKinley, 1985. Chemical Composition of Groundwater in the Yucca Mountain Area, Nevada, 1971-1984, U.S. Geological Survey, Denver, CO, OFR-85-484. (NNA.900207.0281)

Bruton, Carol, William E. Glassley, and Brian E. Viani, 1993. *Preliminary Near-Field Environment Report Volume II: Scientific Overview of Near-Field Environment and Phenomena, Chapter 3, Geochemistry,* Lawrence Livermore National Laboratory UCRL-LR-107476 Vol. 2, p. 37–60.

Buscheck, T.A., and John. J. Nitao, 1992, *The Impact of Thermal Loading on Repository Performance at Yucca Mountain,* in Proceedings of the Third International Conference on High Level Radioactive Waste Management, Las Vegas, Nevada, p. 1003–1017.

Buscheck, T.A., John. J. Nitao, and Dwayne A. Chesnut, 1993, *Preliminary Near-Field Environment Report Volume II: Scientific Overview of Near-Field Environment and Phenomena, Chapter 1 Hydrothermal Modeling,* Lawrence Livermore National Laboratory UCRL-LR-107476 Vol. 2, p. 5–27.

Criscenti, L.J., and R.C. Arthur, 1991, The Calculated Effects of Isothermal Boiling on Tuff-Water Interactions, Radiochimica Acta, v. 52/53, p. 513–517.

Glassley, W.E., 1986. Reference Waste Package Environment Report. Lawrence Livermore National Laboratory, Livermore, CA UCRL-53726 (NNA.920506.0035)

Harrar, J.E., J.F. Carley, W.F. Isherwood, E.Raber, 1990. Report of the Committee to Review the Use of J-13 Well Water in Nevada Nuclear Waste Storage Investigations. Lawrence Livermore National Laboratory, Livermore, CA UCID-21867 (NNA.910131.0274)

Helgeson, H.C., 1969. Thermodynamics of Hydrothermal Systems at Elevated Temperatures and Pressures. American Journal of Science, vol. 267, pp. 729–804.

Helgeson, H.C., T.H. Brown, A. Nigrini, and T.A. Jones, 1970. Calculation of Mass Transfer in Geochemical Processes Involving Aqueous Solutions. Geochimica Cosmochimica Acta, vol. 34, pp. 569–592.

Johnson, J. W., Eric H. Oelkers, and Harold C. Helgeson, 1992. SUPCRT92: A Software Package For Calculating The Standard Molal Thermodynamic Properties of Minerals, Gases, Aqueous Species, and Reactions From 1 to 5000 Bars and 0 to 1000°C. Computers and Geosciences, vol. 18. p. 899–947.

Knauss, K.G., 1987. Zeolitization of Glassy Topopah Spring Tuff Under Hydrothermal Conditions, Mat. Res. Soc. Symp. Proc., vol. 84, p. 737–745. (NNA.920302.0050)

Knauss, K.G., J.M. Delany, W.J. Beiriger, and D.W. Peiffer, 1986, Hydrothermal Interaction of Tonopah Spring Tuff with J-13 Water As a Function of Temperature, Mat. Res. Soc. Symp. Proc., vol. 44, pp. 539–546 (NNA.870407.0364)

Knauss, K.G., and D.W. Peiffer, 1986, Reaction of Vitric Topopah Spring Tuff and J-13 Groundwater Under Hydrothermal Conditions Using Dickson-Type, Gold-Bag

Rocking Autoclaves, Lawrence Livermore National Laboratory, Livermore, CA UCRL-53795 (NNA.891102.0117)

Nitao, J.J., T.A. Buscheck, and D.A. Chesnut, 1992, The Implications of Episodic Nonequilibrium Fracture-Matrix Flow on Site Suitability and Total System Peformance, in Proceedings of the Third International Conference on High Level Radioactive Waste Management, Las Vegas, Nevada, p. 279–296.

Ogard, A.E., and J.F. Kerrisk, 1984. Groundwater Chemistry Along Flow Paths Between a Proposed Repository Site and the Accessible Environment. Los Alamos National Laboratory, Los Alamos, NM, LA-10188. (NNA.890907.0118)

Wolery, T.J., 1992a, EQ3/6, A Software Package for Geochemical Modeling of Aqueous Systems: Package Overview and Installation Guide. Lawrence Livermore National Laboratory, Livermore, CA UCRL-MA-110662 PT. I

Wolery, T.J., 1992b, EQ3NR, A Geochemical Program For Aqueous Speciation-Solubility Calculations: Theoretical Manual, User's Guide, and Related Documentation. Lawrence Livermore National Laboratory, Livermore, CA UCRL-MA-110662 PT. III

Wolery, T.J., and S. A. Daveler, 1992, EQ6, A Computer Program for Reaction Path Modeling of Aqueous Geochemical Systems: Theoretical Manual, User's Guide, and Related Documentation (Version 7.0). Lawrence Livermore National Laboratory, Livermore, CA UCRL-MA-110662 PT. IV

Yang, I.C., A.K. Turner, T.M. Sayre, and P. Montazar, 1988. *Triaxial-Compression Extraction of Pore Water from Unsaturated Tuff, Yucca Mountain, Nevada*, U.S. Geological Survey, Water Resources Investigations Report 88-4189 (NNA.890309.0161)

3.4.2 Testing EQ3/6 and GEMBOCHS Using Fluid-Mineral Equilibria in the Wairakei Geothermal System, by Carol Bruton, Lawrence Livermore National Laboratory

3.4.2.1 Introduction. It is necessary to establish well defined bounds on the range of chemical conditions that may develop within a nuclear waste repository in order to evaluate the extent to which corrosion of waste containers, dissolution of waste forms, and transport of radionuclides may occur. This information forms part of the basis for total system and sub-system performance assessment evaluations, and site suitability determination.

To achieve this goal, simulations of geochemical processes over long time periods (i.e., thousands of years) are required, since experimental studies can be conducted only for a few years, at most. However, the accuracy and precision of numerical simulations is often limited by the supporting thermodynamic and kinetic data that are used in the simulations. One method for ascertaining the accuracy and precision of simulation capabilities is to compare the results of simulations with observed geochemical and mineralogical characteristics of natural systems in which the same processes occur that are anticipated in the potential repository.

The ability of the EQ3 and EQ6 geochemical modeling codes and the GEMBOCHS thermodynamic data bases (Wolery, 1992; Wolery and Daveler, 1992) to simulate geochemical changes in the post-emplacement environment at the potential repository at Yucca Mountain was tested using observed mineral-fluid relations in the Taupo Volcanic Zone of New Zealand. This site was selected for use in the comparisons because of its close geological similarity to the potential repository site, and because processes of interest and an extensive data base are accessible for study (Bruton et al., 1995). Comparisons between observed equilibria and simulations of field relations in the Wairakei geothermal system were used to test the codes and data bases in high temperature (>200°C) systems. Tests at lower temperatures have been planned, but have yet to receive funding.

The conditions selected for initial evaluation are those that most closely approximate processes in the near-vicinity of emplacement drifts. Numerical models of the post-emplacement temperature field (Buscheck and Nitao, 1993) show the potential for peak temperatures about 200°C near the waste, and attendant changes in relative humidity, "drying-out," boiling, condensation, one- and two-phase fluid flow, mineral precipitation and dissolution, ion exchange, and surface complexation. The work described here documents tests conducted to evaluate the ability of the EQ3/6 geochemical modeling codes and their associated GEMBOCHS thermodynamic data bases to model mineral-fluid relations in order to:

1. Test the conditions and manner in which EQ3/6 can be used to forecast changes in rock and fluid chemistry during the flow of heated fluids through silicic rocks;
2. Test the thermodynamic data in GEMBOCHS and to select appropriate thermodynamic data when multiple sources exist.

To accomplish this work, it is necessary to select representative water and gas compositions from Wairakei wells (called boreholes), reconstruct downhole fluid compositions, calculate the minerals predicted to be in equilibrium with each fluid, and compare simulation results with observed vein and vug mineralogy.

All calculations described were carried out using version 7.2a R134 of EQ3 and version 7.2a R130 of EQ6. The SUPCRT and COM subsets of the R24 version of GEMBOCHS were used as indicated.

3.4.2.2 Fluid chemistry: choice of representative waters and gases. Reyes, Giggenbach and Christenson (1993) reviewed available well discharge data for the Wairakei area. Details of the process of reconstructing downhole fluid chemistry from surface gas and water analyses are described in Bruton (1995). Tables 3.4-1 and 3.4-2 summarize the as-analyzed and reconstructed fluid analyses used in this study.

Redox state was set by the $SO_4^{=}/H_2S$ buffer, assuming an initial concentration of aqueous H_2S of 0.3 mg/kg in WK-28 based on concentration data from nearby wells. This assumption represents an initial test of modeling strategies regarding control of redox in the subsurface. This initial study did not focus on phases containing Mg, Fe,

and/or S as primary components. The latter two elements are strongly dependent on redox state, which can vary significantly in hydrothermal systems owing to boiling. Chlorite is the major mineral phase containing Mg in these systems, but no chlorite solid solutions are provided for in the SUPCRT data base. The COM data file provides for an ideal solid solution model for chlorite as well as saponites, which are Mg-rich smectites.

3.4.2.3 Alteration mineralogy. Alteration mineralogy seems to be strongly controlled by temperature. A representative set of minerals, called a mineral facies, is composed of secondary minerals which commonly occur in a given temperature range. The minerals in the facies occur in various combinations, called mineral assemblages. Different mineral assemblages in a given facies can coexist on spatial scales as small as a single hand specimen or petrographic thin section (Bruton, et al., 1994).

Mineral assemblages identified at downhole temperatures of 240-260°C in the main feed zones at Wairakei (wells WK-28, 72 and 81) (Reyes, Giggenbach and Christenson, 1993; Steiner, 1977) include: wairakite; adularia (a variety of K-feldspar); epidote solid solution; wairakite ± quartz; quartz + adularia; wairakite+epidote±calcite; albite+quartz+epidote+chlorite+calcite; prehnite; wairakite+prehnite.

The above mineral assemblages represent the secondary minerals that coexist with the fluids described in the previous section.

3.4.2.4 Calculational approach. Three reconstructed downhole fluids were used to compute predicted secondary mineralogy at depth, which was then compared to observed mineral assemblages.

The approach taken was as follows.

- Select representative sets of coexisting water and gas analyses from Wairakei wells and reconstruct downhole fluid chemistry by adding steam and gases lost during production back into the liquid phase.
- Identify mineral assemblages along fractures and flow zones closely associated with source of produced fluids.

- Calculate affinity (A) of potential secondary minerals where $A=RT\ln(Q/K)$[1] using version R24 of the SUPCRT and COM subsets of the GEMBOCHS thermodynamic data base.
- Compare calculated and observed mineral assemblages.

Phase relations were examined with the use of affinity-temperature diagrams. Affinity is a measure of a mineral's saturation state. If:

$A=0$, the mineral is at equilibrium with the solution

$A<0$, the mineral is undersaturated with respect to the solution

$A>0$, the mineral is supersaturated with respect to the solution.

Potential mineral assemblages are inferred when multiple affinity-temperature curves have a common intersection at $A=0$. Identification of potential mineral assemblages in this manner is especially useful when thermodynamic data may be suspect or kinetics controls the formation of precipitates. Downhole temperature can be estimated by noting the temperature at which the affinity curves converge on zero (equilibrium).

Calculations assume that pressures correspond to the liquid/vapor saturation curve for H_2O. Solid solutions for epidote and muscovite were considered. Clinozoisite as used in this paper refers to the clinozoisite end member of an ideal epidote solid solution (Bird and Helgeson, 1980) with an activity of 0.4, as calculated from microprobe analyses of epidote at Wairakei. Muscovite refers to the muscovite end member of an ideal illite solid solution with an activity of 0.5, estimated by analogy to illite from the Kawerau geothermal field in New Zealand.

3.4.2.5 Results: Water-rock equilibrium calculations. Comparisons between predicted and observed mineral stabilities that will be described in the following sections allowed us to determine:

1. Quartz solubility data that best describes controls of aqueous silica concentrations at temperatures greater than about 200°C.
2. Importance of gas phase chemistry to mineral equilibria, and mineral indicators of variations in pH.

1. Q = ion activity product; K = equilibrium constant; R = gas constant; T = temperature in K.

3. Thermodynamic data for aqueous Al species that best describe mineral stabilities at temperatures greater than about 200°C.
4. Corrections to thermodynamic data for wairakite, a high temperature zeolite.
5. Need for better usage and interpretation of calorimetric thermodynamic data for zeolites.
6. Appropriateness of utilizing the mineral facies concept to infer mineral stability rather than exact prediction of the precise secondary minerals to precipitate at temperature.

In all affinity-temperature diagrams shown below, some discretion was used to select the minerals to be plotted. Phases were chosen based on their occurrence in observed mineral assemblages, and their extent of supersaturation or closeness to equilibrium. Minerals that were generally depicted on the diagrams include: quartz, K-feldspar, albite, muscovite, calcite, prehnite, wairakite and clinozoisite. These minerals most often appear in stable mineral assemblages identified by Reyes in the temperature range 240-260°C (Reyes, et al., 1993).

3.4.2.5.1 Choice of quartz solubility data: Well WK-81. Figure 3.4-15 shows differences in the concentrations of SiO_2 (aq) predicted according to quartz solubility data from Walther and Helgeson (1977) and Fournier (1983). Fournier's data predict significantly higher SiO_2 (aq) concentrations in solution than the quartz solubility data of Walther and Helgeson (1977) at temperatures exceeding about 150°C.

Figures 3.4-16 and 3.4-17 contrast computations of mineral equilibria in Wairakei well WK-81 using Fournier (1983) and Walther and Helgeson (1977) data, respectively. The adiabatic quartz geothermometer based on data from Walther and Helgeson predicted a downhole temperature of 263°C, whereas that of Fournier predicted 240°C. As can be seen from Figs. 3.4-16 and 3.4-17, the affinity curves seem to converge more closely on the downhole temperature predicted using the Fournier (1983) quartz solubility data. It is apparent that calculated mineral equilibria more closely correspond to observed mineralogy when Fournier's (1983) quartz geothermometer is used.

Ragnarsdottir and Walther (1983) measured the pressure dependence of quartz solubility at 250°C, and concluded that the pressure dependence accounts for the

discrepancy between results of Fournier and Walther and Helgeson. Calculations with GEMBOCHS are currently restricted to the liquid/vapor saturation curve for H_2O. However, according to the results of Ragnarsdottir and Walther (1983), the hydrostatic fluid pressures maintained at Wairakei are not large enough to impact quartz solubility significantly.

For calculations of quartz solubility above about 200°C at the present time, the quartz solubility data of Fournier (1983) should be used in place of that of Walther and Helgeson (1977), which is contained in all current versions of GEMBOCHS.

3.4.2.5.2 Impact of changes in gas chemistry: **WK-72.** Vapor compositions vary with time owing to production and the partitioning of components between vapor and liquid phases. Figure 3.4-18 shows the variation of CO_2 with time in wells WK-28, 72 and 81. Changes of this magnitude will greatly impact calculated fluid-mineral equilibria owing to its impact on pH. The variation of component ratios, discharge enthalpy and other well parameters with time can be used to try to derive reasonable estimates of the quantity of volatile species in the original, undisturbed fluids. However, uncertainties persist.

Use of different gas compositions for a given fluid analysis can produce significant changes in predicted mineralogy owing to the impact of CO_2 on pH. The greater the CO_2 content of the produced vapors, the lower the predicted pH of the reconstructed downhole fluid. For example, the calculated downhole pH is reduced from 6.2 to 5.9 when the 3/78 gas analysis for WK-72 with 258 mmol CO_2/mol TD is used rather than the 5/61 analysis with 102 mmol CO_2/mol TD, where TD is defined as the total discharge, that is, the combined chemistry of the steam and liquid phases.

Figures 3.4-19 and 3.4-20 illustrate the mineralogical consequences of using the high (3/78) and low (5/61) CO_2 gas estimates, respectively. The stabilities of K-feldspar and albite are largely unaffected by changes in pH, whereas the stabilities of prehnite, muscovite and calcite are sensitive to pH, as reflected by the shift of their affinity-temperature curves. The dissolution/precipitation of muscovite, prehnite and calcite may thus serve as sensitive indicators of changes in downhole fluid

chemistry. In contrast, the stabilities of K-feldspar and albite are largely unaffected by uncertainties in gas chemistry and pH, and are therefore good tests of equilibrium and the adequacy of thermodynamic data for aqueous Al species.

Figures 3.4-19 and 3.4-20 also suggest that the earlier, lower CO_2 gas analysis better represents downhole conditions, as shown by the fact that the curves tend to converge more closely on the downhole temperature than in the high CO_2 gas case.

This finding may have implications for Yucca Mountain with regard to the timing and mass of ^{14}C release. If released as CO_2 and in sufficient quantities while water is present, the waters can be made more chemically aggressive if initially neutral, or neutralized if initially alkaline from contact with cementitious materials in the engineered barrier system. The consequences of interactions with cementitious materials before contact with tuff must also be taken into account.

Of perhaps more importance is the variation in gas phase chemistry, particularly CO_2 content, in the vapor phase in the two-phase (gas and water) zones predicted to occur by Buscheck and Nitao (1993). The CO_2 content will control the pH of the fluid with which it is in contact, and thus the extent and type of fluid-rock interaction. The fluid-rock interaction, in turn, may have a large impact on tuff permeability and fluid flow pathways. Bruton and Viani (1992) suggested that water may behave as if it were 100% saturated at liquid saturations greater than about 20% at temperatures up to 100°C. However, the coexisting gas phase will have a large impact on the water's chemical reactivity. Any forecasts of fluid-rock interaction in two-phase zones will require the gas phase chemistry to be considered, as addressed in the boiling scenarios evaluated by Criscenti and Arthur (1991) and Arthur and Murphy (1989).

3.4.2.5.3 Thermodynamic data for aqueous Al species: WK-28. Downhole mineral equilibria in well WK-28 were calculated using two different data bases that are in current use. One is based on SUPCRT92, and the other is an updated version of the same data base but with thermodynamic data for aqueous Al species from Pokrovskii and Helgeson (1995) (SUPCRT R24). The latter data will be used in GEMBOCHS.

Figure 3.4-21 shows the simulation results using data from Pokrovskii and Helgeson, whereas Fig. 3.4-22 was constructed using the SUPCRT92 data base. The convergence of affinity curves at zero affinity (equilibrium) at the downhole temperature in Fig. 3.4-21 for phases that are observed as secondary phases suggests that Pokrovskii and Helgeson's data for aqueous Al species work quite well. In contrast, the data in SUPCRT92[2] do not reproduce downhole mineralogy well. In these calculations, measured Al concentrations were used; that is, they were not automatically set using mineral equilibria as is often done, especially at lower temperature (e.g Bowers and Burns, 1990; Chipera, Bish and Carlos, 1995).

Given the above results, thermodynamic data for aqueous Al species should be sourced from Pokrovskii and Helgeson (1995). Further simulations should be undertaken in the range 100-200°C to evaluate the Al data bases at lower temperature. However, less discrepancy may be observed at lower temperatures because the main cause of discrepancy is the log K for reaction between Al^{3+} and AlO_2^-. The two log Ks agree well at low temperature, but deviate increasingly with increasing temperature until a difference of about 0.4 log units exists at 250°C, producing the observed differences in the affinity vs. temperature figures.

The log K for reaction between Al^{3+} and AlO_2^- from Bourcier and Knauss (1993) used in GEMBOCHS COM versions prior to R24 also reproduces observed mineralogy well. Users of GEMBOCHS data bases should identify the $Al(OH)_4^-/Al^{3+}$ log K specified in the data base they are using, and ascertain that it is appropriate for their needs. Of course, reactions which are written balanced on Al, such as those incorporated in many activity diagrams (e.g Bowers and Burns, 1990; Chipera, Bish and Carlos, 1995), will not be affected.

3.4.2.5.4 Thermodynamic data for wairakite. Figures 3.4-17 through 3.4-22 illustrate that wairakite is predicted to be about 1 to 1.5 kcal/mol undersaturated in all wells at about 250°C. In contrast, wairakite commonly occurs at Wairakei as a

2. Versions of SUPCRT have been published and distributed without data for AlO_2^-, the most important Al aqueous species under many conditions. The calculations in this paper provided for this species.

secondary phase at this temperature. Therefore, the calculations suggest that the free energy of formation from the elements of wairakite in SUPCRT92 (Helgeson et al., 1978), and in all current verions of GEMBOCHS, should be decreased by approximately 1-1.5 kcal/mol at about 250°C to increase its stability.

Thermodynamic data for wairakite may not seem to be relevant to the Yucca Mountain Project. However, if temperatures exceed 200°C with water present, wairakite would tend to be the stable zeolite relative to clinoptilolite, heulandite, and mordenite. Given the uncertainty in thermodynamic data for lower temperature zeolites such as clinoptilolite, heulandite, and mordenite (discussed below), it is useful to have some measure of data reliability for at least one zeolite with which to reference the other zeolites.

3.4.2.5.5 Thermodynamic data for zeolites. The simulations represented in Figs. 3.4-17 through 3.4-22 were run with the SUPCRT data base instead of the COM data file in part because the COM file contains thermodynamic data for zeolites such as analcime, clinoptilolite, mordenite, heulandite, stilbite, mesolite, scolecite and natrolite from Johnson and co-workers (1982, 1983, 1985, 1991, 1992) and Howell et al. (1990). These data were obtained through careful calorimetric studies. When kinetic constraints are not considered and purely thermodynamic equilibrium calculations are made, one of the above zeolites is present in the computed equilibrium assemblage at temperatures as high as 250°C, even though they are generally not expected to be stable at such high temperature in natural systems.

Figure 3.4-23 shows a calculation of zeolite stability in well WK-28 under conditions identical to that in Fig. 3.4-21, but using GEMBOCHS version COM R24 which contains Johnson's calorimetric data for zeolites. Figure 3.4-21 can be combined with Fig. 3.4-23 to show the affinities of zeolites relative to other minerals. Note the supersaturation with respect to scolecite, mesolite, stilbite and the Ca end-member of a clinoptilolite solid solution (discussed by Viani and Bruton, 1992) at the downhole temperature of 246°C.

Owing to this discovery, the first tests of the codes were made using data bases that do not contain Johnson's data for zeolites. At this time, simulations using the COM data base containing Johnson's zeolites must be made by suppressing the

zeolites to artificially reflect their disappearance from natural assemblages at temperatures greater than about 200°C.

The thermodynamic data at elevated temperature for the above zeolites from Johnson and co-workers are uncertain for a number of reasons.

First, the third law entropies (S^o) for clinoptilolite, mordenite, stilbite, mesolite, scolecite, and natrolite in the COM data file are actually values for $S^o(T)-S^o(0)$, because the configurational entropies at 0 K ($S^o(0)$) were not available. Johnson and co-workers attempted to estimate configurational entropies when possible, and warned that the configurational entropy must be taken into account when computing mineral equilibria. We have not devoted effort to estimating configurational entropies because their contribution would increase zeolite stability, whereas the problem is that they seem to be too stable already.

Secondly, it is possible that H_2O vapor adsorption occurred during the cooling of Johnson's drop calorimetry experiments. The exothermic reaction would produce excess heat capacity at elevated temperature (see Carey, 1993 for full discussion). Carey (1993) suggested that the heat capacity of H_2O in clinoptilolite is temperature-insensitive, rather than increasing monotonically with temperature, as shown by Johnson et al. (1991).

Thirdly, the hydration state of zeolites may decrease with increasing temperature, which would affect their stability. Water in zeolites is generally considered to have a lower free energy than bulk water, such that water desorption is endothermic. Johnson measured the thermodynamic properties of his zeolites at 50% relative humidity in recognition of their potential for changing hydration state. This potential for changing hydration state is not currently provided for in the EQ3/6 codes and data bases, however.

If the configurational entropy were appropriately accounted for, and the heat capacities corrected for readsorption phenomena, the stability of zeolites would increase because their free energies of formation would be more negative. However, zeolite stability would have to decrease if errors in thermodynamic data were the cause for the predicted stability of zeolites at temperatures greater than about 200°C.

Clearly, alternate approachs similar to that illustrated by the affinity-temperature diagrams should be adopted to determine the potential for mineral stability. The calculations described in Figs. 3.4-3 through 8 suggest that fluid-mineral equilibria determined in this manner agree well with observed mineralogy.

3.4.2.5.7 Vein/vug vs. matrix mineralogy and mineral assemblages. Alteration mineralogy at Wairakei is controlled strongly by temperature in veins and vugs, and by both temperature and mineralogy in the matrix. Replacement minerals in the matrix are controlled in identity, morphology and location by the primary mineralogy. That is, replacement mineralogy is controlled by the dissolving phase; the components of the dissolving mineral tend to re-precipitate as secondary minerals next to the dissolving grain. This link is much weaker or non-existent, in vein- and vug-fills.

The stabilities of fracture-, vein- and vug-filling minerals are controlled by solution composition and temperature with apparently limited control by the matrix. Alteration minerals in veins and vugs are the same as those found as replacement minerals in the matrix, but they occur in assemblages composed of fewer phases. It is striking that vein and vug fills, which obviously have precipitated from solution, are characterized by one to three secondary minerals, fewer than the number of different replacement minerals in the matrix as a whole. The above findings suggest that the fractures, veins and vugs represent fluid-dominated systems, whereas the matrix represents a rock-dominated system.

Petrographic observations suggest that the minerals replacing plagioclase in the matrix are those that commonly comprise fracture/vein/vug mineralogy; both seem to be Ca-dominated systems. At this time, our working hypothesis is that vein mineralogy is controlled mainly by fluid chemistry in the flowing system with negligible interaction with the host rock. The number of fracture-filling minerals may be controlled by the phase rule for mobile components.

In the post-emplacement environment at Yucca Mountain, replacement mineralogy in the matrix would be expected to be controlled by temperature and primary mineralogy, provided sufficient water is present to effect such changes, whereas the stability of minerals along flow paths such as fractures would be

controlled by the evolution of water composition as well as temperature. Factors that could effect impact water composition include boiling/condensation, interactions with cementitious and other manufactured materials including metal waste package components, and so on.

The degree of mass transfer between matrix and fractures in the New Zealand systems should be evaluated. If there is little chemical exchange between the matrix and fractures, mineral dissolution/precipitation during fluid flow in coupled hydrogeochemical models can be simulated much more simply because diffusion to and from the matrix does not have to be considered.

3.4.2.6 Conclusions. Vein and matrix minerals are predicted to be in equilibrium with subsurface fluids at downhole temperatures greater than 240°C. The proximity of a variety of minerals to equilibrium suggests that small differences in fluid chemistry, temperature or pressure can significantly impact mineral assemblages. This might account for the wide variety of mineral assemblages observed at Wairakei.

The SUPCRT92 data base, combined with the data of Pokrovskii and Helgeson (1995) for aqueous Al species describes, equilibrium relations between measured Al concentrations and observed mineral equilibria better than data in the current SUPCRT92 data base. Observed changes in the stability of calcite, prehnite and illite (muscovite) can be indicative of changes in the gas content of the downhole fluid. Feldspar stabilities are largely independent of pH provided that pH values do not deviate greatly from neutrality.

Quartz solubility data from Fournier (1983) describe observed mineral assemblages better than data from Walther and Helgeson (1977). The free energy of wairakite from Helgeson et al. (1978) should be decreased by approximately 1–1.5 kcal/mole at about 250°C. Additional work is required to determine why calorimetric data for clinoptilolite, stilbite and other zeolites from Johnson and co-workers appear to overestimate the stability of these minerals at elevated temperature.

Fluid-mineral interactions at temperatures >200°C are generally believed to be controlled by equilibrium, and so were chosen as the starting point for the EQ3/6

code and data base tests. This assumption is supported by the excellent convergence observed for computed and observed assemblages. Further studies should focus on fluid-mineral reactions in the temperature range of about 100–200°C at the Wairakei and Kawerau geothermal fields. Zeolites such as mordenite, dachiardite and clinoptilolite have been identified in this temperature interval. Extension of the tests to lower temperature allows us to address the controls of kinetics vs. equilibrium on mineral stability, and to determine the stability of zeolites similar to those found at Yucca Mountain.

3.4.2.7 References

Arthur, R.C. and Murphy, W.M., 1989, An analysis of gas-water-rock interactions during boiling in partially saturated tuff: Soc. Geol., Bull., v. 42, p. 313–327.

Bird, D.K. and Helgeson, H.C., 1980, Chemical interaction of aqueous solutions with epidote-feldspar mineral assemblages in geologic systems. 1. Thermodynamic analysis of phase relations in the system CaO-FeO-Fe_2O_3-Al_2O_3-SiO_2-H_2O-CO_2: Am. Jour. Sci., v. 280, p. 907–941.

Bourcier, W.L. and Knauss, K.G., 1993, Aluminum hydrolysis constants to 250°C from boehmite solubility measurements: Geochim. et Cosmochim. Acta, v. 57, p. 747–762.

Bowers, T.S. and Burns, R.G., 1990, Activity diagrams for clinoptilolite: Susceptibility of this zeolite to further diagenetic reactions: Am. Min., v. 75, p. 601–619.

Bruton, C.J., 1995, Testing EQ3/6 and GEMBOCHS using fluid-mineral equilibria in the Wairakei geothermal system: Yucca Mountain Project letter report, Milestone MOL206, Chemical and Mineralogical Properties of the Waste Package Environment:, Natural System Simulations, WBS Element 1.2.3.12.1), August 28, 1995.

Bruton, C.J., Glassley, W.E. and Bourcier, W.L., 1994, Field-based tests of geochemical modeling codes using New Zealand hydrothermal systems: Lawrence Livermore National Laboratory UCRL-ID-118009.

Bruton, C.J., Glassley, W.E. and Meike, A., 1995, Geothermal areas as analogues to chemical processes in the near-field and altered zone of the potential Yucca Mountain, Nevada, repository: Lawrence Livermore National Laboratory UCRL-ID-119842.

Bruton, C.J. and Viani, B.E., 1992, Geochemical modeling of water-rock interactions in the unsaturated zone: In Water-Rock Interaction 7, Y.K. Kharaka and A.S. Maest, eds., A.A. Balkema, Netherlands, p. 705–708.

Buscheck, T.A. and Nitao, J.J., 1993, Repository-heat-driven hydrothermal flow at Yucca Mountain, Part 1: Modeling and analysis: Nuclear Tech., v. 104, p. 418-448.

Carey, J.W., 1993, The heat capacity of hydrous cordierite above 295 K: Phys. Chem. Min., v. 19, p. 578–583.

Chipera, S.J., Bish, D.L. and Carlos, B.A., 1995, Equilibrium modeling of the formation of zeolites in fractures at Yucca Mountain, Nevada: In D.W. Ming and

F.A. Mumpton, eds., Natural Zeolites '93: Occurrence, Properties, Use: Intl. Comm. on Natl. Zeolites, Brockport, N.Y., p. 565–577.

Criscenti, L.J. and Arthur, R.C., 1991, The calculated effects of isothermal boiling on tuff-water interactions: Radiochim. Acta, v. 52/53, p. 513–517.

Fournier, R.O., 1983, A method of calculating quartz solubilities in aqueous sodium chloride solutions: Geochim. et Cosmochim. Acta, v. 47, p. 579–586.

Howell, D.A., Johnson, G.K., Tasker, I.R. and O'Hare, P.A.G., 1990, Thermodynamic studies of the zeolite stilbite: Zeolites, v. 10, July/August, p. 525–531.

Johnson, G.K., Flotow, H.E. and O'Hare, P.A.G., 1982, Thermodynamic studies of zeolites: analcime and dehydrated analcime: Am. Min., v. 67, p. 736–748.

Johnson, G.K., Flotow, H.E. and O'Hare, P.A.G., 1983, Thermodynamic studies of zeolites: natrolite, mesolite and scolecite: Am. Min., v. 87, p. 1134–1145.

Johnson, G.K., Flotow, H.E. and O'Hare, P.A.G., 1985, Thermodynamic studies of zeolites: heulandite: Am. Min., v. 70, p. 1065–1071.

Johnson, G.K., Tasker, I.R., Flotow, H.E., O'Hare, P.A.G. and Wise, W.S., 1992, Thermodynamic studies of mordenite, dehydrated mordenite, and gibbsite: Am. Min., v. 77, p. 85–93.

Johnson, G.K., Tasker, I.R., Jurgens, R. and O'Hare, P.A.G., 1991, Thermodynamic studies of zeolites: clinoptilolite: J. Chem. Thermo., v. 23, p. 475–484.

Pokrovskii, V.A. and Helgeson, H.C., 1995, Thermodynamic properties of aqueous species and the solubilities of minerals at high pressures and temperatures - The system Al_2O_3-H_2O-NaCl: Am. Jour. Sci., v. 295, p. 1255–1342.

Ragnarsdottir, K.V. and Walther, J.V., 1983, Pressure sensitive "silica geothermometer" determined from quartz solubility experiments at 250°C: Geochim. et Cosmochim. Acta, v. 47, p. 941–946.

Reyes, A.G., Giggenbach, W.F. and Christenson, B.W., 1993, First Report for the LLNL-Inst. Geol. Nuclear Sciences EQ3-EQ6 Code Validation Contract: Inst. Geol. Nuclear Sciences Client Report 722305.15A.

Steiner, A., 1977, The Wairakei geothermal area, North Island, New Zealand: New Zealand Geological Survey Bull. 90.

Viani, B.E. and Bruton, C.J., 1992, Modeling fluid-rock interaction at Yucca Mountain, Nevada: A progress report: Lawrence Livermore National Laboratory UCRL-ID-109921.

Walther, J.V. and Helgeson, H.C., 1977, Calculation of the thermodynamic properties of aqueous silica and the solubility of quartz and its polymorphs at high pressures and temperatures: Am. Jour. Sci., v. 277, p. 1315–1351.

Wolery, T.J., 1992, EQ3NR, A computer program for geochemical aqueous speciation-solubility calculations: Theoretical manual, user's guide, and related documentation (Version 7.0): Lawrence Livermore National Laboratory Report UCRL-MA-110662 PT III.

Wolery, T.J. and Daveler, S.A., 1992, EQ6, A computer program for reaction path modeling of aqueous geochemical systems: theoretical manual, user's guide, and related documentation (Version 7.0): Lawrence Livermore National Laboratory Report UCRL-MA-110662 PT IV.

3.4.3 Mineralogy-Petrology Observations Regarding the Near-Field Environment, by David L. Bish, J. William Carey, Schon S. Levy and Steve J. Chipera, Los Alamos National Laboratory

3.4.3.1 Introduction. In order to model accurately the short- and long-term effects of repository-induced heating on the properties of rocks in the near-field environment (NFE) at Yucca Mountain, an understanding of the host rock mineralogy, past mass transfer in the host rocks, and the anticipated changes in mineral and glass stability due to emplacement of high-level radioactive waste are required. Bish and Chipera (1989) compiled a summary of mineral distributions with depth in drill holes at Yucca Mountain using available non-Q core. A more recent report (Chipera et al., 1995b) has provided similar mineralogical information using Q core. Levy (1991) and Levy and O'Neil (1989) described the application of petrologic and isotopic methods to the understanding of past mass transfer in the host rocks. A large amount of research has been conducted on the effects of repository-induced heating on the long-term stability of minerals and glasses in the near-field environment. This includes studies of the dehydration behavior of clays and zeolites in tuffs (Bish, 1984, 1988a, 1988b, Kranz et al., 1989; Carey and Bish, 1994, 1996; Chipera et al., 1994) and on the hydrothermal stability of tuffs (Blacic et al., 1986; Duffy, 1983a, 1983b, 1993). The data reported here from drill holes USW NRG-6 and UE-25 UZ#16 are the only Q data available; all other mineralogical data are non-Q as they were obtained from non-Q core and cuttings.

3.4.3.2 Host Rock Mineralogy. The discussion of host-rock mineralogy will be confined primarily to portions of Yucca Mountain most likely to experience repository-induced conditions departing significantly from ambient conditions. This region consists primarily of the Topopah Spring Tuff and the underlying Calico Hills Formation within the repository exploration block (Fig. 3.4-24).

3.4.3.2.1 Mineralogical Data. The thin but hydrologically important upper vitrophyre of the Topopah Spring Tuff lies beneath the nonwelded Paintbrush bedded tuffs. This vitrophyre has a significant hydrologic effect despite its meager thickness (3–7 m) because it is the greatest single barrier to downward recharge into the unsaturated zone (Flint et al., 1993).

One of the important features examined in this vitrophyre across Yucca Mountain has been the extent of alteration, indicating whether this glassy barrier has been compromised by 12 Myr of potential recharge into the unsaturated zone. The upper vitrophyre is composed primarily of unaltered volcanic glass. There is some noteworthy alteration of up to 11% smectite in the glassy portions. More detailed sampling in drill hole UE-25 UZ#16 showed that the upper vitrophyre has been altered significantly by past fluid flow, with up to 18% smectite and 18% clinoptilolite-group zeolite.

The clinoptilolite-group zeolites in this zone have 020:200 intensity ratios indicative of heulandite. To confirm the identification of heulandite, aliquots of samples from drill hole UE-25 UZ#16 were heated overnight at 400°C and 550°C. The samples were analyzed by X-ray diffraction after each heating to determine if the structure had collapsed as expected for heulandite (Mumpton, 1960; Alietti, 1972). Although heating produced significant collapse, the structure was not completely destroyed below 350°C as expected for a "type 1" heulandite (Mumpton, 1960). Likewise, the zeolite cannot be a pure clinoptilolite which should remain stable to temperatures in excess of 700°C.

The amount of collapse observed suggests that the zeolite in these samples is either a mixture of heulandite with minor clinoptilolite, or it is structurally and compositionally an intermediate "type 2" heulandite (Alietti, 1972). The presence of zeolites and smectite in this zone suggests "ponded" alteration above the relatively impermeable upper vitrophyre, it is, however, impossible, given existing data, to determine whether the extent of alteration in the upper Topopah vitrophyre is variable across Yucca Mountain. If such variability could be documented, it might then be possible to map those portions of the mountain where recharge has been, and is likely to be, concentrated.

The restriction of zeolites to the thin interval above the upper vitrophyre of the Topopah Spring Tuff, and the identification of a heulandite component in these zeolites associated with abundant cristobalite, may indicate a very early episode of zeolitization during initial heat loss from the underlying vitrophyre. This interpretation is in accord with studies of the lower vitrophyre of the Topopah

Spring Tuff, where the formation of heulandite at the margin of the vitrophyre is related to the moderate-temperature events that occurred with late-stage cooling of the tuff (Levy and O'Neil, 1989).

One of the inferences that can be drawn from this interpretation is that the zeolitization observed sporadically above the upper vitrophyre of the Topopah Spring Tuff does not represent any significant accumulation of water over the last 12 million years. This inference should be considered critically in further studies of mineralogy from this interval, for although the occurrences of heulandite-above-glass are similar in both the lower and upper Topopah Spring vitrophyres, the alteration setting is quite different. Heulandite formation in the lower vitrophyre is associated with passage from the overlying devitrification front into the vitrophyre, whereas the heulandite that formed above the upper vitrophyre marks a boundary between two vitric zones (welded and nonwelded) with markedly different porosity and transmissivity. It is also possible that the formation of this upper zeolitic zone was favored by the presence of minor amounts of perched water captured due to the low permeability of the underlying upper vitrophyre. Whatever the timing and mode of heulandite formation above the upper vitrophyre, the upper vitrophyre itself is remarkably unaltered, indicating little water/rock interaction in this relatively impermeable interval since tuff emplacement.

Mineralogic evidence of ongoing infiltration may best be found in the potentially ongoing alteration of glass to smectite and in the minor but significant accumulation of calcite in the lower part of the Paintbrush Tuff nonwelded interval in drill hole UE-25 UZ#16. It is important to note that the quantities of smectite and calcite that occur in this interval vary markedly across Yucca Mountain. Up to 40% calcite and 40% smectite occur to the north in USW G-2, and 40% smectite but only a trace of calcite occur in UE-25a#1. A possible implication of this variability is that those portions of the mountain where recharge has been greatest might be delineated by examining the extent of underlying alteration in the nonwelded tuffs between the Tiva Canyon and Topopah Spring Tuffs. This implication deserves serious consideration.

The main central portion of the Topopah Spring Tuff, which consists of densely welded, devitrified rhyolitic tuff (e.g., Broxton et al., 1989), is critical to site characterization because it is the host rock for the potential high-level nuclear waste repository.

The potential repository horizon includes the interval below the zone of abundant (>15%) lithophysal cavities in the upper Topopah Spring Tuff and above the unit's basal vitrophyre. The Topopah Spring Tuff is chemically homogeneous, but the mineralogy is variable, primarily in the relative abundances of silica polymorphs (quartz, cristobalite, and tridymite).

Hematite and smectite are common minor phases, and Mn-oxides are common fracture coatings in the upper portion of the unit. However, within the exploration block, there is little variation in the mineralogy of the repository horizon, and over 98% of the mineral content of the rocks can be ascribed to tridymite, cristobalite, quartz, and alkali feldspar. The abundance of feldspar varies between about 55 and 65%, with the remainder of the rock consisting of variable proportions of crystalline silica polymorphs. Thus, the *total* of the crystalline silica polymorphs is quite consistent throughout much of the Topopah Spring Tuff.

In most cores, tridymite occurs throughout this interval of the Topopah Spring Tuff but is most abundant in the upper portion. Quartz is often absent in the upper portion of this interval but occurs in the lower portions in tuffs with reduced tridymite abundance. Based on higher sampling densities in UE-25 UZ#16 and USW NRG-6, there appears to be a pronounced break in the distribution of silica polymorphs at between 15 and 20% of the way downward through the Topopah Spring Tuff. This is where the transition from quartz-latite to rhyolitic composition occurs. At this point, a maximum in tridymite abundance is reached and quartz becomes more important.

Cristobalite varies markedly in relation to quartz below this transition depth. X-ray diffraction data suggest that there may be a general reduction in cristobalite and rise in quartz with depth, beginning near the middle nonlithophysal zone.

These silica polymorphs are important, because the least stable of them (cristobalite and tridymite) can elevate the aqueous silica activity in local

unsaturated-zone waters. These less stable silica minerals provide a ready source of silica for dissolution, transport, and deposition under the thermal perturbations of a repository. Cristobalite is particularly abundant in the potential repository horizon (Bish et al., 1984), and as such may be an important health hazard consideration. In addition to effects on aqueous silica activity, cristobalite is important in the near-field environment because it undergoes a displacive phase transformation, with an associated 5% volume increase, at about 220°C (Peacor, 1973).

Recent studies of drill hole UE-25 UZ#16 (Chipera et al., 1995b) emphasized our limited understanding of the rocks within the exploration block. In this drill hole, stellerite, a Ca-rich ($Ca_4Al_8Si_{28}O_{72}\bullet 28H_2O$) orthorhombic mineral similar to stilbite, was discovered in significant amounts in the central 50% of the Topopah Spring Tuff. This zeolite occurs in bulk-rock samples between 191.5 and 332.4 meters in depth, in concentrations up to 14 wt% (avg. ~3 wt%) and is obviously not restricted to fractures. The occurrence of this hydrous mineral within the potential repository horizon was completely unexpected as it had previously been found only in fractures from drill holes USW G-1, G-2, and UE-25a#1. Its significance in the remainder of the exploration block is unknown. Future analyses of cores from drill holes SD-7, SD-9, and SD-12 may clarify the stellerite distribution with the exploration block. Naturally this hydrous mineral will be particularly sensitive to changes in temperature and water-vapor pressure, and it loses most of its water below 200°C (Gottardi and Galli, 1985).

The effects of thermal alteration by hot emplaced waste may be most pronounced in the basal vitrophyre of the Topopah Spring Tuff, closely underlying the potential repository horizon. This vitrophyre is variably altered across Yucca Mountain, with devitrification-associated heulandite formation penetrating its highly irregular upper surface (Levy and O'Neil, 1989).

As noted by Bish et al. (1984), the so-called Zeolite Interval I occurs at the top of the basal vitrophyre. This is a 2–5-m thick interval, commonly containing up to 30% of a clinoptilolite-heulandite mineral and 45% smectite. Alteration to zeolites and smectite is often gradational in the upper and lower margins of the basal vitrophyre,

and smaller amounts of other zeolites (e.g., erionite) also invade the lower and upper margins, usually in fractures. The minerals in Zeolite Interval I are potentially quite important in the near-field environment because (1) they represent the first occurrence of significant amounts of sorptive minerals beneath the repository horizon; and (2) they represent the first occurrence of minerals that are particularly sensitive to changes in temperature and/or water-vapor pressure.

The basal vitrophyre itself is a 10- to 30-m thick zone consisting predominantly of densely welded glass (40-90%), with smaller amounts of feldspar, quartz, and opal-CT. Perlitic fractures in the vitrophyre are commonly lined with smectite or zeolites. The perlitic glass in this interval contains from 2.8 to 4.6% water, approximately three-fourths of which is lost at temperatures below 300°C in dry heating experiments (Vaniman et al., 1993).

In the eastern portion of Yucca Mountain, the nonwelded base of the Topopah Spring Tuff and all of the underlying Calico Hills Formation are extensively zeolitized to clinoptilolite and mordenite. These zeolitic rocks contain up to 83% clinoptilolite and up to 43% mordenite. The primary silica phase associated with this zeolitization is authigenic opal-CT, with minor amounts of quartz and alkali feldspar in the highly zeolitized horizons. Percentages of smectite up to 50% occur in the Topopah Spring Tuff bedded tuffs immediately underlying the lower vitrophyre, but the thoroughly zeolitized rocks at greater depth typically contain very little smectite. In the western portion of Yucca Mountain, the few core samples available suggest that this entire interval is vitric and largely unaltered. This vitric interval consists of moderately welded to non-welded glassy tuffs, with 30 to 80% glassy shards and minor amounts of alkali feldspar, cristobalite, and quartz. Alteration to smectite is minor in this interval.

The available data suggest that an alteration front may have been associated with past rises in the static water level (SWL), giving rise to zeolitized Calico Hills Formation rocks to the east. However, the nature of this zeolitic/vitric transition and the implications for past fluctuations in the SWL will remain speculative until further core samples from the potential repository block (e.g., SD-7, -9, and -12) are

analyzed. The nature of the lateral and vertical transitions between zeolitic and vitric portions of the Calico Hills Formation is of fundamental importance to understanding (1) the maximum amount of zeolitic tuff between the host rock and the static water level; (2) the transport pathways from the potential repository toward the saturated zone and (3) the potential for thermal alteration or dehydration of existing zeolites and possible formation of new zeolites from heated glass (Vaniman and Bish, 1995).

The Calico Hills Formation at the potential repository site is underlain by the mostly devitrified, poorly welded Prow Pass Tuff of the Crater Flat Group. The devitrified portions of the Prow Pass Tuff are composed of feldspar and a silica mineral. Available data show that cores taken from locations in which the Prow Pass is high above the SWL and underlies vitric portions of the Calico Hills Formation contain the same variable silica-polymorph associations (tridymite, cristobalite, and quartz) found in the devitrified Topopah Spring Tuff (e.g., USW H-3 and H-5). In cores where the Prow Pass is closer to or within the saturated zone and is overlain by zeolitized portions of the Calico Hills Formation, only quartz is preserved. If borne out in further drill cores, this alteration-associated variability in the Prow Pass may prove to be an important component in predicting the future silica activity, and hence the extent of silica mobilization, to be expected in thermally-perturbed portions of the Prow Pass Tuff.

3.4.3.2.2 Distribution of Silica Phases. As noted above, the nature of the silica phases is particularly important in the NFE. Alteration reactions in the tuffs involving zeolites and smectite are quite sensitive to the aqueous silica activity (e.g., Chipera et al., 1995a). In addition, cristobalite and the hydrous silica phases are susceptible to thermally induced modifications.

The variability of silica polymorph distributions throughout the unsaturated zone reveals a stratigraphy of minerals capable of generating widely varying silica activity in water/rock interactions. Earlier studies (Bish et al., 1984) of core samples showed a crude stratigraphy of silica polymorphs in the Topopah Spring Tuff, with tridymite concentrated in the upper portions of the devitrified tuff. It was principally concentrated in the quartz-latite portion that was erupted from a

significantly hotter part of the magma chamber than the rhyolite; see Lipman, 1971. Quartz was restricted to the lower, rhyolitic portions where tridymite is only a minor phase. Cristobalite is ubiquitous throughout the Topopah Spring Tuff.

More recent studies show that although this stratigraphic model continues to be upheld, the lower portion of the Topopah Spring devitrified zone generally contains all three of these crystalline silica polymorphs. Small amounts of tridymite (~0–6%) and larger amounts of cristobalite (typically 10–20%) occur throughout the rhyolitic portion of the Topopah Spring Tuff. Thus, in most drill holes examined within the repository block, even at the potential repository horizon, cristobalite and usually tridymite are present to provide relatively soluble silica for dissolution, transport, and deposition under repository thermal conditions.

Recently completed analysis of samples from the Exploratory Studies Facility (ESF) suggest that the ratio of total crystalline silica polymorphs to alkali feldspar is reasonably constant at 0.75±0.03 within the host rock. Within the host rock in the ESF, cristobalite is the dominant silica polymorph at 23±5%, with quartz at 12±5% and tridymite at 4±1%.

The distribution of the least-stable silica form in Yucca Mountain cores (apart from volcanic glass), opal-CT, was outlined by Bish and Chipera (1989). The occurrence of this phase is strongly correlated with stratified occurrences of zeolites (clinoptilolite/mordenite), where it averages 18% of zeolitic rocks, and with the lower vitrophyre of the Topopah Spring Tuff, where it averages 10% of these glassy rocks. Opal-CT in earlier-analyzed drill cores was lumped together with cristobalite, hence one can obtain the mistaken impression from the earlier data that this correlation does not hold. The occurrence of opal-CT in the lower vitrophyre is not universal (e.g., absent in core UE-25a#1; Bish and Chipera, 1989). Moreover, opal-CT has not been found in the upper vitrophyre, although small amounts of cristobalite occur there (1–2% in UE-25 UZ#16 and in trace amounts in other cores near the exploration block). The presence or absence of opal-CT in glassy tuffs is important to note, suggesting different environments of alteration. As with the potentially different origins of heulandite in upper and lower vitrophyres, the silicification of

the lower vitrophyre and not of the upper vitrophyre point to different alteration regimes. It is possible that alteration was predominantly associated with the advancement of a devitrification front into the lower vitrophyre, whereas alteration may be largely associated with "ponding" above the upper margin of the upper vitrophyre.

3.4.3.3 Past Mass Transfer in Host Rock Tuffs

3.4.3.3.1 Syngenetic Alteration of the Topopah Spring Tuff. The Topopah Spring Tuff was emplaced at temperatures up to 700 to 800°C and probably required about 10^2 to 10^3 years to cool (Riehle, 1973). Early in the cooling period, the interior welded by viscous flow and compaction of the glass particles. The process of welding continued to temperatures as low as 475°C in the basal vitrophyre (Rosenbaum, 1986). After substantial welding had occurred, the tuff in the hottest parts of the interior devitrified, that is, it crystallized to an assemblage of feldspars and silica minerals. Escaping gases created gas cavities (lithophysae or lithophysal cavities) with vapor-phase mineral deposits. The faster cooling upper and lower margins of the deposits did not weld and experienced little or no devitrification. Some of the moderately to densely welded portions toward the outer margins did not devitrify and have survived in a glassy state (upper and lower vitrophyres). Localized alteration, caused by a combination of trapped water and infiltrating meteoric water that interacted with the rock, occurred during the very late stages of cooling, at near-ambient temperatures. The tuffs were also subject to fracturing, faulting, and brecciation during cooling.

The alteration history of the Topopah Spring Tuff have been reconstructed from field studies and examination of outcrop samples, drill core and cutting samples, and rock samples from the ESF. Thin sections of samples were examined by optical microscopy. Scanning-electron microscopy, using an ISI model DS-130 scanning electron microscope (SEM) operated at 19 kV with a Kevex model 7000 energy-dispersive X-ray analytical system, provided details of textural relations. Minerals were identified from energy-dispersive X-ray spectra and crystal morphology. X-ray powder diffraction data and quantitative mineral analyses were obtained as

described above. All of the data in this section are non-Q because they are derived from non-Q drill core. The data-tracking numbers are LA000000000024.001 and LA000000000101.001. The record packages containing traceability information are EES-1-9-92-5 and LA-EES-1-TIP-94-008.

3.4.3.3.2 Alteration in the lower Topopah Spring Devitrified-Vitric Transition Zone. The lower Topopah Spring Tuff devitrified-vitric transition zone marks the downward change from the pervasively devitrified, densely welded tuff (Tptpln) to underlying vitrophyre (Tptpv3: densely welded, glassy tuff). The transition zone is an interval of slightly to almost completely devitrified vitrophyre in which devitrification is sporadic and localized around fractures (Levy, 1984a). In the uppermost parts of the transition zone, where devitrification is almost complete, the tuff is distinguishable from ordinary devitrified tuff by the presence of incompletely devitrified pumice clasts that have been replaced primarily by clinoptilolite-heulandite. Further down, the most common alteration features are fractures with devitrified borders up to 0.3 m thick. Some of the devitrified borders are downward extensions from the overlying completely or predominantly devitrified tuff.

The transition zone is an interval of variable vertical dimension, extending from about 3 m to 30 m downward into the vitrophyre, with discontinuous distributions of secondary minerals both vertically and horizontally. This altered zone does not possess the attribute of thickness in the sense that intervals of zeolitized nonwelded tuffs elsewhere in the pyroclastic section have reliably measurable thicknesses and km-scale lateral continuity.

The devitrified fracture borders have a common textural and mineralogic zonation developed more or less symmetrically about the fracture traces. The inner margins of devitrified borders are mineralogically and texturally similar to the overlying devitrified rock, but with increasing amounts of yellow cryptocrystalline devitrification toward the outer margins. The outermost margins of devitrified borders contain clinoptilolite-heulandite, smectite, and minor silica. Dissolution cavities may be present in the adjacent vitrophyre. Quartz, chalcedony (microscopically fibrous quartz), opal, and clinoptilolite-heulandite are locally

abundant as fracture and void fillings, along with small quantities of iron and manganese minerals. Minute to major quantities of erionite may also be present.

Field and microscopic textural relations show a ubiquitous association between the hydrous minerals and devitrification features within the transition zone. The relations indicate that hydrous mineral crystallization was connected to devitrification during cooling of the pyroclastic unit. The observed textural relations, together with evidence for abundant fluid flow along fractures downward into the vitrophyre, indicate that devitrification, glass dissolution, and hydrous mineral deposition were caused by downward movement of heated water from the central hottest part of the cooling tuff. Temperatures calculated from oxygen isotope geothermometry of quartz associated with zeolite in fracture fillings and secondary pore fillings are in the range of 40° to 100°C (Levy and O'Neil, 1989).

There is textural evidence that alteration in the transition zone resulted in the genesis, transport, and deposition of colloidal material (Levy, 1992). Pores and fractures contain layered or nonlayered accumulations of colloidal particles. These accumulations, or gels, later crystallized to clinoptilolite-heulandite, silica, and zeolite-silica mixtures. Silica products include opal, chalcedony, and cristobalite, locally in combination with each other. Additional minor gel products include hematite and manganese minerals. Relict colloidal accumulations also fill primary and secondary pores in moderately welded tuffs below the vitrophyre.

3.4.3.3.3 Mass Transfer During Natural Alteration. Glasses representative of the starting materials, smectite, and zeolites in the altered rocks were analyzed by electron probe microanalysis using a Cameca model Camebax electron microprobe operated at 15kV accelerating potential and 5 to 15 nA beam currents. Normalized analyses of starting materials and secondary mineral products, plus the calculated elemental mass per unit volume for selected elements, are presented in Table 3.4-3. Glass analyses used as input for mass balance calculations were recalculated to a uniform 3 wt % water content. The 3% value falls within the range of 2.8% to 4.6% water measured in Topopah Spring Tuff lower vitrophyre samples (Vaniman et al., 1993). The materials used in those studies were not collected as natural-state samples

to preserve *in situ* moisture contents. In addition, the samples are perlitic and may not represent the water content of glasses at the onset of alteration.

Normalization of the water content in glasses, as well as in clay and zeolites, eliminates compositional variability due solely to differences in water content at the time of analysis. The use of this convention means that chemical changes during glass hydration (i.e., the earliest stage of alteration) are not represented in the calculations and are not accounted for in mass-transport determinations. Clinoptilolite-heulandite analyses were recalculated to a water content of 17 wt % corresponding to measured values at ~100% relative humidity and 23°C; smectite analyses were recalculated to a water content of 30 wt % (Chipera, personal communication, 1994).

Mass-balance and transport calculations used published density data for minerals. The composition of cristobalite was assumed to be 100% SiO_2 with a density of 2.30 (Deer et al., 1963), yielding a calculated value of 0.03828 mole Si/cm^3. A grain density value for Topopah Spring Tuff lower vitrophyre from a depth of 369.9 m in drill hole GU-3 (Anderson, 1984) was used for the calculations.

3.4.3.3.4 Alteration of Topopah Spring Basal Vitrophyre Glass. The effects of vitrophyre glass alteration on rock porosity depend in part on the amounts of secondary minerals formed during the alteration process, whether natural or repository-related. There is substantial lateral variation in the abundances and proportions of alkali feldspar, smectite, clinoptilolite-heulandite, and silica that comprise the characteristic secondary-mineral assemblage (Table 3.4-4). Instead of attempting to determine abundance values of general validity, the alternative approach taken here is to calculate bounding values for the amounts of secondary minerals that could form from the constituents of dissolved glass.

Alkali feldspar is typically the most abundant component of the natural alteration in the upper part of the devitrified-vitric transition zone, closest to the completely devitrified rock (candidate host rock). However, alteration assemblages from lower in the transition zone, with little or no feldspar, are simpler to model and may be more representative of alteration products to be expected in a waste repository-induced hydrothermal regime (Knauss and Peifer, 1986).

Dissolution of vitrophyre glass and precipitation of secondary minerals is represented qualitatively by the reaction

$$\text{glass} \rightarrow \text{smectite} + \text{heulandite} + \text{cristobalite} \qquad (1)$$

Smectite and zeolite, alone or in combination, were typically the first-formed alteration products of glass dissolution. SEM photographs suggest that these minerals were commonly deposited at or near the dissolution sites. Silica was more likely to be transported and deposited elsewhere as fracture or pore fillings of cristobalite, chalcedony, quartz, or opal. Aluminum was the limiting constituent that determined the maximum amount of smectite or zeolite that was produced, so long as no additional Al was introduced in solution or colloidal suspension. Figure 3.4-25 is a graphic representation of reaction (1), balanced for all possible combinations of smectite and clinoptilolite-heulandite. Input values for the figure are from Table 3.4-3. The graph balances the reaction with respect to Al and Si, but not Na, Ca, K, or other elements. Also, the very small primary porosity was not factored into the calculations.

The most important result illustrated in Fig. 3.4-25 is that any combination of secondary minerals produces an increase in volume of 13 to 24 % over the volume of the reacted glass. The higher volume increase is for a smectite-rich assemblage in which the smectite accounts for less than the original glass volume and cristobalite is almost half of the original volume. In a zeolite-dominated assemblage, the volume of zeolite produced is approximately equal to the volume of glass consumed, with cristobalite comprising the additional 13%.

For vitrophyre with a bulk porosity around 1.4% (Anderson, 1984), alteration products in principle could seal all of the porosity in a volume of rock at least ten times larger than the volume of altered vitrophyre. This has not been observed in the naturally altered rock. Bulk porosity in the vitrophyre probably corresponds to the pervasive perlitic fracture system (Blacic et al., 1982), but larger-aperture through-going fractures also exist. The wider fractures, along with devitrification cavities, provided pathways for fluid flow and space for secondary-mineral

deposition during the period of alteration. The alteration must have caused an overall reduction in porosity, but this does not appear to have resulted in pervasive sealing or plugging of flow paths below the repository horizon.

3.4.3.4 Effects of Repository-Induced Thermal Load on Minerals And Glasses in the Near-Field Environment

3.4.3.4.1 Rationale and approach. The purpose of this section is to summarize thermodynamic and kinetic data on minerals and glass relevant to the near-field environment. These data are necessary to model mineral development in the near-field environment as a function of their thermodynamic properties and of the mineral reaction kinetics. The implications of the thermodynamic and kinetic data on the factors controlling stability of minerals and glasses at Yucca Mountain and anticipated changes in these factors are discussed in some detail. The observed range of mineral assemblages at Yucca Mountain as a function of depth and paleotemperatures suggests that the following materials are the likely reactants and products of any mineralogical reactions in response to heat derived from the high-level nuclear waste: (1) Reactions of unstable silica polymorphs tridymite, cristobalite, and opal-CT to quartz; (2) Reaction of alkali feldspar under hydrothermal conditions to gibbsite, kaolinite, illite, smectite, analcime, and/or clinoptilolite; (3) Hydrothermal alteration of vitric units to assemblages of smectite, clinoptilolite/heulandite, and mordenite; (4) Dehydration/hydration reactions of clinoptilolite, mordenite, and smectite in response to changing temperature and fluid saturation; (5) Decomposition of clinoptilolite and smectite in response to elevated temperatures or changed fluid compositions.

The minerals discussed in detail here are clinoptilolite (hydration/dehydration reactions, solubility, kinetics of dissolution/precipitation), analcime (solubility and kinetics of dissolution/precipitation), smectite (hydration/dehydration reactions), and cristobalite (solubility and kinetics of dissolution/precipitation). Additional data gathered from the recent literature are presented on the thermodynamic and kinetic properties of these and other minerals.

3.4.3.4.1.1 Silica polymorph control of mineral stability. Mineral assemblages observed in a wide variety of low-temperature volcanic environments indicate that

the silica polymorph plays a determinative role in mineral stability. For example, it has been observed that the presence of clinoptilolite is correlated with the occurrence of cristobalite or opal-CT, and analcime with that of quartz (Duffy, 1993). These relations indicate that metastable silica polymorphs allow other metastable mineral assemblages to persist and suggest that the evolution of mineral assemblages may be at least partly controlled by the kinetics of silica reactions.

The primary silica phases at Yucca Mountain are quartz, cristobalite, tridymite, and opal-CT. The ground water sampled at Yucca Mountain and vicinity is generally supersaturated with respect to quartz and cristobalite, with an aqueous silica activity between amorphous silica and opal-CT solubility. The equilibrium silica polymorph is quartz. Because the solutions are saturated or even supersaturated with respect to cristobalite, there is no thermodynamic driving force for the dissolution of cristobalite, even though it is metastable with respect to quartz. In such aqueous systems, the primary thermodynamic driving force is for the precipitation of quartz. Therefore, the rate-limiting step for the conversion of cristobalite to quartz appears to be the precipitation of quartz. As quartz precipitates, the aqueous silica content decreases, and then some cristobalite can dissolve. This is consistent with the model presented by Duffy (1993). Similarly, analcime may be stable with respect to clinoptilolite at quartz saturation but metastable at cristobalite saturation. As a consequence, there is no thermodynamic driving force for the dissolution of clinoptilolite and precipitation of analcime until the silica solubility drops below that of cristobalite.

Duffy (1993) considered the reactions of clinoptilolite to analcime, clinoptilolite to smectite, analcime to albite, and feldspar to illite, to all be effected by the silica polymorph in equilibrium with the fluid.

3.4.3.4.2 Stability of Selected Minerals and Glass

3.4.3.4.2.1 Clinoptilolite (and heulandite). Compositions of clinoptilolite and heulandite at Yucca Mountain are highly variable, with Si/Al ratios between 3 and 5 and the dominant exchangeable cation varying between Na^+, K^+, and Ca^{2+} (Broxton et al., 1987). Consequently, it is evident that thermodynamic and kinetic models capable of addressing the effect of compositional variations in clinoptilolite

minerals are essential for accurate prediction of the dissolution or precipitation of clinoptilolite and heulandite. Because clinoptilolite is the most abundant zeolite at Yucca Mountain, considerable attention has been focused on the thermodynamic properties of this mineral. The work that will be reviewed here includes the following:

1. The effect of exchangeable cation in clinoptilolite on molar volumes (Bish, 1984);
2. Thermal analysis investigations of the dehydration behavior of clinoptilolite and heulandite (Bish, 1988a);
3. The effect of dehydration on molar volume (Bish, 1995);
4. Estimation of the thermodynamic properties of clinoptilolite and heulandite as a function of chemical composition (Chipera et al., 1995a);
5. Determination of the equilibrium water content of clinoptilolite as a function of exchangeable cation (Carey and Bish, 1996a);
6. Determination of the energetics of hydration and dehydration processes in clinoptilolite as a function of exchangeable cation (Carey and Bish, 1996b); and
7. The solubility and kinetics of dissolution and precipitation of Na-clinoptilolite (MacInnis et al., 1995; Barnes and Wilkin, 1995).

3.4.3.4.2.2 *Thermodynamic Stability.* The thermodynamic properties of clinoptilolite and heulandite have been investigated by modeling, calorimetry, and solution chemistry. The various results are difficult to compare because of differences in Si/Al ratio and exchangeable cation (Table 3.4-5). Note that Barnes and Wilkin (1995) conducted solubility measurements on an almost completely exchanged Na-clinoptilolite that should be a very useful end-member in thermodynamic calculations. The complete results of Barnes and Wilkin's solubility data from 25 to 265°C are summarized in Table 3.4-6. The Gibbs free energy of formation of Na-clinoptilolite calculated from the measured solubility products is almost linear in temperature (Fig. 3.4-26). A linear regression of these values provided the enthalpy of formation and the third-law entropy for Na-clinoptilolite (Table 3.4-5).

3.4.3.4.2.3 Effect of cation-exchange. The thermodynamic data for Na-clinoptilolite (Barnes and Wilkin, 1995) provide a basis for the calculation of the end-member thermodynamic properties of K- and Ca- and Sr-clinoptilolite by incorporating the results of Pabalan (1994) and Pabalan and Bertetti (1994). The latter studies are binary cation-exchange experiments for Na-K, Na-Ca, and Na-Sr compositional pairs. Calculation of the integral Gibbs free energy of exchange combined with the Gibbs free energy of formation of the aqueous cations and Na-clinoptilolite gives end-member thermodynamic properties that differ by 180 to 97 kJ/mol from Na-clinoptilolite (72 oxygen basis; Table 3.4-7). These differences are small compared with the differences reported in Table 3.4-3. Consequently, the variability of results in Table 3.4-3 reflects either the large energetic affect of Si/Al substitutions or some other source of difference or error (e.g., Al/Si order/disorder).

As is common with many other natural zeolites, the energetic preference for cations is in the order K>Sr>Ca>Na (cf., Sherry 1969). Pabalan (1995) demonstrated that clinoptilolite is enriched in K relative to Na in aqueous solutions. The situation for the exchange of Ca and Sr for Na is more complex: dilute, Na-rich solutions favor preferential sorption of Ca and Sr; whereas concentrated, Na-poor solutions show enrichment of Na in clinoptilolite. These relations indicate that the presence of K-rich, Ca-poor, dilute solutions will result in clinoptilolite with compositions significantly removed from the Na end-member. In such solutions, clinoptilolite will be stabilized relative to Na-rich minerals that do not readily cation exchange, such as analcime and albite.

3.4.3.4.2.4 Effects of hydration/dehydration of clinoptilolite. Hydration and dehydration of clinoptilolite may have significant consequences in the near-field environment. Dehydration will destabilize clinoptilolite relative to less hydrous assemblages (albite and analcime); release significant amounts of H_2O; have a significant effect on the thermal budget; and result in porosity changes due to changes in molar volume. The experimental data necessary to assess all of these factors have been obtained by Bish (1995) and Carey and Bish (1996a and b).

3.4.3.4.2.5 Equilibrium. The equilibrium H_2O contents of clinoptilolite as a function of temperature (25–250°C), water-vapor pressure (0–35 mbar), and

exchangeable cation (Na^+, K^+, and Ca^{2+}) were determined by Carey and Bish (1996a). These experiments were conducted by determining the equilibrium mass of clinoptilolite at a measured temperature and water-vapor pressure using a thermogravimetric balance.

These experiments show that clinoptilolite hydrates and dehydrates reversibly up to temperatures ≤215°C (Fig. 3.4-27). Above 215°C, Na-clinoptilolite suffers a slight loss in water adsorption capacity. K- and Ca-exchanged clinoptilolite maintain reversibility to temperatures >250°C. Equilibration time for hydration and dehydration of powders is on the order of an hour, so that the kinetics of hydration/dehydration do not appear to be relevant to processes at Yucca Mountain. The H_2O content of clinoptilolite is a smooth function of temperature and pressure (Fig. 3.4-28), and there are no discontinuities in the dehydration behavior at the boiling point of water. Clinoptilolite retains substantial H_2O to temperatures > 150°C, even in a nominally dry atmosphere.

The measured thermogravimetric equilibrium data were fit to a thermodynamic function describing the reaction:

$$\text{anhydrous clinoptilolite (aCpt)} + H_2O \leftrightarrow \text{hydrous clinoptilolite (hCpt)} \qquad (2)$$

The equilibrium constant, K_{ideal}, containing ideal mixing terms for this reaction is:

$$\ln K_{ideal} = \left(\frac{\theta}{(1-\theta) f_{H_2O}} \right) \qquad (3)$$

where θ is the ratio of the amount of H_2O in clinoptilolite relative to the maximum amount clinoptilolite contains.

The thermodynamic function was determined by analysis of the equilibrium constant as a function of temperature and composition (Fig. 3.4-29). The variations

in K were described with an equation giving the Gibbs free energy of hydration, the enthalpy of hydration, and two mixing parameters (W_1 and W_2):

$$-R\,ln\,K = \frac{\Delta\mu^{o}_{Hy}}{T_o} + \Delta\overline{H}^{o}_{Hy}\left(\frac{1}{T} - \frac{1}{T_o}\right) - 3R\left(ln\left(\frac{T}{T_o}\right) + \left(\frac{T_o}{T} - 1\right)\right) + \frac{W_1}{T}\theta + \frac{W_2}{T}\theta^2 \qquad (4)$$

Fits of the data yielded thermodynamic parameters describing hydration in Na-, K-, and Ca-exchanged clinoptilolite (Table 3.4-8; Figs. 3.4-28 and 3.4-29). The results indicate that the energetics of hydration increase from K<Na<Ca clinoptilolite (Table 3.4-9).

The results for clinoptilolite are energetically similar to those of mordenite and intermediate between strongly (analcime) and weakly (cordierite) interacting systems. The similarity of the integral values of hydration for mordenite and clinoptilolite suggest that in the absence of additional thermodynamic data the hydration energetics of mordenite may be approximated by those of clinoptilolite. Note that the energetics of hydration are significantly greater than condensation of water vapor.

As discussed by Pabalan (1994), cation-exchange in clinoptilolite is accompanied by hydration and dehydration reactions. Consequently, the Gibbs free energy of exchange measured by Pabalan contains a contribution due to hydration reactions in addition to cation-exchange. The results described here may be used to "correct" the Gibbs free energy of exchange data to give energetics solely due to cations.

The equation of state for clinoptilolite (Equation 4) allows calculation of the equilibrium water content of clinoptilolite under conditions of interest in the NFE. Under conditions of rising temperature, clinoptilolite dehydrates even in the presence of an aqueous phase (Fig. 3.4-30). However, if dryout of the rock units occurs, as may happen if temperatures rise above 100°C, the degree of dehydration of clinoptilolite increases markedly. The equilibrium water content as a function of maximum sustainable water-vapor pressure, is shown in Fig. 3.4-30 for maximum pressures ranging between 1 and 20 bars.

3.4.3.4.2.6 Energetics. The energetics of hydration and dehydration of clinoptilolite have been measured calorimetrically by Carey and Bish (1996b). In these experiments, Na-, K-, and Ca-exchanged clinoptilolite samples were partially dehydrated, sealed in an evacuated ampoule, and placed in water where the heat of immersion was measured. The enthalpy of hydration (which is equivalent to the heat of immersion in the experiments) increases with decreasing water content in clinoptilolite (Fig. 3.4-31). This demonstrates that the energetic cost of dehydration increases as dehydration proceeds. The partial molar enthalpy of hydration was fit to an equation of the form (Table 3.4-10; Fig. 3.4-32):

$$\Delta\overline{H}_{Hy} = \Delta\overline{H}^{o}_{Hy} + W_1\theta + W_2\theta^2 \tag{5}$$

A combination of the equilibrium and calorimetry studies can be used to assess the potential effects of hydration and dehydration processes on heat flow and pore saturation at Yucca Mountain. A simple numerical model was used that considers the thermal and hydrologic evolution of a thermally insulated block of clinoptilolite that receives a constant source of thermal energy. In the model, a 1 m^3 box has 10% porosity, is initially at 25°C, 100% relative humidity, and receives a thermal flux of 14 watts while maintaining a uniform temperature (the value of the thermal flux is representative of those considered for Yucca Mountain). The thermal flux is consumed by the heat capacity of clinoptilolite and by dehydration processes. It is assumed that the box is porous to water vapor and a maximum pressure of 1 bar is attained. The temperature achieved by the box is dramatically lower when clinoptilolite is allowed to dehydrate (Fig. 3.4-33). The model without dehydration reached 395°C after 844 days, whereas that allowing dehydration reached only 250°C over the same period. The kink in the temperature evolution at 100°C is the point at which the pores attained the maximum water-vapor pressure of 1 bar. During the dehydration process, the clinoptilolite released 1.63 pore volumes of liquid water. In other words, the model constraints require that an amount of water equal to 16% of the rock volume must drain away (10% porosity).

These calculations demonstrate that dehydration and hydration of clinoptilolite can affect the temperature and saturation field in the NFE. Whether clinoptilolite has a significant effect depends on the interplay of factors such as: the rate of heating versus the rate of thermal dissipation; and the ratio of water released by clinoptilolite to the amount infiltrating the rock unit in a given period of time. These can only be quantitatively addressed using coupled numerical models of clinoptilolite hydration/dehydration and thermo-hydrologic processes.

3.4.3.4.2.7 Changes in Molar Volume of Clinoptilolite. The molar volume of clinoptilolite is a sensitive function of temperature, exchangeable cation, and hydration state (Bish, 1984; Bish, 1995). Changes in molar volume of clinoptilolite may be important in the Calico Hills Formation, where clinoptilolite constitutes from 50 to 70% of the rock. Bish (1984) observed that decreases in molar volume on heating to 300°C ranged from 1.6 to 3.6 to 8.6% for K-, Ca-, and Na-exchanged samples, respectively. Apparently the bulk of the volume decrease was a direct result of dehydration. For a rock with 50% clinoptilolite, an 8% decrease in volume could result in the development of 4% additional rock porosity.

3.4.3.4.2.8 Analcime

3.4.3.4.2.8.1 Thermodynamic Stability. Natural analcime is Na-rich with a Si/Al ratio that varies from nearly stoichiometric (Si/Al = 2) in hydrothermal environments to siliceous compositions (Si/Al = 2.55) typical of sedimentary or diagenetic environments (e.g., Gottardi and Galli, 1985). The analcime at Yucca Mountain is a siliceous, sodic variety with Si/Al ~ 2.75 (Broxton et al., 1987). Most studies of the thermodynamic properties of analcime have been conducted on nearly stoichiometric material derived from hydrothermal environments. Thus the important effect of variations in Si/Al ratio on the stability of analcime were largely unknown until recently.

As a part of the mineralogical investigations at Los Alamos National Laboratory, a study of the solubility of two analcime samples with Si/Al ratios of 2.0 and 2.55 were conducted in collaboration with Pennsylvania State University and Yale University (Barnes and Wilkin, 1995). These data complement the calorimetric studies reported by Robie et al. (1979) and Johnson et al. (1982) and the solubility

study of Murphy et al. (1996) on stoichiometric analcime. The study by Barnes and Wilkin allows the direct calculation of the energetic effect of the substitution Na + Al = Si and, as discussed below, provides a basis for determining the effect of similar substitutions in other zeolites, such as clinoptilolite.

The reported uncertainty in the measured Gibbs free energy of formation of analcime varies between 3 and 5 kJ/mol (Table 3.4-11; Fig. 3.4-34). Note, however, that Johnson et al. (1992) revised their measured value for analcime by almost 9ÊkJ/mol due to a change in the reference value of silica and gibbsite used in the solution calorimetry. This revised value may be more accurate than the earlier result, but earlier work and many internally consistent thermodynamic data bases are implicitly built on the previous reference states. As a consequence, it is probably advisable to retain the old value until a consensus on the most useful reference value for silica can be achieved. The results of Barnes and Wilkin (1995) for both samples (Si/Al = 2 and 2.55) were obtained by extrapolation from experiments at 50 to 300°C. The *measured* solubility at 25°C for the Mt. St. Hilaire (Si/Al = 2) sample is also provided in Table 3.4-11, but Barnes and Wilkin showed that their results at 25°C are not consistent with results extrapolated from higher temperatures.

Thermodynamic values for analcime have also been derived from phase equilibria constraints by Helgeson et al. (1978) and estimated by using polyhedral summation methods by Chermak and Rimstidt (1989) and Chipera et al. (1995a; Table 3.4-12 and Fig. 3.4-34). The summation methods allow calculation of the Gibbs free energy of formation for arbitrary compositions, but such summations must be checked against actual measurements.

The data presented by Barnes and Wilkin allow calculation of an empirical relationship giving the relationship of the Gibbs free energy of formation of analcime as a function of Si/Al ratio:

$$\Delta G_f^{analcime} = -3090 + 98.8\left(Si/_{Al} - 2\right) \qquad (6)$$

Their results agree well with the intermediate value measured by Johnson et al. (1982; Fig. 3.4-34), and they noted that their results are consistent with the ideal solution model of Wise (1984) for Si/Al mixing in analcime.

The value derived by Helgeson et al. (1978) is also in good agreement with the measurements. The estimation methods of Chermak and Rimstidt (1989) are slightly high and those of Chipera et al. (1995a) are somewhat better. Interestingly, these estimation methods also provide reasonable estimates of the trends in the value of the Gibbs free energy of hydration as a function of Si/Al ratio. The equation derived from Chermak and Rimstidt is (in kJ/mol):

$$\Delta G_f^{analcime} = -3099 + 298(Si - 2) \tag{7}$$

and that of Chipera et al. is

$$\Delta G_f^{analcime} = -3094 + 281(Si - 2) \tag{8}$$

These conclusions regarding the compositional effects of analcime thermodynamics are consistent with the calorimetric study of Petrovic and Navrotsky (1995) on the energetics of the Na + Al = Si substitution in faujasite. They found that the increase in the enthalpy of formation per mole of Si was 267ÊkJ/mol, very similar to the values of 281 and 298 for the Gibbs free energy of formation obtained by estimation (Equations 7 and 8).

For a variety of common reactions involving analcime, the relations in Equations 6, 7, and 8 indicate that siliceous analcime is destabilized relative to stoichiometric analcime with respect to sodium end-member phases such as albite or clinoptilolite (Fig. 3.4-35). The degree of destabilization for a reaction balanced on aluminum of analcime relative to another sodic framework-aluminosilicate (such as albite or clinoptilolite) can be calculated with the aid of one of these equations. For example, for the reaction

$$(18\text{-}3x/(1\text{-}x))\ SiO_{2\,aq} + 6/(1\text{-}x)\ Na_{1-x}Al_{1-x}Si_{2+x}O_6{\cdot}H_2O + 19\ H_2O = Na_6Al_6Si_{30}O_{72}{\cdot}20H_2O \quad (9)$$

the degree of destabilization corresponds to

$$\frac{1}{RT2.303}\left(\Delta G_f^{o,\,anal}\left(\frac{-x}{1-x}\right) - 98.8\left(\frac{3x}{(1-x)^2}\right) + \Delta G_{f,\,SiO_2}^{o,\,aqueous}\left(\frac{3x}{1-x}\right)\right) = \left(\frac{3x}{1-x}\right) log\left(a_{SiO_2}^{aqueous}\right) \quad (10)$$

where Equation 7 has been used to calculate the effect.

The effects of a 5 kJ/mol uncertainty in the Gibbs free energy of formation on phase relations involving analcime are considerable (Fig. 3.4-36). The uncertainty introduced by analcime for a given reaction in terms of the equilibrium constant can be calculated as

$$log\,K = \pm n\frac{5000\ \text{J/mol}}{2.303RT} = \pm n(0.876)@25\ ^oC \quad (11)$$

where n is the stoichiometric coefficient of analcime in the reaction. For example, the breakdown of clinoptilolite to analcime calculated by Chipera et al. (1995a):

$$(K_{0.3}Na_{0.1}Ca_{1.5})Al_{3.4}Si_{14.6}O_{36}{\cdot}10.8H_2O\ \text{(clinoptilolite)} + 3.3Na^+ + 3.95\ H_2O \Leftrightarrow 4.25Na_{0.8}Al_{0.8}Si_{2.2}O_6{\cdot}H_2O\ \text{(analcime)} + 0.3\ K^+ + 1.5\ Ca^{2+} + 5.25Si(OH)_4 \quad (12)$$

is shifted by ±2.5 log units on activity-activity diagrams commonly used to analyze phase relations at Yucca Mountain (Fig. 3.4-36).

Thermodynamic data for analcime at elevated temperature was obtained by Barnes and Wilkin (1995) using solubility data at temperatures between 25 and 300°C. The Gibbs free energy of formation of analcime was calculated from these data (Table 3.4-13). Linear regression of the Gibbs free energy of formation as a function of temperature provided the enthalpy of formation and standard state

entropy (the heat capacity of the dissolution reaction was assumed to be zero; Table 3.4-14). Additional high-temperature data include heat capacity measurements of analcime between 25 and 350°C (Johnson et al., 1992). However, Carey (1993) argued that the heat capacity of hydrous analcime above 25°C is more accurately given by the sum of the heat capacities of anhydrous analcime (Johnson et al., 1992), H_2O vapor (Robie et al., 1979), and a constant factor accounting for H_2O sorption which is equal to the gas constant.

3.4.3.4.2.8.2 Estimated Thermodynamic Properties of Zeolites and Clays. Thermodynamic data are limited for several important zeolites and clays and still less available for treating compositional variation of these phases (see also Section 3.4.2). One method of addressing this deficiency is to make semi-quantitative calculations using estimated thermodynamic properties. Chipera et al. (1995a) provide the most comprehensive example of this method, obtaining estimated Gibbs free energies and enthalpies of formation, third-law entropies, and heat capacity values for zeolites and clays with compositions representative of those at Yucca Mountain (Table 3.4-15). These data provide a very useful framework for understanding potential reactions among zeolites and clays as a function of temperature, pressure, and solution chemistry (Chipera et al., 1995a).

3.4.3.4.2.9 Smectite. Hydration and dehydration reactions in smectite have a H_2O significant effect on smectite stability and molar volume (due to swelling/collapse of the aluminosilicate layers). These reactions may also affect pore-water saturation, fracture filling, and the osmotic swelling capacity (Bish, 1988b). The hydration and dehydration behavior of smectite is difficult to model thermodynamically because of the pronounced hysteresis in molar volume and water content (Fig. 3.4-37). Although the hydration/dehydration behavior of smectite is an important component in modeling the effects of repository-induced heating on the repository water budget, the highly reversible nature of these reactions suggests that the long-term effects on rock properties may be minor. One of the most important phenomena observed during heating of smectites is the dramatic decrease in osmotic swelling ability after only short-term heating under steam conditions (e.g., Couture, 1985). Such behavior can have very important implications for the long-

term behavior of smectites in the NFE and for their importance in affecting transport. For example, it is likely that NFE conditions will be conducive to the total loss of osmotic swelling capacity of smectites that occur both in fractures in the host rock and in the altered zone immediately underlying the host rock. Such a reaction would thus dramatically increase the hydraulic conductivity of smectite-lined fractures.

Data obtained from drill cores taken from the north and east of the exploration block show that the well-known reaction of smectite to interstratified illite/smectite occurs with increasing depth (Bish, 1989). Both experimental data and field observations demonstrate that this transformation develops progressively from 100 to 250°C. The swelling capacity of smectite is steadily reduced during this diagenetic reaction from 25 to 100°C (cf. Bish, 1989, for a more complete discussion).

3.4.3.4.2.10 Vitrophyre (volcanic glass). The effects of elevated temperatures on Yucca Mountain volcanic glasses have been studied experimentally (see Chapter 10 for a discussion of glass alteration in the presence of water, and Knauss and Peiffer, 1986, Knauss, 1987). Dehydration and hydration of a sample of the basal vitrophyre of the Topopah Spring Tuff were studied by thermogravimetry and by long-term dry heating experiments (Vaniman et al., 1993). The glass initially contained 2.8 to 4.6Êwt% H_2O. Approximately three-fourths of the water was lost during long-term heating at 200°C, but ~1 wt% H_2O was not lost at temperatures less than 400°C, even after long-term heating. Rehydration of the samples at room temperature and 79% relative humidity was continuous but did not reach completion after 10,000 hours. No devitrification reactions were observed during the dry heating experiments, even at 400°C for 10,000 hours, but up to 60% of the fluorine in the glass was evolved.

3.4.3.4.2.11 Kinetics of Dissolution and Precipitation. The long-term fate of minerals in the NFE cannot be determined without measurements of the kinetics of reactions as a function of degree of saturation and temperature. These measurements are usually made by dissolution or precipitation of a given mass of material of known surface area (typically a BET surface area) in a known volume of fluid. The studies are conducted either in a batch mode with continuously changing

solution compositions (e.g., Murphy et al., 1996) or preferably in flow-through devices at constant solution composition (e.g., Nagy et al., 1991). The results reported below have been interpreted using transition state theory (e.g., Nagy et al., 1991) in which the rate of dissolution or precipitation is expressed as

$$R(\text{moles/m}^2\text{ - s}) = -k_{diss}\left(1 - {IAP}/{K_{eq}}\right) \tag{13}$$

where the ratio of the ion-activity-product (IAP) to the equilibrium constant (K_{aq}) expresses the degree of saturation and k_{diss} is the rate constant for the dissolution reaction. The parameter k_{diss} is not an intrinsic rate parameter but may depend on pH and other surface-adsorbed species (Nagy et al., 1991). Equation 13 indicates that the rate of dissolution reaches a constant value ($-k_{diss}$) for significant degrees of undersaturation but that the rate of precipitation increases without bound for increasing supersaturation. Table 3.4-16 summarizes relevant data pertinent to phases important at Yucca Mountain, in addition to more recent data obtained for clinoptilolite and analcime by Murphy et al. (1996) and MacInnis et al. (1995).

3.4.3.4.2.12 Kinetic data for clinoptilolite and analcime. The dissolution rate obtained for clinoptilolite by MacInnis et al. (1995) using a flow-through apparatus appears to be anomalous with respect to other minerals and is not in agreement with the batch study of Murphy et al. (1996). Unfortunately, the study of MacInnis et al. is the only source of data for dissolution rates of clinoptilolite at elevated temperatures (50, 80, and 125°C). Their results were expressed as

$$R = -k_o\, exp\left(-{E_a}/{RT}\right) a_{H^+}^{-0.54}\left({IAP}/{K_{eq}}\right) \tag{14}$$

where $k_o = 2 \pm 27 \times 10^5$ mol/m^2-s; $E_a = 35.1 \pm 9.2$ kcal/mol; and the experiments were conducted at pH 7.5 to 9.0. The difference between Equations 13 and 14 is a consequence of the fact that MacInnis et al. did not observe a constant dissolution rate at significant undersaturation, but they showed data indicating a linear

relationship between rate and undersaturation. Consequently, the dissolution process they observed may be distinct from that modeled by transition state theory (Equation 13). MacInnis et al. also observed some evidence of inhibition by aqueous Al, but were unable to quantify this effect.

There is no single study providing rate data for analcime at more than one temperature. Lasaga et al. (1994a) determined the dissolution of analcime at 80°C with flow-through methods. Their rate equation is similar to that determined by MacInnis et al. (1995) in which the rate depends linearly on the degree of saturation:

$$R = -10^{-12.4} a_{Al(OH)_4^-}^{-0.27} \left(\left| \Delta G \text{ kcal mol}^{-1} \right| \right)^{1.05} \tag{15}$$

where the measurements were made at pH 8.6-8.9 and the degree of saturation is represented by the Gibbs free energy of the dissolution reaction. Typical values at 80°C for the net dissolution rate constant, $\log(k_{diss})$, are approximately -11. Again, these rate constants do not agree well with the batch study values of Murphy et al. (1996) where rates were -11 at 25°C.

In summary, the available kinetic data for both analcime and clinoptilolite are not well constrained and reflect the incomplete status of kinetic data measurement for these minerals. Based on existing data, the dissolution of clinoptilolite does appear to be slower than analcime, by a factor near 100.

3.4.3.5 Acknowledgements

We are grateful to D. Vaniman for a thorough review of this manuscript.

3.4.3.6 References

Alietti, A. (1972) Polymorphism and crystal-chemistry of heulandites and clinoptilolites. *American Mineralogist*, **57**, 1448–1462.

Anderson, L. (1984) Rock property measurements on large-volume core samples from Yucca Mountain USW GU-3/G-3 and USW G-4 boreholes, Nevada Test Site, Nevada. *U. S. Geological Survey Open-File Report*, **USGS-OFR-84-552**, 39 p.

Barnes, H. L., and Wilkin, R. T. (1995) Kinetic measurements on the silicates of the Yucca Mountain potential repository (Yucca Mountain final report for FY95, Los Alamos National Laboratory).

Barrer, R. M., and Cram, P. J. (1971) Heats of immersion of outgassed and ion-exchanged zeolites. In *Molecular Sieve Zeolites-II*, E. M. Flanigen, and L. B. Sand , eds., 105-131. American Chemical Society, Washington, D.C.

Berman, R. G., and Brown, T. H. (1985) Heat capacity of minerals in the system Na_2O-K_2O-CaO-MgO-FeO-Fe_2O_3-Al_2O_3-SiO_2-TiO_2-H_2O-CO_2: Representation, estimation, and high temperature extrapolation. *Contributions to Mineralogy and Petrology*, **89**, 168–183.

Bish, D. L. (1984) Effects of exchangeable cation composition on the thermal expansion/contraction of clinoptilolite. *Clays & Clay Minerals*, **32**, 444–452.

Bish, D. L. (1988a) Effects of composition on the dehydration behavior of clinoptilolite and heulandite. In *Occurrence, Properties and Utilization of Natural Zeolites*, D. Kallo and H. S. Sherry, eds. Akademiai Kiado, Budapest.

Bish, D. L. (1988b) Smectite dehydration and stability. Applications to radioactive waste isolation at Yucca Mountain. *Los Alamos National Laboratory Report*, **LA-11023-MS**, 31 pp.

Bish, D. L. (1989) Evaluation of past and future alterations in tuff at Yucca Mountain, Nevada, based on the clay mineralogy of drill cores USW G-1, G-2, and G-3. *Los Alamos National Laboratory Report*, **LA-10667-MS**, 40 pp.

Bish, D. L. (1995) Thermal behavior of natural zeolites. In *Natural Zeolites '93: Occurrence, Properties, Use*, D. W. Ming and F. A. Mumpton, eds., 259–269.

Bish, D. L., and Chipera, S. J. (1986) Mineralogy of drill holes J-13, UE-25A#1, and USW G-1 at Yucca Mountain, Nevada. *Los Alamos National Laboratory Report*, **LA-10764-MS**. HQS.880517.1957

Bish, D. L., and Chipera, S. J. (1988) Problems and solutions in quantitative analysis of complex mixtures by X-ray powder diffraction. *Advances in X-Ray Analysis*, **31**, 295-308. NNA.890405.0178

Bish, D. L., and Chipera, S. J. (1989) Revised mineralogic summary of Yucca Mountain, Nevada. *Los Alamos National Laboratory Report*, **LA-11497-MS**, 68 pp. NNA.891019.0029.

Bish, D. L., and Chipera, S. J. (1991) Detection of trace amounts of erionite using X-ray powder diffraction: Erionite in tuffs of Yucca Mountain, Nevada, and central Turkey. *Clays & Clay Minerals*, **39**, 437–445.

Bish, D. L., and Chipera, S. J. (1995) Accuracy in quantitative X-ray powder diffraction analyses. *Advances in X-ray Analysis*, **38** 47–57.

Bish, D. L., and Reynolds, R. C., Jr. (1989) Sample preparation for X-ray diffraction. In *Modern Powder Diffraction*, D. L. Bish and J. E. Post, eds., Mineralogical Society of America, Washington, D.C., Vol. 20, 73–99.

Bish, D. L., Ogard, A. E., Vaniman, D. T., and Benson, L. (1984) Mineralogy-petrology and groundwater geochemistry of Yucca Mountain tuffs. *Materials Research Society Symposium Proceedings*, **26**, 283–291.

Blacic, J., Carter, J., Halleck, P., Johnson, P., Shankland, T., Anderson, R., Spicochi, K., and Heller, A. (1982) Effects of long-term exposure of tuffs to high-level nuclear waste-repository conditions: Preliminary report. *Los Alamos National Laboratory Report*, **LA-9174-PR**.

Blacic, J. D., Vaniman, D. T., Bish, D. L., Duffy, C. J., and Gooley, R. C. (1986) Effects of long-term exposure of tuffs to high-level nuclear waste repository conditions: Final Report. *Los Alamos National Laboratory Report*, **LA-9330-MS**, 33 pp.

Broxton, D. E., Warren, R. G., Hagan, R. C., and Luedemann, G. (1986) Chemistry of diagenetically altered tuffs at a potential nuclear waste repository, Yucca Mountain, Nye County, Nevada: *Los Alamos National Laboratory Report*, **LA-10802-MS**, 160 pp.

Broxton, D. E., Bish, D. L., and Warren, R. G. (1987) Distribution and chemistry of diagenetic minerals at Yucca Mountain, Nye County, Nevada. *Clays and Clay Minerals*, **35**, 89–110.

Broxton, D. E., Warren, R. G., Byers, F. M., Jr., and Scott, R. B. (1989) Chemical and mineralogic trends within the Timber Mountain-Oasis Valley caldera complex: Evidence for multiple cycles of chemical evolution in a long-lived silicic magma system. *Journal of Geophysical Research*, **94**, 5961–5985.

Buscheck, T. A., and Nitao, J. J. (1992) The impact of thermal loading on repository performance at Yucca Mountain. *High-Level Radioactive Waste Management, Proceedings of the 3rd Annual International Conference*, April 27–May 1, 1992, Las Vegas, Nevada.

Byers, F. M., Jr. (1985) Petrochemical variation of Topopah Spring tuff matrix with depth (stratigraphic level), drill hole USW G-4, Yucca Mountain, Nevada. *Los Alamos National Laboratory Report*, **LA-10561-MS**.

Byers, F. M., Jr., and Moore, L. (1987) Petrographic variation of the topopah spring tuff matrix within and between cored drill holes, Yucca Mountain, Nevada. *Los Alamos National Laboratory Report*, **LA-10901-MS**.

Carey, J. W. (1993) The heat capacity of hydrous cordierite above 295 K. *Physics and Chemistry of Minerals*, **19**, 578–583.

Carey, J. W. (1995) A thermodynamic formulation of hydrous cordierite. *Contributions to Mineralogy and Petrology*, **119**, 155–165.

Carey, J. W., and Bish, D. L. (1994) Hydration energetics of zeolites. *Proceedings of the 31st Annual Meeting of the Clay Minerals Society*, Saskatoon, Saskatchewan, p. 52.

Carey, J. W., and Bish, D. L. (1996a) Equilibrium in the clinoptilolite-H_2O system. *American Mineralogist* (in press).

Carey, J. W., and Bish, D. L. (1996b) Calorimetric measurement of the enthalpy of hydration of clinoptilolite (submitted to Clays and Clay Minerals).

Carlos, B. A. (1987) Minerals in fractures of the saturated zone from drill core USW G-4, Yucca Mountain, Nye County, Nevada. *Los Alamos National Laboratory Report*, **LA-10927-MS**, 32 pp.

Carlos, B. A., Chipera, S. J., Bish, D. L., and Raymond, R. (1995a) Distribution and chemistry of fracture-lining zeolites at Yucca Mountain, Nevada. In *Natural Zeolites '93: Occurrence, Properties, Use*, D. W. Ming and F. A. Mumpton, eds., 547_563.

Carlos, B. A., Chipera, S. J., and Bish, D. L. (1995b) Distribution and chemistry of fracture-lining zeolites at Yucca Mountain, Nevada. *Los Alamos National Laboratory Report*, **LA-12977-MS**, 92 pp.

Carlos, B. A., Chipera, S. J., and Snow, M. G. (1995c) Multiple episodes of zeolite deposition in fractured silicic tuff. In *Proceedings of the 8th International Symposium on Water-Rock Interaction—WRI-8*, Y. K. Kharaka and O. V. Chudaev, eds; Balkema, Rotterdam, 67–71.

Chermak, J. A., and Rimstidt, J. D. (1989) Estimating the thermodynamic properties (Gf and Hf) of silicate minerals at 298 K from the sum of polyhedral contributions. *American Mineralogist*, **74**, 1023–1031.

Chipera, S. J., and Bish, D. L. (1988) Mineralogy of drill hole UE-25P#1 at Yucca Mountain, Nevada. *Los Alamos National Laboratory Report*, **LA-11292-MS**.

Chipera, S. J., and Bish, D. L. (1995) Multi-reflection RIR and intensity normalizations for quantitative analyses: Applications to feldspars and zeolites. *Powder Diffraction*, **10**, 47–55.

Chipera, S. J., Carey, J. W. and Bish, D. L. (1994) The nature of interlayer water in smectite. *Proceedings of the 31st Annual Meeting of the Clay Minerals Society*, Saskatoon, Saskatchewan, p. 53.

Chipera, S. J., Bish, D. L., and Carlos, B. A. (1995a) Equilibrium modeling of the formation of zeolites in fractures at Yucca Mountain, Nevada. In *Natural Zeolites '93: Occurrence, Properties, Use*, D. W. Ming and F. A. Mumpton, eds., 565–577.

Chipera, S. J., Vaniman, D. T., Carlos, B. A., and Bish, D. L. (1995b) Mineralogic variation in drill core UE-25 UZ#16, Yucca Mountain, Nevada. *Los Alamos National Laboratory Report*, **LA-12810-MS**, 39 pp.

Chung, F. H. (1974) Quantitative interpretation of X-ray diffraction patterns of mixtures. I. Matrix-flushing method for quantitative multicomponent analysis. *Journal of Applied Crystallography*, **7**, 519–525. NNA.890405.0179

Couture, R. A. (1985) Steam rapidly reduces the swelling capacity of bentonite. *Nature*, **318**, 50_52.

Czarnecki, J. B. (1985) Simulated effects of increased recharge on the ground-water flow system of Yucca Mountain and vicinity, Nevada-California. *U. S. Geol. Survey Water Resources Invest. Report*, **84-4344**.

Deer, W., Howie, R., and Zussman, J. (1963) *Rock-Forming Minerals*. Vols. 3 and 4. Longmans, London.

Domenico, P. A., and Schwartz, F. W. (1990) *Physical and Chemical Hydrogeology*. John Wiley & Sons, New York.

Duffy, C. J. (1983a) Hydrothermal stability studies. In *Research and Development Related to the Nevada Nuclear Waste Storage Investigations July 1-September 30, 1982*, W. R. Daniels, B. R. Erdal, and D. T. Vaniman, compilers, *Los Alamos National Laboratory Progress Report*, **LA-9577-PR.**

Duffy, C. J. (1983b) Permeability, porosity, and hydrothermal reactions. In *Research and Development Related to the Nevada Nuclear Waste Storage Investigations January 1–March 30, 1983*, K. Wolfsberg, D. T. Vaniman, and A. E. Ogard, compilers, *Los Alamos National Laboratory Progress Report*, **LA-9793-PR.**

Duffy, C. J. (1993). Preliminary conceptual model for mineral evolution in Yucca Mountain. *Los Alamos National Laboratory Report*, **LA-12708-MS**.

Ervin, E. M., Luckey, R. R., and Burkhardt, D. J. (1993) Summary of revised potentiometric-surface map for Yucca Mountain and vicinity, Nevada. In *High*

Level Radioactive Waste Management, American Nuclear Society and American Society of Civil Engineers, Proceedings of the 4th Annual International Conference, Las Vegas, Nevada, 1554–1558.

Fabryka-Martin, J., Dixon, P., Levy, S., Liu, B., Turin, J., and Wolfsberg, A. (1996) Systematic sampling for chlorine-36 in the Exploratory Studies Facility. Las Alamos National Laboratory YMSCP letter report.

Flint, A. L., Flint, L. E., and Hevesi, J. A. (1993) The influence of long term climate change on net infiltration at Yucca Mountain, Nevada. In *High Level Radioactive Waste Management*, American Nuclear Society and American Society of Civil Engineers, Proceedings of the 4th Annual International Conference, Las Vegas, Nevada, 152–159.

Glassley, W. E. (1995) Characterization of chemical and mineralogical changes in the post-emplacement environment. YMSCP Study Plan for SCP Section 8.3.4.2.4.1, R1, p. 69.

Gottardi, G., and Galli, E. (1985) *Natural Zeolites*. Springer-Verlag, Berlin, 409 pp.

Helgeson, H. C., Delany, J. M., Nesbitt, H. W., and Bird, D. K. (1978) Summary and critique of the thermodynamic properties of rock-forming minerals. *American Journal of Science*, **278-A**, 229 p.

Hemingway, B. S., and Robie, R. A. (1984) Thermodynamic properties of zeolites: low-temperature heat capacities and thermodynamic functions for phillipsite and clinoptilolite. Estimates of the thermochemical properties of zeolitic water at low temperature. *American Mineralogist*, **69**, 692_700.

Holland, T. J. B. (1989) Dependence of entropy on volume for silicate and oxide minerals: A review and a predictive model. *American Mineralogist*, **74**, 5_13.

JCPDS (1986) *Mineral Powder Diffraction File Data Book*. International Centre for Diffraction Data, Swarthmore, Pennsylvania.

Johnson, G. K., Flotow, H. E., O'Hare, P. A. G., and Wise, W. S. (1982) Thermodynamic studies of zeolites: Analcime and dehydrated analcime. *American Mineralogist*, **67**, 736–748.

Johnson, G. K., Flotow, H. E., O'Hare, P. A. G., and Wise, W. S. (1985) Thermodynamic studies of zeolites: Heulandite. *American Mineralogist*, **70**, 1065–1071.

Johnson, G. K., Tasker, I. R., Jurgens, R., and O'Hare, P. A. G. (1991) Thermodynamic studies of zeolites: Clinoptilolite. *Journal of Chemical Thermodynamics*, **23**, 475–484.

Johnson, G. K., Tasker, I. R., Flotow, H. E., O'Hare, P. A. G., and Wise, W. S. (1992) Thermodynamic studies of mordenite, dehydrated mordenite, and gibbsite. *American Mineralogist*, **77**, 85–93.

Klug, H. P., and Alexander, L. E. (1974) *X-ray Diffraction Procedures for Polycrystalline and Amorphous Materials*, John Wiley & Sons, Inc., New York.

Knauss, K. (1987) Zeolitization of glassy Topopah Spring tuff under hydrothermal conditions. Mat. Res. Soc. Symposium, v. 84, p. 737–745.

Knauss, K., and Peifer, D. (1986) Reaction of vitric Topopah Spring Tuff and J-13 ground water under hydrothermal conditions using Dickson-type, gold-bag rocking autoclaves. *Lawrence Livermore National Laboratory Report*, UCRL-53795.

Kranz, R. L., Bish, D. L., and Blacic, J. D. (1989) Hydration and dehydration of zeolitic tuff from Yucca Mountain, Nevada. *Geophysical Research Letters*, **16**, 1113–1116.

Lasaga, A. C. (1984) Chemical kinetics of water-rock interactions. *Journal of Geophysical Research*, **89**, 4009–4025.

Lasaga, A. C., Ganor, J., and MacInnis, I. N. (1994a). Progress report on the kinetic measurements of the reactions of the silicates at the Yucca Mountain potential repository site (August, 1994) Los Alamos National Laboratory.

Lasaga, A. C., Soler, J. M., Ganor, J., Burch, T. E., and Nagy, K. L. (1994b) Chemical weathering rate laws and global geochemical cycles. *Geochimica et Cosmochimica Acta*, **58**, 2361_2386.

Levy, S. S. (1984a) Studies of altered vitrophyre for the prediction of nuclear waste repository induced thermal alteration at Yucca Mountain, Nevada. In: *Scientific Basis for Nuclear Waste Management VII*, G. L. McVay, ed., Elsevier, New York, 959–966.

Levy, S. S. (1984b) Petrology of samples from drill holes USW H-3, H-4, and H-5, Yucca Mountain, Nevada. *Los Alamos National Laboratory Report*, **LA-9706-MS**, 77 pp.

Levy, S. S. (1991) Mineralogic alteration history and paleohydrology at Yucca Mountain, Nevada. In *High Level Radioactive Waste Management*, American Nuclear Society and American Society of Civil Engineers, Proceedings of the 4th Annual International Conference, Las Vegas, Nevada, 477–485.

Levy, S. S. (1992) Natural gels in the Yucca Mountain area, Nevada, USA. *Applied Clay Science*, **7**, 79_85.

Levy, S. S., and O'Neil, J. R. (1989) Moderate-temperature zeolitic alteration in a cooling pyroclastic deposit. *Chemical Geology*, **76**, 321–326.

Lipman, P. W. (1971) Iron-titanium oxide phenocrysts in compositionally zoned ash-flow sheets from southern Nevada. *Journal of Geology*, **79**, 438–456.

MacInnis, I. N., Wilkin, R. T., Mercy, M. A., Barnes, H. L., and Lasaga, A. C. (1995) A rate law for clinoptilolite dissolution/precipitation at 50–125°C in basic solutions. YMSCP Milestone No. LA3445. Los Alamos National Laboratory, LA-EES-1-TIP-95-017.

Marshall, B. D., Peterman, Z. E., and Stuckless, J. S. (1993) Strontium isotopic evidence for a higher water table at Yucca Mountain. In *High Level Radioactive Waste Management*, American Nuclear Society and American Society of Civil Engineers, Proceedings of the 4th Annual International Conference, Las Vegas, Nevada, 1948_1952.

Mumpton, F. A. (1960) Clinoptilolite redefined. *American Mineralogist*, **45**, 351–369.

Murphy, W. M., Pabalan, R. T., Prikryl, J. D., and Goulet, C. J. (1996) Reaction kinetics and thermodynamics of aqueous dissolution and growth of analcime and Na-clinoptilolite at 25°C. *American Journal of Science*, **296**, 128–186.

Nagy, K. L., Blum, A. E., and Lasaga, A. C. (1991) Dissolution and precipitation kinetics of kaolinite at 80 C and pH 3: The dependence on solution saturation state. *American Journal of Science*, **291**, 649–686.

Pabalan, R. T. (1994) Thermodynamics of ion exchange between clinoptilolite and aqueous solutions of Na^+/K^+ and Na^+/Ca^{2+}. *Geochimica et Cosmochimica Acta*, **58**, 4573–4590.

Pabalan, R. T., and Bertetti, F. P. (1994) Thermodynamics of ion exchange between Na^{+}/Sr^{2+} solutions and the zeolite mineral clinoptilolite. In *Scientific Basis for Nuclear Waste Management XVII,* Barkatt, A., and Van Konynenburg, R. A., eds., Materials Research Society Symposium Proceedings 333, 731–738.

Paces, J. (1996) "Submission of Milestone: 3GQH455, Due February 29, 1996," Memorandum to R. W. Craig, Chief, Yucca Mountain Project Branch, WRD, Las Vegas, NV, February 23, 1996.

Peacor, D. R. (1973) High-temperature single-crystal study of the cristobalite inversion. *Zeitschrift für Kristallographie,* **138**, 274–298.

Petrovic, I., and Navrotsky, A. (1995) Thermochemistry of Na-faujasites with varying Si/Al ratios (submitted to Microporous Materials).

Renders, P. J. N., Gammons, C. H., and Barnes, H. L. (1995) Precipitation and dissolution rate constants for cristobalite from 150 to 300°C. *Geochimica et Cosmochimica Acta,* **59**, 77–85.

Riehle, J. R. (1973) Calculated compaction profiles of rhyolitic ash-flow tuffs. *Geological Society of America Bulletin, 84,* 2193–2216.

Rimstidt, J. D., and Barnes, H. L. (1980) The kinetics of silica-water reactions. *Geochimica et Cosmochimica Acta,* **44**, 1683–1699.

Robie, R. A., Hemingway, B. S., and Fisher, J. R. (1979) Thermodynamic Properties of Minerals and Related Substances at 298.15 K and 1 Bar (10^5 Pascals) Pressure and at Higher Temperature. *U. S. Geological Survey Bulletin,* **1452**.

Rosenbaum, J. G. (1986) Paleomagnetic directional dispersion produced by plastic deformation in a thick miocene welded tuff, southern Nevada: Implications for welding temperatures. *Journal of Geophysical Research,* **91**, 12,817–12,834.

Sheppard, R. A., Gude, A. J., 3rd., and Fitzpatrick, J. J. (1988) Distribution, characterization, and genesis of mordenite in Miocene silicic tuffs at Yucca Mountain, Nye County, Nevada. *U. S. Geological Survey Bulletin,* **1777**, 22 pp.

Sherry, H. S. (1969) The ion-exchange properties of zeolites. In *Ion Exchange,* J. A. Marinsky , ed., Marcel Dekker, Inc., New York, 89–133.

Smith, D. K., Nichols, M. C., and Zolensky, M. E. (1983) POWD10, A FORTRAN IV Program for Calculating X-Ray Powder Diffraction PatternsÑVersion 10. Pennsylvania State University, College of Earth and Mineral Sciences report. NNA.890602.0030

Smyth, J. R., and Bish, D. L. (1988) *Crystal Structures and Cation Sites of the Rock-Forming Minerals.* Allen & Unwin, London, 332 pp.

Vaniman, D. T., and Bish, D. L. (1995) The importance of zeolites in the potential high-level radioactive waste repository at Yucca Mountain, Nevada. In *Natural Zeolites '93: Occurrence, Properties, Use,* D. W. Ming and F. A. Mumpton, eds., 533–546.

Vaniman, D., Bish, D., and Chipera, S. (1993) Dehydration and rehydration of a tuff vitrophyre. *Journal of Geophysical Research,* **98**, 22309–22320.

Wise, W. S. (1984) Thermodynamic studies of zeolites. Analcime solid solutions. In *Proceedings of the Sixth International Zeolite Conference,* D. Olson , and A. Bisio, eds., Butterworths, Surrey, UK, 616–622.

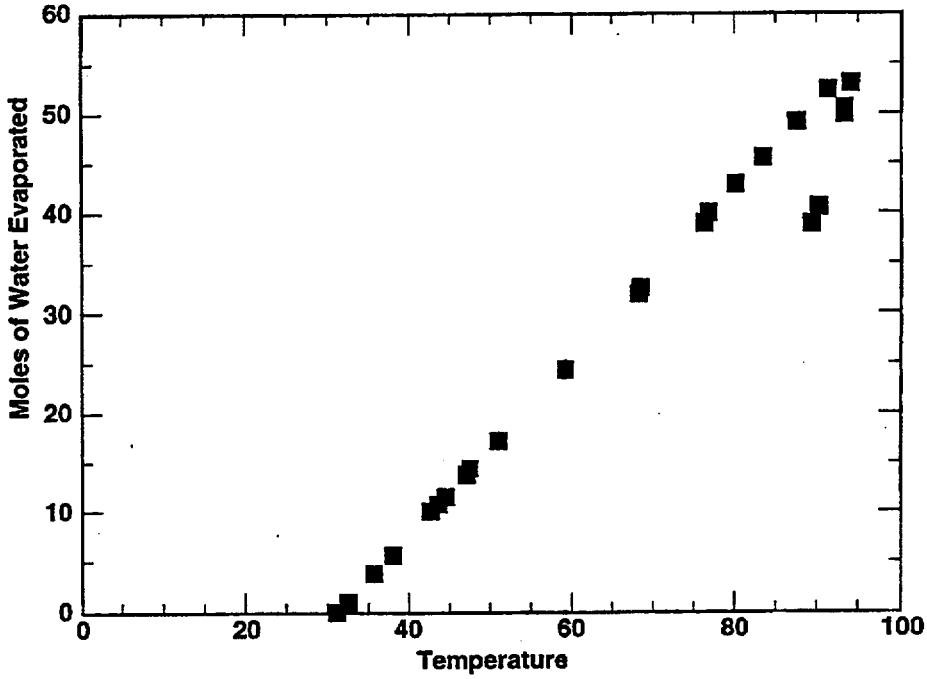

Figure 3.4-1. The trend of number of moles of water evaporated, as a function of temperature. Two different trends at the high temperature end of the sequence were used in the calculations to determine to what extent such differences would influence the chemical and mineralogical evolution of the system. In all cases, the results derived from the two trends differed by less than 1% (relative).

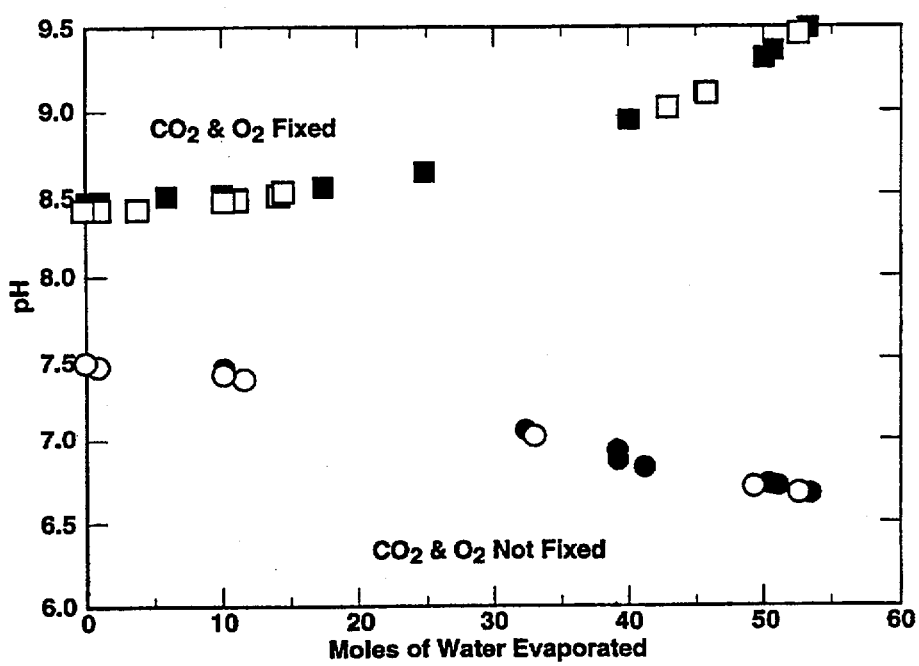

Figure 3.4-2. pH as a function of moles of water evaporated. In this, and in all subsequent figures, square symbols represent results obtained from simulations in which CO_2 and O_2 fugacities were fixed at atmospheric values throughout the runs, circles represent results obtained from simulations in which CO_2 and O_2 fugacities were not fixed, filled symbols indicate runs in which precipitation of solids was not restricted, and open symbols indicate runs in which quartz, tridymite, and talc were suppressed.

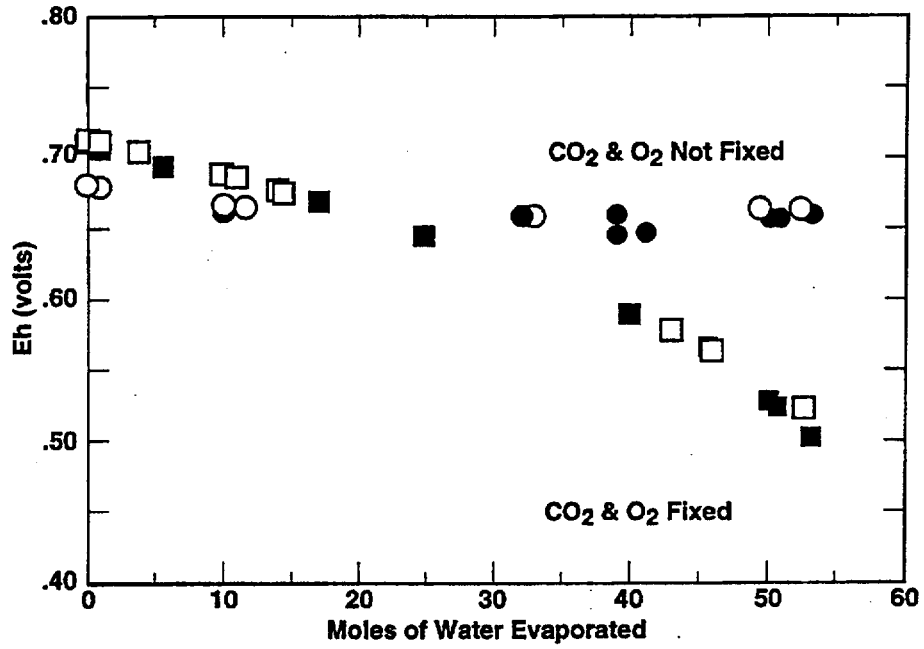

Figure 3.4-3. Eh, in volts, as a function of moles of water evaporated. Symbols as described in caption to Figure 3.4-2.

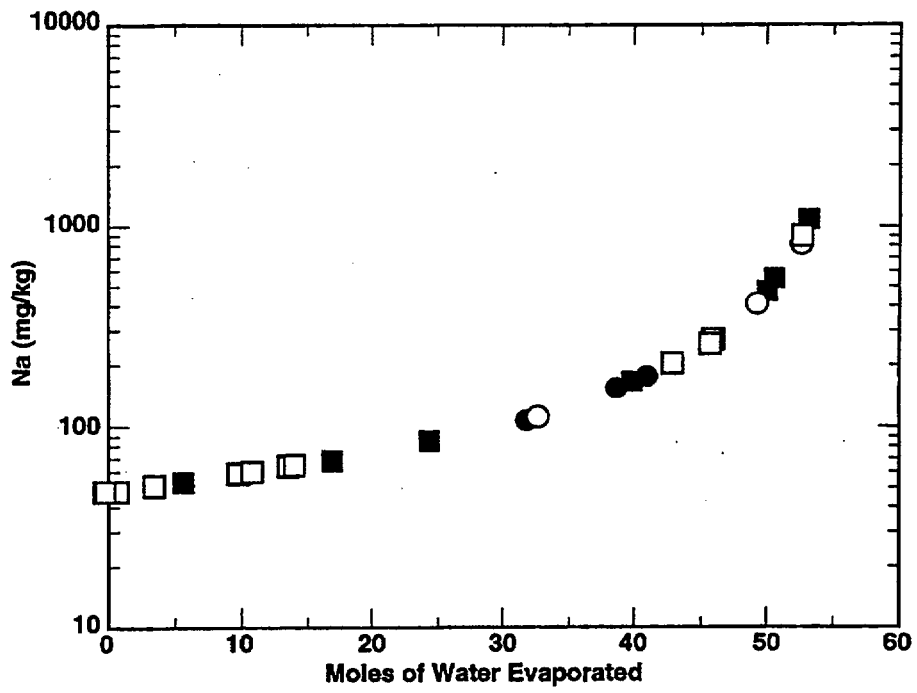

Figure 3.4-4. Total Na in solution, in mg/kg, as a function of moles of water evaporated. Symbols as described in caption to Fig. 3.4-2.

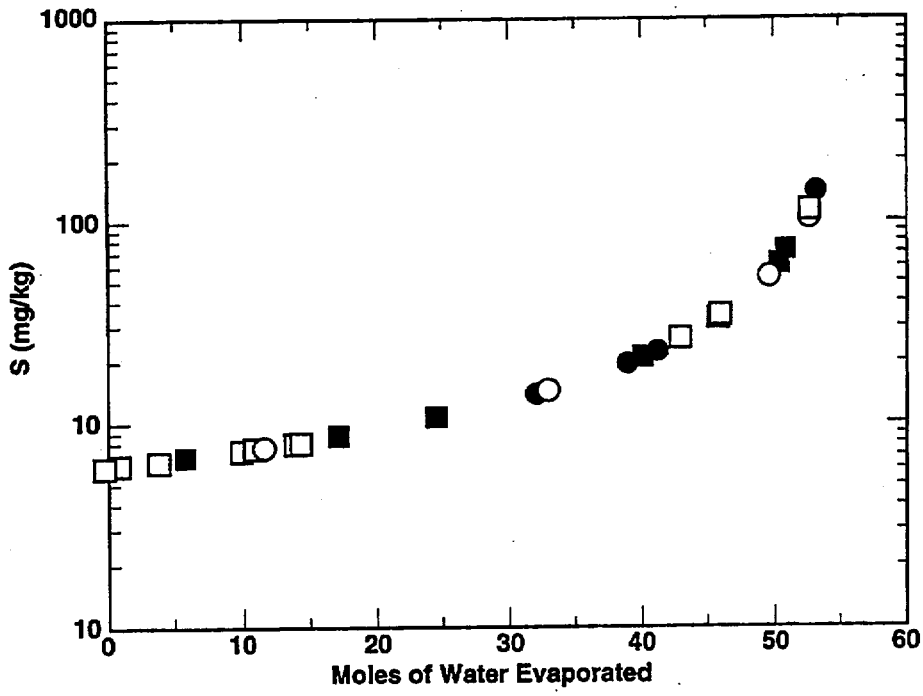

Figure 3.4-5. Total S in solution, in mg/kg, as a function of moles of water evaporated. Symbols as described in caption to Fig. 3.4-2.

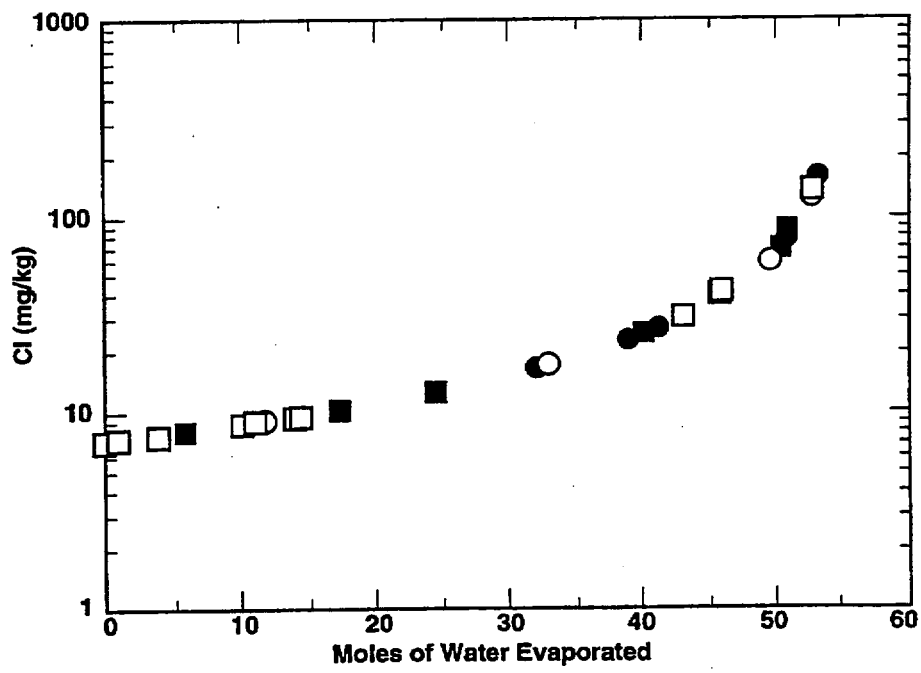

Figure 3.4-6. Total Cl in solution, in mg/kg, as a function of moles of water evaporated. Symbols as described in caption to Fig. 3.4-2.

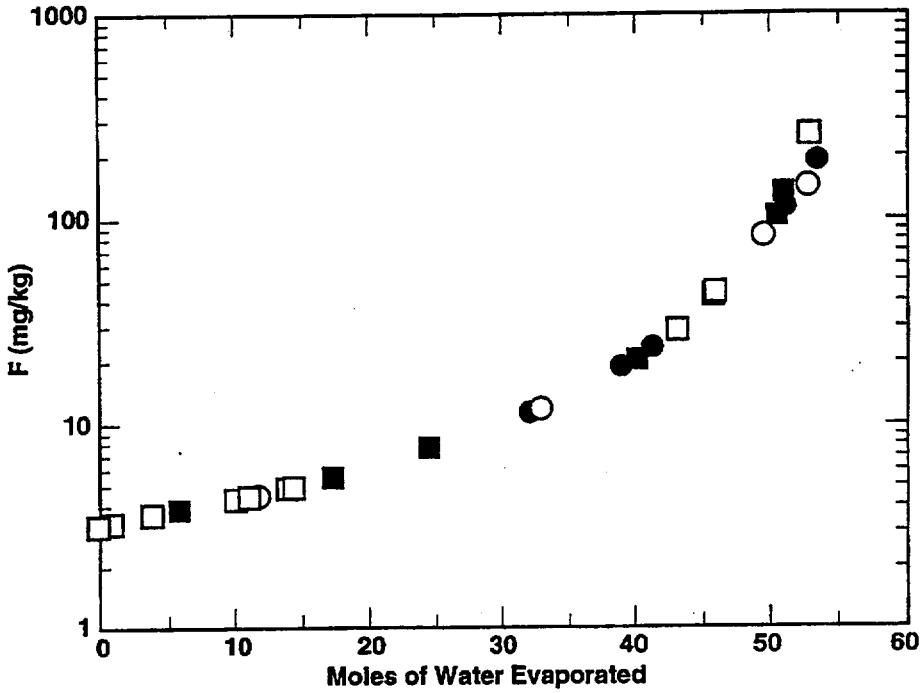

Figure 3.4-7. Total F in solution, in mg/kg, as a function of moles of water evaporated. Symbols as described in caption to Fig. 3.4-2.

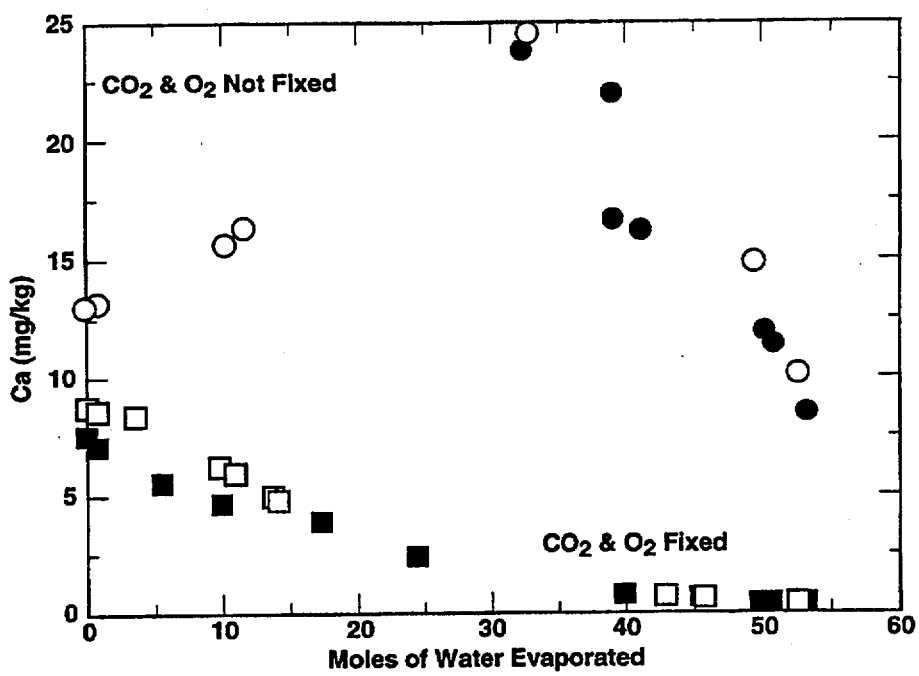

Figure 3.4-8. Total Ca in solution, in mg/kg, as a function of moles of water evaporated. Symbols as described in caption to Fig. 3.4-2. Note that the peak concentration for the uncontrolled CO_2 and O_2 case corresponds to calcite saturation (compare with Fig. 3.4-11).

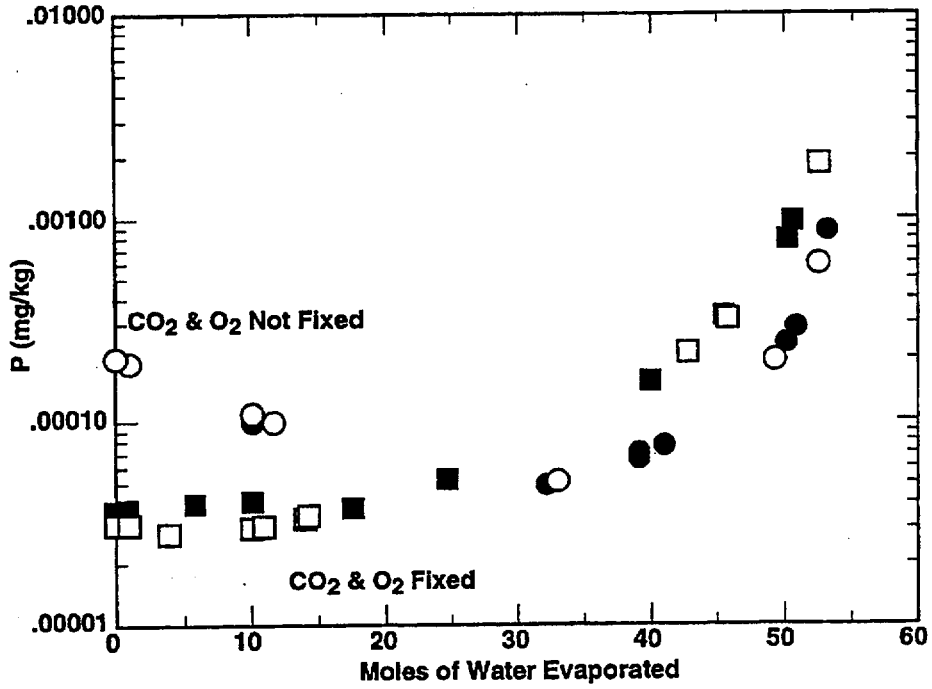

Figure 3.4-9. Total P in solution, in mg/kg, as a function of moles of water evaporated. Symbols as described in caption to Fig. 3.4-2.

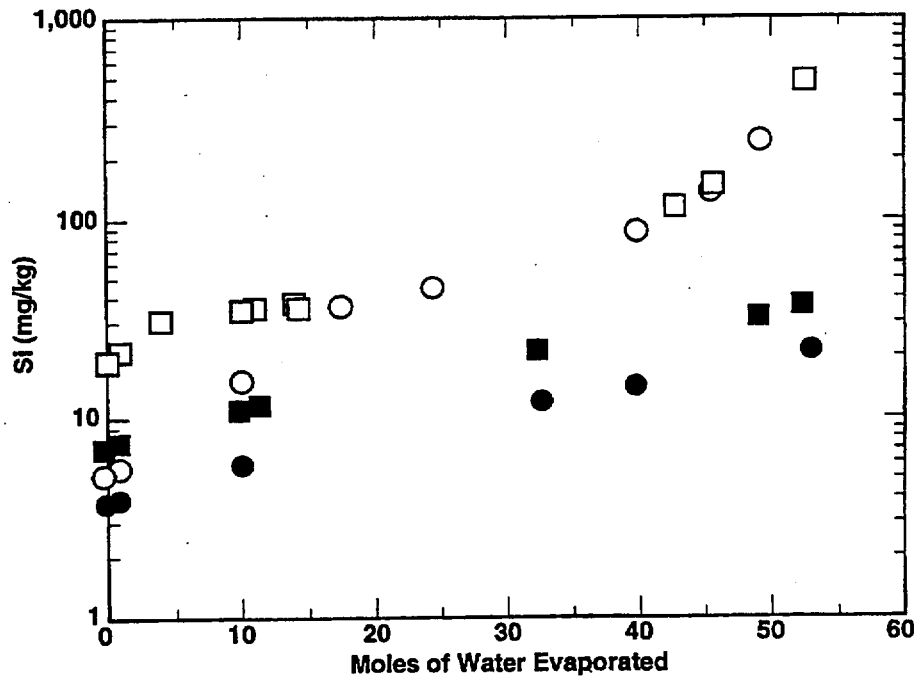

Figure 3.4-10. Total Si in solution, in mg/kg, as a function of moles of water evaporated. Symbols as described in caption to Fig.3.4-2.

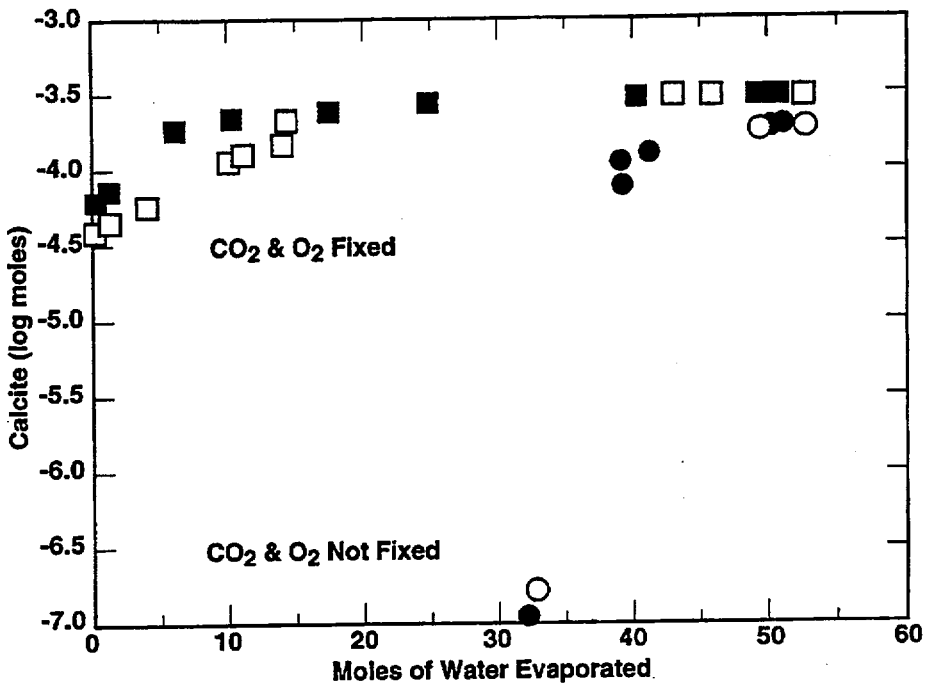

Figure 3.4-11. Log of the number of moles of calcite precipitated, as a function of moles of water evaported. Symbols as described in caption to Fig. 3.4-2.

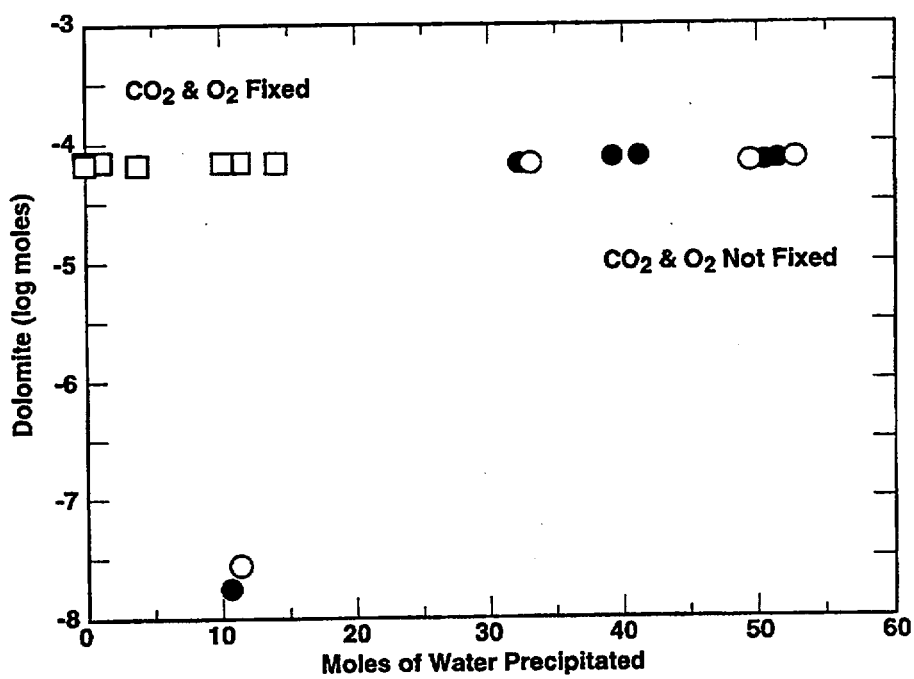

Figure 3.4-12. Log of the number of moles of dolomite precipitated, as a function of moles of water evaported. Symbols as described in caption to Fig.3.4-2.

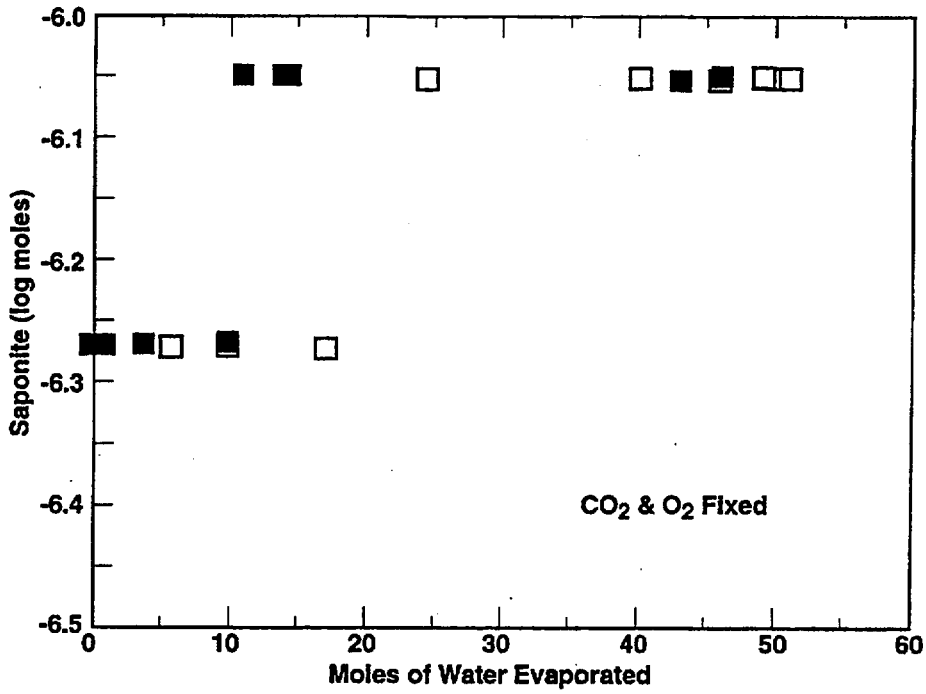

Figure 3.4-13. Log of the number of moles of saponite precipitated, as a function of moles of water evaported. Symbols as described in caption to Fig. 3.4-2.

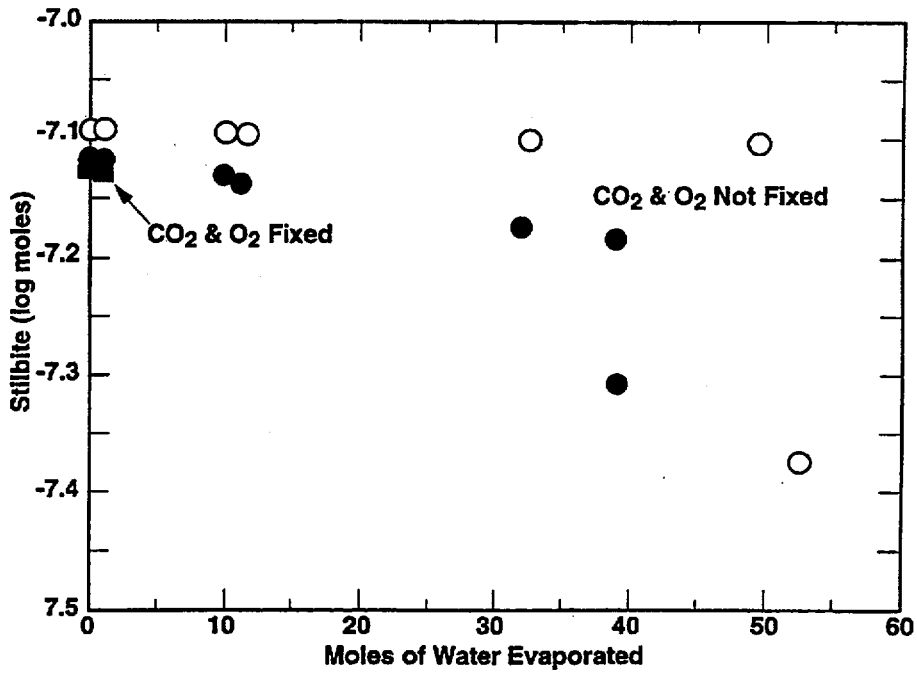

Figure 3.4-14. Log of the number of moles of stilbite precipitated, as a function of moles of water evaported. Symbols as described in caption to Fig. 3.4-2.

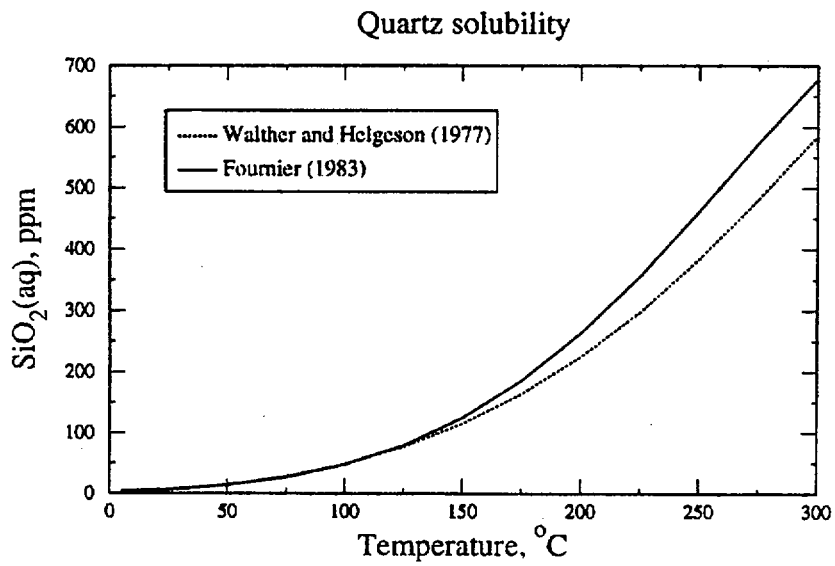

Figure 3.4-15. SiO_2(aq) concentrations in equilibrium with quartz using thermodynamic data from Walther and Helgeson (1977) and Fournier (1983).

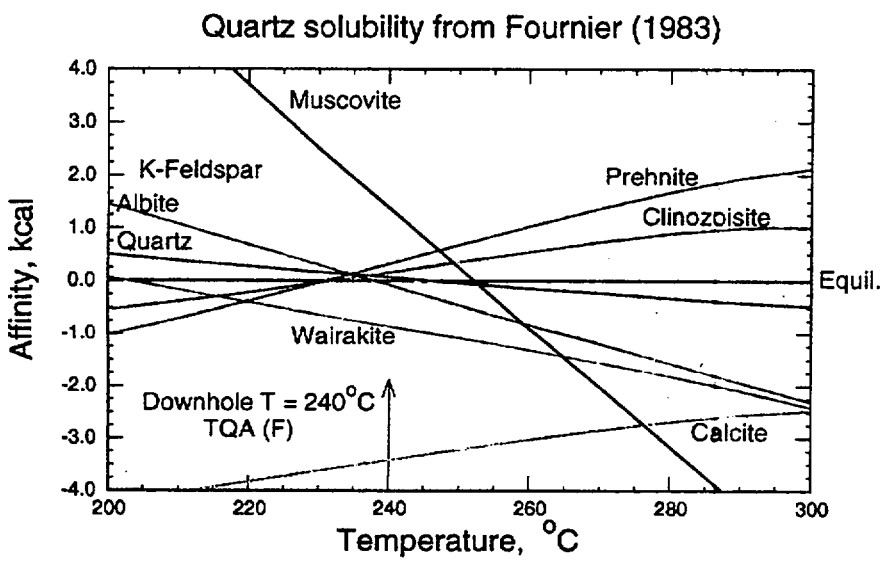

Figure 3.4-16. Affinity vs. temperature diagram for well WK-81 using quartz solubility from Fournier (1983).

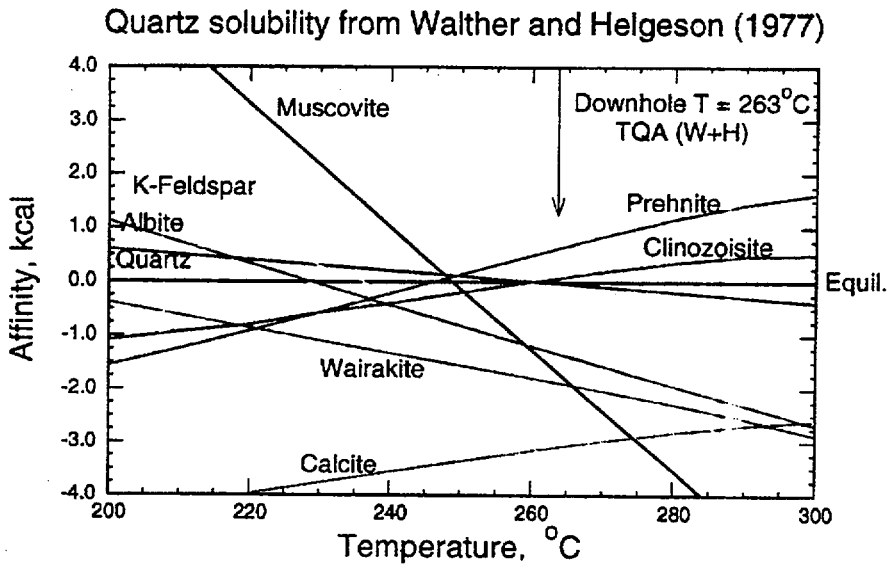

Figure 3.4-17. Affinity vs. temperature diagram for well WK-81 using quartz solubility from Walther and Helgeson (1977).

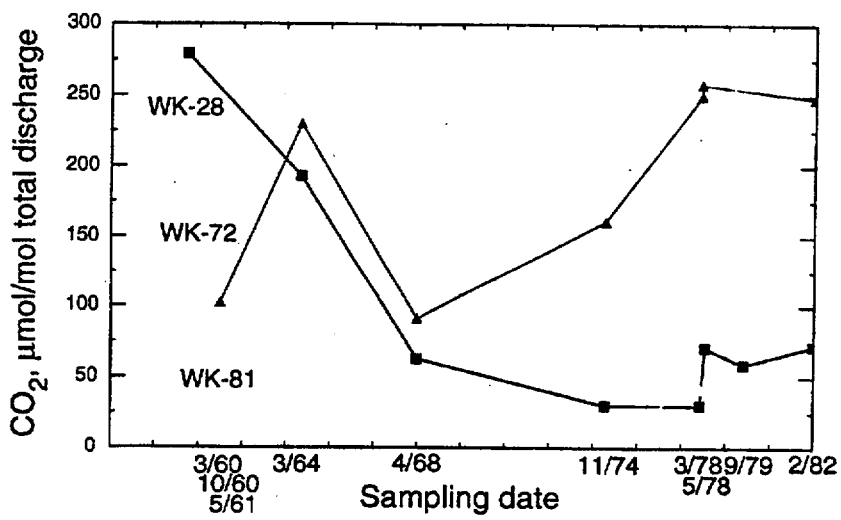

Figure 3.4-18. CO_2 concentrations (in µmol/mol water) measured in Wairakei wells WK-28, 72 and 81 as a function of time.

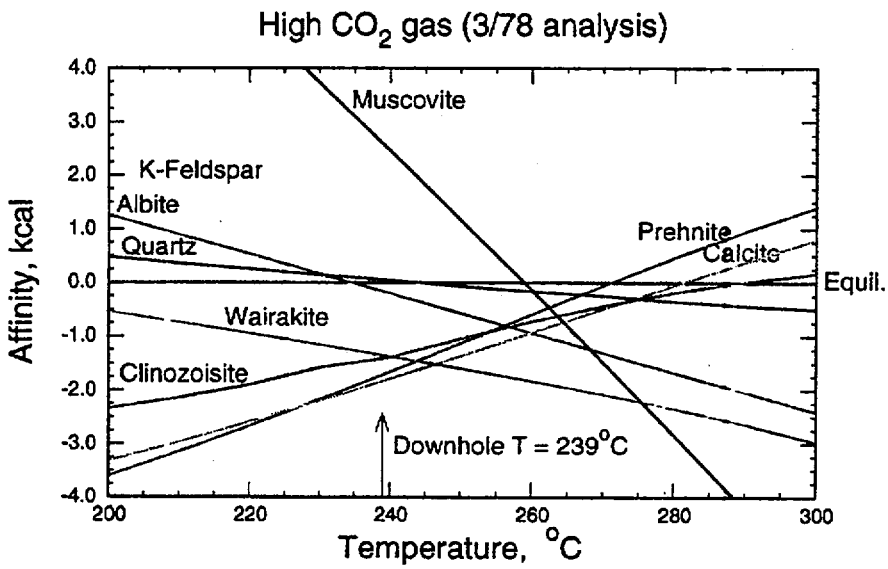

Figure 3.4-19. Affinity vs. temperature diagram for well WK-72 using 3/78 gas analysis with 258 mmol CO_2/mol TD (see text). Quartz data from Fournier (1983).

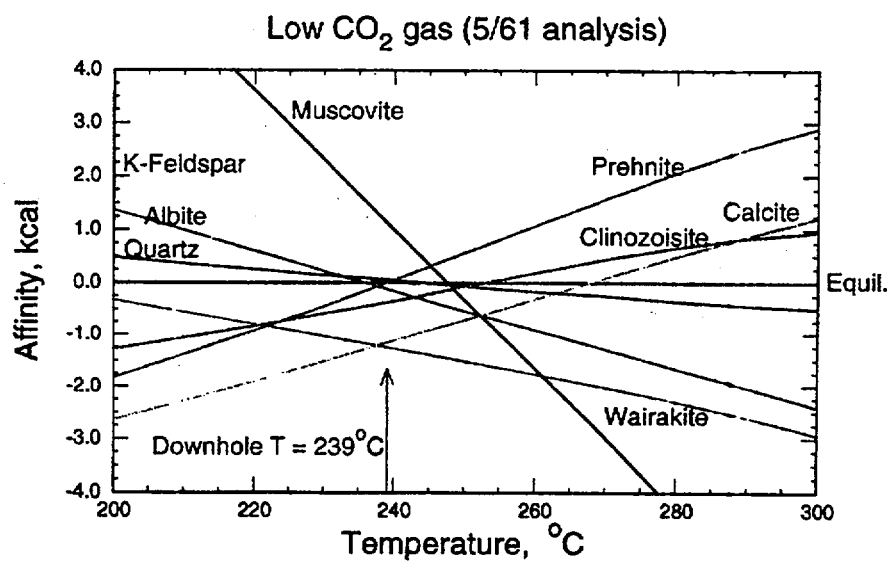

Figure 3.4-20. Affinity vs. temperature diagram for well WK-72 using 5/61 gas analysis with 102 mmol CO_2/mol TD (see text). Quartz data from Fournier (1983).

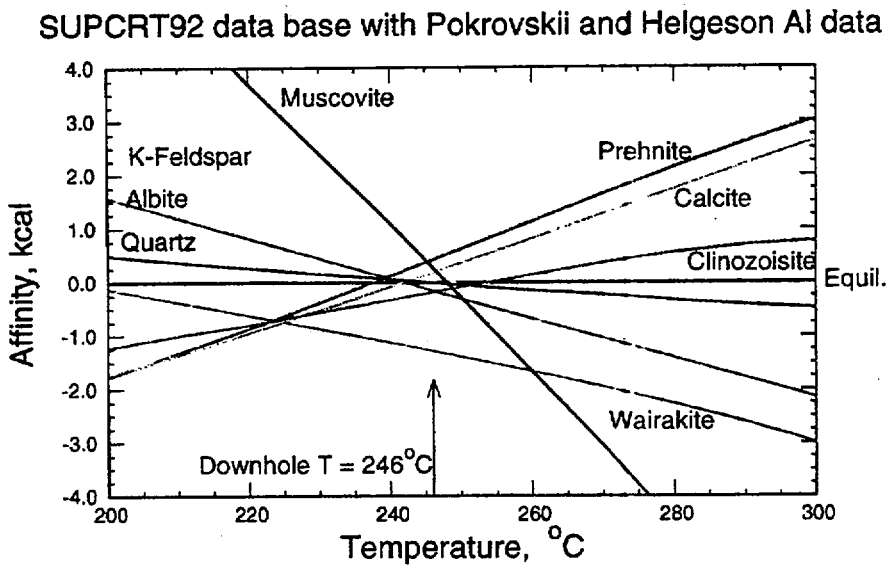

Figure 3.4-21. Affinity vs. temperature diagram for well WK-28 using thermodynamic data for Al aqueous species from Pokrovskii and Helgeson (1995). Quartz data from Fournier (1983).

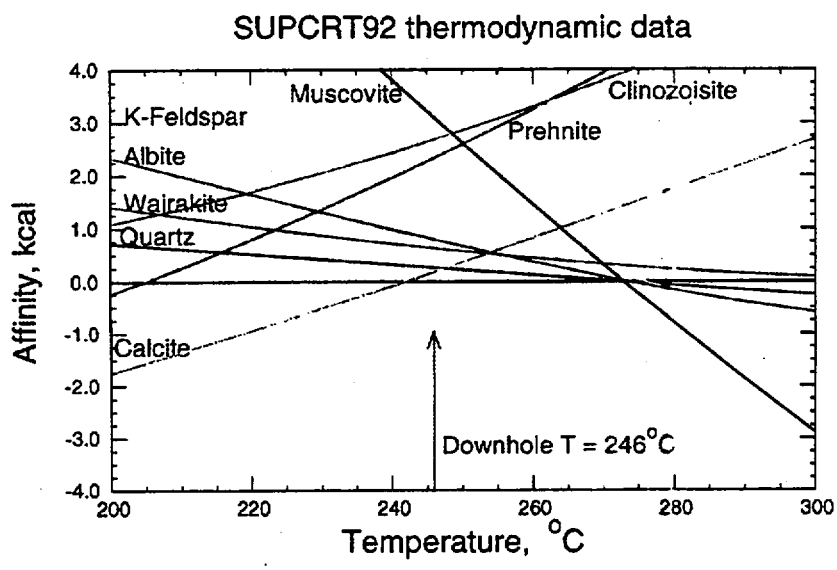

Figure 3.4-22. Affinity vs. temperature diagram for well WK-28 using thermodynamic data for Al aqueous species from the SUPCRT92 version of the GEMBOCHS data base. Quartz data from Fournier (1983).

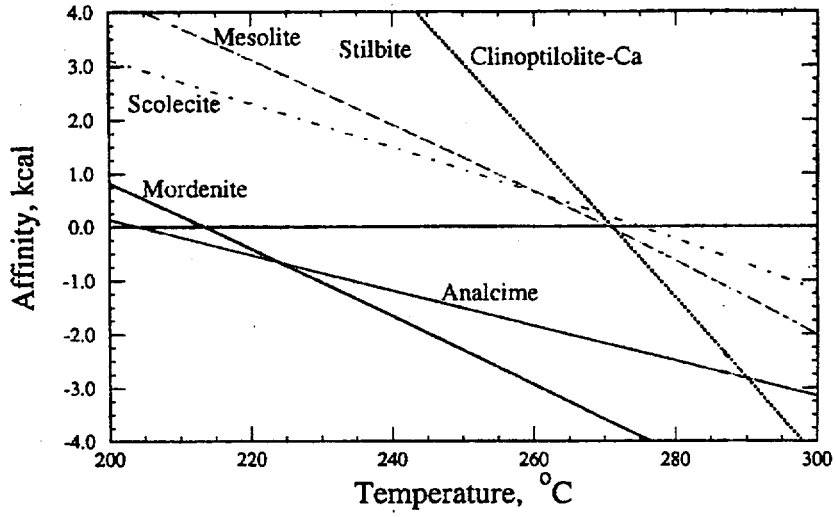

Figure 3.4-23. Zeolite affinities vs. temperature diagram for well WK-28 using thermodynamic data for Al aqueous species from Pokrovskii and Helgeson (1995). See Figure 7 for stabilities of additional minerals. Clinoptilolite-Ca refers to the Ca end-member of a clinoptilolite solid solution. Quartz data from Fournier (1983).

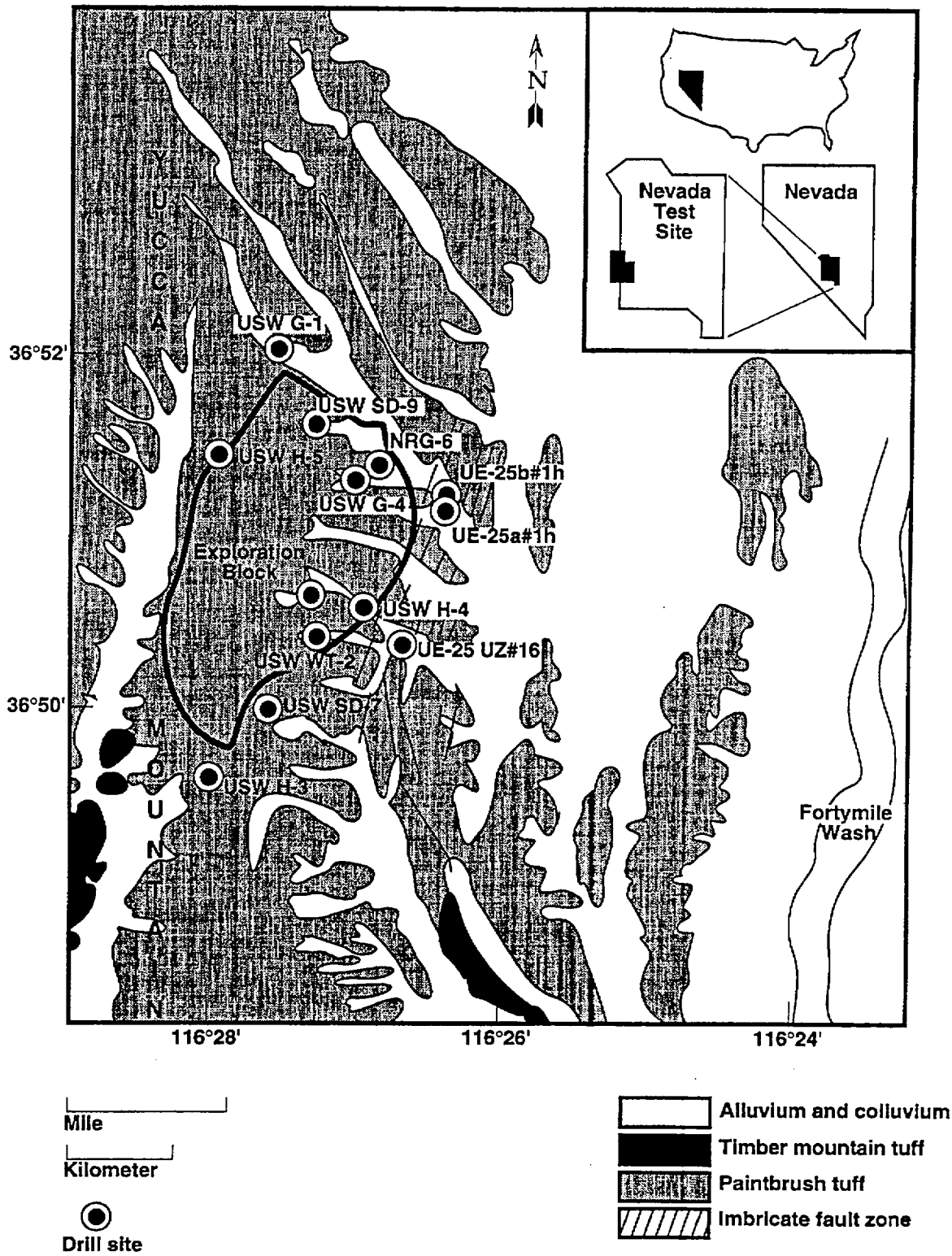

Figure 3.4-24. Map of Yucca Mountain, Nevada, showing locations of drill holes within or near the exploration block where mineralogical data have been collected mentioned in the appendices.

Alteration of Vitrophyre Glass

	Moles cation/cm^3			
	Glass	Smectite	Heul-clinopt.	Cristobalite
Si	0.029	0.014	0.024	0.038
Al	0.006	0.008	0.006	0

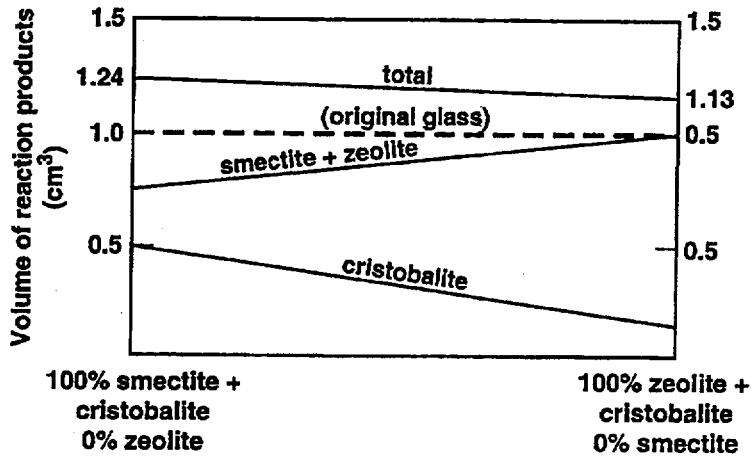

Figure 3.4-25. Graphic representation of reaction (1), balanced for all possible combinations of smectite and clinoptilolite-heulandite.

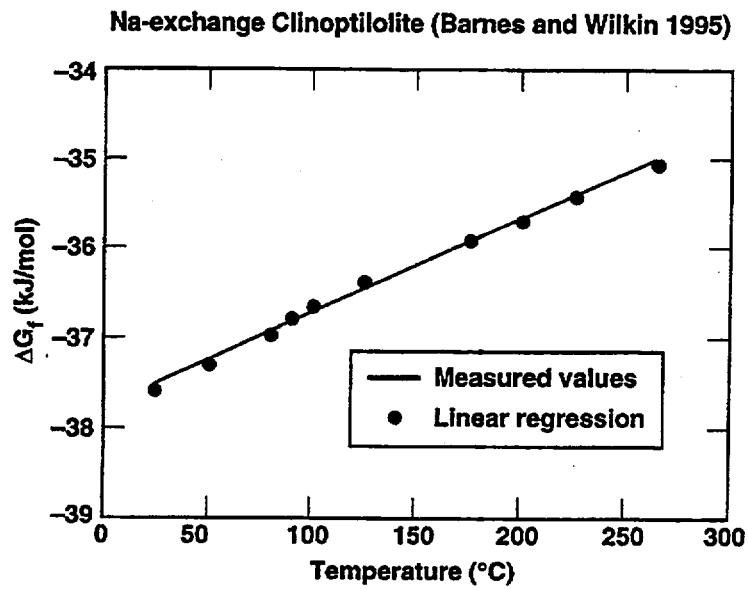

Figure 3.4-26. The Gibbs free energy of formation of Na-exchanged clinoptilolite derived from solubility measurements (Barnes and Wilkin, 1995). The solid line is a linear regression of the data from 50 to 265°C .

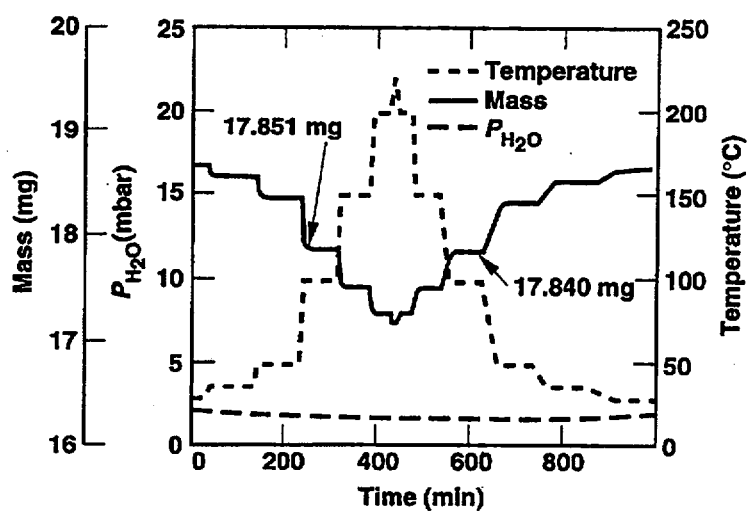

Figure 3.4-27. Results of a single thermogravimetric experiment on Ca-clinoptilolite conducted over a series of isothermal stages from 25 to 220 °C at an approximately constant water-vapor pressure of 2 mbar (Carey and Bish 1996a). Two mass measurements at 100°C are indicated to illustrate reversible hydration and dehydration.

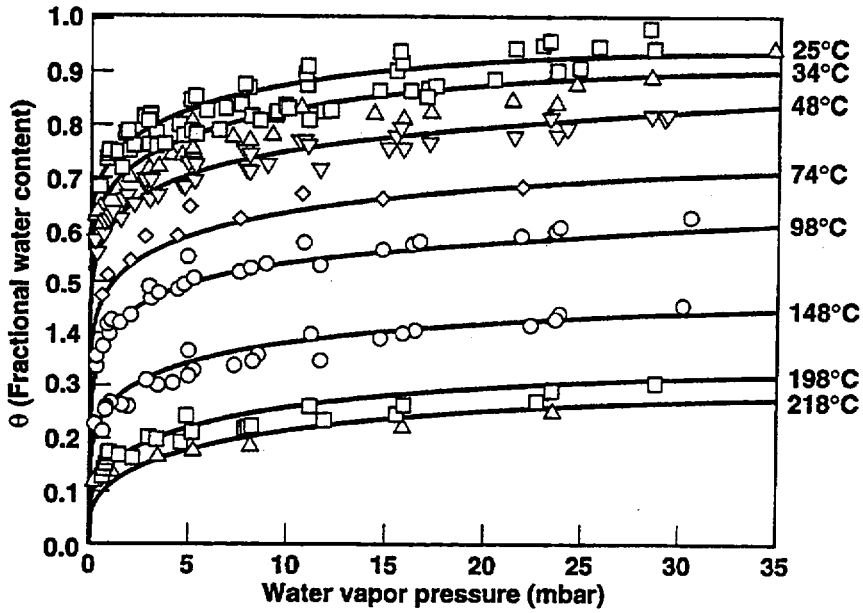

Figure 3.4-28. Equilibrium H_2O content of Na-clinoptilolite determined by thermogravimetry between 25 and 218 °C (Carey and Bish 1996a). The fractional water content, θ, is the observed H_2O content divided by the maximum H_2O content. The calculated lines were derived by a single linear regression of all the data.

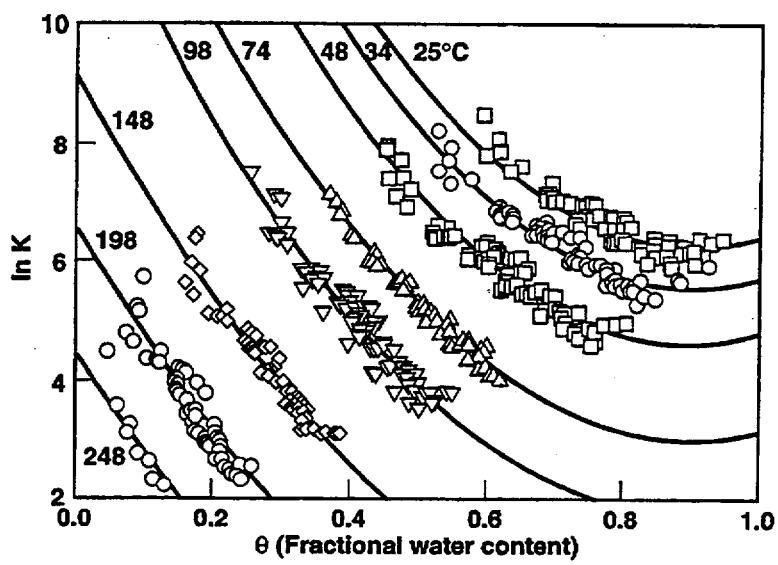

Figure 3.4-29. Comparison of the experimental data for K-clinoptilolite (symbols) with the calculated fit (solid lines) for water content versus equilibrium constant at several temperatures (Carey and Bish 1996a). The numbers labeling the curves are the temperature (°C) of the experiment. lnK is defined as ln(θ/(1-θ)/P), and θ is the ratio of the observed water content to the maximum water content at 25°C.

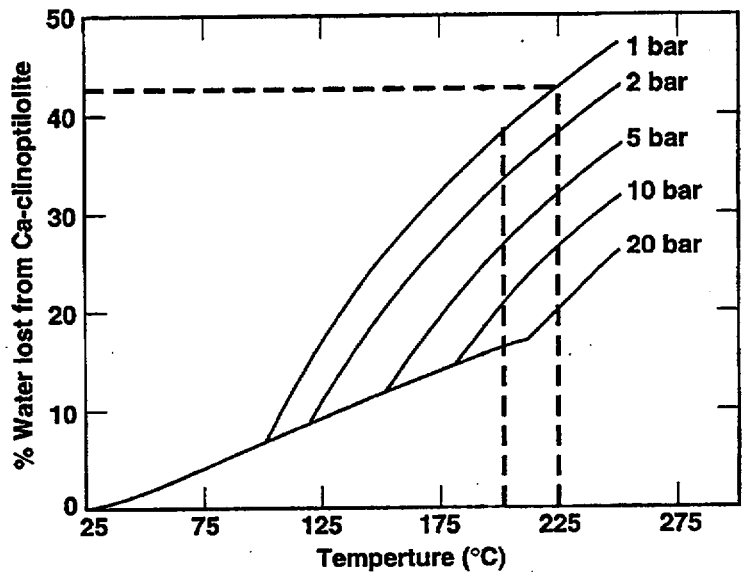

Figure 3.4-30. Calculated dehydration evolution of Ca-clinoptilolite under conditions of rising temperature and differing maximum pressures. Dehydration occurs along the boiling curve until the maximum pressure is reached (Carey and Bish 1996a).

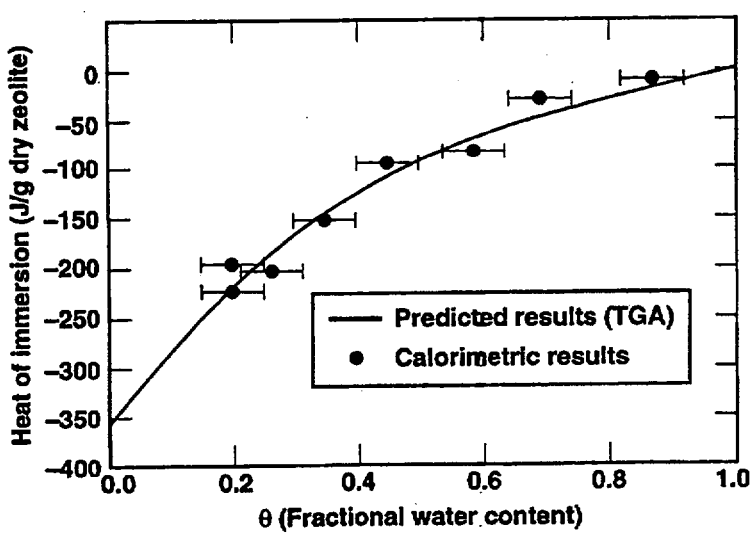

Figure 3.4-31. Calorimetric measurements of the integral heat of immersion of Ca-clinoptilolite (Carey and Bish 1996b) and calculated heats of immersion (TGA) from the study of Carey and Bish (1996a).

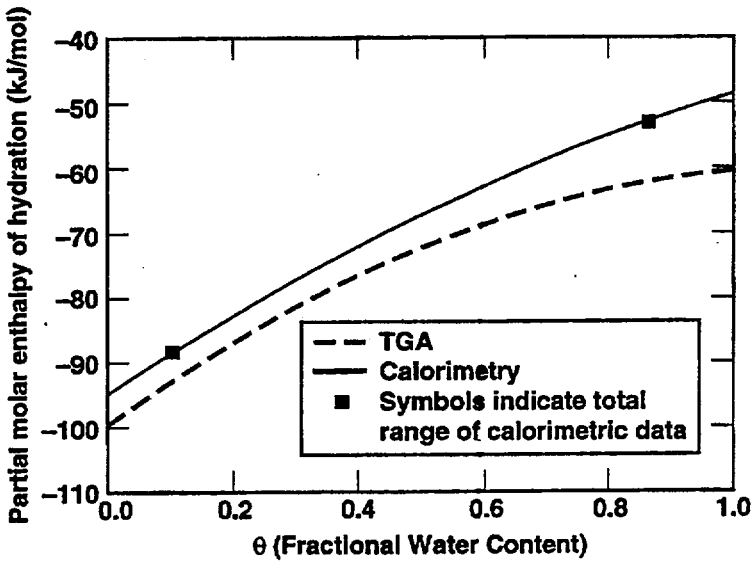

Figure 3.4-32. Partial molar enthalpy of hydration of Na-clinoptilolite derived from linear regression of the immersion calorimetry data (Carey and Bish 1996b) compared to the thermogravimetric results (TGA) of Carey and Bish (1996a).

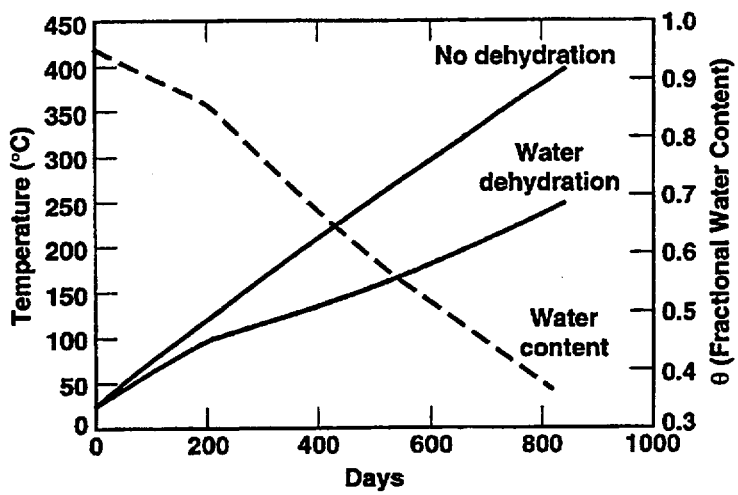

Figure 3.4-33. Calculated thermal and hydrologic evolution of a 1 m^3 block of K-clinoptilolite with 10% porosity, insulated boundaries, maximum water-vapor pressure of 1 bar, and receiving 14 watts of thermal energy. The two solid lines show the temperature of a block with K-clinoptilolite that dehydrates and one which does not dehydrate. The dotted line shows the water content of the clinoptilolite in the dehydrating block (Carey and Bish 1996a).

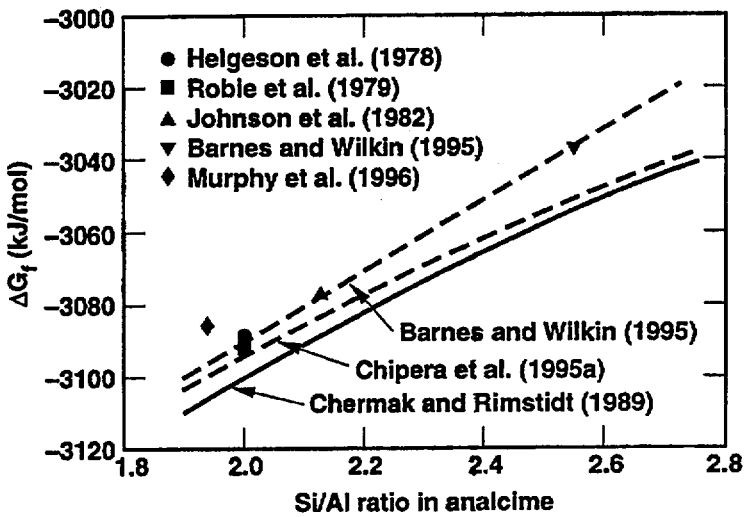

Figure 3.4-34. The Gibbs free energy of formation of analcime of differing Si/Al ratio determined by calorimetry, solubility measurements, phase equilibria analysis, and by estimation methods.

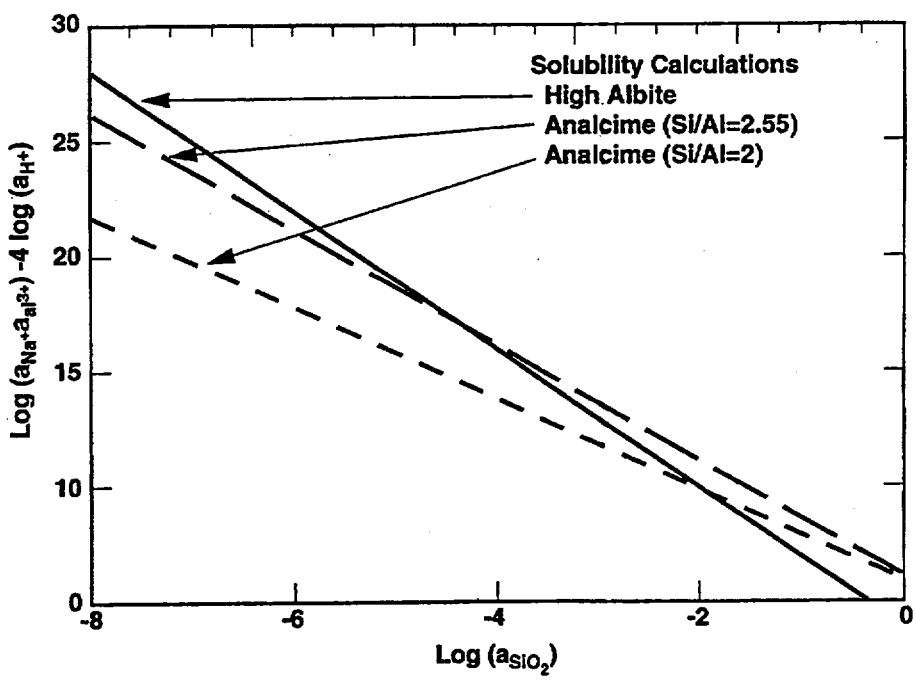

Figure 3.4-35. Solubility of stoichiometric and siliceous analcime (Barnes and Wilkin 1995) compared to the solubility of high albite (EQ3 Com data base).

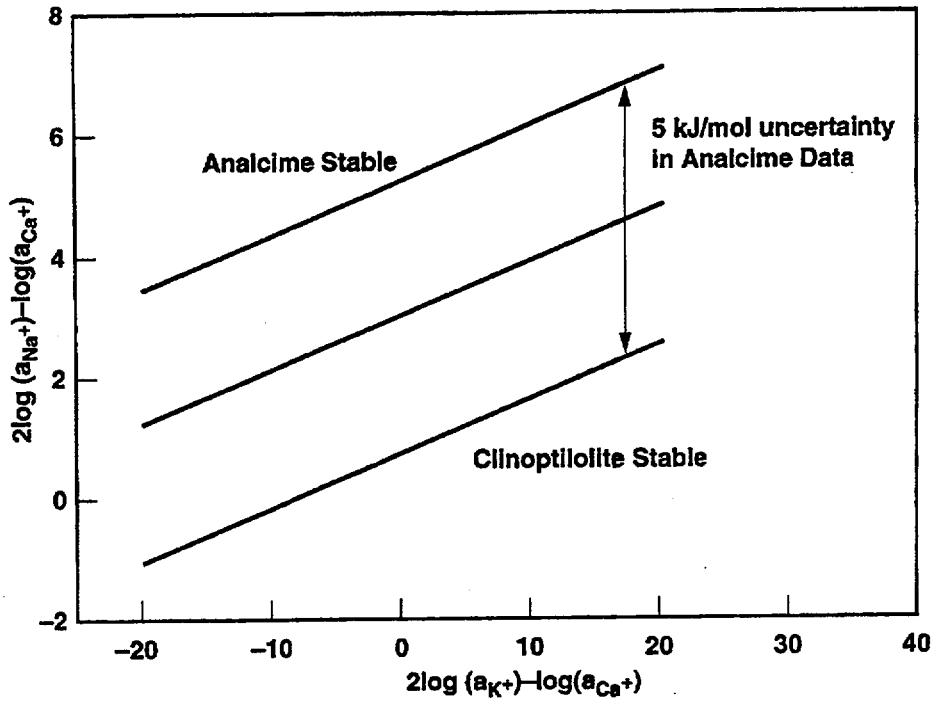

Figure 3.4-36. Reaction of clinoptilolite and analcime, balanced on aluminum, and plotted at cristobalite saturation. The reaction corresponds to Equation 12 of the text and uses the thermodynamic properties of analcime and clinoptilolite shown in Table 3.4-15.

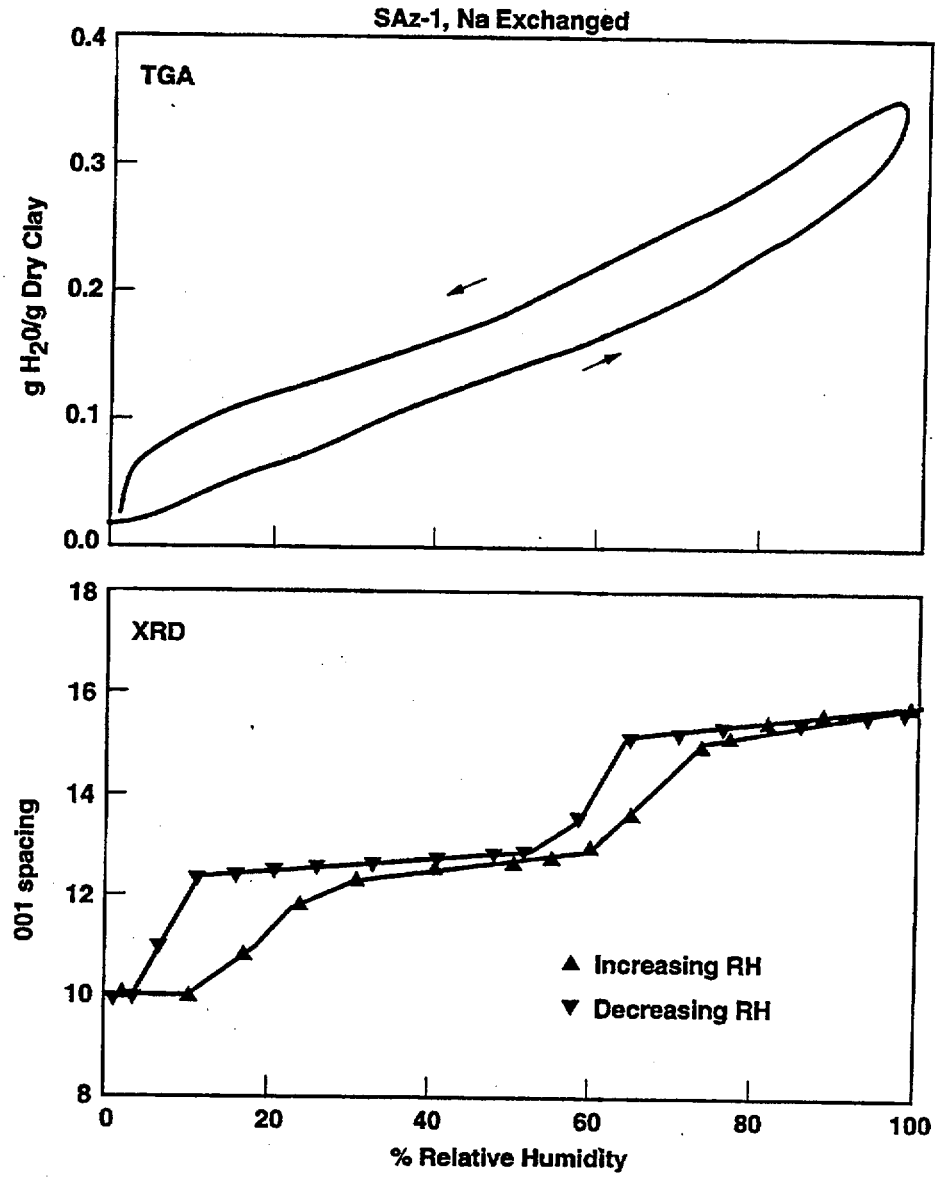

Figure 3.4-37. Hysteresis in Na-exchanged smectite as a function of relative humidity at 25°C. The H_2O contents were determined by thermogravimetry and the 001 d-spacings were determined by X-ray diffraction.

Table 3.4-1. Major constituents of discharge from Wairakei wells WK-28 (sampled on 3/60), WK-72 (sampled on 4/61) and WK81 (sampled on 10/74) (in mg/kg) (from Reyes, Giggenbach and Christenson, 1993).

Component	WK-28 analyzed	WK-28 corrected*	WK-72 analyzed	WK-72 corrected*	WK-81 analyzed	WK-81 corrected*
Na	1260	898	1295	942	1256	917
K	200	142	215	157	182	133
Ca	16	11.4	18	13	22	16
Mg	0.035	0.025	0.014	0.01	0.0035	0.0026
Fe *	NA	0.6e-6	NA	0.38e-3	NA	0.19e-2
Al **	NA	0.27	NA	0.26	0.37	0.27
Rb	NA	NA	NA	NA	2.52	1.8
Li	14	10	12.9	9.4	11.8	8.6
Cs	NA	NA	NA	NA	2.4	1.8
B	28.2	20	NA	NA	25.3	19
Cl	2213	1530	2241	1636	2083	1587
HCO_3	48	979	NA	345	NA	41
SO_4	34	24	34***	20	34	25
H_2S****	NA	15	NA	9	NA	4
SiO_2	660	470	600	438	612	447
pH	8.2(20°C)	6.3 (246°C)	8.3 (20°C)	6.2 (239°C)	7.4 (20°C)	6.1 (240°C)
TQA*****		246°C		239°C		240°C

*** Corrected for steam and gas loss; calculated assuming equilibrium with pyrite at TQA; Cl adjusted to obtain electrical neutrality**
**** From analysis of other samples from same wells3**
***** From average of other samples from WK-72**
****** Analyzed value for all samples assumed to equal 0.3 mg/kg, typical of WK-28 waters.**
******* Downhole temperature calculated from the adiabatic quartz geothermometer (TQA) using quartz solubility data from Fournier (1983)4**

3 The previous study by Bruton, Glassley and Bourcier (1994) assumed that Al concentration was controlled by equilibrium with K-feldspar.

4 Implications of using data from Fournier (1983) vs. Walther and Helgeson (1977) for quartz solubility are discussed in the text.

Table 3.4-2. Major chemical components of vapors discharged from Wairakei wells WK-28, 72 and 81 sampled on 3/60, 5/61 and 11/74, respectively (in μmol/mol water)

Component	WK-28	WK-72	WK-81
CO_2	279	102	12
H_2S	8	4.5	1.9

Table 3.4-3. Chemical Compositions of Glass and Secondary Minerals

	GU-3 1195C glass	H-5 1666 smectite	GU-3 1195 heulandite
Weight Percent			
SiO_2	74.1	43.2	64.8
TiO_2	0.09	0.13	0.00
Al_2O_3	12.4	21.4	12.0
FeO	0.82	1.57	n.d.*
MnO	0.00	0.05	0.09
MgO	0.02	0.89	0.88
CaO	0.19	2.48	3.84
BaO	0.06	0.00	0.00
Na_2O	3.55	0.14	0.59
K_2O	5.77	0.15	0.78
H_2O	3.0	30.0	17.0
Total	100.0	100.0	100.0
Density, g/cm^3			
	2.36†	2.00‡	2.20‡
Mole/cm^3			
Si	0.02904	0.01437	0.02372
Al	0.00560	0.00840	0.00550
Ca	0.00008	0.00088	0.00160
Na	0.00270	0.00009	0.00045
K	0.00288	0.00006	0.00039

*n.d. = not detected
†Anderson (1984)
‡Deer et al.(1963)

Table 3.4-4. X-ray diffraction mineralogy of altered Topopah Spring vitrophyre (weight percent)

Sample	Depth (m)	Smec-tite	Heulan-dite	Quartz	Cristo-balite	Alkali feldspar	Opal-CT	Other
GU-3*								
1195.7	364.5	n.d.§	~1	8±2	22±3	70±5	n.d.	trace†
G-4*								
1299	395.9	2±1	5±2	8±2	23±4	62±10	n.d.	trace†
1314	400.5	45±10	28±5	2±1	14±4	11±5	n.d.	
H-5								
1666	507.8	37±16	20±5	3±1	n.d.	24±7	15±7	~0.6‡

*From Bish and Chipera (1989).
§n.d. = not detected.
†mica.
‡erionite. Special techniques to detect erionite were used for this sample only (Bish and Chipera , 1991).

Table 3.4-5. Summary of standard state thermodynamic data for clinoptilolite and heulandite.

Reference	Johnson et al. (1991)	Johnson et al. (1991)*	Hemingway and Robie (1984)	Murphy et al. (1996)	Barnes and Wilkin (1995)	Johnson et al. (1985)	Johnson et al. (1985)*
Sample	Malheur, OR clinoptilolite	Malheur, OR clinoptilolite	Mojave county, AZ clinoptilolite	Death Valley Junction, CA clinoptilolite	Castle Creek, ID clinoptilolite	Gunnadah, Australia, heulandite	ref. state modified heulandite
Study type	Calorimetric	Calorimetric	Calorimetric	Solubility	Solubility	Calorimetric	Calorimetric
Na (72 O)	1.908		0.56	5.412	6.36	1.532	
K	1.086		0.98	0.369	0.18	0.528	
Ca	1.522		1.50	0.009	0	2.34	
Mg	0.248		1.23	0.105	0	0	
Mn	0.004			0	0	0	
Ba	0.124			0	0	0.26	
Sr	0.072			0	0	0.7	
Fe	0.034		0.3	0.132	0	0	
Al	6.900		6.7	5.841	6.6	8.66	
Si	29.066		29	30	29.4	27.34	
O	72		72	72	72	72	
H_2O	21.844		22	22.29	21	24	
Si/Al	4.21		4.33	5.14	4.45	3.16	
ΔG_f kJ/mol	-38156.8	-38042.4		-38124	-37506	-39228	-39114
ΔH_f kJ/mol	-41290	-41176			-40646	-42490	-42376
S° J/mol-K	2966.10	2966.10	2872.3		2830.32	3068.72	3068.72
high T data**	yes		no	no	yes		yes

*These values have been corrected back to a reference state based on quartz (cf. Johnson et al., 1992 and discussion in the section on analcime).
**Indicates whether data at temperatures above 25∞C were collected.

Table 3.4-6. Gibbs free energy of formation of Na-clinoptilolite determined by solubility measurements (Barnes and Wilkin, 1995).

Temperature (°C)	$\Delta G_f°$ kJ/mol
25	-37577.4
50	-37282.8
80	-36958.2
90	-36785.4
100	-36633.0
125	-36375.6
175	-35910.0
200	-35679.0
225	-35404.8
265	-35031.0

Table 3.4-7. Calculated Gibbs free energies of formation of end-member clinoptilolite.

	ΔG binary exchange for Na J/mol	ΔG_f kJ/mol
Na-clinoptilolite	0	-37506
K-clinoptilolite	-7980	-37688
Ca-clinoptilolite	-925	-37604
Sr-clinoptilolite	-1371	-37624

Table 3.4-8. Standard-state values for the thermodynamics of hydration in cation-exchanged clinoptilolite with errors derived from regression analysis. The values (except entropy) are used in Equation 4.

Parameter*	Ca-Exchanged		Na-Exchanged		K-Exchanged	
	Value	std error	Value	std error	Value	std error
$\Delta\mu^o_{Hy}$ (J/mol)	-79685	2414	-55080	3273	-48949.2	1171
$\Delta\overline{H}^o_{Hy}$ (J/mol)	-120477	2232	-99593	2910	-91183	1031
$\Delta\overline{S}^o_{Hy}$ (J/mol/K)	-136.82	3.08	-149.30	5.03	-141.65	1.86
W_1 (J/mol)	137070	3332	72214	34123	74649	1277
W_2 (J/mol)	-74935	2129	-32111	2248	-41726	920

*Excess significant figures are retained for calculations.

Table 3.4-9. Molar values of the thermodynamics of hydration for cation-exchanged clinoptilolite determined in this study compared with values measured in clinoptilolite, other zeolites, and H_2O.

Material	$\Delta\tilde{G}_{Hy}$ (kJ/mol-H_2O)	$\Delta\tilde{H}_{Hy}$ (kJ/mol-H_2O)	$\Delta\tilde{S}_{Hy}$ (J/mol-H_2O/K)
Ca-Cpt[1]	-36.13 ± 3.02	-76.92 ± 2.88	-136.8 ± 3.1
Na-Cpt[1]	-29.68 ± 3.77	-74.19 ± 3.46	-149.3 ± 5.0
K-Cpt[1]	-25.53 ± 1.37	-67.78 ± 1.25	-141.7 ± 1.9
Sodic-Cpt[2]	n.d.	-65.5	n.d.
Na-Cpt[3]	n.d.	-66.1	n.d.
H_2O[4]	-8.57	-44.02	-118.9
Cordierite[5]	-9.5	-41.8	-108.2
Analcime[6]	-44.9	-84.9	-133.8
Mordenite[7]	-33.5	-73.8	-134.8

[1]This study. Uncertainties are derived from the standard errors of the egression coefficients.
[2]Johnson et al. (1991) adiabatic and solution calorimetry.
[3]Barrer and Cram (1971) immersion calorimetry.
[4]Robie et al. (1979) condensation of water vapor.
[5]Carey (1995) phase equilibria.
[6]Johnson et al. (1982) adiabatic and solution calorimetry.
[7]Johnson et al. (1992) adiabatic and solution calorimetry.

Table 3.4-10. Parameters for the calculation of the partial and integral molar enthalpy of hydration from calorimetric data (cal). Also included are the less accurate values derived from the thermogravimetric experiments (TGA).

Clinoptilolite	$\Delta\bar{H}^{o}_{Hv}$ J/mol	W_1 J/mol	W_2 J/mol	$\Delta\ddot{H}_{Hv}$ kJ/mol
Ca (Cal)	-95274	34169	14400	-73.4
Na (Cal)	-94760	66112	-19468	-68.2
K (Cal)	-99161	100460	-52575	-66.5
Ca (TGA)	-120477	1370706	-74935	-76.9
Na (TGA)	-99593	72214	-32111	-74.2
K (TGA)	-91183	74649	-41726	-67.8

Table 3.4-11. Standard-state Gibbs free energy of formation of analcime from the elements determined from calorimetric and solubility measurements.

Sample	Si/Al Ratio	ΔG_f kJ/mol	Uncertainty kJ/mol	Reference
Mt. St. Hilaire	1.94	-3085.4	5	Murphy et al. (1996)
Table Mountain	2	-3091.73	3.682	Robie et al. (1979)
Mt. St. Hilaire	2	-3090*	5	Barnes and Wilkin (1995)
Mt. St. Hilaire	2	-3105.3**	5	Barnes and Wilkin (1995)
Skookumchuck	2.125	-3077.2	3.3	Johnson et al. (1982)
Skookumchuck	2.125	-3086.1†	3.3	Johnson et al. (1982)
Wikieup	2.55	-3036	5	Barnes and Wilkin (1995)

*Value obtained by linear regression from 50 to 300°C
**Actual value measured at 25°C (Barnes and Wilkin, 1995).
†Revised value (Johnson et al., 1992).

Table 3.4-12. Standard-state thermodynamic properties of analcime derived from phase equilibria constraints or by polyhedral estimation techniques.

Sample	Si/Al Ratio	ΔG_f kJ/mol	Reference
Phase equilibria studies	2	-3088.22	Helgeson et al. (1978)
Arbitrary composition	2	-3093.77	Chipera et al. (1995a)
Arbitrary composition	2.75	-3037.5	Chipera et al. (1995a)
Arbitrary composition	2	-3099.72	Chermak and Rimstidt (1989)
Arbitrary composition	2.75	-3040.1	Chermak and Rimstidt (1989)

Table 3.4-13. Gibbs free energy of formation (kJ/mol) of analcime determined from solubility data by Barnes and Wilkin (1995). Predicted values from linear regression

Temperature (°C)	Mt. St. Hilaire*	Predicted	Wikieup**	Predicted
25	-3105.3	-3089.95		-3035.82
50	-3080.5	-3071.31		-3017.49
80	-3048.1	-3048.95		-2995.5
90	-3036.2	-3041.49	-2989	-2988.17
125	-3010.4	-3015.4	-2961.7	-2962.5
175	-2977.5	-2978.13	-2925.2	-2925.84
225	-2939.8	-2940.86	-2889.8	-2889.19
275	-2905	-2903.59		-2852.53
300	-2887.2	-2884.96		-2834.2

*$Na_{0.99}AlSi_2O_6 \cdot H_2O$ (minor K ignored).
**$Na_{0.86}Al_{0.84}Si_{2.14}O_6 \cdot H_2O$ (minor K, Ca, Mg ignored).

Table 3.4-14. Enthalpy of formation and standard-state entropy of analcime derived by linear regression of the solubility data of Barnes and Wilkin (1995). Johnson et al.'s (1982) data on Mt. St. Hilaire analcime are shown for comparison.

	Mt. St. Hilaire	Wikieup	Johnson et al. (1982)
ΔH_f kJ/mol	-3312.19	-3254.42	-3296.9
S° J/mol-K	220.05	223.71	226.75

Table 3.4-15. Thermodynamic data estimated using representative chemical formulae for Yucca Mountain zeolites.

Mineral and Representative Formula	ΔG_f° (kJ/mol)	ΔH_f° (kJ/mol)	S° (J/mol•K)	Volume (cm^3/mol)	k_0 x 100	k_1 x 10^{-2}	k_2 x 10^{-5}	k_3 x 10^{-7}
Analcime (Broxton et al., 1986)								
$Na_{0.8}Al_{0.8}Si_{2.2}O_6 \bullet 1.0H_2O$	-3040.1	-3256.2	220.2	97.3	380.95	-22.05	-94.81	139.49
Chabazite (Gottardi and Galli, 1985)								
$K_{0.6}Na_{0.2}Ca_{1.5}Al_{3.8}Si_{8.2}O_{24} \bullet 10.0H_2O$	-13850.3	-15047.4	1194.3	499.4	2022.86	-138.50	-301.581	419.459
Clinoptilolite (Broxton et al., 1986)								
$K_{0.6}Na_{0.2}Ca_{3.0}Al_{6.8}Si_{29.2}O_{72} \bullet 1.6H_2O$	-38078.2	-41247.2	2897.0	1264.0	5206.30	-348.32	-902.94	1271.38
Erionite Approximated from USW UZ-14 1364 data								
$K_{2.5}Na_{0.1}Ca_{3.1}Al_{8.8}Si_{27.2}O_{72} \bullet 28.0H_2O$	-43261.3	-43751.1	3317.0	1344.0	5848.04	-401.03	-896.74	1260.92
Erionite USW H-5 1666 (Levy, 1984b)								
$K_{2.0}Na_{0.4}Ca_{3.2}Al_{8.8}Si_{27.2}O_{72} \bullet 28.0H_2O$	-40252.4	-43743.4	3310.4	1344.0	5842.07	-399.82	-904.39	1272.49
Heulandite USW UZ-14 1364								
$K_{2.0}Na_{0.1}Ca_{3.6}Al_{9.3}Si_{26.7}O_{72} \bullet 26.0H_2O$	-39936.6	-43324.2	3150.9	1266.4	5671.68	-385.22	-895.82	1253.00
Heulandite USW H-5 1666 (Levy, 1984b)								
$K_{0.4}Na_{0.5}Ca_{3.3}Al_{7.5}Si_{28.5}O_{72} \bullet 26.0H_2O$	-39348.6	-42746.9	3091.5	1266.4	5606.63	-381.26	-909.32	1280.34
Heulandite USW G-2 1488 "prismatic" (Carlos et al., 1995b)								
$K_{0.4}Na_{0.3}Ca_{2.3}Sr_{0.2}Mg_{1.0}Al_{7.7}Si_{28.3}O_{72} \bullet 26.0H_2O$	-39373.0	-42776.5	3081.6	1266.4	5604.98	-380.84	-917.90	1289.88

Table 3.4-15: continued.

Heulandite USW G-2 1505 "prismatic" (Carlos et al., 1995b)								
$K_{0.5}Na_{0.3}Ca_{2.5}Sr_{0.2}Mg_{0.8}Al_{7.8}Si_{28.2}O_{72}$•26.0 H_2O	-39413.9	-42815.8	3087.3	1266.4	5609.67	-381.20	-914.91	1285.32
Heulandite UE-25a#1 1243 "tabular core" (Carlos et al., 1995c)								
$K_{0.2}Na_{0.5}Ca_{2.8}Sr_{0.7}Mg_{0.1}Al_{7.9}Si_{28.1}O_{72}$•26.0 H_2O	-39364.4	-42771.6	3069.6	1266.4	5609.98	-381.02	-909.99	1277.85
Heulandite UE-25a#1 1243 "tabular rim & prismatic" (Carlos et al., 1995c)								
$K_{0.1}Na_{0.2}Ca_{2.3}Sr_{0.2}Mg_{1.2}Al_{7.7}Si_{28.3}O_{72}$•26.0 H_2O	-39469.8	-42869.2	3091.0	1266.4	5596.09	-380.29	-918.16	1287.96
Laumontite (Gottardi and Galli, 1985)								
$K_{0.2}Na_{0.2}Ca_{1.8}Al_4Si_8O_{24}$ • 8.0H_2O	-13431.2	-14525.9	1011.2	406.4	1842.70	-122.73	-301.22	414.72
Mordenite (Carlos, 1987; Broxton et al., 1987; Sheppard et al., 1988)								
$K_{0.3}Na_{0.7}Ca_{0.5}Al_2Si_{10}O_{24}$ • 7.3H_2O	-12621.0	-13677.6	986.1	424.5	1752.07	-116.17	-317.63	456.08
Phillipsite USW GU-3 1200.1 (Carlos et al., 1995b)								
$K_{0.7}Na_{0.7}Ca_{1.1}Al_{3.6}Si_{12.4}O_{32}$ • 12.6H_2O	-17817.7	-19375.1	1491.9	609.2	2608.70	-177.81	-415.85	591.77
Stellerite USW G-2 1488.5 and 1505 (Carlos et al., 1995b)								
$Ca_{3.9}Na_{0.1}Al_{7.9}Si_{28.1}O_{72}$ • 28.0H_2O	-39960.1	-43468.5	3224.3	1331.0	5774.01	-396.39	-898.38	1257.38

1 Gibbs free energies and enthalpies of formation were estimated using Chermak and Rimstidt (1989).
2 Entropies of formation were estimated using Holland (1989).
3 Volumes from Smyth and Bish (1988).
4 Heat capacity terms (k) estimated using Berman and Brown (1985) for equation $C_p = k_0 + k_1T^{-0.5} + k_2T^{-2} + k_3T^{-3}$ in units of J/mol·K.

Table 3.4-16. Summary of 25°C dissolution rate constants for minerals.

Mineral	Log k_{diss}*	Log K normalized to 2 structural oxygen	Molar Volume (cc/mole)
analcime**	-11	-11.48	97.1
gibbsite	-11.45	-11.63	31.956
sanidine	-12	-12.60	109.008
albite	-12.26	-12.86	100.07
prehnite	-12.41	-13.19	140.33
microcline	-12.50	-13.10	108.741
epidote	-12.61	-13.42	139.2
Na-clinoptilolite**	-13.15	-14.23	420.87
amorphous silica†	-12.2	-12.20	29
β-cristobalite†	-12.34	-12.34	27.38
muscovite	-13.07	-13.85	140.71
kaolinite	-13.28	-13.93	99.52
α-cristobalite†	-12.77	-12.77	25.74
quartz	-13.39	-13.39	22.688
Na-clinoptilolite‡	-15.623	-17.18	1262.6

*k_{diss} in moles/m^2-s
All values from Lasaga et al. (1994b) except as noted.
**Murphy et al. (1996)
†Rimstidt and Barnes (1980)
‡MacInnis et al. (1995)

Contents

Chapter 4.0 Geomechanics 4-2
4.1 Introduction 4-2
4.2 Ambient Conditions 4-3
4.2.1 Physical, Thermal, and Mechanical Properties of Rock Mass and Intact Rock 4-3
4.2.2 Temperature and Stress 4-9
4.3 Processes That Perturb the Waste Package Environment 4-12
4.3.1 Excavation of the Repository 4-13
4.3.2 Thermal Effects of Waste Emplacement 4-13
4.3.3 Time-Dependent Effects 4-15
4.3.4 Radiation Effects of Waste Emplacement 4-17
4.3.5 Seismic Loading 4-18
4.4 Geomechanics Modeling 4-20
4.4.1 Discussion of Model Approaches 4-20
4.4.2 Applications to the Near Field Environment at Yucca Mountain 4-24
4.5 References 4-26

Chapter 4.0 Geomechanics

Stephen C. Blair
Patricia A. Berge

4.1 Introduction

Information on the geomechanical characteristics of the near-field environment (NFE) is needed for design of the waste package (WP) and engineered barrier system (EBS) and for the assessment of their performance over the lifetime of the repository. Specifically, information is needed on (1) the amount and type of rock-induced loading that might be expected on the waste package, (2) the geomechanical properties of rock in the NFE and how they will change over time, and (3) any coupling of changing geomechanical properties to other near-field properties (e.g., geochemical or hydrologic). Two types of rock-induced loading need to be considered: impact loads and static loads. Impact loads may be caused by the sudden movement of blocks of rock along pre-existing fractures, or by sudden spalling of excavation walls. The WP must be able to withstand the maximum expected impact load without damage. Static loads may result from spalling or sloughing of rock chips from the drift walls, or from slow movement of rock blocks. Static loads provide contact between the rock and the Waste Package, transport pathways into the wall rock, and sites for surface corrosion of the WP. The WP and EBS must be designed to accommodate the expected static loads and still meet the performance objectives over the lifetime of the repository.

Changes in the mechanical properties of the near-field rock over time are also very important. Several processes including creep, microfracturing, radiation damage, and others could contribute to changes in hydrologic and geochemical processes that affect transport. Information on the geomechanical properties of near-field rock away from excavations is also needed to assess the transport properties of the NFE over time.

4.2 Ambient Conditions

4.2.1 Physical, Thermal, and Mechanical Properties of Rock Mass and Intact Rock

The most effective way to determine the ambient physical, thermal and mechanical properties of the rock mass forming the NFE is to tunnel into the rock mass, observe composition and fracture distributions, take samples of the rock for laboratory testing, and perform in situ tests of the thermal-hydrologic-mechanical-chemical (THMC) performance. At the time of writing of this report a tunnel boring machine (TBM) is creating a tunnel through the potential repository horizon, a thermal testing alcove is under construction, and rock samples obtained from the tunnel are being tested in various laboratory facilities. In addition, a series of boreholes has been drilled into the potential repository horizon, and these holes have been logged and samples from them have been tested and characterized in several ways. The ESF operations and studies of associated boreholes have produced a significant amount of new data describing the properties of the ESF. However, because the studies at the ESF are ongoing at this time of writing, the ESF data presented here are subject to frequent revision, and the reader is cautioned to check for updates to the data base.

An extensive series of laboratory tests on core samples obtained from boreholes that intersect the potential repository horizon has been done over a period of several years. The results of these tests have been compiled in the *Yucca Mountain Project Reference Information Base* (*RIB*) (DOE, 1994). It is important to note that the values presented in the *RIB* are subject to frequent revision and that references for some of the values in the *RIB* are not readily available. Consequently, an evaluation of the significance of differences between values reported in the *RIB* and published values cannot be made at this time.

4.2.1.1 Physical Properties. Physical properties including porosity, grain density, bulk density at in situ saturation, and dry bulk density have been determined from core samples and values for these parameters are given in Table 4-1. These values were obtained from a statistical analysis of available data and can be found in chapter 1, sections 1.1321 and 1.1325 of the *RIB*; additional data can be found in Price et al. (1985), Martin et al. (1994), and Roberts and Lin (1995).

4.2.1.2 Thermal Properties. Thermal properties of the repository horizon are presented in Tables 4-1, 4-2, and 4-3. The values for matrix and in situ thermal conductivity in Table 4-1 are from Nimick (1990) and reflect the values from the

RIB. The coefficient of thermal expansion for welded tuff is determined by the tuff's mineralogy (as reflected in matrix conductivity), matrix porosity, matrix saturation, and fracture porosity.

Measurements of linear thermal expansion have been made on samples from the Topopah Spring welded unit, lithophysae-poor layer (TSw2) and Table 4-2 presents the coefficients of linear thermal expansion. These coefficients are the tabulated results of a statistical analysis of thermal expansion data and can also be found in Chapter 1, section 1.1326 of the *RIB*. The values represent coefficients of linear thermal expansion during heating, and the coefficients shown for the intact rock should be used for calculations that do not involve very near-field regions. Coefficients of linear thermal expansion during heating for very near-field regions are also shown and apply only to welded, devitrified tuffs that are near or at a free surface and are in an essentially unconfined initial-stress state. Table 4-2 gives the mean coefficient of linear thermal expansion ($\bar{\alpha}$); the standard deviation of the sample group (s); and the number of samples analyzed (n). Note that these coefficients should not be used for calculations of displacements or stresses during cooling; thermal expansion behavior is hysteretic and depends on the maximum temperature reached by the material. Coefficients of linear thermal expansion ($\bar{\alpha}$) are assumed to be identical for both intact rock and the rock mass. This assumption will be evaluated during the underground heater tests that are currently planned to be conducted in the ESF.

Unconfined thermal expansion measurements on silicate rocks generally show an increase in the expansion coefficient as temperature increases. This is thought to result from a mismatch between the expansion coefficient of constituent grains, which results in local distortions and the formation of new microcracks in an uncracked material or in the shear-related opening of pre-existing microcracks (Cooper and Simmons, 1977). The presence of a mineral, such as cristobalite, that undergoes a phase transformation at a temperature of about 230° C (±20° C) (Meike and Glassley, 1990) with an accompanying 5% increase in volume (Cohen and Klement, 1975), will also cause thermal expansion to vary with temperature. The SiO_2 polymorphs cristobalite and tridymite make up as much as 30% by volume of Topopah Spring tuff groundmass in some parts of the formation (Connolly, 1991, 1994). However, the volume of rock expected to be heated above 200° C is a small percentage of the total rock mass.

Martin et al. (1996) conducted thermal expansion measurements as a function of confining pressure and at temperatures to 250°C on core samples of Topopah Spring

tuff. These authors found that the coefficient of thermal expansion for welded tuff increased with temperature. At temperatures below 100°C the value of this parameter was in the range 7.7 to 10.8 x 10^{-6}°C^{-1}, and as temperature was increased to near 250°C, values of the coefficient of thermal expansion increased to between 14.2 and 20.6 x 10^{-6}°C^{-1}. These authors found that confining pressure had a small effect of the coefficient of thermal expansion.

Thermal capacitance has also been estimated for the Topopah Spring welded unit, lithophysae-poor layer (TSw2) for various temperatures, and the values listed in Table 4-3 are reported in section 1.1326 of the *RIB*. This value incorporates an estimate of rock-heat capacity based on bulk chemical analyses of the rock, the effects of the transformation of the minerals tridymite and cristobalite, the boiling of pore water, and the decrease in saturation of pore water as temperature is increased from 95 to 115 °C. Figure 4-1 is taken from the *RIB* and shows thermal capacitance in more detail. This figure plots values computed from a series of equations presented in section 1.1326 of the *RIB* for thermal capacitance of unit TSw2.

4.2.1.3 Mechanical Properties. To properly characterize the mechanical behavior of the NFE it is necessary to know the mechanical properties of the rock mass forming the NFE. The mechanical properties of a rock mass are difficult to measure directly and depend on the properties of both the intact rock and the fractures making up the rock mass.

The mechanical properties for intact rock of the potential repository horizon have been extensively studied via tests on core samples (Martin et al., 1995a, 1994, Price et al., 1987; Price, 1983; Price and Jones, 1982; Price, 1986; and Nimick et al., 1987). Mechanical properties for TSw2 have been analyzed statistically; the results of the statistical analysis are included in section 1.322 of the *RIB* and are summarized here in Table 4-4. Recent measurements of mechanical properties such as ultimate strength and elastic moduli for tuff by Teufel and McNamee (1991) and Martin et al. (1993, 1994, 1995a) are in general agreement with the values given in Table 4-4. Lin et al. (1993b) used information about intact rock mass properties and fracture/joint characteristics to develop models of rock mass properties and rock mass qualities.

The mechanical data indicate that the intact rock is quite strong with a uniaxial strength of 155 MPa (±59 MPa) and a high deformation modulus. Uncracked samples have stress-strain curves that show nearly linearly elastic behavior until failure. Samples with cracks exhibit nonlinear stress-strain behavior as expected when stress is above 50% of the failure stress. Typical stress-strain curves for 50.8-mm-diam saturated samples are shown in Fig. 4-2.

Martin et al. (1993, 1994, 1995a) measured unconfined compressive strength, static Young's modulus and Poisson's ratio, and elastic wave velocities for Topopah Spring tuff samples from Busted Butte and from the USW NRG-6 and USW NRG-7/7A boreholes at Yucca Mountain. These holes intersected the path of the north ramp of the Exploratory Studies Facility (ESF) and are part of a series of holes identified as the North Ramp Geotechnical (NRG) holes. All measurements were made at ambient temperature conditions. They also made confined compressive strength and indirect tensile strength measurements for the samples from the boreholes. The unconfined compressive strength and static Young's modulus and Poisson's ratio values that they found showed more scatter than the results reported in the *RIB*, and some of the values were much lower than corresponding *RIB* results. The Topopah Spring tuff samples are apparently quite heterogeneous, representing a wide range of porosities, and some samples can be much weaker than those described in the *RIB*. For example, some of the borehole samples failed at pressures well below 100 MPa (Martin et al., 1994, 1995a) rather than having strengths between approximately 100 and 200 MPa as described in the *RIB*. Poisson's ratio values for the borehole samples of TSw2 ranged from about 0.14 to 0.40 (Martin et al., 1994, 1995a), and the TSw2 samples from Busted Butte had static Poisson's ratio values of about 0.09 (Martin et al., 1993).

Elastic wave velocity measurements on laboratory samples are useful as they provide data for comparison with velocities measured in the field, and a means of estimating the dynamic moduli, including Poisson's ratio for the rock. They also provide a convenient method for characterizing anisotropy in the rock behavior. Compressional and shear wave velocity measurements were made at frequencies of about 300 to 800 kHz for the Busted Butte samples and about 300 kHz to 1 MHz for the borehole samples, for both the dry and the saturated cases by Martin et al., 1993, 1994, 1995a. This corresponds to wavelengths of a few mm to a few cm in the tuff. Measurements were made along the core axis for the Busted Butte samples, and both parallel to and perpendicular to the core axis for the borehole samples. But since the shear wave velocities were not measured for waves propagating perpendicular to the core axis and having polarization perpendicular to the core axis (i.e., the expected fast shear wave direction for the case of transverse isotropy), these data cannot be used to quantify any velocity anisotropy. Further discussion of anisotropy in Topopah Spring tuff can be found in Martin et al. (1992).

The compressional wave velocities for the Busted Butte samples were about 4.5 to 4.7 km/s for both the dry and the saturated cases (Martin et al., 1993). The

borehole samples had similar velocities except that a few samples had velocities as low as 4.0 to 4.3 km/s (Martin et al., 1994, 1995a). These velocities found for cores measuring a few cm are higher than the velocities found for the G-tunnel heated block experiment at the 1-m scale (Zimmerman et al., 1986), but are in excellent agreement with compressional wave velocities measured at ambient temperature and pressure conditions for a block of Topopah Spring tuff at the 0.5 m scale (Blair and Berge, 1996).

The shear wave velocities for the Busted Butte samples were about 2.5 to 2.8 km/s for the saturated case, and 2.7 to 2.8 km/s for the dry case (Martin et al., 1993). The borehole samples of tuff had only two shear wave velocity measurements for the saturated case, 2.7 and 2.9 km/s (Martin et al., 1994, 1995a). For the dry case, the borehole samples had shear wave velocities of 2.4 to 3.0 km/s (Martin et al., 1994, 1995a).

Martin et al. (1993) used the velocity measurements to estimate dynamic Young's modulus and Poisson's ratio for the Busted Butte samples. They found values of about 41 to 44 GPa for dynamic Young's modulus in the dry case, and about 39 to 45 GPa for the saturated case. The Poisson's ratio estimates were about 0.20 to 0.22 in the dry case and about 0.23 to 0.28 for the saturated case. The dynamic Young's modulus values were slightly higher than the measured static values for the Busted Butte samples (about 34 GPa). A separate study of the effect of frequency on Young's modulus and elastic wave attenuation (Price et al., 1994) found that Young's modulus for Topopah Spring tuff varied slightly with frequency, having values near 38 GPa for frequencies of about 10^{-2} Hz and higher values near 40 GPa for frequencies up to about 10^{6} Hz. For these measurements, saturation had a greater effect on Young's modulus than the frequency had.

The values that Martin et al. (1993) observed for Poisson's ratio are quite low, 0.09±0.067, when compared to values presented in the *RIB*, about 0.22 to 0.30. Martin et al. (1993) were unable to explain these anomalously low values for Poisson's ratio. One likely explanation is that their samples may have contained significant amounts of α-cristobalite. This mineral has a negative Poisson's ratio for single crystals and polycrystalline aggregates (Yehaneh-Hari et al., 1992; Keskar and Chelikowsky, 1993), which means that rocks containing significant amounts of α-cristobalite may have anomalously low values for Poisson's ratio.

Price (1986) studied the effect of sample size on mechanical properties of Topopah Spring tuff (Tpt) and found that both the ultimate strength and axial strain at failure are inversely related to sample diameter, while Young's modulus and

Poisson's ratio are independent of sample diameter. Price (1986) used power-law models to describe the behavior of ultimate strength and axial strain at failure as a function of sample size and proposed the following two equations:

$$s_u = (1944)\,(D)^{-0.846} + 69.5 \tag{4-3}$$

and

$$e_u = 11.6\,D^{-0.268}, \tag{4-4}$$

where

s_u = ultimate strength (uniaxial) (MPa),
e_u = axial strain at failure (millistrain),
D = sample diameter (mm).

Price illustrates the effect of sample size on ultimate strength using saturated samples in Fig. 4-3.

To date, most compressive-strength experiments have used samples that were saturated with water and then tested under drained conditions. The results represent a minimum value because rocks are generally weaker when saturated with water. Olsson and Jones (1980) show that for Grouse Canyon tuff, which is similar to rock in the potential NFE, saturated samples are about 24% weaker than dry samples in unconfined compression.

The physical properties of the rock mass must also be determined for evaluation of the NFE. Rock-mass compressive strength is defined as the strength of a representative volume of intact- and jointed-rock matrix material. Estimates of rock-mass strength are based on (1) the known behavior of intact rock, (2) the known joint characteristics, and (3) the presence of applied or confining stresses. A rock-mass strength criterion of

$$(\sigma_1)_{ultimate} = 16.0 + 10.2\,(\sigma_3)^{0.602}, \tag{4-5}$$

where $0 < \sigma_3 < 25$ MPa, is presented in item 1.2.6 of the *RIB*. Equation (4-5) is based on an assumed rock-mass rating (RMR) of 61 and an unconfined compressive strength of 16.0 MPa. The equation reflects the current understanding of the nonlinear empirical relationship between rock-mass strength and confining stress and is subject to revision as more field and laboratory data for rock characteristics become available.

4.2.2 Temperature and Stress

In situ stress values for the potential repository horizon have been determined from measurements in drill holes USW G-1, USW G-2, and USW G-3 (Stock et al., 1984, 1985). Table 4-5 shows the average mean value and range for vertical stress, which is the maximum principal stress and is due to the overburden rock at the site, in addition to the ratios of minimum and maximum horizontal stresses to vertical stress, and the bearings of minimum and maximum horizontal stresses.

A calculated stress profile for the in situ stress near the Exploratory Studies Facility (ESF) is reported in chapter 1, section 1.27 of the *RIB*. The results of the analysis are shown in Fig. 4-4. The stress values are estimated using two-dimensional finite-element analysis in which the gravitational stress is the only loading mechanism modeled (Bauer et al., 1985). The calculated values are similar to those reported in both Bauer et al. (1985) and Bauer and Holland (1987), and to the values of Yucca Mountain in situ stress measurements (Stock et al., 1985). The calculations assumed plane-strain conditions and a linearly elastic material response. The maximum horizontal stress was assumed to be equal to twice the minimum horizontal stress. The values of in situ bulk density and elastic properties for the rock mass used in the finite-element analysis were slightly different than those reported in Table 4-5 and can be found in section 1.27 of the *RIB*.

4.2.2.1 Cracks and Fractures. Current knowledge of cracks and fractures in the potential repository horizon is based on observations in exploratory vertical drill holes and from recent observations made in the Exploratory Studies Facility. However, at the time of this writing, fracture mapping from the ESF are not available, but preliminary analysis indicates that the main observations determined from the drill hole data are representative of the data derived from the ESF. The drill hole indicates that jointing in the Topopah Spring welded unit, lithophysae-poor layer is mostly vertical. Scott and Catellanos (1984) reported a fracture density of about $40/m^3$ in the potential repository horizon, and evaluation of these data (Wilder, 1990) indicate that the fracture spacing in the rock mass may be less than ~30 cm (1 ft). Fracture data are also given in chapter 1, section 1.142 of the *RIB*. Data on the distribution and characteristics of fractures in the Topopah Spring welded unit, lithophysae-poor layer (TSw2) along the 2800 m route of the north ramp of the Exploratory Studies Facility have been collected from several boreholes by Brechtel et al. (1995). Brechtel et al. (1995) averaged values over 3 m, (10 ft) lengths along the boreholes and found that the most frequent joint spacing was from 60 - 200mm, with the joint condition characterized as slightly rough, separation < 1mm, and

slightly weathered walls. These data confirm the conclusions of earlier work by Scott and Catellanos (1984) which indicated that potential repository horizon contained a significant number of fractures.

Lin et al. (1993a) reviewed the fracture data from drill holes USW G-1, USW G-4, USW GU-3 and UE-25a#1 and present a description of the fracture spatial location and abundance and physical characteristics and estimated Rock Quality Designation (RQD) for the Topopah Spring member and other geologic formations intersected by the drill holes. Table 4-6 summarizes their findings for the potential repository horizon. These values are similar to those presented by MacDougall (1987). However, because these data are generated from only four exploratory vertical drill holes, additional data and analyses are needed to fully assess the potential for block movement for either borehole or drift emplacement. Moreover, additional data are currently being collected from the ESF, but these data are not available at the time of this writing.

The constitutive properties of fractures and joints present in the potential repository horizon are also important for assessment of the thermal-mechanical and thermal-hydrologic behavior of the rock. Olsson and Brown (1994) measured constitutive properties of seven fractures from drill holes NRG-4 and NRG-6 using a rotary shear apparatus. They found that the peak friction ranged from 0.89 to 1.11, and residual friction ranged form 0.76 to 1.00. They also report that dilation angle ranged from 5.29° to 11.28°, and that the roughness characteristics for the fracture surfaces are in qualitative agreement with the mathematical model of Brown (1994). Olsson also examined the effect of sliding velocity on the mechanical response of an artificial joint in Topopah Spring tuff to determine the velocity-dependence of shear strength. Olsson found that different initial conditions affected the character of the stress-slip curve. In particular, slide-hold-slide tests exhibited time-dependent strengthening, while hold-slide tests produced slip weakening. No joint creep was observed in these tests.

Blair and Berge (1996) monitored the deformation under compression of a fracture zone in a 0.5m scale block of Topopah Spring welded unit, lithophysae-poor layer (TSw2). The test is shown schematically in Fig. 4-5, and a stress-strain curve is shown in Fig. 4-6. This figure shows that deformation is nonlinear with increasing stress, and modulus increases as vertical stress increases above 4 MPa. The modulus value computed for vertical stress below 4 MPa is ~ 4 GPa, and that value increases to ~ 6 GPa as applied stress is raised above 4 MPa. These values are considerably lower than modulus values measured on core samples, and reflect that the block

contains vugs and fractures. The increase in deformation modulus with increasing vertical stress can be attributed to closure of fractures and vugs that occur in the subhorizontal zone. Moreover, the curve exhibits the banana shape that is associated with the hysteretic behavior of fractures. The hysteresis shown during the initial stage of unloading is attributed to the cohesion of fractures. The plot shows that the cohesion for this zone is ~ 1 MPa, which is an order of magnitude weaker than values often used in numerical models of rock behavior that incorporate discrete joints and fractures. As the load continues to decrease, the slope of the unloading curve decreases gradually. This is relevant to hydrologic calculations of flow during the cool down period when stresses are expected to decrease, as the opening of fractures will increase the permeability of the near field region.

Knowing the properties of the intact rock and the fractures provides basic elements for understanding rock mass behavior, and empirical methods have been developed that use information on the properties of intact rock and fractures, as well as the number and orientation for fractures to estimate properties of the rock mass. The two most widely used methods are the Rock Mass Rating (RMR) method (Bieniawski, 1979), and the "Q" method (Barton et al., 1994). Brechtel et al. , 1995) used data from the NRG holes in conjunction with other data from standard laboratory tests on cores from the drill holes to estimate the condition of the rock mass using these two methods. Results indicate fair to good rock conditions in the Topopah Spring welded unit, lithophysae-poor layer. Brechtel et al. (1995) also analyzed the rock quality data using the methodology of Hardy and Bauer (1991) to estimate values of the mechanical properties of the rock mass. These estimates are derived from the RMR and Q values and were computed for input for numerical modeling of thermomechanical and seismic loading of the ESF. Results of their analysis for the TSw2 layer are summarized in Table 4-7. This table shows that estimated rock mass strengths are substantially lower than strength values determined from laboratory measurements on intact rock samples form the NRG drill holes. In particular, the estimated compressive strength for unit TSw2 is 18.8 MPa, which is approximately 10% of the mean value of compressive strength measured from intact core samples. It is interesting that the estimated Young's modulus is similar to that measured on intact core. However, these are only estimated values and more tests and analyses in both the laboratory on blocks containing multiple fractures, and in the field need to be conducted to better define the anticipated rock mass compressive strength.

Comparison of the estimated mechanical properties for the rock mass and the values measured on intact core, indicates that the properties of the rock mass are scale dependent. This is primarily due to the presence of cracks and fractures, and unfortunately, the scaling relations for the behavior and properties of fractured tuff are not well developed. Recently, Lin et al. (1995) proposed an intermediate scale test to aid in the development of scaling relations. This test is known as the Large Block Test and is described in detail in Chapter 9 of this report. Also, Blair and Berge (1996) have measured deformation on a 0.5m scale block of Topopah Spring welded unit, lithophysae-poor layer (TSw2) that contained several cracks and fractures. These authors observed Young's modulus to be about 6 GPa, with most of the deformation occurring across fractures. This indicates that the estimated value of Young's modulus given in Table 4-4 may be too high.

4.3 Processes That Perturb the Waste Package Environment

Development of a subsurface nuclear waste repository will significantly affect the geomechanical conditions of the near-field rock. Excavation of the repository drifts will increase the level of stress in the rock within a few meters of the excavations. Emplacement of the waste containers will cause an immediate and rapid increase in temperature in the walls of the excavations. The maximum temperature reached will depend on the nature of the waste emplaced and the repository design, but temperatures as high as 230 °C are predicted (O'Neal et al., 1984). The thermal loading will affect the stress, strength, and other properties of the rock near the excavations. The overall stress in the WP environment will increase as the rock heats and tries to expand. As heating proceeds, however, some zones of the repository may actually experience tension due to excavation and heating geometries. During cooling, the overall stress will decrease and zones put in tension will return to a compressive state. The heating and cooling of the near-field rock will also cause moisture distribution in the near field to be time-dependent and will impose a drying and rewetting cycle on the rock. Since the rock strength at elevated temperature is also a function of the water content, this must be considered in analysis of near field behavior. Finally, the emplacement of waste may impose a radiation field on rock in the first few centimeters of an excavation wall.

When imposed over long time periods, these changes in the environmental conditions may cause physical and mechanical changes in the rock that need to be considered in the design and assessment of the waste package. While the effect of

these parameters on the mechanical behavior of the NFE has not been studied for the period after closure, it has been studied for the period before closure; the results of some of these studies are summarized below.

4.3.1 Excavation of the Repository

The excavation of repository drifts can alter the mechanical properties of the rock near the openings. Blasting creates fractures while damage due to mechanical excavation depends on the particular technique used. Pusch (1989) evaluated the influence of several excavation techniques on the structure and physical properties of rock around large boreholes and found that "the procedure employed in the excavation of canister disposition holes affects the structure and physical properties of the 'near-field rock.'" Pusch considered percussion, full-face and core drilling, and smooth blasting and found that "except for smooth blasting, the generated damage appears to be less important than the increase in 'axial' hydraulic conductivity that is caused by stress-release effects, but both combine to yield significant local flow passages. This is particularly obvious where the rock structure yields steep wedges." Pusch concludes that core drilling has the least effect, while percussion drilling causes fine-fissuring and discing within one centimeter of the borehole wall. Full-face drilling causes more extensive fissuring and the generation of new fractures in addition to the growth of pre-existing ones within several decimeters from the borehole wall. Pusch's results also indicate that smooth blasting produces a particular form of regular fractures that appear to control the hydraulic conductivity of the near-field rock. Pusch did not consider excavation of the drifts by tunnel-boring machines. It is expected that this method would minimize rock damage around the drifts. While not directly applicable to the drift excavation, Pusch's results are indicative of the types of effects that could be expected in drift excavation.

Excavation of emplacement drifts will also alter the stress field in the rock near because the repository horizon is under lithostatic and regional tectonic stress. When sections of the rock are removed, the stress previously supported by the excavated rock is redistributed in the remaining rock. Generally, stress levels and stress gradients near the excavated openings increase and can result in time-dependent deformation of the excavations.

4.3.2 Thermal Effects of Waste Emplacement

The thermal cycle, during which the rock will rapidly heat and then slowly cool, will affect the geomechanical behavior of the NFE. Figure 4-7 shows temperature

profiles predicted at 150, 500, 1,000, 5,000, and 10,000 yr after waste emplacement at a density of 83.4 mtu. This figure shows that temperatures in the near-field will remain in excess of 100°C for over 1,000 yr. Additional estimates of temperatures in the near field are shown in Fig. 1.10.5.2.1. The thermal loading of the NFE will alter the stress in the rock near the emplacement excavation as a function of time. During the period of temperature increase, the stress in the rock will increase as the rock tries to expand. However, because of the geometry of the excavated drifts, the stress field in the NFE will be complex and, as stated previously, some zones may even be put in tension for an extended period of time. As the temperature decreases, the overall stress levels will decrease and the entire stress field will again be compressive.

In addition, the effect of temperature on the strength of near-field rock is not well defined at this time. Rock strength, however, generally decreases with increasing temperature. Price et al. (1987) report that for samples from the potential repository horizon, Young's modulus decreases an average of 16% as temperature is raised from 22 to 150°C. The mean ultimate strength also decreases 16% as temperature is raised from 22 to 150°C at both 0 and 5 MPa confining pressures.

Several numerical modeling studies have been conducted to assess the stability of underground excavations at Yucca Mountain for the preclosure period and a synopsis of these studies is presented by Ehgartner and Kalinski (1988). All of the studies cited by Ehgartner and Kalinski show that drifts and shafts should be stable through repository decommissioning. However, none of the studies examined the stability of openings at times beyond decommissioning.

Several studies have also evaluated the stability of boreholes if borehole emplacement is selected including Arulmoli and St. John (1987) and Christianson and Brady (1989). Moreover, Christianson and Brady (1989) in investigating the stress field around boreholes for both vertical and horizontal emplacement geometries found for specific geometries that there were locations where compressive stresses were adequate to form zones of rock failure that occurs either prior to heating or develops as heating progresses. Christianson and Brady (1989) also estimated that for horizontal emplacement, zones of joint slip will develop prior to heating. Except for joints dipping at 45°, heating has the effect of reducing the tendency for joint slip, implying that there should be no progressive deformation of the borehole as heating proceeds. The opposite conclusion applies to joints dipping at 45° with a local principal stress ratio of unity. In that case, progressive deterioration of the borehole may accompany heating.

To predict the postclosure geomechanical environment, time-dependent rock properties may be important because stresses in the near field are predicted to remain at levels of 20–40 MPa for well over 100 years. Estimates of the geomechanical behavior of rock around the emplacement drift that incorporate time-dependent rock properties are still to be made. In addition, it is important to note that spalling and/or slip along fractures is expected to occur within the first 50 yr. after waste emplacement at a time when (1) the monitoring of drifts will be practical, and (2) drift support could be relied on.

4.3.3 Time-Dependent Effects

4.3.3.1 Microcracking and Subcritical Crack Growth. Microcracking and subcritical crack growth in the near-field rock over long periods of time is of concern because the formation, growth, and coalescence of microcracks in the rock at or near excavations could lead to excavation damage and the formation of rock chips or blocks. These chips or blocks might passively load the container and form transport pathways. The formation of microcracks may also change the physical and geochemical properties of rock in the NFE. Very little work has been done in this area. Kemeny and Cook (1990), however, used a probabilistic approach, which included time-dependent crack growth, to examine borehole emplacement. They estimated that over the lifetime of the repository, slabbing is likely to occur in a significant portion of the emplacement boreholes.

One mechanism that may cause microcracking of the matrix is the phase transformation of the mineral cristobalite. Cristobalite may occur in significant amounts in the repository horizon (Connolly, 1994), and it has been shown to invert from a tetragonal to cubical structure at approximately 230° C (±20° C) (Meike and Glassley, 1990) with an accompanying 5% increase in volume (Cohen and Klement, 1975). This phase transformation could increase stresses on a local scale and cause cracking of the rock matrix.

At the elevated temperature and stress conditions expected in the near field, significant crack growth may occur even at low-crack-growth rates. Moreover, rates of subcritical crack growth may be such that, when considered over the lifetime of the repository, changes in crack length and density cannot be dismissed when estimating rock behavior. Increases in stress, temperature, and moisture have been shown to cause substantial increases in subcritical crack-growth rate for such rock types as granite and gabbro (Atkinson and Meredith, 1987). Although tests of this type are still to be made on tuff, a similar effect is expected.

Martin et al. (1995b) performed laboratory experiments to investigate creep in Topopah Spring tuff samples at ambient and elevated temperatures. They found that the observed creep deformation was consistent with a mechanism of time-dependent crack growth, particularly at stresses above 90% of the uniaxial compressive strength of the tuff. The stress necessary to produce failure appeared to decrease with increasing temperature, but the data were not sufficient to quantify that effect. Temperature did cause a reduction in strength, but further tests would be required to constrain the strength and creep deformation of tuff as a function of temperature, saturation, and applied load.

Blair and Berge (1996) found that imposing low levels of compressive stress for periods of a few days on 0.5m blocks of Topopah Spring tuff caused time-dependent inelastic crack closure to occur for cracks oriented parallel to the applied stress.

4.3.3.2 Joint Properties. MacDougall et. al (1987) have reported the following joint mechanical properties: joint cohesion = 0.1 MPa and joint-friction angle = 28.4°. Olsson (1987, 1988) investigated joint properties in rock samples from the potential repository horizon and found that the strength of a joint may increase with the time of stationary contact and that joint properties are dependent on stress history. However, he indicated that the latter area needs to be investigated further. To date, data on the effect of environmental variables (e.g., temperature, moisture content, and stress history) on joint properties are not available.

Lin et al. (1993a) present a description of the abundance, orientation, and physical characteristics of fractures and rock quality designation for the stratigraphic units of the potential repository at the Yucca Mountain site. Wibowo et al. (1993) and Olsson (1994) conducted laboratory experiments on fractures and joints in tuff to examine slip behavior and fracture surface damage during shear.

Blair and Berge (1996) found that imposing low levels of compressive stress for periods of a few days on 0.5m scale blocks of Topopah Spring tuff caused time-dependent, non-repeatable behavior to occur for cracks oriented both parallel and perpendicular to the applied stress. Under the long-term loading cracks/vugs oriented perpendicular to the applied stress showed significant closure beyond that observed in the 1-day tests performed by these authors and discussed earlier. In addition, the long-term loading caused pre-existing hairline cracks oriented in the direction parallel to the applied stress to open, which significantly reduced compressional wave velocities in this direction. Increasing temperature caused closure of some of the vertical cracks, which increased horizontal velocities.

Increasing the temperature also caused a softening of the mechanical response in the direction of loading.

Blair and Berge (1996) postulate that some properties of the rock mass may become increasingly anisotropic with time. For instance, if cracks, vugs and fractures oriented parallel to the maximum principal stress undergo time-dependent closing, permeability in this direction will be reduced and deformation modulus will increase. Moreover, opening of pre-existing hairline cracks that occur near the drift wall and are oriented parallel to it, will increase the permeability in this direction and will change the geochemical environment by exposing different mineral assemblages.

4.3.4 Radiation Effects of Waste Emplacement

The effect of radiation on the geomechanical properties of rock from the potential repository horizon is uncertain. Radiation is expected to have a negligible effect on the overall geomechanical behavior of the rock mass. This supposition is based on the work of Durham et al. (1986) who conducted a series of unconfined compression tests on cylinders of quartz monzonite, half of which were irradiated with gamma radiation and half of which were not. A similar series of tests were conducted by Durham et al. on samples of Westerly granite. These experiments showed no statistically significant change in unconfined compressive strength for either rock type. Null results were also found for the effect of gamma irradiation on Young's modulus and Poisson's ratio. Durham et al. concluded that gamma irradiation has no effect on the strengths of either rock type.

However, more recently Blair et al. (1996) have presented results of a suite of uniaxial compressive tests conducted to provide laboratory data to determine how radiation affects the compressive strength of Topopah Spring tuff. This study was patterned after that of Durham et al. (1986), mentioned above. Results indicate that for homogeneous, uncracked samples of Topopah Spring welded unit, lithophysae-poor layer, TSw2, exposure to gamma radiation had no discernible effect on the unconfined compressive (peak) strength or the Young's modulus. However, results for samples that contained partially healed, preexisting vertical or subvertical cracks, indicate that radiation may cause some degradation of the strength and Young's modulus.

A possible explanation of the observed behavior for the cores containing partially healed cracks is that exposure to radiation weakened the cementing material in the cracks and fractures that were present in these samples, leading to the lower values

of peak strength and Young's modulus. The cementing material is thought to be largely composed of carbonates and the authors discuss two possible mechanisms that could weaken the cementing material when it is exposed to radiation (Blair et al., 1996).

These results are preliminary, and additional studies are warranted to evaluate whether radiation does weaken cementing materials in welded tuff. However, if this is a real phenomenon, it has implications for the behavior of rock in the near-field region of a nuclear waste repository. The radiation field is expected to affect only rock exposed on the surface of excavated drifts and to penetrate only a few centimeters into the rock. However, the rock in this region will also experience the highest temperatures and stresses in a repository as well as high humidity. Weakening of fracture-filling materials may cause unanticipated spalling, which may change the amount and nature of rock fragments that come in contact with the waste containers. However, there are several processes that would be likely to occur that would minimize the impact of the radiation. First, radiation penetration is limited to a few centimeters of rock, and if spalling were to occur, the rubble would bulk up and form a radiation shield.

4.3.5 Seismic Loading

Earthquakes and explosions generally affect underground excavations through either fault slip or shaking. Damage due to fault slip will occur when an emplacement drift passes through a fault zone. Under such circumstances, damage is generally restricted to the fault zone, and may range from minor cracking of a tunnel liner to collapse of a portion of the excavation, depending on the fault displacement and the engineering properties of the NFE. If an emplacement drift is found to cross an active or potentially active fault zone, the appropriate sections of the drift will be abandoned because fault slip cannot be prevented.

Excavation damage as a result of shaking or vibratory motion has been widely investigated. For unlined underground excavations in rock, such damage occurs as rock fall, spalling, local opening of rock joints, and block motion. Subramanian et al. (1990) have provided recommendations for seismic parameters for the design of the shafts associated with the ESF. Their recommendations are summarized in section 1.22 of the *RIB*. They concluded that the shafts need only be designed to adequately ensure worker safety and reasonably uninterrupted functions. The working group concluded that deterministic methods were appropriate for establishing conservative levels of ground motion for consideration in the ESF design, and

probabilistic methods were appropriate for confirming that the resulting motions are unlikely to be exceeded during the operating lifetime of the ESF. The recommendations, which were based on available site-specific seismic and geologic data, include design parameters for natural earthquakes that may occur at or near the potential repository site and for underground nuclear explosions (UNE) that may occur at the Nevada Test Site (NTS) and are given in Table 4-8.

Recommended surface-control motion values that are used for the natural earthquake design are 0.30 g horizontal acceleration and 30.0 cm/s peak horizontal velocity (Subramanian et al., 1990; Table 2-1). Subramanian et al. recommend the use of control motions 1.67 times these design-basis values for performance evaluations of the ESF.

Attempts to catalogue records of the performance of underground excavations subjected to seismic loading and develop simple empirical design criteria have indicated a damage threshold of approximately 20 cm/s (8 in./s). No damage should be experienced if the peak particle velocity is beneath that threshold. It is important to note, however, that ground motion resulting from earthquakes can last for several seconds, subjecting the excavation to repeated stress cycles; the number of stress cycles is critical to determining how much permanent deformation will occur within a rock mass around a tunnel when subjected to earthquake loading.

Phillips and Luke (1991) conducted at Tunnel Dynamics Experiment (TDE) to document tunnel damage corresponding to measured and observed ground motions and compared the TDE ground motions with the design basis motions for Yucca Mountain. Their analysis indicated that the design basis motions are relatively small and can be accommodated in the design of the repository drifts.

Implications of seismic loading for the near field environment are that over extended times, the drifts may experience shaking. At the elevated temperature and stress conditions around openings, they may be less stable than during the preclosure and spalling may occur. Backfill of the drifts will prevent contact between this rock and the surface of the cansiter. Kana et al. (1989) recently reviewed the literature on seismic loading for an underground repository and found that because studies completed to date have ignored both time-dependent fracture properties and the duration of shaking, they are of limited use in predicting the rock response to seismic loading by earthquakes. They conclude that further investigation is needed to resolve this issue.

4.4 Geomechanics Modeling

4.4.1 Discussion of Model Approaches

Available Approaches

As mentioned in the above discussion, the rock mass forming the NFE is expected to be a fractured, welded tuff. Several numerical codes have been developed for simulation of rock mass behavior which provide for discrete cracks and fractures. These codes employ finite element (FEM), distinct element, and boundary element numerical techniques, and can incorporate a wide variety of constitutive models. Some have been generalized to three dimensions. To predict rock damage over long periods, and at changing temperature and moisture conditions, existing codes must accommodate the appropriate constitutive equations for elasto-plastic moduli of the rock mass, nonlinear properties of the joints, and fracture propagation. Included properties of the rock are compressive and tensile strength, coefficient of friction, fracture stiffness, and fracture toughness, among others. The codes use these parameters along with boundary stresses and thermally induced stresses to obtain a stress distribution throughout the region of interest in the NFE.

The most common modeling approach utilizes either the finite element or finite difference technique. In this approach, the rock mass is assumed to be a continuum, and the network of cracks and fractures contained in the rock behave in a manner similar to an individual crack. Equations describing the response of an ensemble of cracks is assumed to be identical in form to that describing the response of a single isolated crack. These models handle the creation of new cracks and fracture in various ways. One method is to derive a damage vector D which describes the number of cracks and fractures accumulated during the entire history of deformation (Costin, 1987).

One numerical code which uses a time-dependent finite difference algorithm is called FLAC, which is an acronym for Fast Lagrangian Analysis of Continua. This code is capable of treating both mechanical and thermally induced stresses and deformations. In this code, materials are represented by arbitrarily shaped, quadrilateral zones, and several built-in constitutive models are available for describing material behavior. FLAC is often used in 2-D, assuming plane strain geometry, and linear mechanical and thermal properties where mechanical properties (e.g., elastic moduli) and thermal properties (e.g., thermal expansion

coefficient) are independent of stress and temperature. Constitutive relations are often either isotropic elastic or else make use of the ubiquitous joint model capability of the FLAC code. The thermal response is usually isotropic heat conduction. FLAC has recently become available in 3-D, and this new version is currently being configured to allow simulation of the 3-D stress and displacement field in the NFE over time (see discussion below).

Another widely available code is ABAQUS. This is a 3-D finite element code with capability for time-dependent analysis of thermal and mechanical behavior. The numerical model is weakly coupled in the sense that the temperature field produces thermal stresses, but that these stresses do not in turn influence temperatures. The temperature field is calculated as a function of time from a thermal diffusion model. The mechanical model uses the temperature field at various times to apply thermal loading.

The distinct element approach represents a fundamentally different approach to analysis of the mechanical behavior of a fractured rock mass. In the distinct element method, the rock mass is composed of an assembly of deformable blocks that are interfaced by discontinuities. In some of the distinct element models the blocks are discretized by means of triangular zones where the strains are assumed to be constant. In a distinct element code, fractures in the rock mass are entered individually. One of the most commonly used distinct element codes is called UDEC, and Millard et al. (1995) discuss the use of UDEC in a thermal-hydro-mechanical simulation.

Another very different type of modeling available for study of the NFE is statistical modeling. This type of modeling can be used to study fracture processes as well a deformation and stress in rock especially at elevated temperatures and at long times (Blair, 1994). It can be used to construct ideal systems in which all physical properties are known; this allows the effect of rock heterogeneity on the overall rock behavior to be examined in a quantitative way. In a statistical model, the body of interest is simulated using a lattice or a network of sites, bonds, or both. The behavior of each site or bond is governed by simple, one-dimensional (1-D) rules. For instance, a material may be represented by a network of springs, and each spring is assigned a modulus and a breaking strength. Stress, displacement, and/or temperature contidions are then applied, and the network is solved to determine the stress in each spring. If for a particular spring the stress exceeds the strength assigned to the spring, it is "broken" and removed from the network. Lattices of sites can be used in the same manner, or a network of sites and bonds can be

constructed where both sites and bonds have properties. This approach provides a way to study complex systems using simple elements. Using simple brittle-bond elements this type of model can produce globally ductile behavior for a network where material shows strain-softening.

One of the major advantages of a statistical model for studying fracture in rock is that local heterogeneity can be incorporated very easily. Statistical models include a variety of lattice, network, molecular-dynamics, cellular-automata, field-theory, and other pseudo-continuum models. Herrmann and Roux (1990) have compiled a comprehensive volume describing statistical models and how they can be used to study fracture in rock.

Validity Studies

An international co-operative research project was established for theoretical and experimental studies of coupled thermal, hydrological, and mechanical processes in hard rocks. This project is called DECOVALEX and is described by Jing, Tsang, and Stephansson (1995). In this work, different mathematical models and computer codes have been used to study problems of interest to geologic disposal of nuclear waste. In particular, 11 codes were evaluated including both 2-D and 3-D finite element codes in which the rock was modeled as a porous/fracture media and a 2-D discrete element code in which the rock was modeled as discrete deformable block assemblages. Much of the work done for DECOVALEX is documented in a special issue of the *International Journal of Rock Mechanics* (Stephansson, 1995).

As part of the DECOVALEX program, two inter-code bench mark comparisons were carried out. The bench mark test BMT1 considered a large-scale (km) mass of rock and is described by Millard et al. (1995). The bench mark problem BMT2 involved a system of nine blocks of intact hard rock separated by two pairs of soft fractures and is described by Chan et al. (1995). For each of these exercises, both finite element and distinct element methods were used. Chan et al. (1995) found that for BMT2, heat convection significantly affects the distribution of temperature, thermal stresses, and displacements, and that the predominant coupled effect is fracture closure caused by thermal expansion of the rock blocks. Thus, coupled models of the near field need to incorporate this effect. Results for DECOVALEX also indicate that for studies BMT1 and BMT2, the different modeling techniques produced very similar results. This indicates that use of the continuum codes is merited for study of the near field. This is important because continuum codes are generally easier to use than the distinct element codes.

Other work conducted in conjunction with the DECOVALEX program includes development of an analytical solutions for coupled thermo-hydro-mechanical behavior by Rehbinder (1995), and study of thermal-mechanical-hydrological behavior of sparsely fractured rock by Nguyen and Selvadurai (1995). In addition, Jiao and Hudson (1995) have presented a fully coupled model for rock engineering systems.

Model Development

One of the necessary tasks for simulation of the geomechanical behavior in the near field is coupling of the thermal-mechanical models to the sophisticated hydro-thermal models used by the hydrologic community (discussed in Chapter 1). Recently, we have initiated coupled 3-D modeling of thermal-mechanical-hydrologic behavior of the near field. The methodology being used to model the coupled behavior is as follows. Thermal-hydrologic models are used to compute the temperature distribution, this information is then passed to the thermal-mechanical model for computation of stress and deformation fields. The thermal-mechanical model is set-up with the same grid as the thermal-hydrologic model (see Chapter 1, Fig. 1.10.5.2.1). The particular models being used are NUFT for the thermal-hydrologic behavior, and FLAC-3D for the thermal-hydrologic behavior. Progress to date includes completion of the translating program which passes the NUFT grid into FLAC-3D, and initial testing of the mechanical behavior using this grid.

As mentioned above, statistical methods also offer promise for the study of rock behavior over long periods in the NFE and Blair (1994) has developed a statistical model for fracture of rock in compression that allows rock heterogeneity to be introduced at a variety of scales. This model utilizes a *field theory* approach to the analysis of fracture, and incorporates the concept of superposition and the techniques of boundary element analysis and percolation theory to form a simple yet powerful method for the study of progressive fracture of rock. A conduction temperature model has been implemented into this *field-theory* code and using this or other statistical models, temperature-dependent behavior could be linked to the chemical state of any given site. This could be used to evaluate the behavior of Topopah Spring Tuff at conditions equivalent to those expected in the NFE. This formation is known to contain significant amounts of the mineral cristobalite and at temperatures between 175° and 225°C this mineral undergoes a phase transformation and expands in volume by 5% or more. In addition, bound water may be given off and flash to steam when this phase transformation occurs. This

provides a considerable amount of energy at the site of the mineral. The model could be used to simulate the mechanical effects of this phase transformation by assigning a portion of the sites to be cristobalite sites and imparting some special properties to these sites. When temperature reaches the transformation temperature, these sites break and impart strain energy to the system. Chemistry-dependent properties could also be included by assigning to each site an appropriate chemical parameter(s) that represent the chemical state and a timer. For time-dependent strength, or strength that is dependent on time and chemical environment, the time and chemical environment can be tracked and at time *t* the strength of the site is decreased.

4.4.2 Applications to the Near Field Environment at Yucca Mountain

Blair, Berge, and Wang (1995) analyzed the thermal mechanical behavior of a 3m x 3m x 5m block of fractured rock as part of the analysis done in anticipation of the Large Block Test (LBT) planned for Fran Ridge near Yucca Mountain (Lin et al. 1995). The purpose of this work was to provide analysis and interpretation of coupled thermal-mechanical-hydrological behavior of the block as it is heated. Particular objectives of the modeling were to aid in the experimental design of the test, to evaluate different thermal and constitutive models, and to evaluate different numerical methods. In this study, thermal-mechanical simulations of the heat-up phase of the LBT were conducted using two different numerical codes that are commercially available, a 2-D finite difference model (FLAC, Itasca, 1993) and a 3-D finite element model (ABAQUS).

The purpose of this initial numerical modeling was to calculate temperatures, stresses, and displacements in two and three dimensions for a simplified representation of the large block. In reality, numerous joints and fractures complicate the behavior of the large block significantly. Nonetheless, these simulations provide a general understanding of the thermal-mechanical behavior to be expected in the LBT.

In these simulations, the gridding used in the FLAC models was similar to that used by Lee (1995) for hydrothermal modeling. The second method considered is the 3-D finite element method, and the code ABAQUS was used to evaluate this method. In the 3-D simulations only one-quarter of the block was modeled; therefore, the two symmetry planes were given boundary conditions of zero displacement normal to the plane. ABAQUS requires many of the same material properties as FLAC, and for the simulations conducted in this study, the mechanical

and thermal properties input to ABAQUS were identical to those used in the FLAC elastic model. In the ABAQUS modeling, an elastic model was used to simulate the large block, and no viscoelastic properties or fracture zones were used.

Blair, Berge, and Wang (1996) show that the predicted temperature fields agree well with those predicted by Lee (1995) using a code that incorporates a more sophisticated thermal-hydrological model. Two simulations were conducted in which discrete fractures present in the large block were simulated, and lower levels of stress were predicted in these simulations, indicating that the presence of compliant fractures may reduce the stress levels.

The 2-D, plane strain, FLAC model was constructed in a plane orthogonal to the heater holes proposed for the LBT. The thermal predictions made with this code show a 2-D temperature field near the heaters at early times. At later times, the code predicts a temperature field that is nearly 1-D because all the walls are insulated. Temperature fields in the 3-D simulation were very similar to those predicted by the 2-D FLAC model. For example, the temperature at the top of the block is approximately 65°C after 60 days in the 3-D model and approximately 70°C after 55 days in the 2-D model.

The differences are greater between the 2-D and 3-D mechanical models. The plane strain approximation used in the 2-D model assumes that the length of the heater direction is long compared with the height and width of the block. Further, the plane strain model does not incorporate the stress-free boundary faces parallel to the model plane. The plane strain model generates a large, compressive normal stress in the heater direction to suppress the thermal expansion in that direction.

Blair, Berge, and Wang (1995) conclude that the thermal-mechanical FLAC and ABAQUS modeling produced temperature fields similar to that of Lee (1995) who used a code which contains a more sophisticated thermal-hydrologic model. This suggests that the FLAC and ABAQUS codes could be used with a thermal-hydrological model to better investigate coupled processes. The 2-D modeling was faster and was useful for exploring effects of different constitutive models, but was unable to simulate the outside face of the large block where stresses are highest. This is because the plane strain assumption is equivalent to assuming that the 2-D model lies at the center of the block. Note that most of the instrumentation in the LBT will be located on the outside surface of the block. The 3-D modeling required an order of magnitude more in computer time, but was able to estimate maximum stresses and displacements everywhere in the block's volume.

4.5 References

Arulmoli, K., and C. M. St. John (1987), *Analysis of Horizontal Waste Emplacement Boreholes of a Nuclear Waste Repository in Tuff,* Sandia National Laboratories, Albuquerque, NM, SAND86-7133.

Atkinson, B. K., and P. G. Meredith (1987), "The Theory of Subcritical Crack Growth with Applications to Minerals and Rocks," Fracture Mechanics of Rocks, B. K. Atkinson, Ed. (Academic Press, London).

Barton, N. R., R. Lien and J. Lunde, 1994, "Engineering Classification of Rock Masses for the Desing of Tunnel Support," *Rock Mechanics*, 6, 189-236, (NNA.870406.0237)

Bauer, S. J., and J. F. Holland (1987), "Analysis of In Situ Stress at Yucca Mountain," Proc. of the 28th U.S. Symp. on Rock Mechanics, I. Farmer, Ed. (A. A. Balkema, Rotterdam, The Netherlands), pp. 707–713.

Bauer, S. J., J. F. Holland, and D. K. Parrish (1985), "Implications About In Situ Stress at Yucca Mountain," Proc. of the 26th U.S. Symp. on Rock Mechanics, E. Ashworth, Ed. (A. A. Balkema, Rotterdam, The Netherlands), pp. 1113–1120.

Bieniawski, Z.T., 1979. Engineering Rock Mass Classification, Wiley-Interscience Publication, John Wiley & Sons, New York. (NNA.901005.0044)

Blair, S. C. (1994), "Analysis of compressive fracture in rock using statistical techniques," Ph.D. Thesis, Dept. of Materials Science and Mineral Engineering, U. C. Berkeley, Berkeley, CA.

Blair, S. C. and P. A. Berge, "Uniaxial compression behavior of small blocks of welded tuff," in *Proceedings of the 1996 Int'l High Level Radioactive Waste Management Conference*, April 29 - May 3, 1996, Las Vegas, NV, published by American Nuclear Soc and American Society of Civil Engineers, pp. 409-411.

Blair, S. C, P. A. Berge, and H. F. Wang (1995), "Geomechanical Analysis of the Large Block Test," UCRL-ID-122898, Lawrence Livermore National Laboratory, Livermore, CA.

Blair, S. C., J. M. Kelly, O. Pine, R. Pletcher, and P. A. Berge, "Effect of radiation on the mechanical properties of Topopah Spring tuff," UCRL-ID-122899, Lawrence Livermore National Laboratory, Feb. 1996.

Brechtel, C.E., M. Lin, E. Martin, and D.S. Kessel, 1995. Geotechnical Characterization of the North Ramp of the Exploratory Studies Facility, SAND95-0488/1 and -0488/2, Yucca Mountain Site Characterization Project, Sandia National Laboratories, Albuquerque, NM. (MOL.19950502.0004)

Brechtel, C.E., S. C. Carlisle, and J. Pott, 1993. "Rock Mass Quality Estimation, North Ramp Starter Tunnel, Upper Bench," SLTR93-7001, DTN:SNF28021693001.001, Sandia National Laboratories, Albuquerque, NM.

Brown, S.R. 1994. Simple Mathematical Model of a Rough Fracture, SAND92-2216J, Sandia National Laboratories, Albuquerque, NM. MOL 19941006.0040.

Chan, T, K., Khair, L. Jing, M. Ahola, J. Noorishad, and E. Vuillod (1995), "International comparison of coupled thermo-hydro-mechanical models of a multiple-fracture bench mark problem: DECOVALEX Phase I, bench mark test

2," in Thermo-Hydro-Mechanical Coupling in Rock Mechanics, *Int. J. Rock Mech. Min. Sci. & Geomech. Abstr.*, 32(5).

Christianson, M. C., and B. Brady (1989), *Analysis of Alternative Waste Isolation Concepts*, U.S. Nuclear Regulatory Commission, Washington, DC, NRC-FIN D1016, NUREG/CR-5389.

Cohen, L. H., and W. Klement, Jr. (1975), "Differential Thermal Analysis Investigation of the High-Low Cristobalite Inversion under Hydrostatic Pressure to 7 kbar," *Jour. Am. Cerm. Soc.* 58(5-6), 206–208.

Connolly, J. R. (1991), Mineralogy, Petrology and Whole-Rock Chemistry of Selected Mechanical Test Samples of Yucca Mountain Tuffs, Sandia National Laboratories, Albuquerque, NM, SAND90-7058. (101 pp., accession number NNA.911202.0029)

Connolly, J. R. (1994), Mineralogical, Petrologic, and Whole-Rock Chemical Analysis of Fran Ridge Tuff Used in the SNL Backfill Thermal Properties Experiment, FR-88-62-SNL Petrology Report, written communication from Univ. of New Mexico to Sandia National Laboratories.

Cooper, H. W., and G. Simmons (1977), "The Effects of Cracks on Thermal Expansion of Rocks," *Earth and Planetary Science Letters* 36, 404.

Costin, L. S. (1987), "Time-dependent deformation and failure in Fracture Mechanics of Rock," B. K. Atkinson editor, pp. 167–215, Academic Press, London. ISBN: 0-12-066265-5.

DOE (U.S. Department of Energy) (1994), *Yucca Mountain Project Reference Information Base, Version 4*, Yucca Mountain Site Characterization Project Office, Las Vegas, NV, YMP/CC-0002. (NNA 890330.0077)

Durham, W. B., J. M. Beiriger, M. Axelrod, and S. Trettenaro (1986), "The Effect of Gamma Radiation on the Strength and Elasticity of Climax Stock and Westerly Granites," *Nuclear and Chemical Waste Management* 6, 159–168.

Ehgartner, B. L., and R. C. Kalinski (1988), *A Synopsis of Analyses (1981–1987) Performed to Assess the Stability of Underground Excavations at Yucca Mountain*, Sandia National Laboratories, Albuquerque, NM, SAND88-2294.

Gertsch, R. and L. Ozdemir (1992), Performance Prediction of Mechanical Excavators from Linear Cutter Tests on Yucca Mountain Welded Tuffs, Sandia National Laboratories, Albuquerque, NM, SAND91-7038. (accession number NNA.920819.0247)

Hardy, M.P., and S.J. Bauer, 1991. Drift Design Methodology and Preliminary Application for the Yucca Mountain Site Characterization Project, SAND89-0837, Sandia National Laboratories, Albuquerque, New Mexico. (NNA.910808.0105)

Herrmann, H. J., and S. Roux (1990), *Statistical Models for the Fracture of Disordered Media* (North-Holland Elsevier Science Publishers B. V.).

Itasca Consulting Group, Inc. (1993), *FLAC User's Manual*, vol. I-III, Minneapolis, MN.

Jiao, Y., and J. A. Hudson (1995), "The full-coupled model for rock engineering systems", *Int. J. Rock Mech. Min. Sci. & Geomech. Abstr.* 32(5).

Jing, L., C.-F. Tsang, and O. Stephansson (1995), "DECOVALEX-an international co-operative research project on mathematical models of coupled THM processes

for safety analysis of radioactive waste repositories," *Int. J. Rock Mech. Min. Sci. & Geomech. Abstr.* 32,5.

Kana, D. D., B. H. G. Brady, B. W. Vanzant, and P. K. Nair (1989), *Critical Assessment of Seismic and Geomechanics Literature Related to a High-Level Nuclear Waste Underground Repository*, Nuclear Regulatory Commission, Center for Nuclear Waste Regulatory Analyses, San Antonio, Texas.

Kemeny, J., and N. Cook (1990), "Rock Mechanics and Crustal Stress," Demonstration of a Risk-Based Approach to High-Level Waste Repository Evaluation, R. K. McGuire, Ed., Electric Power Research Institute, Palo Alto, CA, EPRI-NP-7057.

Keskar, N. R., and J. R. Chelikowsky (1993), Anomalous Elastic Behavior in Crystalline Silica, *Phys. Rev. D*, **48**, 16,227-16,233.

Lee, K. H. (1995), "Progress report on pre-test calculations for the Large Block Test," UCRL-ID-118669, Lawrence Livermore National Laboratory, Livermore, CA.

Lin, M., M. P. Hardy, and S. J. Bauer (1993a), Fracture Analysis and Rock Quality Designation Estimation for the Yucca Mountain Site Characterization Project, Sandia National Laboratories, Albuquerque, NM, SAND92-0449. (accession number NNA.921204.0012)

Lin, M., M. P. Hardy, J. F. T. Agapito & Associates, and S. J. Bauer (1993b), Rock Mass Mechanical Property Estimations for the Yucca Mountain Site Characterization Project, Sandia National Laboratories, Albuquerque, NM, SAND92-0450. (accession number NNA.921204.0013)

Lin, W. L., D. G. Wilder, J. A. Blink, S. C. Blair, et al. (1994), "The testing of thermal-mechanical-hydrological-chemical processes using a large block," in *Proceedings of the 5th Intl. High-Level Rad. Waste Mgmt. Conf.*, Las Vegas, ASCE (May, 1994).

Lin, W. D.G. Wilder, J. A. Blink, S. C. Blair, T. A. Buscheck, W. E. Glassley, K. Lee, M. W. Owens, & J. J. Roberts, (1995) "A heated large block test for high level nuclear waste management," in *Proceedings of the Second International Conference on the Mechanics of Jointed and Faulted Rock*, Vienna, Austria, April, 1995.

MacDougall, H. R., L. W. Scully, and J. R. Tillerson, (Compilers) (1987), *Site Characterization Plan Conceptual Design Report*, Sandia National Laboratories, Albuquerque, NM, SAND84-2641.

Martin, R. J., III, R. H. Price, P. J. Boyd, and J. S. Noel (1993), Unconfined Compression Experiments on Topopah Spring Member Tuff at 22° C and a Strain Rate of 10^{-9} s^{-1}: Data Report, Sandia National Laboratories, Albuquerque, NM, SAND91-0894. (accession number NNA.930728.0088)

Martin, R. J., III, R. H. Price, P. J. Boyd, and R. W. Haupt (1992), Anisotropy of the Topopah Spring Member Tuff, Sandia National Laboratories, Albuquerque, NM, SAND91-0894. (28 pp., accession number NNA.920522.0041)

Martin, R. J., J.S. Noel, P.J. Boyd, and R.H. Price, 1996, "Thermal expansion as a function of confining pressure for welded tuff from Yucca Mountain," in *Proceedings of the 2nd North American Rock Mechanics Symposium*, Montreal, Canada, June 19-21, 1996, Aubertin, Hassani, and Mitri eds. Balkema. Rotterdam.

Martin, R. J., R. H. Price, P. J. Boyd, and J. S. Noel (1994), Bulk and Mechanical Properties of the Paintbrush Tuff Recovered from Borehole USW NRG-6: Data

Report, Sandia National Laboratories, Albuquerque, NM, SAND93-4020. (92 pp., accession number MOL.19940811.0001)

Martin, R. J., R. H. Price, P. J. Boyd, and J. S. Noel (1995a), Bulk and Mechanical Properties of the Paintbrush Tuff Recovered from Borehole USW NRG-7/7A: Data Report, Sandia National Laboratories, Albuquerque, NM, SAND94-1996. (93 pp., accession number MOL.19950316.0087)

Martin, R. J., III, R. H. Price, P. J. Boyd, and J. S. Noel (1995b), Creep in Topopah Spring Member Welded Tuff, Sandia National Laboratories, Albuquerque, NM, SAND94-2585. (53 pp., accession number MOL.19950502.0006)

Meike, A., and Glassley, W. E. (1990), In-Situ Observation of the Alpha/Beta Cristobalite Transition Using High Voltage Electron Microscopy, MRS Symp. Proc., 176, 631-639.

Millard, A., N. Durin, A. Stietel, A. Thoraval, E. Vuillod, H. Baroudi, F. Plas, A. Bougnoux, G. Vouille, A. Kobayashi, K. Hara, T. Fujita and Y. Ohnishi (1995), "Discrete and continuum approaches to simulate the thermo-hydro-mechanical couplings in a large, fractured rock mass," *Int. J. Rock Mech. Min. Sci. & Geomech. Abstr.* 32(5).

Nguyen, T. S., and A. P. S. Selvadurai (1995), "Coupled thermal-mechanical-hydrological behaviour of sparsely fractured rock: implications for nuclear fuel wasted disposal," *Int. J. Rock Mech. Min. Sci. & Geomech. Abstr.* 32(5).

Nimick, F. B. (1990), *The Thermal Conductivity of Seven Thermal Mechanical Units at Yucca Mountain, Nevada,* Sandia National Laboratories, Albuquerque, NM, SAND88-1387.

Nimick, F. B., R. G. Van Buskirk, and A. F. McFarland (1987), *Uniaxial and Triaxial Compression Test Series on Topopah Spring Member from USW G-2, Yucca Mountain, Nevada,* Sandia National Laboratories, Albuquerque, NM, SAND85-0703.

Olsson, W. A. (1987), *Rock Joint Compliance Studies,* Sandia National Laboratories, Albuquerque, NM, SAND86-0177.

Olsson, W. A. (1988), *Compliance and Strength of Artificial Joints in Topopah Spring Tuff,* Sandia National Laboratories, Albuquerque, NM, SAND88-0660.

Olsson, W. A. (1994), The Effect of Sliding Velocity on the Mechanical Response of an Artificial Joint in Topopah Spring Member Tuff, Sandia National Laboratories, Albuquerque, NM, SAND92-2333. (18 pp., accession number NNA.940209.0001)

Olsson, W. A., and S. R. Brown (1994), Mechanical Properties of Seven Fractures from Drillholes NRG-4 and NRG-6 at Yucca Mountain, Nevada, Sandia National Laboratories, Albuquerque, NM, SAND94-1995. (29 pp., accession number MOL.19941007.0081)

Olsson, W. A., and A. K. Jones (1980), *Rock Mechanics Properties of Volcanic Tuffs from the Nevada Test Site,* Sandia National Laboratories, Albuquerque, NM, SAND80-1453.

O'Neal, W. C., D. W. Gregg, J. N. Hockman, E. W. Russell, and W. Stein (1984), *Preclosure Analysis of Conceptual Waste Package Designs for a Nuclear Waste Repository in Tuff,* Lawrence Livermore National Laboratory, Livermore, CA, UCRL-53595.

Phillips, J. S., and B. A. Luke (1991), Tunnel Damage Resulting from Seismic Loading, Sandia National Laboratories, Albuquerque, NM, SAND90-1721C. (27 pp., accession number NNA.910424.0001)

Price, R. H. (1983), *Analysis of Rock Mechanics Properties of Volcanic Tuff Units from Yucca Mountain, Nevada Test Site*, Sandia National Laboratories, Albuquerque, NM, SAND82-1315.

Price, R. H. (1986), *Effects of Sample Size on the Mechanical Behavior of Topopah Spring Tuff*, Sandia National Laboratories, Albuquerque, NM, SAND85-0709.

Price, R. H., and A. K. Jones (1982), *Uniaxial and Triaxial Compression Tests Series on Calico Hills Tuff*, Sandia National Laboratories, Albuquerque, NM, SAND82-1314.

Price, R. H., F. B. Nimick, J. R. Connolly, K. Keil, B. M. Schwartz, and S. J. Spense (1985), *Preliminary Characterization of the Petrologic, Bulk, and Mechanical Properties of a Lithophysal Zone Within the Topopah Spring Member of the Paintbrush Tuff*, Sandia National Laboratories, Albuquerque, NM, SAND84-0860.

Price, R. H., J. R. Connolly, and K. Keil (1987), *Petrologic and Mechanical Properties of Outcrop Samples of the Welded, Devitrified Topopah Spring Member of the Paintbrush Tuff*, Sandia National Laboratories, Albuquerque, NM, SAND86-1131.

Price, R. H., R. J. Martin, III, and R. W. Haupt (1994), *The Effect of Frequency on Young's Modulus and Seismic Wave Attenuation*, Sandia National Laboratories, Albuquerque, NM, SAND92-0847. (50 pp.)

Pusch, R. (1989), *Influence of Various Excavation Techniques on the Structure and Physical Properties of Near-Field Rock around Large Boreholes*, Swedish Nuclear Fuel and Waste Management Co. (SKB), Stockholm, Sweden, Technical Report 89-32.

Rehbinder (1995), "Analytical solutions of stationary coupled thermo-hydro-geomechanical problems," *Int. J. Rock Mech. Min. Sci. & Geomech. Abstr.* **32**(5).

Roberts, J. R. and W. Lin, 1995, "Permeability of Fractured Tuff as Functions of Temperature oand Confining Pressure, in *Proceedings of the 19965Int'l High Level Radioactive Waste Management Conference*,, Las Vegas, NV, published by American Nuclear Soc and American Society of Civil Engineers

Scott, R. B., and M. Catellanos (1984), *Stratigraphic and Structural Relations of Volcanic Rocks in Drill Holes USW GU-3 and USW G-3, Yucca Mountain, Nye County, Nevada*, U.S. Geological Survey, Denver, CO, OFR-84-491.

Stephansson, O. (1995), "Introduction to Special Issue on Thermo-Hydro-Mechanical Coupling in Rock Mechanics," *Int. J. Rock Mech. Min. Sci. & Geomech. Abstr.* **32**(5).

Stock, J. M., J. H. Healy, and S. H. Hickman (1984), *Report on Televiewer Log and Stress Measurements in Core Hole USW G-2, Nevada Test Site*, U.S. Geological Survey, Denver, CO, OFR-84-172.

Stock, J. M., J. H. Healy, S. H. Hickman, and M. D. Zoback (1985), "Hydraulic Fracturing Stress Measurements at Yucca Mountain, Nevada, and Relationship to Regional Stress Field," *J. Geophys. Res.* 90(B10), 8691–8706.

Subramanian, C. V., J. L. King, D. M. Perkias, R. W. Modd, A. M. Richardson, J. C. Calovini, E. VanEeckhout, and D. D. Emerson (1990), *Exploratory Shaft Seismic*

Design Basis Working Group Report, Sandia National Laboratories, Albuquerque, NM, SAND88-1203.

Teufel, L. A., and M. J. McNamee (1991), Tensile Strength Testing of Topopah Spring Tuff, Sandia National Laboratories, Albuquerque, NM, SAND91-0044. (13 pp., accession number NNA.910322.0056)

Wibowo, J., B. Amadei, S. Sture, R. H. Price, and A. B. Robertson (1993), Effect of Boundary Conditions on the Strength and Deformability of Replicas of Natural Fractures in Welded Tuff: Data Report, Sandia National Laboratories, Albuquerque, NM, SAND92-1853. (accession number NNA.930907.0001)

Wilder, D. G. (1990), "Engineered Barrier Systems and Canister Orientation Studies for the Yucca Mountain Project, Nevada," Proc. of International Symp. on Unique Underground Structures (Colorado School of Mines Press, Colorado).

Yehaneh-Hari, A., D. J. Weidner, and J. B. Parise (1992), Elasticity of α-Cristobalite: A Silicon Dioxide with a Negative Poisson's Ratio, Science, 257, 650-652.

Zimmerman, R. M., R. L. Schuch, D. S. Mason, M. L. Wilson, M. E. Hall, M. P. Board, R. P. Bellman, and M. L. Blanford (1986), Final Report: G-Tunnel Heated Block Experiment, Sandia National Laboratories, Albuquerque, NM, SAND84-2620.

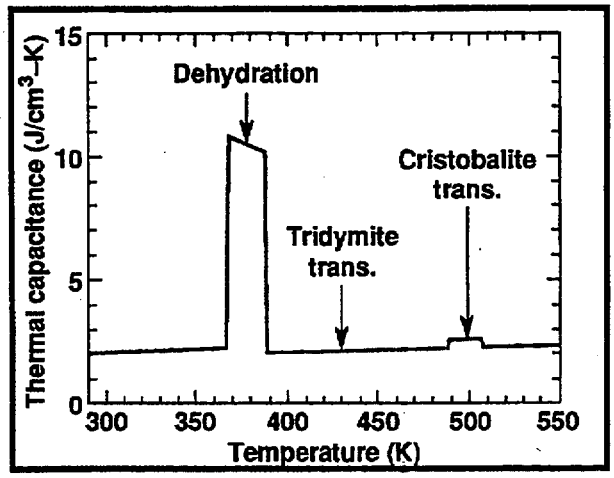

Figure 4-1. Rock-mass thermal capacitance of unit TSw2 showing the effects of dehydration and cristobalite transformation. The temperature of tridymite transformation is shown for reference. Adapted from the Yucca Mountain Project Reference Information Base (DOE, 1994).

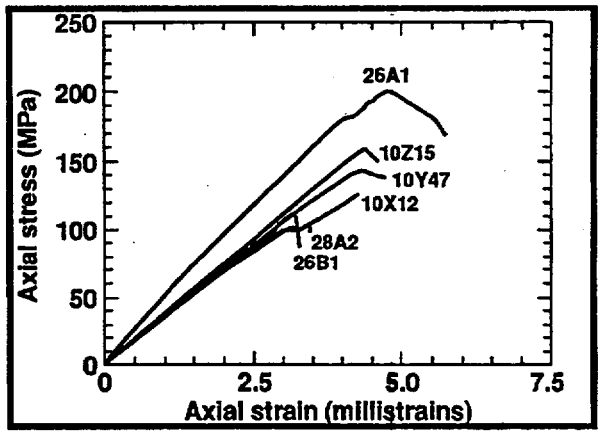

Figure 4-2. Plots of axial stress vs axial strain for uniaxial measurements on 50.8-mm saturated Tpt samples at 22°C. Measurements were taken at a strain rate of $10^{-5}s^{-1}$. Adapted from Price (1986).

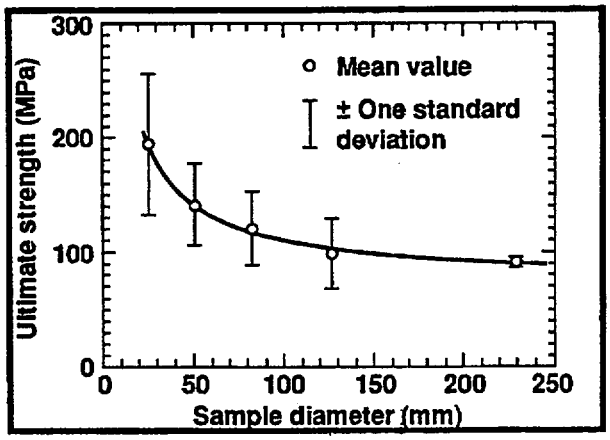

Figure 4-3. Plot of ultimate strength vs sample diameter for uniaxial measurements on saturated Tpt samples at 22°C. Measurements were taken at a strain rate of $10^{-5}s^{-1}$. Adapted from Price (1986).

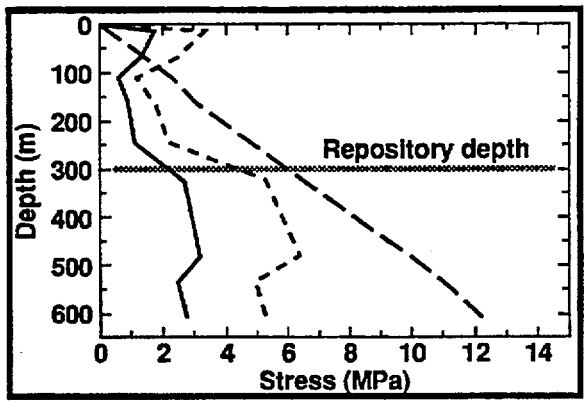

Figure 4-4. Stress profile along an exploratory shaft near the Exploratory Studies Facility. The solid line is the minimum horizontal stress, the long dashed line is the maximum horizontal stress, and the short dashed line is the vertical stress. Adapted from the *Yucca Mountain Project Reference Information Base* (DOE, 1994).

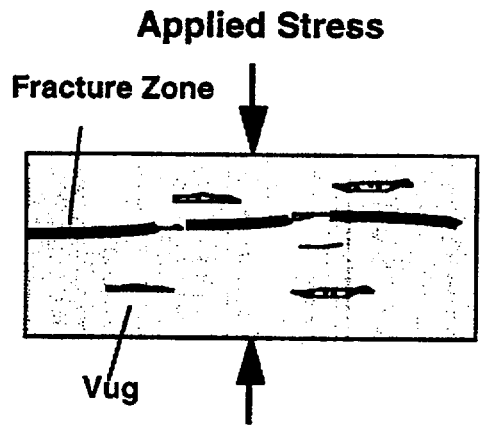

Figure 4-5. Schematic of compression test on 0.5m scale block of Topopah Spring tuff.

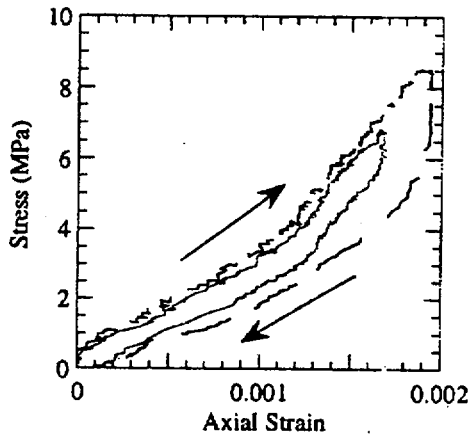

Figure 4-6. Stress-strain behavior for repeated loading of a single fracture in a 0.5m block of Topopah Spring tuff. Adapted from Blair and Berge, 1996.

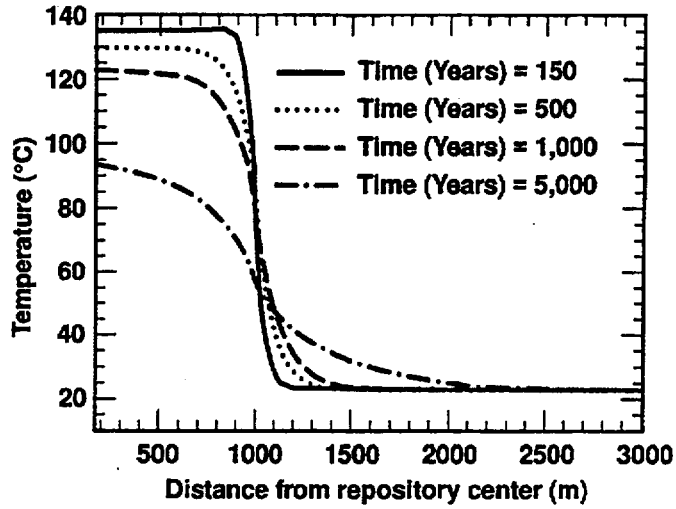

Figure 4-7. Temperature profile predicted in the rock forming the repository at 150, 500, 1000, and 5000 yrs after emplacement of waste at a thermal density of 83.4 MTU per acre.

Table 4-1. Physical and thermal properties of rock in the Topopah Spring welded unit, lithophysae-poor layer (TSw2).

Parameter	Value
Physical Properties	
Porosity (%)	12 ± 4a
Grain density (g/cm^3)	2.55 ± 0.03a
Bulk density at in situ saturation (g/cm^3)	2.30 ± 0.09a
Dry bulk density (g/cm^3)	2.22 ± 0.10a
Thermal Properties	
Dry matrix thermal conductivity (W/mK)	2.51 ± 0.17[b]
Saturated matrix thermal conductivity (W/mK)	—
Dry in situ thermal conductivity (W/mK)	2.1 ± 0.2[b]
Saturated in situ thermal conductivity (W/mK)	2.1 ± 0.2[b,c]

a DOE (1994)
b Nimick (1990)
c 0.65 ± 0.19 in situ saturation with lithophysal cavities and fractures assumed dry.

Table 4-2. Coefficients of linear thermal expansion (10^{-6}/°C) for Topopah Spring welded unit, lithophysae-poor layer (TSw2) during heating.

	Temperature Range (°C)						
	25–50°	50–100°	100–150°	150–200°	200–250°	250–300°	
Type	$\bar{\alpha}$ s	$\bar{\alpha}$ s	$\bar{\alpha}$ s	$\bar{\alpha}$ s	$\bar{\alpha}$ s	$\bar{\alpha}$ s	n s
Intact rock	9.1 1.3	8.2 0.8	6.8 0.5	9.7 — 1	— —	— —	9
Very near field	5.4 2.2	8.0 1.5	9.8 1.7	17.0 11.6 12	25.0 15.7 11	35.6 10.8 7	12

$\bar{\alpha}$ = mean coefficient of linear thermal expansion
s = standard deviation of the sample group
n = number of samples analyzed

Table 4-3. Values of rock-mass thermal capacitance for Topopah Spring welded unit, lithophysae-poor layer (TSw2) at selected temperatures (DOE, 1994).

Temperature (°C)	Thermal capacitance (J/cm3K)
25	2.0324
50	2.1280
94	2.2638
95	10.7683
105	10.4690
114	10.1984
115	2.0065
155	2.1114
195	2.1912
235	2.2692
275	2.3410

Table 4-4. Mechanical properties of intact rock for unit TSw2 (DOE, 1994).

Mechanical property	Value
Unconfined compressive strength (MPa)	155 ± 59
Young's modulus (GPa)	32.7 ± 4.6
Poisson's ratio	
USW G-1, USW GU-3	0.22 ± 0.03
USW G-4	0.30 ± 0.05
Cohesion (MPa)	
USW G-2	18.3 ± 5.2
UE-25a#1, USW G-4, USW GU-3	37.8 ± 12.4
Angle of internal friction	
USW G-2	19.7° ± 5.2°
UE-25a#1, USW G-4, USW GU-3	36.5° ± 9.0°

Table 4-5. Values and ranges of principal stresses in the potential repository horizon at Yucca Mountain (Stock et al., 1984, 1985).

Parameter	Average value[a]	Range
Maximum principal stress (vertical)	7.0 MPa (1015 psi)	5.0 to 10.0
Ratio of minimum horizontal stress to vertical stress	0.5	0.3 to 0. 8
Ratio of maximum horizontal stress to vertical stress	0.6	0.3 to 1.0
Bearing of minimum horizontal stress	N57°W	N50°W to N65°W
Bearing of maximum horizontal stress	N32°E	N25°E to N40°E

[a] Average value for a depth of about 0.3 km (1000 ft).

Table 4-6. Corrected linear fracture frequency (m^{-1}) the Topopah Spring welded unit, lithophysae-poor layer (TSw2) at Yucca Mountain (Lin, 1993a).

	0 –10°	10–20°	20–30°	30–40°	40–50°	50–60°	60–70°	70–80°	80–90°
Upper range	0.50	0.60	0.46	0.35	0.35	0.44	0.89	5.92	24.07
Mean	0.25	0.29	0.25	0.22	0.23	0.24	0.56	2.51	11.28
Lower bound	0.05	0.05	0.07	0.05	0.05	0.06	0.09	0.81	2.99

Table 4-7. Comparison of Rock Mass Strength Estimates to Intact Strength Data for Topopah Spring welded unit, lithophysae-poor layer (TSw2), adapted from Brechtel (1995).

Estimated Rock Mass Strength (MPa)	Intact Strength (MPa)	Intact Standard Deviation (MPa)	Ratio of Rock Mass to Intact Strength (%)	Rock Mass Elastic Modulus (GPa)	Rock Mass Poisson's Ratio
18.8	178.5	78.3	10.6	23.51	0.21

All values were computed using Hardy and Bauer (1991) classification 5 which is designed to include 90% of the rock in a particular unit.

Table 4-8. Recommended motions for the design-basis UNE (Subramanian et al., 1990).

Component	Median predicted value	Design-basis UNE values [95% nonexceedance level (1.65 σ)]
Vertical acceleration (g)	0.05	0.2
Radial acceleration (g)	0.03	0.1
Transverse acceleration (g)	0.03	0.1
Vertical velocity (cm/s)	4	9
Radial velocity (cm/s)	4	12
Transverse velocity (cm/s)	3	12
Vertical displacement (cm)	1	2
Radial displacement (cm)	1	3
Transverse displacement (cm)	1	4

Contents

Chapter 5.0 Radiation Effects 5-2
5.1 Reference 5-2

Chapter 5.0 Radiation Effects

Richard A. Van Konynenburg

When the previous report version was being written, we considered waste packages with relatively thin-walled containers. The gamma-ray dose rates outside such packages would be high enough that observable radiation–chemical effects would be produced in the near field, so a detailed discussion of such effects was presented. Since that time, a new waste package design philosophy has emerged. For this design, our objective is to make the waste package walls sufficiently thick, providing enough radiation shielding to reduce the dose rates to levels that will eliminate concerns about radiation–chemical effects on package corrosion (100 R/hr or less and uneventful). No experiments have been funded to determine the dose rate at which effects on corrosion are no longer observed, but based on the literature, it is probably an order of magnitude higher than 100 R/hr, although experiments would be required to confirm this. At such levels, it is likely that effects on important near-field geochemical parameters such as pH and Eh will also be minimal. Certainly, radiation effects will not extend beyond a few centimeters of rock or backfill. Therefore, no further discussion of radiolytic effects will be presented here. Refer to the PNFER (Wilder, 1993) for a discussion of the environmental effects that could occur if the radiation dose were many times higher than the current design allows.

5.1 Reference

Wilder, D. G. (1993), *Preliminary Near-Field Environment Report Volume II: Scientific Overview of Near-Field Environment and Phenomena,* Lawrence Livermore National Laboratory, Livermore, CA, UCRL-LR-107476.

Contents

Chapter 6.0 Introduced (Man-Made) Materials 6-2
6.1 Materials Identification and Evaluation 6-2
6.1.1 Original Post-Construction Conditions 6-2
6.1.2 Evaluation of Materials by Function 6-18
6.1.3 Tracers, Fluids and Materials Database: Retrieval of Information 6-22
6.1.4 Assessment of Materials Considered for Repository Construction 6-24
6.2 Post-Closure Chemical Processes That May Modify Predicted Geochemistry 6-25
6.2.1 Abiotic Chemistry 6-27
6.2.2 Biotic Chemistry (microbially mediated chemistry) 6-58
6.2.3 Discussion 6-74
6.3 Understanding the Processes 6-75
6.3.1 Experimental Studies 6-75
6.3.2 Historical Analogs as Long Term Experiments 6-83
6.3.3 Modeling Activities 6-84
6.4 Summary and Conclusions 6-95
6.5 Acknowledgments 6-95
Appendix A: Polymer Chemistry 6-112
Appendix B: Curing of Cementitious Material 6-116

Chapter 6.0 Introduced (Man-Made) Materials

Annemarie Meike

6.1 Materials Identification and Evaluation

The present appraisal of the potential effects of introduced materials on the chemistry and mineralogy of the post-emplacement environment is presented in three sections. The first section of this chapter seeks to identify potential inherent chemical reactions and uncertainties that are inherent in the pre-closure repository design.

The chemical significance of the materials and the chemical processes that involve them are influenced by temperature, degree of water saturation, fluid composition, and the ratio of material surface area to fluid volume. We expect heat to be generated by the waste packages and some water to enter the near-field environment, which will affect the character of the chemical and hydrological processes and the timing of their occurrence. These processes, which are part of the post-closure perturbation of the repository, are addressed in the second section.

The third section is a discussion of the status of modeling intended to predict the processes, their outcomes, and the timing of events discussed in section 6.5. Ultimately these models will be used in conjunction with geological and hydrological models to describe likely chemical and hydrological interactions among water, the host rock, the waste packages, introduced materials, and organisms. However, even in the absence of such sophisticated modeling capability, an iterative exchange between the identification and evaluation of materials, computer modeling, and performance assessment can positively influence design decisions.

6.1.1 Original Post-Construction Conditions

The original as-built design has inherent chemical reactions which become important parameters for predicting the chemical environment of a waste package (WP). A broad spectrum of materials and organisms may be introduced into a radioactive-waste repository as a result of its construction and operation. More than 260 items used in a mine construction setting (the Exploratory Shaft Facility) were inventoried by West (1988), together with the known chemical effects of those materials at 25°C. A further discussion of materials that could be located in the near-field

environment and some potential chemical consequences has been presented in Rev. 0 of the Near Field Environment Report. However, it is not sufficient to simply identify materials and their chemical effects in isolation. The chemical impact of a material depends upon its context: its concentration, distribution, reaction rates and products, and other materials with which it is in contact or in close proximity. In addition, the heterogeneous distribution of materials will create pH and chemical concentration gradients that may in themselves drive chemical reactions. The examination and comparison of these materials assemblages as chemical systems that influence water chemistry and hydrology will most effectively support design decisions. In order to develop a useful system of comparison and decision making, we identify materials assemblages, or collections of materials that represent the various options that are available to perform a specific function (e.g., transportation, mucking, excavation, and stabilization). The materials assemblages are based on observations drawn from the construction of the Exploratory Studies Facility (ESF).

In this chapter we will need to depart from the terminology of the Waste Isolation Evaluations (WIE) in which it is recognized that the terms "permanent," "non-permanent," and "temporary" are used for materials disbursement in a specific manner. For materials disbursement purposes "temporary" and "non-permanent" refer to items that are removed prior to operation of a potential repository. "Permanent" refers to materials that are used at the site during the operations period, but which may be removed at closure of the potential repository. The WIE therefore uses the words "committed" and "non-committed," in which "non-committed" refers to substances are only those which are not being purposely introduced into the environment and for which reasonable assurance exists that the bulk of the substance would be removed at closure and "committed" refers to substances that are expected to be retained in the environment after closure. Because all of these terms have been applied in such a way as to imply intent, none of them are applicable to the present study. The purpose of the present study is to identify materials that may be introduced into a repository setting, and to determine the longevity of the potential chemical impact, part of which depends on the residence time of the substance. Other factors include concentration, degradation rate and environmental factors. We will use different terminology to underscore our purpose, which is to discover the residence time from actual usage data rather than to record the original intent. For our purpose we will use the terms "short-residence" and "extended-residence."

At present, although the Advanced Conceptual Design (ACD) for the potential Yucca Mountain Repository has been released, many aspects of drift engineering that

are required to carry out that design are not complete. Some materials such as metals, bonding agents, and concrete may serve as active parts of the designed engineered barrier. Other materials that are introduced to serve other purposes, including surveillance (thermocouples, gauges), construction and operation (drilling rigs, roadbeds, exhaust fumes, chemical toilets, concrete, grout, rebar), and lubrication (petroleum-based products, rope dressing) may not be removed because they have either become inaccessible or have not been identified as items to be removed. In normal mining operations extended residence materials also include waste material and spills. The introduced materials will exist in gas, liquid, and solid phases, as inorganic and organic compounds, and in various reactive states. Some materials, such as concrete, may be present in large quantities. As of this writing, precast concrete is being considered as a major part of the non-removable mechanical support system as well as invert material.

Although this lack of information directly affects our present ability to predict the chemistry of the near-field environment, we have the potential to provide input to those engineering decisions that may increase the confidence of future predictions by examining and assessing materials that have a high probability of being used in a repository setting.

6.1.1.1 Evaluation of Materials from ESF Construction

We have monitored excavation practices at the Exploratory Studies Facility (ESF) assuming that the construction methods used at the ESF represent a baseline for standard construction activities in a repository setting. Based on an examination of ESF construction techniques, we have concluded that detailed relational information is key to obtaining good estimates of construction material usage and, thus, our ability to model drift-scale chemical, hydrological and mechanical processes. Our purpose has been to obtain relational information and methods for estimating materials usage during the construction of a proposed repository at Yucca Mountain. Work in this area was initiated in December 1994 and halted in September 1995. We have attempted to determine the extent to which actual materials usage during construction and operation of an actual repository may be known or predicted, in order to more tightly constrain bounding conditions for the chemical impact of introduced materials in the near-field environment.

Materials used. Our expectation and that of many contacts from whom we requested information was that much of the materials usage information should be archived and readily available from the Tracers, Fluids and Materials (TFM) database.

However, these data were not readily available (Meike and Spragge, 1995) as of September 1995. Inadequacies exist in the areas of obtaining, archiving and retrieving data. We understand that, partly because of our needs in this area, some of these inadequacies are presently being addressed.

More specific compositional information will be needed to support the needs of drift-scale modeling. However, in the absence of that information, we have begun to identify and quantify materials usage, and to recognize patterns of usage and deviations from those patterns, in order to build estimation methods and bounding parameters for the usage of various materials. In this report we identify and demonstrate important factors that affect the patterns of usage and, if monitored, will ultimately lead to more accurate predictive capabilities include geology, construction function, regulations, and procedural developments. For example, the pattern of variation between estimated and as-built materials is a function of structural and stratigraphic geological factors. The following observations have been made about materials usage and the relationship of these materials to materials called out in a design plan. In our description of materials usage we will make these important distinctions explicit.

Clearly, extended residence materials will have chemical effects, some of which may significantly impact the post-closure chemistry. What may not be so obvious is that extended residence materials include not only those materials that are explicitly named in a repository design, but also the unspecified and necessary associated materials. For example, a repository design concept that calls for precast invert sections does not necessarily explicitly include the polymer gasket that appears between many of the invert sections in the ESF. Similarly, excelsior, pine 4x4's (cribbing) and other cellulose materials have been placed in open fractures and behind steel sets for stabilization purposes and will probably remain in place permanently. Our documentation of the use of these materials and their functional relationships is well underway, although actual quantities are still to be retrieved from the TFM database when that becomes a possibility. Another category of extended residence, non-explicit materials is spills. Although major efforts have been taken to minimize the accidental introduction of material by reducing the occurrence of spills, cleaning them up when they occur, and reporting them, it is important to quantify that minimum. This includes a thorough documentation of reporting limits (e.g., how much diesel fuel can be spilled before a report must be filed?) and relational information (e.g., hydraulic oil is usually spilled near the TBM), as well as reported amounts.

Even "non-permanent" materials can affect the post-closure chemical environment. Short residence materials may leave a residue of significant chemical or hydrological importance, even after they have been removed. For example, a conveyor belt is used for mucking operations in the ESF. It appears to be depositing a fine layer of black organic matter on the left drift wall. More obvious are the talus piles of conveyer belt shreds and rock powder that pile up at the junction between conveyor segments. With respect to such short-residence materials, we document residual effects as a function of quantity, usage, and duration of emplacement.

We have aimed to recognize useful classification schemes and significant categories of materials for the purpose of supporting design decisions. A useful and elucidative category for discussion is the materials assemblage that represent functional units. Some of these functional units (e.g., for mechanical stabilization: steel sets or fibercrete) are substitutional.

There is also a certain amount of flexibility that is an inherent and necessary part of any construction design. For example, it is not possible to predict precisely how many rockbolts will be required to stabilize a particular section of drift. This depends on information that is acquired as the drift is excavated and must be determined to some extent by the contractor.

6.1.1.2 Uncertainty and Variability in Materials Used

The ability to translate from repository design concepts to the realities of the as-built drift, which may be the greatest source of uncertainty in estimating materials usage, has developed substantially from observations of ESF construction. We have aimed to recognize useful methods of quantification, whether they are threshold values, mean values and deviations, or degrees of uncertainty.

For data that can be quantified, we wish to obtain materials usage data at a resolution significant to the Yucca Mountain Project, which can be determined through sensitivity tests using chemical modeling codes. This degree of resolution is expected to vary depending on the material.

For data that cannot be estimated, such as unpredictable events or the results of irregular activities, we wish to determine first the significance of the information using sensitivity analyses and secondly whether bounding or statistical analyses can be used to bracket or otherwise characterize the data. This type of determination is critical to performance assessment evaluations.

Clearly, adequate data is not yet available to be used as described above. However, these goals are reflected in the manner in which the data is presented below.

6.1.1.3 Materials explicitly named in construction drawings

Metals

Steel Sets. Steel set and lagging installation documentation is in hand for the ESF North ramp from the start of TBM operation at tunnel segment 00+58 through section 06+00, with tunnel sections divided into and reported by the following 200 m tunnel increments:

00+58 to 02+00

02+00 to 04+00

04+00 to 06+00

Within these 200-m sections of tunnel the as-built quantities of the following construction items are documented:

Steel Set, five-piece ring (reference drawing BABEAB000-01717-2100-41101-03):

1. Top component, MK#1A
2. Bottom components, MK#1B (two parts per set)
3. Side components, MK#1C (two parts per set)
4. Steel set, shims and Dutchmen (two parts per set)
5. Steel set shims (reference drawing BABEAB000-01717-210041102-03)
6. Steel lagging, C8 × 11.5# channel for steel sets ~4 ft in length
7. Tie rods for steel sets (reference drawing BABEAB000-01717-2100-41102-03)

All components are of steel (see Table 6-1). Specific tunnel locations (other than the 200 m range cited) are not supplied. The lengths of tie rods used are not specified despite the notation of two different lengths on the drawing (see Table 6-2). According to a cover letter sent by the Kiewit/PB project manager, W. Wightman, these were the first of many actual-use TFM reports planned for input to the TFM database by early September. It was the only report available as of November 1995.

Rockbolts. An investigation of rockbolt usage in the ESF has shown that far more rockbolts are used in some sections of drift than are specified in the drawings. This is understandable and necessary because ground support depends on the type of rock encountered and must be left to the discretion of the construction company. However, a few useful observations that can be made. First, the number of rockbolts used is dependent on rock type, and secondly the rockbolt distributions referenced on engineering drawings can be considered minimum (non-conservative) values.

Rails. It is evident that rails are used presently for hauling personnel and materials in the ESF. Ultimately, rails may be used for the emplacement of waste packages. It is possible that these rails will not be removed.

Concrete

Fibercrete™. Fibercrete™ is composed of ordinary Portland cement (OPC) grout, sand, and short, flat Flex-Ten steel fibers combined in a slurry that has a viscosity low enough to be extruded at high velocity through hoses. It is used primarily for drift consolidation, often in combination with wire mesh and after rockbolts have been emplaced. Table 6-3(a–c) shows the composition of the cementitious material in the Fibercrete™. The source of the sand is specified in the MSDS. Although this provides tracking information, the mineralogy can vary considerably. The MSDS composition lists quartz, calcite, clinozoisite, and feldspars (albite and anorthite), as identified by x-ray diffraction (XRD). Gypsum, phlogopite, and bassanite may also be present.

Rockbolt Grout. The grout composition for the Williams™ rockbolts is stipulated by a Transmittal of Shop Drawings, Equipment Data, Materials Samples, or Manufacturer's Certificates of Compliance (SDT) (Form #AP-5.26) dated 16 January 1995. It stipulates that the grout is type E-1 (K) and specifies the brand Wil-X-Cement™ thixotropic grout. A water/cement ratio (w/c) of 0.4 by weight is stipulated, not to exceed 0.5. It should be noted, however, for the purpose of establishing water introduced into the repository environment, that the mixing of concrete is not exact. According to the SDT, the actual amount of water is left to the operator's discretion, as it needs to be. The operator must assure that w/c does not exceed 0.5, even though 5/6 of the total amount of water to be used is added to the tank before the grout is added.

Invert. The composition of grout and aggregate for the precast invert have not yet been obtained. However, it is clear that each invert segment is reinforced with a rebar cage. Figure 6-1 illustrates the shape of an individual segment.

6.1.1.4 Materials Implicit in Construction and Operation

Fluid Reports and Consumables. Reports of water usage and equipment fluid consumption have been requested. The inventory of all water documented as used in the ESF will be complete upon the receipt of this information. As of November 1995 informal records of materials which are logged into the Exploratory Studies Facility and assumed consumed within a certain segment of tunnel had not been provided. These "records" have been described as having been made without standard documentation. Examples of these materials are paints and sealers (D. Wayman, personal comm.). However, to this date no records separate from the provided as-builts have been obtained.

A separate, but similar issue has to do with materials that may be used in much larger quantities. These materials included cribbing (metal and wood) and excelsior,

which, according to LANL's weekly ESF reports, were used when poor ground conditions rendered the tunnel boring machine (TBM) gripping mechanisms inadequate. LANL's weekly reports cite use of wood cribbing, fibercrete, shotcrete, sand, and a cement-water slurry. For the same time period that these LANL's weekly reports cover, use of these materials is not documented in the Kiewit/PB TFM reports. A list of materials that were used in construction of the tunnel, but were missing from any of the materials records were requested (from D. Wayman). The response indicated a belief that no materials were missing from the records (Meike and Spragge, 1995). We suspect that some of the missing materials may be listed as "consumed." This category of materials is misleading if it includes both items that are consumed and removed (e.g., compressed air, packaging materials), as well as items that remain as a permanent part of the ESF structure (e.g., cribbing, excelsior, sand, and fibercrete).

The TFM data record sheets of the as-built starter tunnel were obtained from REECO. Quantities are given of each material used, and annotations as to whether the materials were considered permanently or temporarily emplaced are included. We noted that materials were listed (and archived into the TFM database) by brand name, which will render retrieval of this information very time-consuming, if not impossible. We suggest that a classification system such as the one already used for construction specifications (and thus easily accessible to the construction engineer who must fill out the TFM data record) would also be useful for retrieval of the information from the TFM database and should be part of the Determination of Importance Evaluation (DIE) record requirement. LANL continues to provide, on a weekly basis, information detailing the position of the tunnel face, the advancement of the tunnel boring machine, and the total quantity of water introduced to the tunnel from holding tanks.

Water. Water brought into the ESF from the holding tanks is measured. It is used for dust control, cleanup, and excavation. The weekly ESF TCO report provides information on the amount of actual water use per week and the cumulative amount of water used. However, the term "water use" is actually employed to specify the quantity of water transported into the tunnel. These reports do not specify how much water was removed from the ESF, e.g., by evaporation or sorbed to rock and removed during the mucking operation. Thus, the water value represents a maximum value of water introduced from the holding tanks. Although this is not an issue at ambient temperature, water introduced and stored in solid form (e.g., cement) will be available to the drift environment upon heating and dehydration. Thus, although it is an important component, an estimate of water usage based on the holding tank usage does

not necessarily represent a complete or "conservative" estimate of the introduced water budget in a post-construction repository setting.

We present the available water usage data in order to illustrate a number of the data evaluation methods that will be used. In the future it should be possible to further constrain estimates of the amount of water that remains on the site in both fluid forms by obtaining better information on water retrieval.

The water usage limit specified in the DIE of no more than 7.4 cubic meters of water per linear meter of tunnel excavated has not been exceeded (Fig. 6-2). An average of the total amount of water used to date is 2.47 kL/m. Figure 6-3 illustrates a more detailed week-by-week analysis of water usage. Figure 6-3(a) shows that to a first approximation, water usage mirrors excavation progress. From Fig. 6-3(b) it is clear that normal weekly amounts of water usage of between 2 and 4 kL/m, which is by and large a function of excavation progress, are punctuated by events of large or excess water usage. Therefore, rather than averaging total water usage, we aim to establish an average water usage per meter (of roughly between 2 and 5 kL/m) that can be modified by a statistical distribution of excess water events. The character of the statistical distribution will be determined by further monitoring of water usage in the ESF. The next step is to relate these events to known functions in order to predict water usage more accurately.

Spills. Kiewit/PB has maintained records of spills/releases in the method of the Kiewit/PB Spill Response Plan in accordance with the requirements of YAP-2.8Q. They include:

- Date and time of the spill/release
- Type of material
- Source of spill/release
- Tunnel location
- Quantity
- Estimate of unrecovered quantity
- Time at completion of clean-up
- Whether follow-up cleaning was required

Records of spills for the period 10-December-94 through 09-August-95 were submitted to the TDB for input to the TFM database. Copies of the records signed by the walker/shift superintendent, environmental supervisor, and M&O A/E site representative have been obtained for the period from 10-December-94 through April-14-95. During this period, eleven underground spills/releases were reported (Table 6-4). All were fluid spills, described as hydraulic oil or hydraulic fluid with the

exception of one described as TBM lube oil (See Meike and Spragge, 1995). No specifics as to type or manufacturer were provided by these reports. However, efforts to retrieve these specifics from Kiewit/PB (through D. Wayman) have yielded some material safety data sheets (MSDS) and chemical compositions of the fluids.

Another thirteen spills/releases were recorded from 6-May-95 through 9-August 95 (Table 6-5). However, the only information available to date regarding these spills is the spill number (SRP #) of each and the dates the spills occurred. All other information has been reported to the TFM administrator for entry in the TFM database. Because the spill number (SRP #) of 6-May-95 is consecutive with the SRP of the last April spill reported, it is assumed that no spills were recorded between these two reports.

Cellulose. The use of excelsior for ground stabilization behind steel sets has been observed in the ESF and noted in LANL's TCO report. The use of wood 4x4's (pine or fir) has been similarly noted. These materials, although extended residence by the nature of the way that they are used, have either not been recorded or are recorded with consumables and thus are indistinguishable from items that may be removed (see the discussion above). This category of materials also includes trash that may be incorporated into invert fill material.

Polymers. Polymers are composed of long, chain-like molecules which are formed by the bonding together of relatively small molecular subunits (monomers). Although proteins (i.e., wool and silk), carbohydrates (i.e., starch and cellulose), and condensation polymers (i.e., shellac and "glue"), polynucleotides (DNA), and cellulose are also polymers, the focus here is on the synthetic polymers which have been created over the past 60 years whose many useful properties have lead to incorporation into everyday construction operation. The matter of identification is an issue because there are many "hidden" sources of polymers. For example, almost all paper products contain polymers such as phenol formaldehyde and polyvinyl alcohol. Furthermore, most adhesives are polymers, and polymers are often added to drilling water to increase laminar flow. Given the combination of reporting issues discussed above, and the inexplicit nature in which polymers can be used, our initial aim with respect to polymers has been to review the types of polymers that may be used in a construction setting independent of the ESF context. Below we first present some of the characteristics that are used to evaluate polymers, and then we review the relevant polymer classes. Some comments are made on the relevance of the polymers to the ESF and to a potential radioactive-waste repository. The review is useful in discovering polymers and their usages in the ESF as well as pointing out important distinctions that can be made. Some thermal and degradation mechanisms are mentioned. In section

6.2.1.4 the discussion of relevant degradation mechanisms is continued, as well as the potential significance of these characteristics to the design of a radioactive-waste repository. Concepts fundamental to polymer characterization that are significant to predicting their long-term degradation are outlined in Appendix A.

Relevant Polymers. *Epoxy resin* systems are made up of resin and hardener. There are literally hundreds of epoxies with different chemical structures dependent upon the resin and hardener used. Epoxy is classified as a thermosetting resin and cures from internally generated heat. When the resin and hardener are mixed together, a chemical reaction occurs which causes hardening. Because epoxy easily reacts, chain extension and crosslinking can occur without the elimination of a small molecule such as water. Thus epoxy does not shrink as much as many other thermosets. Curing, which can be carried out either through the epoxy or hydroxyl groups, gives epoxy its crosslinked character. Either catalytic systems or polyfunctional crosslinking agents may be used to link the epoxy resin molecules together. Amines, acids, anhydrides, and mercaptans all may be used as curing agents.

The range of epoxy resin applications becomes apparent when one examines its properties. The high reactivity of the three membered epoxy ring leads to many unique and desirable properties. First, epoxy resins have high chemical and corrosion resistance. This leads to many protective coating applications. Epoxies are heat resistant, with a T_m of approximately 260°C (Brandup and Immergut, 1975). Low shrinkage, high flexibility, high strength and high impact resistance lend epoxy to many mechanical uses. Epoxy also has good electrical properties, is waterproof, and is lightweight. The most well known property of epoxy, however, is its great adhesion. Epoxies are used to bond metals to glass and plastics and even concrete to concrete. In fact, epoxy is often significantly stronger than the material it is bonding. Steel rebar is coated with epoxy to prevent corrosion. However, the long-term effectiveness is questionable, especially if the coating is not uniform. Corrosion can occur at the interface between the epoxy coat and cold-rolled and galvanized steel (Dickie et al.,1990). Another potential use of epoxy at Yucca Mountain will be as rockbolt grout.

Neoprene rubber is a chloroprene polymer and was the first commercially successful synthetic elastomer. It is a thermoset which is crosslinked using the vulcanization process. Vulcanization involves crosslinking of the highly reactive allylic chlorine. The accelerator is usually zinc oxide or magnesium oxide (however, other metal oxides may be used) to create a sulfide crosslink. There are two types of neoprene: dry neoprene and neoprene lattices, each of which may be further classified as general-purpose or specialty types. Latex rubbers are examples of lattice neoprenes. General purpose

neoprenes include those that are used for molding and other product applications. Specialty types, used for adhesives and sealants, tend to crystallize much faster.

Neoprene rubber tubing, probably dry neoprene, has been used in the ESF. It is likely that it contains antioxidants, fillers and plasticizer additives, because these are often present in neoprene rubber. Antioxidants are necessary since neoprene is quite susceptible to oxidation. Processing aids are added which lubricate and tackify. Examples of these are stearic acid, microcrystalline waxes, and low molecular-weight polyethylenes. Carbon black and mineral fillers are used to give more hardness and to increase abrasion and tear resistance. Hydrated calcium silicate and precipitated silicon dioxide fillers of fine particle size are added to neoprene vulcanizates for tensile strength and hot-tear and abrasion resistance (Mark et al., 1985). Inexpensive petroleum derivatives are used as plasticizers, to lower the T_g.

Polyamide is a condensation polymer made from dibasic acid and diamine derived from oil and natural gas. These polymers contain amide groups as part of their monomer unit. Nylon is the most prevalent polyamide used today, with nylon 6,6 being the most preferred due to its properties and manufacturing cost. Nylons are used primarily for fibers and engineering resins. Aromatic polyamides (Kevlar, nomax) exhibit especially good strength and temperature properties. *Nylon* was the first synthetic fiber forming polymer developed. It is strong, tough, lightweight, abrasion and puncture resistant, and resistant to chemicals. Nylon has a very low glass transition temperature of 50°C and degrades thermally to hydrocarbons and carboxyls at 265°C. Nylon is also quite hydrophilic relative to other synthetic fibers and water acts as a plasticizer for nylon. A completely dry nylon fiber will be quite brittle whereas a fiber which is in a humid environment will be more flexible. Nylon ropes have been used at the ESF. Thus, at least some of the possible nylon usage in the potential repository will be in fiber form. *Kevlar* falls into the category of liquid crystalline polymers and is considered a thermoplastic polymer. Kevlar is close to completely crystalline and, thus, is quite strong. The production of Kevlar requires very strong solvents to achieve the maximum liquid crystalline phase. The linear aromatic structure of kevlar yields more strength and high-temperature stability. Kevlar ropes are used in the ESF. Although kevlar has very good thermal stability relative to other polymers, it will degrade in a high-temperature environment. Long-term chemical effects are unknown.

Polybutadiene rubber is the main component of Liquid Nails caulk which is used at the ESF. Polybutadiene is a synthetic rubber which is thermoset via vulcanization. It has a long-chain molecular structure, which gives it toughness and chemical resistance. The structure of polybutadiene has long been of interest due to its symmetry and simplicity.

Its monomer, butadiene, is a highly reactive colorless gas which reacts with the characteristic of having conjugated double bonds. Butadiene reacts through a self condensation reaction to form the polymer. Dependent on length and conformation, the polymer has a melting temperature ranging from 2 to 156°C and a T_g below 0°C.

Polycarbonate (PC) is a thermoplastic of very high molecular weight. It is strong, rigid, transparent, non-toxic, and weather and impact resistant, though it tends to suffer from stress cracking. It has a high glass transition temperature of 135°C and melting temperatures up to 200°C. Since polycarbonate is used for many electrical applications, flame retardants are often added. There are two types of polycarbonate: aliphatic and aromatic. Of the two, aromatic is by far the most prevalent and also the most useful. Aromatic polycarbonates are prepared from a condensation reaction between bisphenols and carbonic acid derivatives. Plexiglas™ covers (e.g., for the ESF percolation test) are made of polycarbonate. It is likely that Plexiglas™ used during the construction of a repository can be removed and, in that case, polycarbonate will be of little or no concern.

Polyester is classified by carboxylate groups in the backbone of the polymer. They are produced by a condensation reaction of ethylene glycol and propylene glycol which are derived from petrochemicals. There are many different polyesters produced for many different chemicals and glycol derivatives, but terephthalate polyester (PET) products appear to be the dominant type used at the ESF. Polyester rope and rein-anchored bolt systems are used. The rope is a thermoplastic polyester which will soften at high temperatures before degrading. PET is produced from a reaction between a terphthalic acid and ethylene glycol. Impurities are then removed in water at elevated temperatures and pressure. Purity is especially important in PET manufacture since the final quality is affected by very small amounts of impurity. Because the intermolecular interactions in polyesters are relatively weak, small changes in structure lead to large differences in properties. PETs have melting temperatures as high as 270°C. The degree of branching of PET determines the crystallinity (less branching, more crystallinity) and thus the toughness and stability. Polyesters are also hydrophobic and oleophillic. Polyesters are useful as both thermosets and thermoplastics. If the resins are saturated, there are no free radicals in the molecular chain for crosslinking to take place, and therefore the material remains thermoplastic. Likewise, if the resins are unsaturated, there are free radicals and crosslinking can take place.

Polyethylene (PE) is a thermoplastic which is polymerized from the monomer ethylene, obtained from the cracking of petroleum or from natural gas. It was polymerized at high temperatures until the birth of the Ziegler-Natta catalyst, which

eliminated the need for high pressures. There are two primary types of polyethylene. High-density polyethylene (HDPE) is processed by low-pressure polymerization. It is tougher than low-density polyethylene (LDPE) and has better chemical and impact resistance. Low-density polyethylene is odorless and non-toxic. Polyethylene is tough, flexible and a good insulator. However, it is easily scratched, stress cracking is common and it has a low T_g (80 to 130°C). Its properties are affected by side branching. During thermal degradation, polyethylene breaks down to hydrocarbons. One use of polyethylene at Yucca Mountain is in the form of sand bags and tubing. Polyethylene is one of the most prevalent polymers and it is likely that it will also be present in other forms.

Polyisocyanate (PI) is manufactured by a condensation reaction of isocyanate monomers. Isocyanates are primarily used to manufacture polyurethanes. Isocyanates are made in the form of diisocyanates from amines. It is a highly reactive monomer and degrades from about 175°C. In addition, it is highly reactive with water. The polymerization of pure diisocyanate leads to polymers (called nylon-1 polymers) that have T_g ranging from 40 to 180°C. These temperatures are dependent upon the length of side chains; the longer the side chains, the less thermally stable. Polyisocyanate has been used above ground at the ESF in the form of foam sealant and synthetic enamel. In addition, it is possible that these products are actually polyurethanes which have been labeled polyisocyanates due to the prevalence of polyurethanes as foams and coatings.

Like polyethylene, *polypropylene (PP)* is an olefin made from carbon and hydrogen and is derived from petroleum. It is formed using the Ziegler-Natta catalyst (consisting of titanium and aluminum). It is a thermoplastic which degrades readily requiring the use of stabilizers. Polypropylene has high impact resistance and flex strength, is scratch resistant and hydrophobic. There is a strong correlation between average molecular weight and the properties of polypropylene. It is possible to have atactic, syndiotactic and isotactic forms, three different conformations, of polypropylene. The isotactic and syndiotactic forms are more readily packed and thus more crystalline than the atactic form. Higher crystallinity leads to a higher melting temperature and greater toughness. Polypropylene has been used in the form of rope and tubing at the ESF. In addition, since it is one of the most prevalent polymers, it may be present in the form of packaging.

Polystyrene (PS) is a thermoplastic. The styrene monomer is made from benzene and ethylene, both of which are petroleum feedstocks. Polystyrene is used for its high-frequency electrical insulation and its optical clarity. It is very brittle; this can be improved with orientation and the addition of plasticizers. It also has a low glass

transition temperature of 80 to 90°C. However, polystyrene has a relatively high melting point of 274°C (syndiotactic PS) (Ravinetti and Zini, 1992). Polystyrene "Styrofoam" insulation has been used at the ESF. In addition, polystyrene auto body filler and fiberglass resin will be used above ground. Because foam has more surface area, it is likely that the Styrofoam will degrade more quickly than a solid chunk of polystyrene.

Polytetrafluoroethylene (Teflon, or PTFE) was first discovered in 1938 by accident while scientists were attempting to produce a new type of Freon. Since then, it has been used for a wide variety of applications, most of which take advantage of its high-temperature stability (the highest of any non-aramid thermoplastic) and its low friction. The frictionless property is due to the strong bond between the fluorine and the carbon backbone, so strong that it repels other substances. Teflon's electrical properties are unchanged by temperature and frequency, lending teflon to radio and power cable applications.

Teflon is polymerized with a peroxide catalyst in the presence of water from a monomer which is a poisonous gas. The result is a polymer which is very inert, chemically resistant (there are no solvents for teflon) and self lubricating. Teflon coating called by the trademarked name Gortex serves as a waterproof coating on the roof of the Denver airport. Teflon will be used for tubes for the heater tests in the ESF. It has also been used as wire pulling lubricant and as lubricating spray. Although not used in large quantities at present, Teflon's applications continue to grow. Its high melting point (330°C) may lend it to more applications in a high-level radioactive-waste repository. If so, a major effort should be conducted to understand its biodegradation.

Polyurethane (PUR) is synthesized in a condensation reaction between isocyanate and a hydroxyl compound. Isocyanate is an ester of isocyanic acid, HNCO. A wide range of physical properties can be obtained due to flexibility in selection of the reacting hydroxyl compound. Although originally produced in the form of fibers competitive with nylon, the main products of polyurethane are a variety of crosslinked polymers foams, coatings, and elastomers. Other applications of polyurethanes are adhesives, sealants, binders, and mine reinforcements. The flammability of polyurethane is reduced with the addition of flame retardants.

No other foam-producing system compares with that of polyurethane. It is easy to produce at a reasonable cost. Flexible and rigid foams can both be produced using polyurethane because catalysts precisely control the balance between polymerization and expansion. Flexible foams are produced by simultaneous polymerization and expanding with carbon dioxide gas. Flexible foams are used mostly as protective and

cushioning materials. The production of rigid foams is similar to that of flexible foams except that expansion is achieved using a low boiling solvent. Rigid foams are used as thermal insulating materials. Although polyurethane has a tendency to burn, this is lessened by the addition of flame retardants and the bulky foam structure lends itself to good insulation properties.

Polyurethane coatings are quite hard yet are flexible. They are also resistant to abrasion, chemicals and solvents. Finally, polyurethane coatings have high light stability and weatherability.

Polyurethane elastomers may be considered block copolymers consisting of alternating polyurethane and polyol segments. Primary or secondary amines, polyester and polyether are all polyol segments which may be used. Some of the main components of polyurethane elastomers are polyester and polyether diols, diisocyantes and chain extenders. Although different polyurethane elastomers possess different properties, they usually have wonderful tear, abrasion, impact and wear resistance as well as resistance to hydrocarbon and aromatic oils.

Cast elastomers are produced from liquid starting materials which differentiates them from other natural and synthetic rubbers. Examples of cast elastomer products are skateboard wheels and O-rings. Thermoplastic elastomers are processed as thermoplastics and hence can be used for various purposes. Examples of thermoplastic elastomer products are adhesives, hose lines and films for laminating. Millable polyurethane gums are used in synthetic rubber application such as machine parts.

Reaction injection molding is a process in which a mixture of two or more reactive low-viscosity materials is injected into a mold where it polymerizes. This process yields crosslinked, network structures. The product is a solid skin over a low-density microcellular core (foam structure) in a single operation. These structural foams use the smooth hard skins as a source of impact strength, heat-distortion, temperature and combustion resistance. An example of a use for reaction injection molding is in the production of automotive body panels. In this case, the car body would be durable yet lightweight. At Yucca Mountain, polyurethane is used for insulation purposes, probably as a foam.

Polyvinyl Chloride (PVC) is one of the oldest and most widely used synthetic polymers. In the past, the vinyl monomer was formed by a reaction between hydrochloric acid (HCl) and acetylene, which is derived from calcium carbide. More recently, however, PVC has been formed from ethylene, which is cheaper than acetylene (Nass and Heiberger, 1986). PVC is a thermoplastic which is used in rigid, non-plasticized form, and flexible, plasticized form. Although the chemical structure of

PVC appears to be quite stable, there are many deviations from the ideal structure. Structural irregularities result from polymerization defects such as branching and double bonds and from oxygenated groups such as carbonyls and peroxide groups. Thus, the commercial success of PVC is dependent on stabilizers. PVC has a glass transition temperature of about 80°C and easily degrades to HCl without stabilizers. In addition, it has very poor chemical resistance. Thus, almost all PVC products contain a significant amount of additives, which can vary their properties greatly. Polyvinyl chloride is widely used in the ESF as cable sheath, cement for pipes, cement primer, conduit, containers, hose piping, portable toilets, sheeting and tubing. Because of its potential acidic degradation products, PVC should be either not used or should be removed from areas of drift excavation in which local acidity is a significant issue.

Silicone is derived from silica or quartz and can have diverse properties dependent upon the length of chain and organic groups, but all silicones are based on a backbone of alternating oxygen (O) and silicon (Si) atoms. Silicones have outstanding resistance to aging and weathering, good thermal stability (up to about 315° C), water repellency, and toughness. In addition, they are inert and frictionless. The first step of production of silicones involves the conversion of silica to silicone in an electric arc furnace. The silicon is then converted to methylchlorosilanes by a direct process reaction with methyl chloride in the presence of copper as a catalyst (Lynch, 1978).

This product then reacts with water to form siloxane monomers, dimers and trimers, which continue to react until termination is reached. The result is a siloxane polymer. Silicone rubber is the crosslinked form of this polymer. At Yucca Mountain, silicone rubber is used as caulk, desiccant and lubricating spray. The thermal degradation products of silicone are low-molecular-weight cyclic oligomers, which are quite inert (Brandup and Immergut, 1975). Thus, the primary concern will be failure of the products used in the repository.

6.1.2 Evaluation of Materials by Function

It is evident that the blueprints show a minimum of materials that are actually used in construction. The following evaluation is intended to categorize standard suites of materials by construction function and, if more than one construction option exists for a particular function, to discriminate suites of materials by construction option. The presentation below represents the state of the work, which was in progress until November 1995. We do not present information on the following functions: utility piping and ventilation, power distribution, or communication and instrumentation.

6.1.2.1 Transportation

Invert. The exact number of invert segments placed in the tunnel has been provided. The tunnel has been divided into the same sections as for the steel sets. All inverts are precast prior to emplacement and are of concrete composition. Rail placement and invert segment plan and sections and detail are shown in reference drawing BABFCCOOO-01717-2100-40178-02, and BABFCCOOO-01717-2100-40179-02. The use of hardware, including lifting anchors, rebar, and strap anchors, is evident from the drawings. A polyethylene foam fill material is explicitly mentioned for placement between invert sections and between invert and the drift wall. Fill material cannot be tracked in this way unless it is on structural drawing 41099. It is not included in the inventory of inverts and is unaccounted for. Further chemical and physical analysis should be conducted on this fill/invert area, given that in an emplacement drift, with the appropriate design, the invert may constitute an engineered barrier.

Crushed rock, an option that has been discussed for emplacement drifts, has not been tried in the ESF.

Rail system. Documentation of the materials used in the rail system had not been initiated when this work was halted. However, it is clear that the system involves the rail, anchors, ceramic inserts and rubber insulation. These aspects should be clarified in the future because they impact the ability to predict microbiology and chemistry in regions close to the waste package.

Diesel Exhaust and Fuel. One of the early concerns of the Yucca Mountain Project, in the area of materials usage, was diesel fuel and its hydrous pyrolysis products. Diesel-powered vehicles are standard and economical for hauling activities, and if they were used, spilled diesel fuel and exhaust products might become part of the post-closure repository environment.

Electric Rail. Use of electrically powered vehicles is an option that has been considered for the ESF and may be considered again for use in a potential repository at Yucca Mountain. The residual material that may be left behind by such a system could be examined by investigating the Bay Area Rapid Transit (BART) or other electric rail systems. Even a cursory examination of BART and other tunnels indicates that a carbon deposit is a likely result from the use of such a system. This and other aspects of environmental modification will need to be examined if electric rail is to be an option in a repository setting.

6.1.2.2 Stabilization

To a great extent the amount of stabilization that is required within a section of tunnel is unknown until that section is reached. However, accurate mapping of the construction materials and correlation with the ESF geologic assessment should allow us to predict materials usage in the repository more accurately than simply from blueprints.

Cribbing. In the ESF, in sections of drift where large fractures have been exposed, both wood and metal cribbing has been used for stabilization.

Steel sets. Steel sets have been used in areas of extreme rock instability, where rockbolts are insufficient. At times stabilization is required behind the steel sets. In the ESF this stabilization material has consisted of sand or excelsior (wood fiber).

Rockbolts. As mentioned above, rockbolts of a number of different lengths and designs are used in the ESF. The emplacement of some rockbolts require grout, while others require a rather large quantity of water (nine gallons per bolt). The number of rockbolts used in a given section of drift varies and is dependent on the stability of the rock and the other components of the stabilization system (Table 6-2). Rockbolts can be associated with wire mesh and with wire mesh and Fibercrete (refer to portal area of the ESF).

Pre-cast Concrete. Although it has not been used in the ESF, pre-cast concrete is presently being considered as a mechanical stabilization method in the context of a potential repository design. Presumably these pre-cast concrete sections will require a polymer material between the sections similar to the invert sections.

Fibercrete. Fibercrete has been used for stabilization in the portal area of the ESF (see the rockbolt discussion above).

6.1.2.3 Mucking, Dust Control and Ventilation

Conveyor system. Although it is believed that a conveyor system used for mucking during repository construction would be removed, it is clear from observation of the ESF conveyor system that the *operation* of the conveyor modifies the environment chemically and physically. The moving conveyor belt generates a lot of rock powder which settles on the walls and floor of the tunnel. This could affect drift-scale hydrological properties. In addition, due to the length of the mucking operation the conveyor is composed of segments. Each segment consists of a belt, which dumps its load on the next belt and so on until the excavated rock is removed from the drift. At the junction between segments, talus piles of rubble and shredded conveyor belt (see

polymer section) are evident. A very fine black deposit is also visible on the left drift wall (rib) throughout the tunnel.

Dust control. Given that the basis for the nuclear waste strategy is the minimization of water in contact with the waste packages, our goal is to minimize, to the extent possible, the amount of introduced water. Data is not available for water usage by function, so water usage is discussed below in terms of total amounts. In addition to the chemical issues, the physical modification of the environment should be acknowledged. Dust control (even pure water) will cause the heterogeneous dispersion of a coagulated rock powder, the long-term impact (hydrological and chemical) of which we have yet to understand. However, in view of the fact that for health reasons a dust suppressant must be used, and that pure water may not be the best option (due to the larger amounts needed in the absence of a surfactant), the present discussion is limited to the dust control products that were under consideration in 1995 and 1996 (see Table 6-6). The salient issues are outlined in memo LLYMP9603087.

The additives were evaluated based on the MSDS information provided for the products. Although the chemical information provided in most cases was not adequate, eight were found to contain hydrocarbons/polymers. From the perspective of test interference in the ESF, we were concerned about the introduction of compounds that might alter the baseline of chemical analyses, which had the potential of severely interfering with and rendering useless the planned Swipe Tests, which were intended to obtain sensitive isotope data of hydrocarbon compounds and air samples in the ESF. The dust control chemicals are especially invasive to those experiments due to the dispersed nature of their usage. If dust suppression is to be conducted in the ESF using these additives, an additional program will be required in order to discriminate between airborne diesel exhaust and vapors, and these dust suppression agents. These distinctions are critical to our ability to supply baseline information toward the understanding of potential ESF test interferences. No chemical information was provided for the last additive considered, Bio Cat 300-1, and therefore no determination can be made at this point. Based on these considerations we advised against the use of the additives that contained hydrocarbons and against Bio Cat 300-1 due to the lack of information. Given that Dustcon™ degrades rapidly, we would want to understand the chemical nature of the biodegradation products in order to make a complete assessment of test interference in the ESF.

Over the long term we are concerned about the formation of colloids and the alteration of the chemical composition of water. However, we can make some preliminary assessments. It is our understanding that tracers are introduced into the

water that is used for dust control. If this is accurate, then although the dust control compound may affect chemical analysis, at least the investigator will be alerted to that fact. In a gross sense the big distinction over the long term between Dustcon™ and the other products appears be pH, because the documentation provided cites the prevention of limestone and salt that otherwise build up at a number points in the dust control system. With the exception of pH, the chemical effects can be considered grossly of the same type at the concentrations under consideration.

Dustcon™ appears to need much less water (especially less than non-modified water) to reduce dust to the required level than the other products under consideration, even though the amount of additive used per volume of water appears to be less than the other products. This has two advantages: first, the dust control agent is minimized, thus limiting the impact on data collected from experiments conducted in the ESF, and secondly, the amount of water introduced into the ESF for the purpose of dust control is minimized. Similar arguments could be applied to the construction of a radioactive-waste repository.

6.1.2.4 Excavation

The tunnel boring machine (TBM) is electrically powered. However, its hydraulic system requires the use of petroleum products. These have been introduced into the tunnel through spillage during maintenance and equipment failure. As mentioned above, a policy is in place regarding the reporting and clean-up of spills. According to the policy, not every spill needs to be reported, but only that above a certain value. Because not every spill is recorded, the spills on record must be regarded as a minimum number. Therefore, in estimates of material usage, the uncertainty factor may be included to account for the spills that are thought to be below the reporting limit and therefore not recorded. Water usage accompanies the excavation operation through the actual excavation, dust control and clean-up of the "dance floor."

6.1.3 Tracers, Fluids and Materials Database: Retrieval of Information

Much of the initial information depends upon the retrieval of large amounts of data supposedly archived in the Tracers Fluids and Materials (TFM) database. Yucca Mountain Project YMP procedural documents identify explicit methods and channels through which this data should be retrievable. Our attempt to retrieve data that has been archived in the TFM database suggests that the large effort expended on developing procedures to collect and archive data is not reflected in the data that can be

obtained. At the time of the assessment, which ended in November 1995, searches have retrieved far more procedural documents than data. Since the assessment was conducted, the operation of the database and collection has been turned over to another group. In order to enhance the utility and retrievability of information we suggest that ANSI or other standard construction material reference numbers be used in addition to brand name. Our experiences suggest that since November 1995 some of these suggestions are being incorporated into the database. We look forward to an improved state of access to archived data and better communication between the construction team, DIE, TFM database and those that require the data, given that, as time progresses, both the quantity of data and the demand for it will increase. This data, once available, will be incorporated and interpreted in subsequent revisions of the NFER.

Routes of information retrieval (other than archival work) that have been explored include the first-hand study of the ESF and interviews with on-site construction staff. These options appear at first glance to be more time intensive than the retrieval of archived data. However, they promise to provide a more comprehensive understanding of materials usage that will ultimately be useful in extrapolating information from the ESF setting to the prediction of materials usage in a potential radioactive-waste repository.

6.1.3.1 GENISES

As should become apparent from the above review, tracers, fluids, and materials data in the form of TFM usage requests and estimates and reports of actual use of TFMs (also known as "as-builts") are a critical aspect of developing the capability to relate a repository design to a materials usage prediction. However, at present, such data remains virtually inaccessible from the YMP TFM database. The current state of the database is such that it is much less easily accessed than both status reports provided by and personal communication with the database administrator would lead one to believe. Currently, there are three databases of TFMs, as cited in the Tracers, Fluids, and Materials (TFM) Database Status Report for the Period April 1995–June 1995. The first consists of the original TFM data compiled by LANL and entered into a system provided by Computer Applications Group, Inc. The transfer of this data into the GENISES database is on hold according to the status report dated June 30, 1995. The second database was compiled and input by EG&G/EM. Because the data was submitted without standards on a variety of forms, the database will need to be retrofitted to the revised TFM system to facilitate retrieval of data. The third database conforms to the specifications of YAP-2.8Q. This database, according to the

aforementioned TFM status report, contains only data reported after May 8, 1995, the effective date of YAP-2.8Q. However, to quote the status report, "no new data have been provided under this procedure." To summarize, it seems that the only readily accessible TFM database contains no data.

The only other self-evident option for obtaining specifics of TFM usage and requests was to request it from the originator. That method resulted in limited amounts of information pertaining to the following construction categories being supplied by D. Wayman of Kiewit/PB:

1. North ramp spill reports
2. North ramp steel sets
3. North ramp rail/segments

This information is reflected in the discussion of materials and materials usage in the previous sections.

6.1.4 Assessment of Materials Considered for Repository Construction

Progress in this area consists primarily of the initiation of modeling capabilities to assess the drift-scale heterogeneity of materials and their distribution, the quantities and location of materials and the chemical composition of some of the more critical materials. To this point, materials have been considered critical if they have the potential of being located in the emplacement drift and in fairly large quantities. This work is of fundamental importance to ability to respond to the needs of Performance Assessment, Repository Design and Waste Package Design Areas of the Yucca Mountain Project.

6.1.4.1 Heterogeneity

It is clear that the emplacement drifts will be both hydrologically and chemically heterogeneous. Given that the driving force behind many important chemical processes are chemical, thermal or other gradients, and that microbial activity is frequently most active in crevices, and that permeability variations in space will affect hydrological properties, attention to heterogeneity is very important. The drift modeling work described later in this report includes an assessment of the chosen software to identify interfaces and to manipulate the level of detail required by this inherent heterogeneity of the as-built system.

6.1.4.2 Materials

The potential significance of a material to the repository environment will be determined by its modification potential (chemical or hydrological), its quantity and its location. Given that some materials may be exposed to temperatures above the standard conditions to which we are accustomed and to a time frame outside of our experience (or even, for that matter, longer than the period of time that the material has been known, e.g., plastics), it is clear that once materials are identified, it may be necessary to conduct experiments or analyze historical analogs in order to understand their potential significance in this environment. The beginning of the materials identification and quantification work has been outlined above. This information is evaluated through the experimental and modeling activities discussed below. The drift-scale model has been chosen to be able to interface with existing hydrological, chemical and coupled codes to create three dimensional renderings of drift-scale processes through time.

6.1.4.3 Materials juxtapositions

Attention to the juxtaposition of materials is critical, not only to identify potential locations of microbial activity and possible microenvironments, but because it is highly likely that the effects of materials in contact at elevated temperatures may also be outside our standard experience. Identifying these juxtapositions is also a goal of the drift-scale modeling activities.

6.2 Post-Closure Chemical Processes That May Modify Predicted Geochemistry

Modifications of the natural environment due to construction of an underground repository would, in themselves, alter the natural chemistry, some aspects of which may be critical to the robustness of the waste package or to the chemistry of the fluid leaving the repository. However, once the materials are emplaced, in the absence of changing extrinsic properties, the chemical evolution of the repository would be fixed to a specific path and hypothetically predictable. The first section of this chapter on introduced materials described the chemical evolution that is brought about by the intrinsic nature of a repository design, and the initial steps that we have taken toward quantifying aspects of repository construction. The present section discusses the aging of repository materials in response to extrinsic conditions such as temperature, relative humidity and aqueous chemistry that will vary during the lifetime of the repository. The ultimate goal of this work is use a combination of post-closure chemical processes

and processes that are determined by repository design and construction to identify the resultant chemistries that are outside the envelope of possible natural chemistries.

The product phases of materials disintegration, biodegradation and corrosion may include oxides of metals, sulfides, chlorides, carbonates, and silicates, as well as organic compounds, alkali metals, and halogen elements. These materials have the potential to alter the pH, ionic strength, and composition of water that may be present at some time in the lifetime of the repository. In addition to aging, gamma radiation effects must be considered in the WP environment as discussed in Van Konynenburg (1986b). The chemical effects of gamma radiation on man-made materials remain largely uninvestigated even though it is known that aggressive substances such as nitric acid can be a product of such processes.

The quality of water, whether present in an aqueous or vapor phase, will directly affect the dissolution of spent fuel, waste glass, and ultimately, the concentration of dissolved or suspended radionuclides in water that exits breached containers. Therefore, the introduction of some man-made materials into the WP environment may influence WP performance. The chemical data for these materials will be gathered from a wide variety of sources that represent their usage in both modern and ancient societies. This data is essential because many chemical consequences specific to the repository setting are to a large extent unknown. The information that is known, summarized below, comes from literature searches that have been initiated for some of the major categories of materials. Therefore the preponderance of data on cement-based materials represents the preliminary nature of this task rather than the relative significance of any of the materials.

In the sections that follow we distinguish between those chemical processes that are biotic, or mediated by living organisms from those that are abiotic, or not dependent on living organisms. As will be discussed in the next section, most of our predictive chemical modeling capabilities are abiotic. Thus to use that modeling capability without explicit recognition of biotic chemical processes implicitly assumes that they are insignificant compared to abiotic processes. Clearly this is untrue for some materials such as some organic compounds over long periods of time in natural environments. Given the potential confusion in terminology, we define at the outset "organic chemistry" as those processes that involve organic compounds as distinct from "biotic chemistry" which involves a living intermediary such as a colony of microbes. As will be discussed in Section 6.2.2, microbially mediated (biotic) processes do not necessarily depend on the presence of organic compounds and can significantly affect inorganic chemistry.

6.2.1 Abiotic Chemistry

In this section the chemistry of inorganic materials and organic materials that are relevant to a high level radioactive waste repository is examined. The choice of subjects examined and the length of the studies was strongly determined by the needs of the project on a yearly and some times shorter term basis.

6.2.1.1 Organic Materials. This examination of potential chemical effects of organic materials concerns two very different goals. The first goal is to assess the potential contamination of studies conducted in the ESF by introduced materials. This work supports the determination of importance evaluation of materials used in the ESF. The second goal is to examine organic materials in the context of a radioactive waste repository and whether they may react with the surrounding rocks causing changes in repository porosity, or react with the waste package or waste form and enhance the mobility of radionuclide species. It does not, however, address microbially mediated degradation.

Diesel Exhaust. A study of long term diesel exhaust effects was conducted using N-Tunnel (Nevada Test Site) as a historical analog (Meike et al., 1995). The study represents a broad approach to material degradation that aimed first to assess the rate determining processes before embarking on the detailed experiments. Biotic and abiotic processes were considered and organic and inorganic materials were analyzed. This study is described in Meike (1995).

Diesel Fuel. Two studies have been conducted on different aspects of diesel fuel contamination. The first was conducted primarily to assess the potential impact of diesel operation on geochemical studies conducted in the ESF. The other study was oriented toward understanding the significant long term degradation processes.

^{14}C in Diesel Fuel from the ESF. Chemical isotope studies of selected introduced materials were conducted in the ESF in support of geochemical tests to determine what the potential effect of contamination would be to those geochemical studies. One effect is the potential contamination of ^{14}C from a number of sources. The objectives of the first stage of the study were threefold. Our first objective was to verify that the sample collection protocol did not contribute "modern" ^{14}C to the fuel sample. The second was to demonstrate reproducibility between samples collected at the same location. The third objective was to verify that the fuel collected from the locomotive motor was isotopically equivalent to fuel collected directly from the fuel tank. This first stage was intended to demonstrate unequivocally that (1) our sample collection protocol was appropriate for these measurements and (2) future samples could be collected exclusively from the storage tank, thus simplifying future collection. These were

necessary precursors to give credence to the second stage of the study which was the actual analysis of the diesel fuel.

Eight samples of ~50 mL each were collected at the ESF at YMP. Five of the eight samples were taken from the storage tank and 3 were collected from the locomotive motor. The ^{14}C in each sample was measured using accelerator based mass spectrometry (AMS). Prior to measurement an aliquot from each sample was combusted to graphite at the LLNL environmental-level graphitization laboratory. The technique used to graphitize samples at LLNL is in widespread use at other AMS laboratories around the world and cross-calibrations with other laboratories are performed routinely. In addition to the samples procedural blanks are also graphitized to verify background activity.

From the AMS measurement an isotopic ratio ($^{14}C/^{13}C$) is derived. The AMS measurement of ^{14}C and ^{13}C is converted to an isotopic ratio by referencing to standards measured during the measurement cycle of the unknowns. The accuracy of the standards is <1%. Within counting statistics all of the samples measured were identical and their ^{14}C activity was not distinguishable from background, i.e., they were ^{14}C dead. The limits on their ages are shown in Table 6-7. All of the samples measured have ^{14}C ages of >48 Kyr. This is essentially the background of the graphitizer-spectrometer system. These samples are unequivocally ^{14}C dead. Furthermore, they are all identical, thus verifying the efficacy or the sample collection protocol. Since the samples collected from the locomotive motor were indistinguishable from those collected directly from the storage tank any future measurements could be performed exclusively on samples collected from the storage tank.

A preliminary interpretation of these results is that any possible contamination of geologic samples taken from ESF by diesel fuels would result in apparent ^{14}C ages older than their real ages. The extent to which mixing of C indigenous to geologic samples taken from ESF with fuel-derived C can be assessed however this task is beyond the scope of this preliminary report. It is significant that apparent young ^{14}C ages from materials taken from could not have been produced by contamination with fuel or exhaust from diesel fuel.

***Hydrous Pyrolysis of Diesel Fuel*.** This study examined the hydrothermal production of carboxylic acid and other aqueous organic species due to thermal degradation of diesel fuel at elevated temperatures. Carboxylic acids are particularly significant because they are known to form complexes with common rock forming cations, and thus can enhance mineral dissolution rates and mineral solubility (e.g., Bell et al., 1992; Gestsdottir and Manning, 1992; Hajash et al., 1992; Fein, 1991; Bennett et al.,

1988). Carboxylic acids are also known to accelerate the corrosion of steel and other alloys (Jones, 1992; Fontana and Green, 1978; Larrabee and Mathay, 1963). Furthermore, carboxylic acids are kinetically metastable for geologically long periods of time at 100-200°C (Palmer and Drummond, 1986). Other hydrocarbons that may be derived from diesel fuel and its degradation products are potential sources of colloidal material for radionuclide transport. These experiments were carried out at 200 and 315°C, temperatures somewhat higher than those expected within a repository emplacement drift of the present reference design, in order to directly determine the rate and products of diesel fuel degradation within a 2 to 3 month laboratory experiment. They thus provide an upper limit for the rate of abiotic degradation within the chemical system studied.

Experimental. Given the complex nature of the potential interactions between diesel fuel, other relevant man-made materials, groundwater, and Yucca Mountain geology, a series of scoping experiments with increasing degree of chemical complexity were undertaken. The experiments (see Table 6-8) also represent an evolution in the development of experimental and analytical protocols. The studies of diesel fuel hydrous pyrolysis were conducted (1) at 200°C (Jackson and Carroll, 1994), (2) at 315°C to accelerate the reactions, (3) in the presence of cementitious material and analog J-13 well water to examine reactions at elevated pH, (4) in the presence of Topopah Spring tuff and analog J-13 well water to examine possible catalytic effects, and (5) in the presence of cementitious material, Topopah Spring tuff, and analog J-13 well water. In addition, a scoping study of hydrothermal cement reactions 200°C was conducted for comparison with the more complicated chemical systems (3 and 5 above).

A wide range of analytical techniques were used because no single instrument is capable of adequately analyzing all of the wide range of substances of interest. Gas Chromatography (GC) with flame ionization (FID) and thermal conductivity (TCD) detectors or Gas Chromatography Mass Spectrometry (GCMS) were used to analyze organic phases (aromatics and alkanes in aqueous and organic solution. Gas Mass Spectrometry (GMS) was used to analyze gas phase extracted from the liquid samples. Liquid Chromatography (HPLC) was used to analyze for dissolved carboxylic acids. Inorganic aqueous species were analyzed with one of two instruments. Cations were detected using Inductively-Coupled Plasma, Atomic Emission Spectrometer (ICP-AES). Anions were detected using Ion Chromotography (IC). Inorganic carbon was detected using a CO_2 Gas Analyzer. The solids were characterized mineralogically using X-Ray Diffractometry (XRD) and morphologically and chemically using Scanning Electron Microscopy (SEM) with energy dispersive spectrometer (EDS) and a beryllium window.

The diesel fuel used in these experiments was obtained from the LLNL motor pool. It is composed primarily of alkanes ranging from C_6 to C_{26} (Table 6-9). The total sulfur concentration is 0.55 wt%, as measured by combustion using a LECO SC132 analyzer. Fibercrete™ wafers, weighing approximately 3 g each were prepared from a sample obtained from the ESF, and is described in Section 6.1.1.3. Topopah Spring Tuff (Tpt) cores taken 1232.2-1232.3 feet below the surface from drill hole USWG-1 were sliced into wafers weighing approximately 3 grams (Knauss et al., 1985a). It consists of a devitrified matrix containing plagioclase phenocrysts, alkali feldspar, cristobalite, quartz, biotite, magnetite, ilmenite, and accessory zircon and apatite, and has an average pore diameter of 0.025 µm and a porosity of 6.54% (see also Warren et al., 1984; Bish et al., 1981). All waters used in the experiments were either distilled MilliQ (17.5 MΩ) filtered water or 3 mM $NaHCO_3$ solution in MilliQ water. The latter composition reflects the most salient chemical feature of J-13 well water (~3 mM $NaHCO_3$) for the purpose of the experiment and will be referred to as J-13 analog water (JAW). J-13 water is considered representative of the natural ground water from Yucca Mountain (Knauss and Peifer, 1986).

The high temperature pyrolysis experiments were run in Dickson-type, gold bag autoclaves (Seyfried et al., 1987). The apparatus has been used extensively for hydrothermal experimentation, and its use in the experimental study of the hydrous pyrolysis of hydrocarbons is well established (Jackson et al., 1992). Within the Yucca Mountain Project the apparatus is standard equipment and is described elsewhere in geochemical studies (Knauss and Beiriger, 1984; Knauss et al., 1985a; Knauss et al., 1985b, Knauss and Peifer, 1986 and Knauss et al., 1987).

During fluid sample extraction autoclave rocking was stopped, but the experimental pressure was maintained by externally pumping deionized water into the pressure vessel. The sampling port was positioned so as to sample the desired immiscible liquid phase: the down position sampled the more dense aqueous phase, and the up position sampled the less dense organic phase. All samples were extracted from the sample port with gas-tight syringes. Approximately 1 mL of liquid was extracted to clear the sampling line, which was not maintained at temperature and pressure, and thus could be contaminated with precipitated phases. Another 1 mL of liquid was taken to measure pH at room temperature, which is not necessarily equal to the pH at temperature. However, given the experimental difficulties of measuring the pH at experimental temperature and the straightforward nature of the calculation, it is standard practice to calculate the value at temperature based on thermodynamic principles. In any case, the trend of pH changes is the same.

An additional two samples were filtered (0.4 μm filter) for ICP-AES analysis of cations: a 3 mL undiluted sample acidified with concentrated nitric acid for trace element analysis, and a 1 mL sample diluted by a factor of 10 with 3 mM $NaHCO_3$ and acidified with concentrated nitric acid for major element analysis. Approximately 0.5 to 1.0 mL of the aqueous phase was sampled for organic analyses. A 1 mL aqueous sample was taken to measure organic anions using HPLC. Prior to filtering samples for HPLC analyses, the gas phase, which exsolves from the sample at room temperature, was removed by passing 20 mL of He gas at atmospheric pressure in a gas-tight syringe through the liquid sample syringe, then the liquid sample was gently shaken for about 1 minute to allow the gas exchange to occur, and the gas was re-injected into the 25 mL He syringe. The total gas volume was measured after adjusting to atmospheric pressure and injected into an evacuated sampling steel cylinder for GMS analysis. This extraction procedure was repeated with the same liquid sample. The gas extractions were analyzed for inorganic and organic gases. Approximately 1 mL of the aqueous phase was sampled for inorganic carbon analysis with the CO_2 gas analyzer.

Simulations using the Geochemist's Workbench (GW) equilibrium geochemical code (Bethke, 1994), and COM.R16 thermodynamic data base (Johnson and Lundeen, 1995) were used to interpret the experimental solution concentrations and solid end products. These calculations were evaluated at 200°C. Sulfur was assumed to be in the form $(SO_4)^{-2}$ and the solutions were charge balanced with Na^+. The lack of detectable $H_2(g)$ in the diesel fuel hydrous pyrolysis experiments suggested that oxidizing conditions existed in the experiments, which were simulated by setting Eh = 0.4 V.

Results. Diesel fuel hydrous pyrolysis is limited at 200 and 315°C over a two to three month reaction period. Low carbon number alkanes and aromatics were dissolved in the aqueous phase (Table 6-10). Carboxylic acids, such as acetic acid and perhaps formic acid, may have been present in the aqueous samples, but their concentrations were below the HPLC working detection limit (4 ppm). The room temperature pH of the sample taken at the end of experiment DF1, equaled 4.5. In experiment DF2, the room temperature pH decreased from 6 to 4.9 during the first 30 days of reaction followed by a slower decrease to pH 4.7 at the end of the experiment. The exception to this trend was taken at approximately 65 days (Fig. 6-4). No $H_2(g)$ or $O_2(g)$ were detected by GMS and $CO_2(g)$ concentrations were on the order of 10^{-5} M. There was no measurable change in the proportions of the alkanes, as illustrated by the normalized concentrations of n-C_{10}, n-C_{12} and n-C_{14} with respect to hexadecane, n-C_{16} for experiment DF1 (Fig. 6-5) or in the final diesel fuel analysis for experiment DF2.

The results of Fibercrete™-water interactions (DF3 and DF4) appear to be independent of the presence of diesel fuel (Fig. 6-6 through 6-8). Solution pH (200°C) decreases from approximately 8.8 to 8.4 in both experiments. Similarly, total sulfur concentrations increase to approximately 15 mM and initial inorganic carbon concentrations decrease from 3 mM to concentrations near the detection limit (~1mM) after the first few days of reaction. The aqueous Si concentrations increase rapidly during the first few days of reaction, followed by a slower increase to approximately 5 mM, whereas the aqueous Al concentrations decrease steadily from 2 to 1 mM. The aqueous Ca concentrations increase as a function of time, however the concentrations measured in the presence of diesel fuel are a factor of two lower than the concentrations measured in the absence of diesel fuel. Aqueous Fe and Mg concentrations hover around 1 mM, near the detection limit of the ICP-AES analytical technique.

In both experiments DF3 and DF4, the reacted Fibercrete™ consists of quartz, calcite, clinozoisite, feldspars (albite and anorthite), and 11Å-tobermorite as identified by XRD (Fig. 6-9). Of these, only 11Å-tobermorite is not found in the unreacted Fibercrete™. Other crystalline Ca-Si-hydrate phases (but not all) that are associated with reactions above 100°C (see Meike et al., 1994); afwillite, xonotlite and foshagite, were not identified in the unreacted Fibercrete™. The absence of xonotlite, afwillite, foshagite, bassanite, phlogopite, and mesolite were not unambiguously determined by XRD, because their major peaks overlap with quartz, calcite, clinozoisite, and 11Å-tobermorite. Two XRD peaks remain unidentified. SEM photomicrographs of unreacted and reacted Fibercrete™ (Fig. 6-10) show dissolution etch pits as well as prismatic growth features in the larger aggregate minerals, quartz and feldspar of the reacted crystal. The Ca-rich precipitate covering the majority of the wafer surface does not form on the aggregate or penetrate the wafer at depth. No Si was detected in association with the Ca, thus it is possible that the Ca-rich precipitate is calcite or an amorphous calcium hydroxide (portlandite) because CO_3 and OH are not detected by these analytical methods. No portlandite was identified by the bulk XRD analysis. Steel fibers were not detected in the reacted Fibercrete™ with backscattering electron imaging (BEI) using SEM. However, because iron was not detected in the solution or the Ca-rich precipitate, it is likely that the corrosion of the steel fibers was minimal and that they were masked by the Ca-rich precipitate.

Modeling simulations regarding Ca-bearing phases must be considered with caution because the COM.R16 database does not contain thermodynamic data for many of the amorphous and crystalline Ca-Si-H_2O phases that are pertinent to this chemical system at this temperature (see e.g., Meike et al., 1994) and that data that is available is not

internally consistent. These simulations suggest that the aqueous phase was supersaturated with respect to mesolite (Na-Ca-Al zeolite), close to saturation with respect to wollastonite, albite, K-feldspar, quartz and calcite, and undersaturated with respect to bassenite (least soluble of the calcium sulfates), anorthite, and gyrolite and 11Å-tobermorite (crystalline Ca-Si-H_2O phases that are found in the COM.R16 database).

GCMS analyses of the organic phases indicated no significant difference between the starting and post-experimental sample (Table 6-11). These results suggest that neither alkaline pH nor the phases present in Fibercrete™ catalyzed the hydrous pyrolysis of diesel fuel at 200°C. However, organic compounds such as the BTEX (benzene, toluene, ethylbenzene, and xylene) compounds are water soluble at this temperature and did partition into the aqueous phase. The aqueous solubility of organic phases has significant implications for their transport which is significant to both colloidal interaction and microbial activity. However, the aqueous organic species did not appear to evolve over the course of the experiment. Within the scatter of the data: average benzene, toluene, ethylbenzene, and p-xylene are 0.04 (±0.01), 0.06 (±0.02), 0.02 (±0.01), and 0.07 (±0.02) mM respectively. The concentrations of aqueous alkanes were approximately an order of magnitude less than the aqueous aromatic hydrocarbons. Little significant change was detected with respect to gases although O_2 gas decreased from 21 to 20 mole percent. No H_2 gas was detected in the GMS analyses.

The results of DF 5, the diesel fuel-Tpt-JAW experiment at 200°C (Figs. 6-11 through 6-13), was similar to previous hydrothermal Topopah Spring Tuff experiments carried out in the absence of diesel fuel (Knauss and Beiriger, 1984; Knauss et al., 1985b; Knauss and Peifer, 1986; Knauss et al., 1987). At 200°C, the system quickly reached a metastable equilibrium. The pH (200°C) decreased slowly from 7.7 to 7.5 over the duration of the experiment. The aqueous sulfur concentration remained constant for the duration of the experiment (near 1 mM). The unusually high value of 5 mM at the end of the experiment requires verification. The inorganic carbon concentration remained constant for the duration of the experiment near its initial concentration of 3 mM. The aqueous Si concentration increased rapidly during the first few days of reaction to approximately 8 mM. The aqueous Al and K concentrations decreased rapidly and reach a constant concentration after 30 days of reaction. The aqueous Ca concentration was constant and close to the detection limit of the analytical technique for the duration of the experiment. No Fe or Mg were detected in the aqueous phase.

XRD analyses revealed no mineralogical differences between the reacted and unreacted tuff. Quartz, cristobalite plagioclase, alkali feldspar, ilmenite, and biotite

were unambiguously identified. SEM photomicrographs of unreacted and reacted Topopah Spring tuff (Fig. 6-14) reveal a Si-rich precipitate on tuff surface. Cristobalite would be consistent with geochemical modeling. The aqueous solutions are calculated to be supersaturated with respect to mesolite (Na-Ca-Al-zeolite) and albite, close to saturation with respect quartz, cristobalite, muscovite, and calcite, and undersaturated with respect to anorthite, wollastonite, and bassenite.

Similar to the Fibercrete™ results (DF3 and DF4), the Topopah Spring tuff did not catalyze the pyrolysis of diesel fuel. No chemical difference was found between the constituents of the final the organic phase and the beginning diesel fuel. The dissolved organics were dominated by aromatic hydrocarbons (Table 6-12). Within the scatter of the data, the BTEX concentrations were seen to increase to a constant value after 30 days of reaction. Average values of benzene, toluene, ethylbenzene, m/p-xylene and o-xylene concentration were 0.030 (±0.003), 0.072 (±0.006), 0.013 (±0.005), 0.04 (±0.01) and 0.013 (±0.004) mM respectively. The concentrations of aqueous alkanes are approximately an order of magnitude less than the aqueous aromatic hydrocarbons. The O_2 gas concentration decreased from 21 to 20 mole percent. No H_2 gas was detected by GMS analyses.

The results of DF6, the diesel fuel-Fibercrete™-Tpt-JAW experiment (Figs. 6-15 through 6-17), indicated little to chemically distinguish it from the Fibercrete experiments (DF3 and DF4). The solution pH (200°C) decreased from 8.5 to 8.2 indicating that the cementitous material dominated the system and that the tuff has little buffering capacity. The total sulfur concentration increased linearly from 1 to 14 mM over the course of the experiment. The inorganic carbon concentration decreased from 3 mM to a final value of 1.5 mM. During the first few days of reaction, the aqueous Si concentration increased rapidly to approximately 10.5 mM, followed by a slower decrease to 9.5 mM at the end of the experiment. The aqueous K concentration decreases from 0.9 mM to a steady-state concentration of 0.25 mM during the first 40 days of reaction. The aqueous Al concentration decreases from a maximum of 0.075 mM to a minimum of 0.025 mM after 15 days of reaction, followed by a slow increase to 0.04 mM by the end of the experiment. The aqueous Ca concentration increases linearly throughout the experiment, with the exception of the questionably high final data point. The aqueous Mg concentrations are at the detection limit of the ICP-AES spectrometer. No aqueous Fe was detected in the aqueous phase.

SEM analysis indicate that the majority of the reacted Fibercrete™ surface is covered with a well crystallized layered Ca-silicate (Fig. 6-18) distinct from the precipitate formed in experiments DF3 and DF4 (Fig. 6-10). This phase does not penetrate the

wafer. An amorphous/poorly crystalline phase can be seen in the spaces between overlapping sheets of the precipitate. It is approximately 5 to 10 μm thick, leaving open pores by not precipitating on the aggregate, as is observed in experiment DF3 and DF4, or around pores of the starting cement material. Although not rigorously determined, the ratio of Ca to Si is similar to that found in tobermorite, which was identified independently by XRD. This phase also contains minor amounts of Al, which is frequently a substitutional element (for Si) in tobermorite. No steel fibers in the reacted Fibercrete™ are observed with backscattered electron imaging (BEI) and no measurable amounts of iron were found in the solution and surface precipitate, indicating little reaction of the steel fibers, indicating that the fibers were covered by the Ca-silicate sheet precipitate. Three different precipitates were observed on the Topopah Spring tuff: (1) small 10-20 micron wide books of the layered Ca-silicate identical to the precipitate found on the Fibercrete™, (2) calcite rhombs, and (3) Si-rich matrix covering the surface, which may have been amorphous silica or cristobalite.

The aqueous organics were dominated by aromatic hydrocarbons (Table 6-11). Average benzene, toluene, ethylbenzene, m/p-xylene and o-xylene are 0.033 (±0.004), 0.081 (±0.011), 0.013 (±0.006), 0.05 (±0.02) and 0.015 (±0.007) mM respectively similar to the previous experiments. The concentrations of aqueous alkanes are approximately an order of magnitude less than the aqueous aromatic hydrocarbons. No H_2 gas is detected with GMS analyses. Analysis of the organic phase at the end of the experiment yields no discernible change from the starting diesel fuel.

At 200°C, this system quickly reaches a steady state, which, according to geochemical calculations is a metastable equilibrium. The aqueous solutions were calculated to be supersaturated with respect to mesolite (Na-Ca-Al-zeolite) and albite, close to saturation with respect quartz, cristobalite, wollastonite, K-feldspar, muscovite and calcite, and undersaturated with respect to anorthite, 11Å-tobermorite, gyrolite, and bassenite.

Discussion. The experiments indicate that the abiotic degradation of diesel fuel is slow with respect to repository lifetime and, unaided by biotic degradation, would remain almost indefinitely. Our experimental results show that hydrothermal degradation of diesel fuel is minimal at mildly acid and alkaline pH over two to three month reaction periods at 200°C and 70 bars. At 200 and 315°C, low carbon number aromatics and alkanes dissolve into the aqueous phase, but the production of carboxylic acids is limited. It is possible that the soluble aromatics and alkanes are intermediate degradation products between diesel fuel and carboxylic acids. The dominant water-soluble organics are aromatic compounds, not aliphatic carboxylic acids. At 315°C, the

diesel fuel is significantly more reactive, although the net production of carboxylic acids is minimal. However, soluble alkanes, aromatics, and carboxylic acids may be intermediates between the unstable diesel fuel and the equilibrium thermal degradation products. A probable reaction path for diesel fuel hydrous pyrolysis may be:

Diesel Fuel ⇒ soluble aromatics and alkanes ⇒ carboxylic acids ⇒ carbonic acid (1)

Although production rates of carboxylic acids at 200 and 315°C are too low to be quantified directly, the final pH values for experiments DF1 and DF2 support the presence of acetic acid, which has a pK_a of 4.8 at 25°C. In contrast to the reaction path proposed above, (Kharaka et al., 1993) and (Lundegard et al., 1992) interpret measured concentrations of carboxylic acids from oil hydrous pyrolysis experiments as simple partitioning between the aqueous and organic phases. However, if that were the case, then the organic acid concentrations and the pH should have been constant over time. In experiments DF1 and DF2, the solution pH continues to decrease slowly as a function of time.

A conservative rate of diesel fuel hydrous pyrolysis can be made from the pH data (measured at 25°C) as a function of time from experiment DF2 (315°C). To make these calculations, it is assumed that the decrease in pH reflects a net increase in total dissolved inorganic carbon (carbonic acid) or total dissolved acetate. In the inorganic carbon system, a total inorganic carbon concentration can be calculated from pH and the carbonic acid dissociation mass balance, charge balance, and total carbon equations. The dissociation reaction (K_a) and mass balance expression for carbonic acid are:

$$CO_2(aq) + H_2O \Leftrightarrow H^+ + HCO_3^- \qquad K_a = ([H^+][HCO_3^-]/[CO_2(aq)]) \qquad (2)$$

where the $pK_a(25^\circ C) = 6.35$ (and $pK_a = \log K_a$). Total inorganic carbon mass balance (C_T) and charge balance equations at the experimental pH are:

$$C_T = [CO_2(aq)] + [HCO_3^-] \qquad (3)$$

and

$$[H^+] = [HCO_3^-], \qquad (4)$$

respectively.

Similar calculations can be made assuming the decreasing pH reflects an increase in the total acetate concentrations as a function of time. The acetate system is chosen to represent carboxylic acids, because the final pH of both experiments DF1 and DF2 is near the acetic acid pK_a. The dissociation reaction for acetic acid and corresponding mass balance expression are:

$$HAc \Leftrightarrow Ac^- + H^+ \quad K_a = ([H^+][Ac^-]/[HAc]) \tag{5}$$

where $pK_a(25^\circ C) = 4.87$. In this model system, the total carbon mass balance and charge balance equations for the experimental pH may be written as:

$$C_T = [HAc] + [Ac^-] \tag{6}$$

and

$$[H^+] = [Ac^-], \tag{7}$$

respectively. The results of both of these simple systems are shown in Fig. 6-19. The calculated inorganic carbon concentrations increase linearly as a function of time, approaching the measured values near the detection limit after 100 days. The calculated total acetate concentrations increase linearly as a function of time, and remain well below the detection limit of the LC analytical technique, 0.4 mM. The calculated increases of inorganic carbon or total acetate can be used as conservative rates of diesel fuel hydrous pyrolysis: 8.3×10^{-6} M C/day from the inorganic carbon model or 7.8×10^{-7} M C/day from the acetate model. In all likelihood, the decrease in pH as a function of time represents contributions from both increasing concentrations of carbonic and carboxylic acids. These low concentrations cannot be accurately measured and thus long term effects remain unknown, however they can be bounded by using the detection limit as a guide.

Thermal degradation of diesel fuel is not enhanced in the presence of cementitious material or at alkaline pH. Similarly, diesel fuel hydrous pyrolysis is not catalyzed by Fibercrete™ or by Topopah Spring Tuff and does not accelerate dissolution of silicate minerals found in these solids at 200°C. These results agree with previous studies that show that water inhibits the catalytic effects of clay minerals in contact with alkanes, alkenes, alcohols, and ethers (Weres et al., 1988; Tannenbaum and Kaplan, 1985). In a preliminary study, Bell et al. (1992) show that acetate decarboxylation reactions are enhanced in the presence of magnetite, hematite, Ca- and Fe- montmorillonite, and non-

stoichiometric pyrite, indicating the Fe^{3+} - Fe^{2+} redox couple as an important catalyst. However, in this study, the presence of metal iron in the steel fibers did not catalyze the hydrous pyrolysis of the complex organic mixture.

Secondary results support the understanding that the presence of cementitious materials will react, affecting the chemistry of the water with which it is in contact, the repository rock its own porosity, as well as its own permeability and mineral assemblage.

6.2.1.2 Cementitious Materials. The number, identity, and significance of potential coupled interactions between man-made materials are as yet not determinable. However, interactions between concrete and some other materials are known to be significant for the chemical environment. The oxidation of rebar creates a chemical environment that increases the degradation rate of concrete. Examples of this effect can be seen in many major bridges and thoroughfares, but knowledge of these processes remains qualitative. Tests in which concretes were leached at 100 to 200°C with either distilled water or Standard Canadian Shield Saline Solution (SCSSS) in contact with a sodium-bentonite, a waste glass, or a silica fume additive have indicated that the identity and concentration of species in solution is time-dependent (Komarneni and Roy, 1983; Burnett et al., 1985; Heimann and Hooton, 1986; Onofrei, 1987; Heimann, 1988a,b).The fate of C-S-H and the cement minerals, and their interaction with the aggregate, are a function of time, temperature, solid and aqueous solution compositions, and the availability of water. Of particular chemical concern is whether the concrete is exposed to air, CO_2 or water, the aluminate and ferrite content of the cement, and the activities of carbonate and sulfate in the water. The preferred rheology of the cement at the time of emplacement dictates the quantity of water added to the dry cement mix and usually exceeds that required for complete hydration. Therefore, extra water is expected in any situation in which wet grout is emplaced. Physical properties, such as interconnected porosity, can regulate the rate of, and the long term susceptibility to chemical attack. Porosity is affected by initial water:cement (w/c) ratios and thus potentially by the method of emplacement. Leaching will preferentially dissolve some minerals such as portlandite from the set material and thus can increase permeability, which will influence the rate of degradation. Sufficiently high activities of sulfate or CO_2 can react with concrete. At elevated temperatures, residual portlandite reacts with carbonates to form calcite (Milestone et al., 1987).

Disintegration and dissolution of cementitious materials may change the pH of water to values as high as 11.5 at 100°C. Tobermorite (14 Å) forms in water at temperatures below 80°C (Fujii and Kondo, 1983). This phase begins to lose interlayer

water at 70°C in dry CO_2-free air to give 11Å tobermorite (Taylor, 1987). Sulfate-resistant cements (Soo and Milian, 1989) are formulated to have a relatively low aluminum content so as to minimize the possibility of forming ettringite after the cement has set. Minimization of the volume of portlandite in the set cement controls the reaction of $Ca(OH)_2$ with sulfate to form gypsum. The large volume increases associated with both ettringite and gypsum formation cause cracking and increase the surface area exposed to degradation.

Insight into the long-term performance of cements has been gained from examinations of (1) groundwaters that issue from rocks containing cement-type minerals, and (2) ancient concretes. Water with a pH as high as 12.5 has been collected from rocks containing portlandite, ettringite, tobermorite, and higher temperature minerals (Khoury et al., 1985; Neal and Stanger, 1984). A preliminary calculation of phases in equilibrium with the water (Barnes et al., 1982) is consistent with these natural data. Ancient Roman concretes often incorporated pyroclastics, including acidic tuffaceous material that may be applicable to modern portland cements in the sense that similar aggregate is being considered for use in the repository. Examination of these ancient materials demonstrates that low-permeability cements, and particularly pozzolanic cements, have the greatest durability (Roy and Langton, 1983, 1989). Optical and compositional comparisons between modern portland cement and a relatively young portland cement that had been submerged in water for 63 years (Rhoderick, 1981) have revealed no significant differences. Whether the resolution of data acquisition in this study is appropriate to predict change over 10,000 years has not yet been established.

The presence of cementitious material may greatly alter the geochemistry of the repository by providing a large reservoir of unstable Ca-silicate phases which will dissolve and reprecipitate at the rock-water interface. Chemical interactions between water and non-thermally treated grout at 20-60°C may well be dominated by the dissolution kinetics of the unstable amorphous and crystalline phases and precipitation kinetics of the metastable or stable phases (e.g., Atkins et al., 1991). This type of low temperature interaction has received much attention internationally and can be found in the radioactive waste disposal literature.

A unique aspect of the Yucca Mountain strategy relative to other high level radioactive waste strategies around the world is that water will probably contact the cementitious material only after it has been exposed to elevated temperatures (>100°C) for an extended period of time (>150 years). It is likely that the cementitous materials will have dehydrated and transformed to a more crystalline mineral assemblage. Many

phases in the crystalline Ca-Si-H_2O system can develop in cement exposed over long periods of time to temperatures above 25°C. The phases themselves are found both naturally and in synthetic systems. As a consequence of their appearance in cements exposed to elevated temperatures, chemical reactions involving these phases can affect not only water chemistry, but also the relative humidity of a radioactive waste repository that contains significant amounts of cement. In order to predict and simulate these chemical reactions, we are developing an internally consistent database of crystalline Ca-Si-hydrate structures. The experimental aspects of the synthesis and characterization of pure phases for the purpose of measuring thermodynamic parameters is discussed elsewhere (e.g., Barnes et al., 1996; Martin, 1995; Bruton et al., 1994; Meike et al., 1994). A complete synopsis of the work in the cement area is not ready at present due to the premature halt of a five year study in this area.

Other reactions known to occur in cementitious materials over time would contribute to alterations in the mineral assemblage and contribute to their degradation and reduction of mechanical strength. These are chloride attack, the alkalai silica reaction (ASR) and delayed ettringite formation. Chloride attack works by the ingress of chloride bearing water through permeable grout or cracks to contact and corrode the metal reinforcement (rebar). Expansion of the rebar due to corrosion causes the cementitious materials to crack and spall. One of the notable sources of chloride attack for the present application is the use of aggregate from desert climates that may contain evaporated salts (Taylor, 1990). Alkali silica reaction occurs when silica bearing aggregate reacts with alkali impurities in the cement paste. As with chloride attack, expansion occurs due to formation of the product phases, causing cracking (Taylor, 1990). Delayed ettrigite formation is also a cracking process due to the late formation of sulfate bearing phases (Taylor, 1990). There is still much debate about the causes of DEF. However, some significant DEF has been related to the heat-curing of sulfate-bearing cements. A phenomenon similar to DEF occurs through the formation of thaumasite, a sulfate-carbonate mineral (Crammond, 1995).

Roy and Langton (1983, 1989) have studied ancient concretes, to ascertain mineral stabilities and instabilities that may be applicable to modern Portland cements. The ancient concretes, which were made from lime formulations, are not completely analogous to the modern concretes which are composed of "alite" and "belite" and require higher temperatures for manufacture. Although made with unknown processes as well as varying starting materials, and mixed using unknown water/cement ratios, ancient Roman concretes often incorporated pyroclastics, including tuffaceous material. A main conclusion that Roy and Langton draw from examination of ancient materials is

that low permeability cements, and particularly pozzolanic cements, have the greatest durability. A study of mortars from the Byzantine basilica of Hagia Sophia, Istanbul suggests that a calcium silicate hydrate phase is present. The degree of crystallinity is not well constrained, however, and the mortar appears to be dominated by a calcium carbonate phase. A cursory examination of a Portland cement that had been submerged in water for 63 years (Rhoderick, 1981a, b, c) suggested no "significant effect" on either composition or microstructure. Notably lacking for the purpose of the Yucca Mountain Project are studies of cementitious materials that have been exposed to elevated temperatures for extended periods of time. It is clear that at elevated temperatures will cause changes in both composition and microstructure, which would ultimately affect the chemistry of the water in contact with the material, as well as its structural integrity.

A different approach to evaluating the long-term performance of cements is to examine the occurrence of hyper alkaline groundwaters issuing from rocks that contain cement-type minerals. One such occurrence had been noted (Khoury, 1985; Neal, 1984): in Jordan, a pH 12.5 water issuing from rocks containing portlandite, ettringite, tobermorite, and higher temperature minerals. Combustion of bituminous marl generated a pre-cursor assemblage of minerals similar to modern cement. Upon contact with water, recognizable calcium silicate hydrate minerals were formed. A somewhat incomplete calculation of phases in equilibrium with the water was reported by Barnes et al. (1982). Since important constituents of the water analysis were not reported, an exact replication of the calculation using EQ3 could not be made. By using additional data from the later literature cited above, the phases showing supersaturation and the degree of saturation via an EQ3 calculation were parallel those reported in Barnes et al. (1982).

Tobomorite synthesis and stability with respect to CO_2. Observations of the extreme sensitivity of tobermorite, a cement phase expected under repository conditions, during its synthesis (Martin et al., 1994) indicate that the formation of tobermorite is sensitive to the partial pressures of CO_2, and at partial pressures of CO_2 greater than ambient compositional and microstructural changes are also to be expected. Ultra-pure samples tobermorite and other crystalline Ca-Si-hydrates have been synthesized and characterized in order to obtain thermodynamic data. The purpose of this thermodynamic is to fill a need for fundamental parameters that are not available in the literature. These parameters are required in order to model the interaction between water and cementitious materials (see the Fibercrete-water experiment discussed above, and Meike et al., 1994).

The starting materials for synthesis were CaO and an aqueous suspension of fumed SiO_2 ("Cab-o-sperse") in a molar ratio of 5:6. The CaO was prepared from $CaCO_3$ heated to 1050°C for >4 hours. The highly reactive SiO_2 had a surface area of 100 m^2/g. In one case hydrochloric acid (HCl) was added before mixing with CaO to neutralize the SiO_2 suspension which had a pH of 9.8. The constituents were mixed in an argon filled glove box to inhibit CO_2 uptake. CO_2 free water was added in excess to obtain a homogeneous sol/gel. The gels were autoclaved at 90 and 120°C in pressure vessels. Individual vessels were sampled multiple times over the total length of the run in the argon glove box. Post run treatment of the aliquots included washing the product with milli-Q water and ethanol before drying in desiccators. To hinder calcite formation and remove excess CaO in the product some of the reacted samples were titrated with HCl to a pH of 7-8.

Powder x-ray diffraction (XRD) was used to identify the mineralogical phases. Two types of run products were obtained, a mixture of 1.1 and 1.4 nm tobermorite at 90°C, and a 1.1 nm tobermorite at 120°C. For the mixed phase runs the intensity of the 1.4 nm peak decreased and the 1.1 nm peak increased over time as the tobermorite became less hydrated (Fig. 6-20). Mixed phase samples heated and dried at 100°C produced a 1.1 nm tobermorite. X-ray diffraction of the higher temperature run indicated a single phase, 1.1 nm tobermorite (Fig. 6-20). In general, tobermorite became more crystalline over time and at higher temperature. Scanning electron microscopy (SEM) was used to determine particle morphology. Photomicrographs of the reacted material showed an aggregation of platy particles similar to those shown by Suzuki and Sinn[3]. No distinct morphological differences were noted between the 1.1 nm tobermorite and the mixed 1.1 and 1.4 nm tobermorite.

Measures were taken to preclude calcite formation but calcite was detected in the product and was probably due to unreacted CaO reacting with atmospheric CO_2 (pH measurements of the run products were high, 11.3). The formation of calcite was not instantaneous. X-ray diffraction patterns indicated an increase in calcite concentration in the longer runs and was most pronounced in the longest run of 161 days. Although aliquots were taken in the argon glove box, they were cooled outside of the box in the laboratory. Carbon dioxide may have diffused through the Teflon lined vessels into the run product.

Carbon dioxide concentrations were measured with a CO_2 analyzer and indicated equivalent $CaCO_3$ concentrations of up to 6%. Calcite concentrations were the highest in samples exposed to atmospheric CO_2 for longer periods of time. Samples titrated with HCl immediately after synthesis did not contain calcite, and XRD analysis of shelved

samples containing calcite indicated that the calcite was removed from the sample with acid titration without affecting the tobermorite. The volume of HCl added to reduce the pH to approximately 8 was equivalent to an excess CaO concentration of approximately 8%, which correlates to a $CaCO_3$ concentration of approximately 14% if completely reacted.

The extreme sensitivity of tobermorite and other crystalline Ca-Si-hydrates that may exist in ordinary portland cement to the partial pressure of CO_2 suggests that, in a repository environment, much of the cementitious material could evolve into $CaCO_3$ phases such as calcite and vaterite. The consequences to the pH are significant. Whereas a young cement- water system could register pH values of 11 or 12, a calcite water dominated system would have a significantly lower pH.

Significance to YMP. It is clear from the extant literature and studies that have been conducted to date, that at temperatures near 25°C water in contact with modern ordinary portland cement can obtain extremely high pHs. However, the effects of other factors, such as microbes, heating and pCO_2 above ambient have not been well established and therefore cannot be well constrained. Therefore for the purpose of chemical performance assessment the addition of cementitious materials widens boundary conditions and increases uncertainty. With regard to the potential survival of concrete, we recognize an important distinction between "performance lifetime," which is linked to the mechanical stability of the structure, and chemical lifetime which represents the duration of the chemical effects of the material long after the material has ceased to perform its function. It will be important to explicitly specify the mechanical performance lifetime required of the cements by the design, because it may be possible to obtain modern high performance formulations that will perform a mechanical function throughout the retrieval period, and perhaps stretching into some of the period after closure. However, it may not be necessary (or even possible) to engineer (or prove the stability of) a cement with a performance lifetime of thousands of years.

It is highly likely that long after the mechanical "performance lifetime" of the cementitous materials has ended, these materials could perform chemical functions such as sorbing radionuclides, especially if the formulation were to contain zeolites as aggregate or pozzolana. In fact, at the point in the evolution of the repository where sorption is required, an invert a material that is considered to have low very long term mechanical performance properties may be an asset. This is because large surface areas predominantly determine the effectiveness of a sorbant, and thus a cementitious material that becomes greatly fractured or disaggregated increases the effectiveness of the constituent sorbant materials.

6.2.1.3 Metals. Metals that are introduced into a repository environment as a result of construction are used for many different functions (see previous section) and are composed of almost as many different alloys. Thus the concern of the introduced materials studies are far different from those that are intended to select a material for the waste package. Many of the high tech alloys considered for waste packaging materials are not used widely in construction. Conversely, the alloys that are used in construction are the more common and cheaper metals that may not make the best waste package. Fortunately, most of the metals used in construction have been used for many years and provide a foundation of knowledge in this area. For that reason, although a significant construction material metals have not been emphasized in these studies to date.

Metals that may be introduced into the WP environment for construction purposes will be primarily iron and iron alloys, which can degrade through several mechanisms. Oxidation is one common degradation process. Such processes are strongly dependent upon the Eh and pH of the environment within which oxidation occurs. Cast iron, if present in large volumes, has the potential to consume large quantities of oxygen and influence the atmospheric chemistry around waste containers. Experimental studies of copper corrosion in sea water and in the presence of sulfide ions (Mor and Beccaria, 1975) indicate that a variety of copper sulfides can form that are also dependent upon pH. The specific conductivity and resistance to corrosion of the metal are dependent upon the corrosion product, which is pH-dependent. In general, the rate at which metal ions are added to the water is dependent on the corrosion products.

Much of our understanding of the long term chemical processes involving metals that may be used in a radioactive waste repository will be based on a firm understanding of historical analogs. Many of the processes that will affect metal construction materials are identical to those that have affected metal archaeological artifacts. Outside the Yucca Mountain Project, interest in the degradation of metals is found in disparate sources from the U.S. Naval Oceanographic and Atmospheric Research Laboratory to many oil companies. Because of this interest, and also because of the length of time that man has been working with metal materials, much more information is available on the long term degradation of metals than most other manufactured materials. A literature review on the corrosion of metal artifacts has been conducted in support of waste package design.

Studies of metal artifacts from a variety of ages demonstrate that some phases that form cannot be predicted from our present knowledge of material degradation. Some products of these man-made materials rarely occur naturally and are therefore not

necessarily predictable from a geochemical data base. Botallackite, a rare hydroxide of copper chloride, for example, has been observed associated with the corrosion of a copper object exposed to chloride ion (Pollard et al., 1989). Stability fields and reactive sequences of the basic copper (II) chlorides have only recently been proposed (Pollard et al., 1989) on the basis of this and other historical data as a complement to experimental data, where experimental data alone has previously failed. That diffusion-controlled phenomena should be expected over time periods of at least 2,000 years is apparent from investigations of corrosion phenomena in ancient bronzes (Scott, 1985). Development of some phases appears to be mediated by the activity of microorganisms (McNeil et al., 1990).

In addition, information on the long-term corrosion of materials is being assembled from the New Zealand analog site (Bruton et al., 1995). In the respect that this data represents materials that are more similar to present construction materials and methods, some data from the New Zealand (e.g., Foster and Tombs, 1962; Soylemezoglu and Harper, 1982; Braithwaite and Lichti, 1981) and other geothermal fields (e.g., Dodd et al., 1960; Hermannsson, 1970; Hanck, and Nekoksa, 1980; Culivicchi et al., 1985) may be more useful to chemical model assessment than much older archaeological artifacts.

6.2.1.4 Polymers. Assessments of the long term chemical affects of those polymers and their reaction products in the repository are based on current understanding in polymer science which can be translated into models, but given the relatively new nature of these materials, experimental data must be gathered to test these models. Several sources have cautioned that polymer behavior can not be compared with that of simpler but similar molecules. Therefore, no conclusions should be made about polymers based on the behavior of smaller molecules. However, some correlations may be made between synthetic and natural polymers and between modern polymers and their predecessors (assuming one is aware of the cautions mentioned previously). Natural polymers such as keratin, cellulose and starch as a rule degrade much more easily than synthetic polymers. One reason is that they are more hydrophilic and another is that nature is more equipped to get rid of them (i.e., enzymes). Correlations may also be drawn between silicone and silica which have the same ancestry. It must be stressed, though, that only general correlations may be drawn and that the specific polymer must be investigated for specific information.

The primary modes of degradation for synthetic polymers are thermal degradation, oxidation, and photodegradation. Biodegradation will also be discussed in the section below. The degradation of a polymer can not be followed by observing the behavior of a similar but simpler molecule. First, there are many small chemical differences between

polymers and less complex molecules. The differences in termination of polymers are dependent on preparation. Often, side branches are incorporated during saturation. Polymers often undergo changes with the environment which are different from similar simpler molecules. Second, the length of polymers makes many reactions possible which are impossible in smaller molecules and reactions can be rapid in long chain molecules. Polymer degradation occurs by one of two primary structural changes: cross-linking or chain scission. Models have been developed to predict specific degradation processes over times significant to a radioactive waste repository (Burnay, 1990) however most models are for normal life times and under normal service conditions (Kenny, 1993). An activation energy must be reached before degradation begins (Ravanetti and Zini, 1992) which can be derived from thermal analysis. The Arrhenius equation is often used to predict the half lives of materials (Barr-Kumarakulasinghe, 1994). It has been found that thermal degradation rate is increased by higher temperatures, the presence of a radiation flux, oxidative agents, some chemical contaminants and light. In addition, many polymers can exhibit dose rate effects or synergism between radiation and temperature or chemical contamination (Burnay, 1990).

Hydrolysis involves the substitution of an OH for an OR of the polymer. For example, in *polyurethane*, a break would most readily occur at the carbon oxygen single bond and hydrolysis would form toluene diamine and polyether, which are almost identical to the starting material. Another method of polyurethane degradation is glycolysis, which involves the "dissolution of polyurethane (usually foam) in hot glycols, polyethers or polyamines. In this way additional monomer can be added to the solution which can then be used for a new product. However, given the difficulty with which glycolysis and hydrolysis are carried out for the purpose of recycling, the processes may not be relevant.

There are two types of thermal degradation. The first, depolymerization, involves the breaking of the main polymer chain backbone so that at any intermediate stage, the monomer units can be recognized (Grassie, 1985). This is common for polymers which give high values of chain scission at ambient temperature (Garrett et al., 1990). The second, substitution reaction, involves the substituents attached to the backbone of the polymer molecules such that the chemical nature of the repeat unit is changed even though the chain structure may remain intact. In this case, volatile products will be unlike the monomer (Grassie, 1985)."

Leedy and Watters (1994) found that rock bolt *epoxy* degrades at temperatures as low as 50°C and should thus not be used long term mechanical support in areas that

will be exposed to elevated temperature. However a variation in degradation behavior exists, probably dependent on the epoxy. It has been found that at 125°C the primary degradation mechanism for epoxy resins is initiated by oxygen attacks rather than a free radical mechanism. Many epoxy resin systems manifest significant oxidative degradation in air at temperatures as low as 100°C (Burton, 1993). A change in mass begins just below 250°C. To 310°C the degradation reaction is primarily dehydration and is identical in air and an inert atmosphere. Chain scission occurs above 310°C with evolution of SO_2. The rates of weight loss are maximal at 350 and 520°C (Rose et al., 1993). Although Tg varies dependent upon the exact epoxy, epoxies tend to have Tgs from 110°C to 135°C (Kaplan, 1991). Improved crystallinity decreases degradation at high temperatures while aromatic linear groups improve stability. Epoxy resins should not be included in the permanent structure, without detailed long term tests.

Kevlar is extremely heat resistant relative to other polymers with a degradation temperature of 601°C; at this temperature, kevlar will degrade at a rate of about 10 percent per minute (Kutty et al., 1992). However, exposure to thermal environments can alter kevlar's properties and performance. It has been found that "after 250 and 6 h exposure to 250 and 350°C, respectively, the fibers turned brittle and crumbled with handling (Parimala and Vijayan, 1993)." Fibers treated at 150°C remained unaffected over known lifetimes. However, given the relative youth of this material, and thus the lack of historical analogs, it is not possible to predict the response to thousands of years of degradation and an extended (100-200 year) thermal pulse at the 100-200°C range.

Neoprene degrades by a scission reaction accompanied by cross-linking. The metal oxides are consumed during the degradation process of primarily auto-oxidation. Chemical products are dependent on additives and temperature, and should be the subject of analysis should neoprene be considered as part of the permanent repository structure.

Depolymerization and extensive chain fragmentation of *polybutadiene* generally take place at temperatures greater than 300°C, when the activation energy needed for degradation is reached, and becomes appreciable at temperatures greater than 380°C. Below this temperature, some volatile products are released as well as some structural changes such as crosslinking but these are minute. The products of thermal degradation of polybutadiene are primarily larger "fragments" but also include monomer, hydrocarbons and "volatile" products (Brandrup and Immergut, 1975). The degradation process is exothermic up to 380°C and above that, it is endothermic. At about 200°C, polybutadiene becomes insoluble, "presumably in consequence of some degree of crosslinking. From NMR and IR spectroscopy, it has been found that "the polymer first

undergoes a saturation-cyclization process, in which the vinyl groups are the first to disappear. But, at 300°C, it becomes soluble again; in fact, after only half an hour at this temperature, "the product becomes soluble, the content of olefinic hydrogens drops to a mere 2.6%, and aromatic structures begin to appear (Schneider et al., 1993). When studying the thermal degradation of polybutadiene (PB) it must be taken in account that different proportions of the possible structural units (cis-1,4, trans-1,4, and 1,2) can be present, and consequently differences in the overall thermal behavior may be expected (Chiantore, 1989). The composition of the solid and condensed liquid products of thermal degradation of PB depends on temperature and time. By prolonged heating at a lower temperature, products comparable to those obtained at higher temperature cannot be generated (Schneider et al., 1993).

Two main thermal degradation products of *polycarbonate* at temperatures up to 400°C are monomer (and dimer and trimer) and *p*-cresol (Imasaka et al., 1992).

At temperatures above the melting temperature at long time periods, *polyesters* undergo chain scission. With PET, this reaction leads to carboxyl and vinyl ester groups. These react to an acetyl ester intermediate to form carboxylic anhydride linkages and acetaldehyde. Polyester salt complexes have been synthesized for potential battery applications. It was found that the thermal stability of these complexes was significantly less than for polyester (Kay et al., 1993). However, it is unknown whether these complexes would occur outside a laboratory.

The thermal degradation of *polyethylene* is dependent on the degree of side branching; the more linear the polymer, the higher the stability. It is assumed that the molecular weight of polyethylene increases due to long-chain branching which increases the polymer viscosity at about 200°C. However, after one hour of heating at 300°C, the spectrum of branched polyethylene exhibits no chemical or conformational changes (Svoboda et al., 1990).

After heating an isotactic (probably high percent crystallinity) *polypropylene* sample at 300°C, polypropylene does not exhibit chemical change. It is assumed that the molecular weight of polyethylene increases due to long-chain branching which increases the polymer viscosity at about 200°C (Svoboda et al., 1990) while the primary degradation mechanism is chain scission Polypropylene has been converted to gasoline range chemicals in the presence of zeolite-catalysts (Mordi et al., 1992). The process took about 2 hours at 350°C and no solid polymer remained at the end of the process. The addition of carbon black decreases the thermal stability while the addition of red pigment increases the stability (Wallius, 1993).

Poly(styrene) is known to undergo thermal degradation above 250°C to yield mainly monomer (Garrett et al., 1990). Between 200 and 300°C, the molecular weight of PS falls, but volatilization is not significant below 300° C (McNeill et al., 1990). Degradation occurs via scission of the carbon backbone, either randomly or at weak links with a peak in degradation at 392°C. Above 300°C, the polystyrene degrades into monomer, small amounts of toluene and a-methylstyrene, and oligomers (very short chains made up of monomer). Among other products, toluene and ethylbenzene have also been found in the decomposed products of polystyrene (Sato et al., 1990; Imasaka et al., 1992).

When exposed to high temperatures (in excess of 300°C), *Teflon* degrades to pure monomer. At high pressures (1013 mbar or higher) Teflon primarily degrades to three and four carbon fluoro-carbons and a poisonous gas monomer

Polyurethane can be subjected to high temperatures in the absence of oxygen to obtain the original petrochemical reactants; isocyanates and alcohols (Kutty et al., 1992). It is common knowledge that the addition of reinforcing high temperature fibers to a polymer system improves many properties such as thermal resistance. In the case of polyurethane reinforced with kevlar fibers, the degradation begins at 245 to 255°C and reaches peaks at 383°C and 448°C (Kutty et al., 1992). However, the transition temperature of polyurethane alone is significantly lower. Serious decrease of foam thermal stability begins above 160°C. The first evidence of weight loss in un-aged PUR foam is at temperatures between 200-300°C and it is caused by rupture of the primary bonds in the polymer. At temperatures between 240-540°C weight loss involves thermal and oxidative degradation. Aged foams showed similar but more pronounced weight loss. The Tg of polyurethane is 82.5°C, the melting temperature 182.5°C and the decomposition temperature 250°C at which the polyurethane foam degraded to urethane units (Rek et al., 1990).

When *PVC* is exposed to elevated temperatures, even below its melting point, PVC loses chlorine which forms HCl and becomes discolored, leading to deterioration of properties (Okieimen and Ebhoaye, 1992; Bisi et al., 1994). The T_g of PVC is about 81°C (Naqvi, 1991). The steps of PVC degradation (initiation, fast zip-elimination of HCl and simultaneous formation of [polyethylenes], and termination of the zip) are the same irrespective of the type of degradation (thermal, thermo-oxidative, photo or mechanical) (Ivan et al., 1991). Between room temperature and 185°C minimal weight change is observed for untreated PVC. HCl is produced between 185°C and 375°C. Structural reorganization occurs between 375°C and 550°C. Structural degradation in which hydrocarbons are evolved occurs above 550°C (Chatterjee et al., 1994). The Yucca Mountain Project will be primarily concerned with the first two stages. In air, the HCl

generation is doubled (Nass and Heiberger, 1986). Since HCl is corrosive and highly reactive, its presence in a potential repository will be of significance. In addition, the formation of chlorinated toxic compounds and/or other noxious substances depend on the different additives commonly used in commercial grade PVC (heat and light effect stabilizers, lubricants, extenders, pigments, dyes, etc.) (Bisi et al., 1994). PVC is intrinsically thermally unstable. PVC undergoes chain scission in the presence of metal soaps.

The great commercial importance of PVC is due to the development of effective means of stabilization. Thermal degradation is generally considered to be initiated at unstable sites within the polymer structure. Thermal stabilizers are known to function by replacing labile atoms in PVC; they inhibit or suppress the elimination of HCl and interrupt the formation of conjugated polyene sequence in the polymer (Okieimen and Ebhoaye, 1992). It has been shown that soaps from rubber seed oil are effective in preventing dehydrochlorination. Metal sterates ($PbSt_2$, $CdSt_2$, $BaSt_2$, $CaSt_2$, and $ZnSt_2$) have been used as stabilizers, reducing the rates of free HCl evolution destroying peroxides and peroxide radicals (Ivan et al., 1991). The main cause of instability in PVC is abnormal internal structures. The rate of dehydrochlorination may depend on internal double bonds, and allylic chlorines located at chain-end (Xu et al., 1989a). The terminal double bonds of PVC affect the intrinsic thermal stability. Fewer or greater terminal double bonds than the optimum has lower thermal stability (Xu et al., 1989b).

Silicone rubber has a useful life of up to 20 years at 120°C or up to five years at 150°C (Lynch, 1978) which is considered outstanding relative to other polymers.

The presence of oxygen in the environment of a polymer almost always speed up degradation. If the polymer contains hetero-atoms, then polarity governs the rate of oxidation. In addition, it is important to note that stability to thermal degradation is not always the same as stability to oxidative degradation for a given polymer. Oxygen susceptibility is dependent on the state of the polymer. For example, polystyrene oxidizes readily in solution but not in solid form. In addition to chemical structure, physical structure affects the rate of oxidation.

Polyethylene is unstable in the presence of oxygen in air, eventually degrading to carbon dioxide and water. This process takes a about 18,000 hours at 20°C, but is expedited at higher temperatures, 31 hours at 80°C (Barr-Kumarakulasinghe, 1994).

The oxidation of *polypropylene* causes the melting point to decrease (Wallius, 1993).

Plasticization and swelling result when solid polymers are exposed to various solvents (Kaplan, 1991), some of which may be present, or may be produced in a repository setting. In a poor solvent, where the interactions within the polymer chain

are strong and the interactions with the solvent are weak, the polymer molecule will have a tight conformation. A stronger solvent causes the molecule to spread out so that there is more interaction between solvent and polymer. In addition, chemicals can degrade polymers. When placed in a swelling agent such as water, hydrophilic glassy polymer networks swell and form gels (Khare et al., 1992). Environmental factors affect the solvent interaction. Often, an increase in pH will lead to an increase in swelling force. Temperature also has an influence on solvent interaction and appears to be consistent with Arrhenius activation theory. The kinetics of equilibrium concentration can be explained by the first-order kinetic rate equation. In addition, most polymer/solvent systems follow Fickian diffusion (Khinnavar and Aminabhavi, 1992).

Epoxy resins vary in sorption characteristics with different cures and different resins. The huge variety of resins, curing agents, additives exacerbate the difficulties in understanding how solvent damage occurs. In addition swelling and plasticization occur to different extents depending on the solvent. Studies conducted at 22, 40 and 50°C indicate that water produces absorption to about 3 percent (Kaplan, 1991). In contrast, methanol, ethyl acetate, 1,2-dichloroethane and toluene are taken up rapidly by the epoxy from 10 to 20 percent. An increase in temperature increases the sorption of various solvents. This is because as temperature increases, there is more motion in the molecular chains and thus more interaction with solvents (Kaplan, 1991).

Polypropylene interacts with a wide variety of solvents in which it either swells or degrades.

PET, in crystalline form and at room temperature, is resistant to dilute aqueous mineral acids, nonbasic salts and many organic compounds while being vulnerable to oxidizing reagents and aqueous alkalis.

The conversion of *PS* to low molecular weight products is dependent upon both the kind of solvent used and the solvent concentration. The conversion was low in solvents that are hydrogen donors. The decrease in solvent concentration brought a rise in the conversion and the tendency was significant in good hydrogen donor solvents. These results were explained through hydrogen abstraction processes from the solvents by the polymer radicals (Murakata et al., 1993)." Specifically, "the conversion of PS to low molecular weight products [is] dependent on the hydrogen donating ability of the solvents used: Solvents with greater donating ability [result] is less conversion of PS (Sato et al., 1990)."

Polymer deformation often occurs when a polymer comes into contact with heat or a highly reactive solvent. Likewise, *polyurethane* elastomers have been found to react with solvents depending on the solvent and the temperature. In tetrahydrofuran, dioxane,

cyclohexanol, acetophenone and benzyl alcohol, the polymer swells, even at room temperature. In pyridine and aniline, there is a loss of physical integrity which leads to chemical degradation reactions (Aminabhavi and Aithal, 1990). Furthermore, the addition of a basic solution would also break down the polyurethane structure.

Silicones have very good chemical resistance and remain chemically resistant at higher temperatures. In contrast, most other polymers loose their chemical resistance at higher temperatures (Lynch, 1978).

6.2.1.5 Radiation Effects. The effect of radiation on polymeric materials has been studied since the construction of the first nuclear power plants in the 1950s. When exposed to high-energy radiation, polymeric materials undergo chemical changes. The energy from the radiation excites the polymer molecules leading to chemical change. Most energy is deposited in the substrate by Compton scattering, whereby the ejection of a valence electron is accompanied by deflection of the incident photon by the electron cloud around the atom. At lower energies, the incident photon is completely absorbed by the substrate atom to produce ionization. Radiation degradation can be measured from changes in the molecular weight from which, the degree of cross-linking and scission can be determined. After irradiation, polymers continue to undergo changes. For example, irradiation in air leads to the formation of peroxides and these compounds have characteristic rate versus temperature relationships for decomposition, usually with significant rates in the range 50°-150°C (O'Donnell, 1990).

Radiation enhances degradation, especially thermal effects, which often occur in parallel with radiation exposure. As energy is added to a system, the temperature is raised. The reaction rates are often quite different in a glass and rubber of a given polymer and undergo changes at the transition temperatures. The deterioration in the properties of polymers may be markedly increased by relatively small rises in temperature (Garrett et al., 1990). This tends to be the case with most chemical reactions due to the energy provided by an increase in temperature. An increase in temperature when combined with radiation leads to an increase in chain scission. Radical reaction kinetics are dependent upon the polymer morphology, crystallinity, molecular weight distribution and the main chain stability as well as its higher structure (morphology) (Kaplan, 1991). Time-temperature-dose rate models have been developed to predict the long-term aging of polymers exposed to radiation (Gillen and Clough, 1989).

The surface effects of radiation tend to be much greater than the effects to the core of a sample due to greater exposure of the surface. The polymer can be affected directly by the radiation or by the products of radiation from the polymer's environment, specifically the thermal and chemical characteristics of the environment. As a result of

energy transfer, molecular components present in only small amounts may be the main sites of chemical change (O'Donnell, 1990). In addition, hydrogen atoms are often yielded due to radiation which can lead to cross-linking. The penetration of low-molecular-weight liquids into the volume of many polymers leads to a decrease in the radiation yield of cross linking (Smirnov and Dubova, 1992). Because light is a type of radiation, some correlations can be made between degradation caused by light (photo-degradation) and gamma radiation. The energy from light is sufficient to break chemical bonds, especially short ones. In addition, chromophoric groups (double bonds) are necessary to absorb the radiation. Strong absorbers are expected to decompose roughly three orders of magnitude faster than weak absorbers (17). Because absorption of radiation is an essential first step to photo degradation, strongly absorbed radiation will be attenuated as it passes through the polymer and reaction will be concentrated in the surface layers. Thus, photolysis is often identified by the evolution of hydrogen, the *development of insolubility* and discoloration. In addition, UV radiation often initiates oxidation. Photo degradation can not readily be predicted from the chemical structure due to small impurities and abnormalities often present in polymer chains. It must be tested experimentally.

Thermosets have much more stability to irradiation that thermoplastics. Counterintuitively perhaps, thermosets exposed to radiation in air degrade more, the *lower* the dose rate. This is because of the oxygen concentration in the interior of samples. The dissolved oxygen reacts with the radiation induced radicals and builds peroxides. Thus, the thermoset becomes unstable and slowly decays by chain scission. The longer the irradiation time, the more complete is the break down of the peroxides and the damage to the material (Wilski, 1990).

Epoxy resins tend to be quite radiation resistant with fillers providing even more stabilization. Most studies have irradiated the epoxy with high doses at short time intervals. In all cases, epoxy plastics proved to be extraordinarily resistant to radiation (7). Samples exposed to a low dose rate for ten years showed the same effects as the short term, high dose samples. Strength remained the same, however surface-dependent properties were markedly influenced by the does rate (Gilfrich and Wilski, 1992).

Not surprisingly, the irradiation of *nylon (polyamide)* is reflected in the mechanical properties. As radiation dose is increase, the structural integrity is decreased. In one particular study on nylon 6 fibers, it was found that melting temperature decreased, as did degree of crystallinity, with radiation dose (Ellison et al., 1989). The presence of oxygen enhanced the effects of the radiation.

Polybutadiene crosslinks when exposed to radiation. The degree of cross-linking can be established using NMR to determine the amount of carbon-carbon double bonds. Radiation causes free radicals to form which then crosslink. "Upon reaching the glass-transition temperature of the elastomers, more than half of the initial radical concentration had decayed (Dole, 1973)." As energy is increased, temperature increases. Once the Tg has been surpassed, segmental motion begins.

The degradation products of *PET (polyester)* exposed to radiation are carbon dioxide, carbon monoxide, methane and hydrogen gas. The products are affected by the exact structure of the PET, chemical composition and the presence of other reactants such as moisture and oxygen (Dole, 1973).

The degree of degradation due to the irradiation of *polythylene* is a function of its crystallinity; the higher crystallinity samples were found to be mechanically stronger after irradiation (Torikai et al., 1990). In addition, irradiation of low density PE yields a lot of cross-linking while chain scission is primarily achieved in medium and high density PE. It is thought that segmental motion of the polymer chains affects the polymer stability (Torikai et al., 1994). Radiation increases the degradation of *polyethylene*, especially when in contact with a solvent such as toluene, xylene or benzene (Smirnov and Dubova, 1992). The degradation products have little effect on plutonium solubility (Greenfield et al., 1993), however the potential formation of colloids is not known. Radiation causes both cross-linking and oxidative degradation. Irradiation of polyethylene caused both oxidative degradation and crosslinking, and the kinetics of the first process were controlled by diffusion of atmospheric oxygen into the bulk of the material (Spadaro, 1993). In addition, the temperature affects the mobility of free radicals.

In the case of *polypropylene*, the lower the crystallinity, the lower the irradiated degradation. In addition, the narrower the molecular weight distribution, the more stable the polymer is to radiation degradation. Four main radical species formed during the irradiation of polypropylene are alkyls, allyls, polyenyls and peroxys (Williams, 1990). Radiation effects on polypropylene are greatest when oxygen is present due to oxidation which is accelerated by radiation. This leads to discoloration and embrittlement. Oxidation occurs at a greater rate on the surface of samples and the degradation continues after radiation exposure. Published results show that post-irradiation degradation of [polypropylene] occurs by oxidative mechanism due to the free macro-radicals trapped in the crystalline regions (Khoylou and Katbab, 1993). One study followed post-radiation affects for 12 months and found that degradation continued via chain scission mechanism. The recommendation was that semi-crystalline

polypropylene should be stabilized against post-irradiation degradation, if it is going to be irradiated by high energy radiation sources (Khoylou and Katbab, 1993). Quenched polypropylene with a lower crystallinity has a higher radiation durability in than unquenched polypropylene. Also, higher molecular weight polypropylene degrades less than does lower molecular weight polypropylene (Ishigaki and Yoshii, 1992).

Polystyrene is quite radiation resistant and has been used in many early applications (Dole, 1973). However, radiation exposure expedites the degradation process. In the case of polystyrene, IR spectrometry has shown that the aromatic and aliphatic groups are broken down exponentially while carbonyl groups are increased (El-Agramy and Shabaka, 1990). Radiation was found to enhance the rate of thermal degradation, corresponding to an increase in temperature of about 100°C (Garrett, 1990).

Although *Teflon* has superior thermal and chemical stability, its well known sensitivity to radiation limits its use in many cases (Wheeler and Pepper, 1990). Radiation damage is usually concentrated on the surface of the material. X-ray photoelectron spectroscopy (XPS) has been used to model Teflon and it is thought that the surface is made up of a network of branched or cross-linked fluorocarbon chains. With radiation, there is a loss of fluorine and an appearance of unsaturation as saturated fluorocarbon gas is evolved (Svoboda et al., 1990). This continues until a certain level of damage is reached, after which the material degrades into saturated and unsaturated fluorocarbons.

As with other polymers, exposure to radiation accelerates degradation reactions. According to Nass and Heiberger (1986), "If unstabilized *PVC* is exposed to heat (temperatures above 100°C), ultraviolet light, or gamma radiation, then depending on the intensity of the exposure and the type of PVC, a cleavage of HCl accompanied by polyene sequence formation and cross-linking along the chain or intermolecularly can occur," which is intensified by the presence of oxygen. However, PVC has been shown to have little effect on plutonium solubility even after extensive α-irradiation (Imasaka et al., 1992).

When *silicone* is exposed to radiation, it initially forms crosslinks but as the radiation generates more heat in the silicone, it degrades. The crosslinks cause the silicone to become more rigid. Thus, the physical lifetime of silicone exposed to radiation is often dependent on the flexibility needed from the sample (Lynch, 1978).

6.2.1.6 Colloid Sorption and Chelation. Colloids exist naturally as fracture-lining materials, clays, bacteria, algae, and humic acid, but they can also be the product of degradation of man-made materials and debris, such as glass, fuels and greases, metals, biomass evolved on introduced materials and organic waste (see e.g., Meike and

Wittwer, 1994). A number of processes have already been identified as potential originators of radionuclide sorbing colloids in the WP environment (Olofsson et al., 1981, 1982a,b). These are:

1. Leaching of the waste form by groundwater.
2. Corrosion of canister material (iron oxides and hydroxides).
3. Degradation of backfill material (if present).
4. Naturally occurring colloids such as clays, organics, and precipitates.
5. Organic materials that result from man-made modification of the NFE.
7. Extracellular and cellular microbial biomass.

Hydrocarbons that result from the thermal decomposition of greases, paints, and other organic items can form ligands that may enhance radionuclide transport. The little data that exists on this subject suggests that organics more effectively complex radionuclides than inorganic complexes or single ions (Raloff, 1990). The presence of colloidal and organic products may thus produce an environment that greatly enhances radionuclide migration. As a result, the movement of radionuclides may not be predictable through inorganic chemistry alone. The number and significance of other materials to be used in the repository that fall into this same category are still unknown.

Polymers do not readily sorb metals, however, there have been many polymers which have been chelated in order to promote sorption of metals. The stereochemistry and the nature of the complexes are markedly dependent upon the molar ratios of the reactants, the pH of the system and the nature of the anions involved (El-Sonbati et al., 1994). There are also data for metal complexes involving aliphatic alcohol compounds binding through deprotonated hydroxyl groups. The data for these complexes indicated that deprotonated hydroxyl binding is strong compared to carboxylate binding, especially at higher pH values (Greenfield et al., 1993). An extensive project undertaken by Raber and Garrison (1983) to determine which materials would limit the effects of radionuclide sorption. It was found that polypropylene and polyethylene sorbed the least.

There have been many studies of metal chelates of polymers for high performance and filtering applications, especially of epoxy. In one study (Kurnoskin, 1992), it was found that synthesized metalliferous epoxy chelate polymers have high thermal stability and chemical resistance when compared to the polymer alone.

Metal adsorption sites on *polypropylene* are likely to be carboxyl and carbonyl groups formed as the surface degrades under the influence of oxygen, heat or light, other sites are contributed by catalysts, plasticizers and fillers (Kim and Hill, 1993). Polypropylene is known to absorb significant amounts of lead from solutions. A study which

compared the sorption of lead to polypropylene and borosilicate glass found that at pH 7.0, polypropylene "adsorbed significantly more lead than borosilicate glass and that at pH 5.5 polypropylene adsorbed less than the glass," indicating a fundamental change in the nature of the polypropylene surface (Kim and Hill, 1993).

Many chelating resins have been developed with the intent to separate and recover metal ions (i.e., from dilute solutions). It has been found that the hydrophobic character of the *polystyrene* backbone negatively affects the access of metal ions to the chelating groups in the resin. The presence of hydrophilic ligands in the polymer network improves chelation (Chessa et al., 1991). Column experiments have shown that pH is also a factor owing to the different rate of formation of the immobilized chelated species. At pH=6, Pt(IV) flows unaffected from a mixture of Pd(II), Pt(IV) and Au(III), whereas Au(III) and Pd(II) are both retained and successively separated by selective elution. From the same mixture at pH ≤ 0 only Au(III) is sorbed by anionic exchange (Chessa et al., 1991).

Russian studies have suggested that the sorption of various radionuclides from sea water on *Teflon* is time dependent. Others have shown that in the presence of tetraphenylboron, there is selective sorption of trace amounts of cesium from aqueous solution onto the hydrophobic surfaces of polyethylene and Teflon (Raber and Garrison, 1983). This same study found that Teflon was the least sorptive of all the polymers tested.

General Significance to YMP. It has been found that at elevated temperatures, and for many polymers, temperatures within the range of potential repository conditions, polymers are quite susceptible to degradation, so much so that the most of the polymers will degrade within hours rather than the thousands of years which the repository must contain the waste. Given this, it may be possible to plan to observe the impacts of polymer degradation during the retrieval period. However, some care will need to be taken with respect to polymers because the high temperature effects will not be observed. Further studies and modeling should then be conducted with such rates in mind. For example, much of the chemical modeling of long-term chemical effects on the NFE may be conducted with the final products of the polymer degradation as reactants. The final products of most polymers are known, the majority are monomer, hydrocarbons and some volatile products such as toluene, xylene and cresol. Polymer resins should not be used in any structural applications and chemical significance should be assessed for each material. Because of a number of potential thermal degradation effects, epoxy resins should not be included in the permanent structure, without detailed long term tests.

6.2.2 Biotic Chemistry (microbially mediated chemistry)

There is growing awareness that biotic factors could affect the integrity of the repository by a number of processes. These include microbially induced corrosion (MIC) of the waste package and construction materials, alteration of the chemical environment, and contributions to the transport of radionuclides. A variety of different types of bacteria normally inhabit the deep subsurface. In the course of construction both new materials and non-endogenous bacteria will be introduced to the repository environment. Conditions after waste emplacement are expected to alter dramatically. Extremely elevated temperatures with accompanying desiccation, and possible radiation exposure, are among the environmental conditions expected to result from radionuclide decay. Microbes can survive and adapt to extreme environmental conditions, take advantage of microenvironments, and remain active in generated spatial gradients. Microorganisms employ extremely diverse modes of metabolism. For the purpose of repository performance, this translates to mean that microbes can be involved in a wide variety of processes in a geological setting (see Horn and Meike, 1995 for a detailed discussion of the issues). Information on the degradation of various materials of significance to a repository are being gathered from diverse sources (see the section on polymer biodegradation below) of particular use are the data that have been collected with respect to the bioremediation of landfills and other forms of chemical waste.

Microbially mediated chemical processes can significantly alter the geochemical environment and have direct impacts on repository materials. Microbes are capable of utilizing a wide range of organic compounds to serve as sources of carbon. Autotrophic organisms are capable of carbon dioxide fixation to satisfy carbon requirements for synthesis of cellular materials. Energy can be derived from either reduced organic or inorganic compounds. Hydrogen gas, nitrogen, ammonia, nitrite, ferrous iron, and reduced sulfur compounds, for example, can all be used as energy sources by various microbial groups. Similarly, oxygen or a wide array of inorganic compounds may be utilized as a terminal electron sink. Nutrient supply, rate of nutrient transport, and the composition of the repository community will govern the specific types of metabolic activities that occur. Bacteria can also bind metals, secrete metal-complexing compounds, and transform metal ions to altered speciation states. These capabilities may enable the transport of radionuclides from the near-field environment. These considerations demonstrate that microbial biota are integral to environmental mass transfer. Thus, microbial contributions to overall environmental chemistry cannot and should not be ignored if prediction of the long-term integrity of a nuclear repository is